



TECHNISCHE UNIVERSITÄT MÜNCHEN

Fakultät für Medizin

**Single-cell transcriptomics and fate-mapping combined with
mathematical modelling reveal mechanisms of CD8⁺ T cell
differentiation and exhaustion**

Albulena Toska

Vollständiger Abdruck der von der Fakultät für Medizin der Technischen Universität München zur Erlangung des akademischen Grades einer

Doktorin der Naturwissenschaften

genehmigten Dissertation.

Vorsitzende/r: Prof. Dr. Heiko Lickert

Prüfende der Dissertation:

1. TUM Junior Fellow Dr. Michael Flossdorf
2. Prof. Dr. Dietmar Zehn

Diese Dissertation wurde am 05.10.2021 bei der Technischen Universität München eingereicht und durch die Fakultät für Medizin am 12.04.2022 angenommen.

Abstract

Upon antigen encounter and activation, CD8⁺ T cells undergo several rounds of cell divisions and differentiate into rapid-proliferating effector (EFF) cells and slow-dividing memory precursor (MP) cells. EFF cells exhibit strong cytolytic functions and mediate pathogen killing, resulting in the resolution of the infection.

Conversely, during chronic diseases, the immune system fails to clear the infection. The persisting antigen has developmental consequences: It triggers the up-regulation of inhibitory molecules and the loss of effector functions, which eventually renders the T cells in a dysfunctional state termed exhaustion.

How the antigen persistence drives the formation of exhausted cell states, which role proliferation plays during the process of exhaustion and which functional subsets deviate from the canonical path of differentiation to become exhausted remain key open questions.

In this thesis, we utilised the mouse models of acute and chronic lymphocytic choriomeningitis virus (LCMV) infection and the bacterial infection system with *Listeria monocytogenes*. We complemented cell division speed measurements with *in vivo* fate-mapping as well as transcriptomic data on a single cell level and performed stochastic mathematical modelling.

First, we performed single-cell RNA sequencing and analysed a time series of the CD8⁺ T cell responses during the acute infections with both model pathogens. Trajectory inference analyses outlined the scheme to construct the mathematical model. The topology of the model resembled the progressive differentiation with a cell cycle drop out effect extension: Naïve T cells differentiate into central MP T cells, then transition through an intermediate effector MP state before they become terminally differentiated EFF cells. Exit out of the cell cycle is possible from each differentiation stage and locks the cells in the preceding state-determining phenotype. We show that the extended progressive model explains the cell variability in response to both utilised models, the viral and bacterial infection.

Second, we investigated the time-resolved single-cell transcriptomes during the expansion phase of the acute and persisting LCMV infection. We found that exhausted memory-like (MEX) and early effector (EEX) T cells separated very early from their functional equivalents. Strikingly, MEX and EEX subsets retained a high degree of plasticity, allowing the rescue of these two subsets from the exhaustion imprinting upon transfer to more favourable conditions.

Third, we compared how the course of the expansion phase during the chronic LCMV infection deviated from the acute infection. We achieved this through the simultaneous fitting and forward selection of the acute and chronic LCMV data, using the extended progressive model. This enabled us to identify the parameters that are altered during the chronic response. We have observed that the transition from EMP to EFF is forty times smaller in the chronic infection setting compared to the acute one, preventing the formation of the latter population. Furthermore, we found that premature division cessation, most presumably mediated through the expression of inhibitory receptors, occurred earlier in the persisting infection. In our model

the differentiation program is proliferation-driven, and division drop-out locks the cells in the quiescent state, which additionally prevents the acquisition of a functional effector phenotype. Fourth, by means of single-cell driven mathematical modelling, we investigated how exhausted T cells emerge from the canonical pathway of differentiation. We constructed the model based on the developmental scheme of differentiation arrest. This model explains the heterogeneity of the exhausted subsets such that functional cells exhausted at different stages of normal development. Our results have supported the arrested exhaustion model and experimental validation revealed that the dysfunctional states are driven by the independent exhaustion of the MP and EMP subsets.

We demonstrate that T cell differentiation follows a conserved scheme, and exhaustion poses a deviation from the canonical path that is reversible at early time points of the chronic infection. Furthermore, we identified cell cycle arrest as an essential regulator of T cell exhaustion. This suggests that combinatorial interventions that target the cell division activity could, in addition to immune checkpoint blockade treatments, improve therapeutic outcomes.

Zusammenfassung

Nach Antigenkontakt und Aktivierung durchlaufen $CD8^+$ T Zellen mehrere Zellteilungsrunden und differenzieren in schnell proliferierende Effektorzellen (EFF) und in sich langsam teilende Gedächtnisvorläuferzellen (MP). EFF-Zellen haben eine starke zytolytische Funktion und sorgen für die Abtötung von Krankheitserregern, was zur Eindämmung einer Infektion führt.

Im Verlauf chronischer Krankheiten hingegen gelingt es dem Immunsystem nicht, die Infektion zu beseitigen. Das Fortbestehen des Antigens hat Folgen für die Entwicklung der Zellen: Es führt zur Hochregulierung hemmender Rezeptoren und zum Verlust von Effektorfunktionen, wodurch die T Zellen schließlich in einen dysfunktionalen Zustand getrieben werden, der als Erschöpfung bezeichnet wird.

In der vorliegenden Dissertation haben wir die Mausmodelle der akuten und chronischen Infektion mit dem lymphozytischen Choriomeningitis Virus (LCMV) sowie das bakterielle Infektionssystem mit *Listeria monocytogenes* verwendet. Wir haben Messungen der Zellteilungsgeschwindigkeit mit *in vivo* Einzelzellnachkommenschaften sowie Einzelzelltranskriptomdaten kombiniert und eine stochastische mathematische Modellierung durchgeführt.

Als erstes führten wir Einzelzell-RNA-Sequenzierungen durch und analysierten eine Zeitreihe der $CD8^+$ T-Zellantworten während der akuten Infektionen mit beiden Modellpathogenen. Anhand von Analysen zur Ableitung von Differenzierungsmustern skizzierten wir das Schema für die Konstruktion des mathematischen Modells. Die Topologie des Modells entsprach der progressiven Differenzierung mit der Erweiterung eines Zellzyklus-Ausstiegseffektes: Naive T-Zellen differenzieren zu zentralen MP T-Zellen, durchlaufen dann einen intermediären Effektor MP-Zustand bevor sie zu terminal differenzierten EFF-Zellen werden. Der Austritt aus dem Zellzyklus ist von jedem Differenzierungsstadium aus möglich und hält die Zellen in dem vorhergehenden zustandsbestimmenden Phänotyp fest. Wir zeigen, dass dieses erweiterte progressive Modell die Zellvariabilität, welche als Antwort auf die Infektion hervorgerufen in beiden verwendeten Mausmodellen, viral als auch bakteriell, erklärt.

Zweitens führten wir eine zeitaufgelöste Untersuchung der Einzelzelltranskriptome während der Expansionsphase der akuten und chronischen LCMV Infektion durch. Wir zeigten, dass sich erschöpfte gedächtnisähnliche (MEX) und frühe Effektor-T-Zellen (EEX) bereits sehr früh von ihren funktionellen Varianten trennen. Auffallend ist, dass die MEX- und EEX-Populationen ein hohes Maß an Plastizität bewahren, was die Rettung dieser beiden Populationen aus dem Erschöpfungsprogramm bei Überführung in günstigere Bedingungen ermöglichte.

Drittens verglichen wir, wie der Verlauf der Expansionsphase während der chronischen LCMV Infektion von der akuten Infektion abwich. Dies erreichten wir durch die gleichzeitige Anpassung und Vorwärtsselektion der akuten und chronischen LCMV-Daten unter der Verwendung des erweiterten progressiven Differenzierungsmodells. Dadurch konnten wir die Parameter identifizieren, die sich während der chronischen Immunantwort verändern. Wir haben festgestellt, dass der Übergang von EMP zu EFF bei einer chronischen Infektion vierzigmal kleiner ist als bei

einer akuten Infektion, wodurch die Entstehung der EFF Population verhindert wird. Darüber hinaus haben wir herausgefunden, dass die vorzeitige Beendigung der Zellteilung, die vermutlich durch die Expression inhibitorischer Rezeptoren vermittelt wird, bei der persistierenden Infektion früher erfolgt. In unserem Modell ist das Differenzierungsprogramm proliferationsgetrieben, und der Teilungsstopp hält die Zellen im jeweiligem Differenzierungszustand fest, was zusätzlich die Erlangung eines funktionellen Effektor-Phänotyps verhindert.

Viertens untersuchten wir mit Hilfe einer von Einzelzellen gestützten mathematischen Modellierung wie erschöpfte T-Zellen aus dem kanonischen Differenzierungspfad hervorgehen. Wir konstruierten das Modell auf der Grundlage des Entwicklungsschemas des Differenzierungsstopps. Dieses Modell erklärt die Heterogenität der erschöpften Populationen, nämlich dass funktionelle Zellen in verschiedenen Stadien der normalen Entwicklung erschöpfen. Diese Ergebnisse und experimentelle Validierungen stützen das Modell der arretierten Erschöpfung und zeigen, dass die dysfunktionalen Zustände auf die unabhängige Erschöpfung der MP- und EMP-Untergruppen zurückzuführen sind.

Wir zeigen, dass die T-Zell Differenzierung einem festen Schema folgt und die Erschöpfung eine Abweichung von diesem klassischen Pfad darstellt, die zu frühen Zeitpunkten der chronischen Infektion noch reversibel ist. Darüber hinaus identifizierten wir den Zellzyklus-Austritt als einen wesentlichen Regulierungsmechanismus für die T-Zell Erschöpfung. Unsere Ergebnisse deuten darauf hin, dass kombinatorische Interventionen, die auf die Zellteilungsaktivität abzielen, zusätzlich zu Behandlungen mit Immun-Checkpoint-Blockaden die Behandlungsergebnisse solcher Infektionen verbessern können.

Contents

1. Introduction	11
1.1. Immune system	11
1.2. The role of CD8 ⁺ T cell immunity	12
1.3. Model systems to study CD8 ⁺ T cell immunity	13
1.4. Acute infection and CD8 ⁺ T cell differentiation	15
1.5. Chronic infection and CD8 ⁺ T cell exhaustion	17
1.6. Mathematical models of T cell responses	22
1.7. Regulation of clonal expansion by cell division speed	25
2. Aim of this thesis	27
3. The CD8⁺ T cell response during the early phase of an acute infection	29
3.1. Distinct division speed of memory precursors and effector T cell subsets	30
3.2. High variability of single CD8 ⁺ T cell responses during LCMV Armstrong infection	36
3.3. Variable recruitment to account for diverse single-cell responses	39
3.4. Time-resolved transcriptional analysis of P14 T cells after acute infection	40
3.5. Towards a uniform model of T cell differentiation during self-limiting infections .	51
3.6. Mathematical modelling corroborates the MP to EFF subset lineage relationship	55
4. Developmental plasticity and the commitment to T cell exhaustion	59
4.1. Early divergence of T cell transcriptomes following acute and chronic infection .	60
4.2. Cessation of cell division halfway before reaching peak response	65
4.3. The extended progressive model of differentiation describes the mechanisms of CD8 ⁺ T cells during the onset of the chronic infection	71
4.4. Early fate plasticity at the onset of a persisting infection	77
4.5. An early differentiation program drives the acquisition of an exhausted phenotype	83
4.6. TOX limits differentiation into the terminal effector subtype	84
4.7. MP and non-MP subsets exhaust independently	87
5. Discussion	93
5.1. Subset-dependent cell cycle speed is conserved between different infections	93
5.2. A uniform model describes CD8 ⁺ T cell responses	94
5.3. Cell cycle quiescence dictates the course of T cell exhaustion	99
5.4. The fate of the CD8 ⁺ T cells from early time points of persisting infection remains plastic	101
5.5. The arrested model of T cell exhaustion	103
5.6. Significance	104

6. Materials and Methods	105
6.1. Materials	106
6.2. Experimental Methods	112
6.2.1. Mice	112
6.2.2. Infections with LCMV	112
6.2.3. Infections with <i>L.m.</i> -OVA	112
6.2.4. Infections with MVA-OVA	112
6.2.5. Purification of T cells from the blood	113
6.2.6. Purification of T cells from the spleen and lymph nodes	113
6.2.7. Adoptive T cell transfers	113
6.2.8. Cell surface staining for flow cytometry	114
6.2.9. Intracellular staining of transcription factors	114
6.2.10. Intracellular staining of phosphorylated proteins and transcription factors	114
6.2.11. BrdU staining for cell cycle phase quantification	114
6.2.12. Single-cell fate-mapping	114
6.2.13. Re-transfer experiments	115
6.2.14. Analysis of flow cytometry data	115
6.2.15. Re-isolation of T cell populations for single cell RNA sequencing	115
6.2.16. Single cell RNA sequencing	116
6.3. Bioinformatics methods	117
6.3.1. Generation of gene expression count matrices	117
6.3.2. Data processing and quality control	117
6.3.3. De-multiplexing of samples	117
6.3.4. Proteogenomics analysis	118
6.3.5. Removal of doublets	118
6.3.6. LCMV data integration and batch correction	118
6.3.7. Cell cycle scoring	119
6.3.8. Dimensionality reduction and clustering	119
6.3.9. Differential gene expression testing and GO term analysis	119
6.3.10. T cell signature scoring	119
6.3.11. Trajectory inference analysis	119
6.3.12. Inferring cell cycle drop out from scRNA-seq data	120
6.3.13. Bioinformatics analysis of OTI T cells derived from <i>L.m.</i> -OVA infection	120
6.3.14. Bioinformatics analysis of LCMV-specific CD8 ⁺ TOX knock-out and wild-type T cells responses during LCMV clone 13 infection	121
6.4. Mathematical and statistical methods	121
6.4.1. Summary statistics	121
6.4.2. Quantification of cell cycle speed and the length of cell cycle phases	122
6.4.3. Mathematical modelling	122

6.4.4. Fitting the model to the data	124
6.4.5. Model comparison and selection	125
6.4.6. Confidence intervals for the model parameters	126
6.4.7. Model simulations	126
7. Abbreviations	127
Bibliography	131
A. Appendix I	166
B. Appendix II	173
C. Appendix III	179
C.1. Summary of experimental data	180
C.2. ODE system for first and second order moments for the cell cycle drop out extended progressive model	181
C.3. ODE system for first and second order moments for the arrested model of T cell exhaustion	185

1. Introduction

1.1. Immune system

The mammalian immune system comprises a complicated network of cellular and molecular mediators that have evolved to protect its host from foreign agents and invading pathogens. The immune system is compartmentalised, and immune responses are divided into two arms, the innate and adaptive immunity (Chaplin 2010).

Two arms of the immune system

The innate immunity acts upon the recognition of conserved pathogenic patterns. It elicits an immediate and unspecific inflammatory response, which allows to efficiently fight various different types of pathogens (Iwasaki et al. 2015). In contrast, defence mechanisms mediated by the adaptive immunity are attuned to specific targets and result in the formation of immunological memory. This ability to learn from the first contact with an infectious agent (primary response) and to store this information, promoting faster and stronger responses after the subsequent encounter (secondary response) represents a unique feature of the adaptive immune response (Farber et al. 2016). Immunological memory is maintained by specialised immune memory cells, and protections conferred by these memory cells can last for long periods, even life-long in some cases (Farber et al. 2016). The mechanism of vaccine-induced protection against infectious diseases is based on efficiently triggering the development of immunological memory (Farber et al. 2016).

Mechanisms of the adaptive response

The adaptive arm of the immune system is further subdivided into B cell-mediated humoral and T cell-driven cellular responses.

B cells secrete soluble antibodies that bind infectious targets and their products and act through neutralisation, opsonisation and activation of the complement system. Neutralisation is driven by the antibodies that bind to the pathogen and hinder it from entering cells and tissues. Furthermore, antibody-coated pathogens can be recognised and taken in by phagocytes (opsonisation). Antibodies bound to a pathogen can also activate proteins of the complement system that directly attack the membrane of the pathogen (Punt et al. 2009).

T cells produce inflammatory cytokines or induce cell apoptosis of target cells through direct interactions. There are two major groups of T cells, supporting or regulating CD4⁺ and cytotoxic CD8⁺ T cells (Laidlaw et al. 2016). The CD4⁺ T cells regulate or support other immune cell types in exerting their functions (Reiner 2007). They can directly interact with CD8⁺ T cells and promote their proliferation and survival. Regulatory CD4⁺ T have opposing functions. They can suppress the CD8⁺ T cell response by modulation of the chemokine and cytokine

milieu without direct cell-cell interactions (Laidlaw et al. 2016). CD8⁺ T cells are able to kill infected target cells directly (Russell et al. 2002). Therefore, successful pathogen clearance relies on the generation of efficient CD8⁺ T cell immunity.

1.2. The role of CD8⁺ T cell immunity

Naïve CD8⁺ T cells have the capacity to massively expand and differentiate into effector and memory cells that migrate through the body to reach the site of infection.

T cell activation

After the completion of the primary thymic development, mature naïve T cells enter the bloodstream and migrate through the lymphatics, where they continually recirculate between the blood to the secondary lymphoid organs, such as the lymph nodes and spleen (Masopust et al. 2013).

The secondary lymphoid organs serve as a site where in the presence of an infection, CD8⁺ T cells are primed by antigen-presenting cells (APCs) (Masopust et al. 2013). APCs, typically dendritic cells (DCs), engulf pathogens and are able to process and present peptides of these pathogens via their surface major histocompatibility complex (MHC) class I molecules (Masopust et al. 2013). Since each one of the CD8⁺ T cells expresses a unique T cell receptor (TCR), they have to scan multiple DCs expressing peptide:MHC class I, while roving through the blood and lymphatics (Masopust et al. 2013). Recognising the presented antigen through the interaction of the TCR-peptide:MHC class I complex is the first of the three signals a CD8⁺ T cell must receive for an efficient priming, leading to the induction of a protective response. The second signal is the interaction of the T cell co-stimulatory receptor CD28 with CD80 and CD86, expressed on APCs (Smith-Garvin et al. 2009). Lack of the follow-on signal 2 during the T cell priming leads to the physical deletion or a non-responsive state of the cell, called anergy (Schwartz 2003). While signals 1 and 2 are sufficient to induce several cell divisions, for extensive proliferation and the development of effector functions, the third signal, stimulation with inflammatory cytokines produced by the APCs, is required (Curtsinger et al. 2010). The cytokines driving the third signal direct the developmental paths of a naïve CD8⁺ T cell.

CD8⁺ T cell functions

Upon activation, CD8⁺ T cells proliferate extensively, leave the lymph nodes and migrate to the site of infection in the peripheral tissues, where they kill the infected cells (Zhang et al. 2011). The killing of the target cell mediated by CD8⁺ T cells is dependent on the release of the cytotoxic granules by specialised lysosomes containing perforin and granzymes (Stinchcombe et al. 2007). Perforin forms pores in the membranes of target cells, which allows the delivery of granzymes inside (Stinchcombe et al. 2007). Granzymes are serine esterases that contribute to

the killing of the target cells by inducing apoptosis (Stinchcombe et al. 2007).

In addition, CD8⁺ T cells produce type I interferon cytokines and tumour necrosis factor (TNF). The release of interferon- γ (IFN- γ) restricts virus replication, while both IFN- γ and TNF activate the expression of MHC class II on APCs (Boehm et al. 2013). TNF can also directly induce apoptosis of the infected target cells through the interaction with TNF-receptors (Boehm et al. 2013; Russell et al. 2002).

1.3. Model systems to study CD8⁺ T cell immunity

Animal models have been widely used to study immunology, and experiments in mice have been performed to model the human immune system. In the next subsection, two infections models using mice are introduced to effectively investigate CD8⁺ T cell immunity.

The LCMV infection model

The strain of lymphocytic choriomeningitis virus (LCMV) infection was discovered in the 1930ies by Charles Armstrong (Muckenfuss et al. 1933; Traub 1936). The LCMV is an enveloped and negative-sense single-stranded RNA virus. Even though, it was primarily isolated from human hosts, its natural reservoirs are rodents, such as the common house mice (Zhou et al. 2012).

LCMV is widely used as a model to study viral pathogenesis and immune responses. Due to its non-cytolytic nature, the LCMV makes a great infection model to study the effector responses *in vivo* since the observed tissue damage and pathology are solely attributed to the immune response and not the virus itself (Zhou et al. 2012).

Using the LCMV Armstrong infection in mice, Doherty and Zinkernagel performed seminal work. They discovered that MHC class I restriction, the ability to recognise LCMV-peptide presented via MHC class I molecules allowed the specific killing of LCMV-infected target cells by cytotoxic T cells (Zinkernagel et al. 1973). For this finding, Doherty and Zinkernagel were awarded the Nobel prize in medicine (Abdel-Hakeem 2019).

Depending on the strain, virus variant, dose and route of infection, LCMV can cause a wide range of immune responses, spanning from a functional effector response during an acute infection setting to an immune dysfunction during a persisting infection.

The application of the LCMV infection model has led to several important findings that enhanced the understanding of biology.

For example, studies using the acute-resolving infection with LCMV Armstrong found that the cells, recognising the H-2D^b-restricted LCMV gp33 epitope, are rare with a frequency of $1 : 2 \times 10^5$ naïve T cells (Blattman et al. 2002). After infection with LCMV Armstrong, naïve gp33-specific CD8⁺ T cells undergo more than 14 divisions in the first week of infection and expand over 10^{3-4} fold, before contracting where only approximately 5 % of the activated gp33-specific CD8⁺ T cells survive and persist long-term within a pathogen-free host (Blattman et al. 2002; Murali-Krishna et al. 1999).

Furthermore, it has been shown that CD8⁺ T cells from LCMV immune-mice protect from a re-occurring infection with the same pathogen (immunological memory) and contributed substantially to the understanding of immune memory (Murali-Krishna et al. 1998, 1999).

In the 1980s, Ahmed and colleagues discovered several mutant strains isolated from different tissues of LCMV Armstrong infected mice. One strain, isolated from the spleen (clone 13), harboured a distinct kinetics of infection and displayed a unique infection pathology (Ahmed et al. 1984). The LCMV clone 13 strain differed from the original strain only by three amino acids in the viral polymerase and glycoprotein, and yet allowed the disease to spread to all inner organs (Matloubian et al. 1990; Sullivan et al. 2011). While the infection with the primary isolate, LCMV Armstrong, results in spontaneous clearance of the virus within a week (Wherry et al. 2003a), the LCMV clone 13 strain persists for up to 90 days before it becomes undetectable from the blood and many organs, with life-long viremia in the spleen.

In addition, in studies using the LCMV clone 13 infection, T cell exhaustion has been first documented as an activated persisting T cell subset that lacks effector functions (Gallimore et al. 1998; Zajac et al. 1998). The development of an exhaustion phenotype will be elaborated in section 1.5.

The mutations found in the clone 13 strain do not affect regions of the T cell epitope (Wherry et al. 2003a). This way, TCR transgenic mice were specifically engineered to generate gp33-specific CD8⁺ T cells (P14 T cells) and have been widely used to study the comparison of CD8⁺ T cell development in an acute and chronic setting.

***Listeria monocytogenes* as a model pathogen**

Another model system to study the mammalian immune response is the bacterial pathogen *Listeria monocytogenes* (*L.m.*). *L.m.* is gram-positive that causes food-borne illness in humans, especially in the most vulnerable of us such as children, elderly, pregnant women and immunocompromised individuals (Khan et al. 2015).

George Mackaness as first used this pathogen as an experimental model in laboratory mice when he investigated protective immunity (Mackaness 1964).

L. m. is able to replicate in the cytosol, and, after the discovery of MHC class I restricted immunity (Zinkernagel et al. 1973), it helped to characterise the T cell response directed to specific bacterial peptides. The researchers found that the clearance of this bacterial pathogen relies mainly on the immune response mediated by CD8⁺ T cells (McGregor et al. 1970). Since then the *L. m.* infection model has been widely used to characterise the formation of the T cell memory and to study the naïve-to-memory CD8⁺ T cell differentiation.

The course of infection with *L. m.* can easily be modulated, for example by the administration of antibiotics. The bacterial susceptibility to antibiotic treatment has been exploited to understand the impact of the inflammatory response on the T cell response (Mercado et al. 2000). The study has demonstrated, that the T cell expansion requires only on a very short activation stimulus, and that this activation does not rely on continuous TCR stimulation (Mercado et al. 2000).

Using the recombinant *L. m.* genetically modified to express ovalbumin (OVA) in combination with engineered OTI T cells, recognising the OVA-peptide, enabled a better comparison of the primary and secondary CD8⁺ T cell responses.

To this end, the *L. m.* infection model provides an alternative experimental system to investigate CD8⁺ T cell immunity.

1.4. Acute infection and CD8⁺ T cell differentiation

Following the activation of naïve CD8⁺ T cells, a cascade of events is initiated that triggers dramatic alterations in the cell cycle, metabolism and protein expression, resulting in the production of a diverse array of cells.

The three phases of an acute infection

During the course of an acute infection, where the disease is resolved within a few days and the pathogen is eliminated, activated T cells transition through three distinct phases: priming and expansion, resolution and contraction, and memory maintenance.

In the first phase of the immune response, the expansion phase, massive proliferation of activated CD8⁺ T cells results in the vast multiplication and the formation of a diverse pool of memory precursor (MP) and effector (EFF) T cells, which reaches its peaks around day eight (Kaech et al. 2012).

The large pool of EFF cells generated during this initial phase of the response is able to control the pathogen and clear the infection.

Following the elimination of the pathogen, the expanded T cell population undergoes a contraction phase where the majority of cells (90-95 %) die of apoptosis. The remaining 5-10 % of cells survive and populate a pool of long-lived memory T cells (Kaech et al. 2012).

Characterisation of CD8⁺ T cell subsets

Heterogeneous subsets are generated during the immune response to fight acute infections.

MP cells form the long-lived memory pool and persist long after the clearance of the infections. MPs are already present early during the initiation phase of the response and can be identified by the increased expression of the interleukin-7 receptor (IL7R) (Kaech et al. 2003). IL-7R signalling in response to IL-7 stimulation ensures homeostatic maintenance by regulating the expression of anti-apoptotic molecules (Schluns et al. 2000).

Also, sensitivity to IL-15 signalling promotes homeostatic proliferation in the absence of antigen (Zhang et al. 1998). In addition, MP cells express co-stimulatory molecules of the TNF receptor family, such as CD27 and OX40 (Croft 2003). CD27 was assigned to play a role during memory development, while its lack leads to a reduced secondary expansion (Hendriks et al. 2000).

Conversely, the absence of the co-stimulation with OX40 does not alter the primary response, but rather compromises the secondary response instead (Hendriks et al. 2005).

MP and also memory subsets can be further distinguished from effector cells by the expression of homing receptors. Central memory (CM) and CM precursors (CMP) are identified by high levels of L-selectin (CD62L) and C-C Motif Chemokine Receptor 7 (CCR7). In contrast, effector memory (EM) cells and their precursors (EMP) lack their expression (Sallusto et al. 1999). Furthermore, in comparison to the EM subset, CM cells display an enhanced ability to persist *in vivo* and are more efficient in mediating protective immunity due to their greater proliferative potential (Wherry et al. 2003b).

Overall, therefore, both EM and CM cells provide an efficient protection against re-infection. Early after priming, MP cells can be further distinguished from short-lived effector cell subsets (EFF). EFF cells exhibit a unique signature related to their phenotype, proliferation and also metabolic activities. Compared to MP cells, EFF cells lack the expression of IL7R, CD62L and CD27. Conversely, they can be characterised by showing elevated levels of Killer cell lectin-like receptor subfamily G member 1 (KLRG1) (Kaech et al. 2003), C-X3-C Motif Chemokine Receptor 1 (CX3CR1) (Böttcher et al. 2015) and exhibit cytolytic functions, such as the capacity to produce granzymes and perforins (Kaech et al. 2012).

Moreover, EFF cells display increased expansion capabilities (Kretschmer et al. 2020; Sarkar et al. 2008). The functional disparity of EFF cells implies specific metabolic needs. In contrast to MP cells, EFF subset cells have a reduced mitochondrial mass and depend mainly on glycolysis as an energy source (Windt et al. 2012).

Overall, the MP and EFF subsets play in concert to eliminate the virus and produce long-lasting protection from secondary infections.

Developmental relationships of CD8⁺ T cell subsets

Although many studies have contributed to the understanding of the developmental relationships between memory and effector T cells and explored the role of transcription factors (Kaech et al. 2012), metabolic profiles (Buck et al. 2016; Sinclair et al. 2013; Windt et al. 2012) and epigenetic modulations (Pace et al. 2018; Youngblood et al. 2017), the underlying process and the order of differentiation are not entirely understood.

It is unlikely that a cells' fate is pre-determined during thymic maturation because two adoptive transfer studies using barcoded single naïve T cells have shown that they are multipotent and produce both effector and memory T cells, including CMP and EMP cells (Buchholz et al. 2013b; Gerlach et al. 2013).

The developmental order of these subsets is a highly debated topic and a number of lineage relationship models describing CD8⁺ T cell differentiation states have been proposed to account for the differential clonal expansion of effector and memory precursor pools that arise during the immune response.

Some studies suggest that the initial cell division accounts for the clonal heterogeneity observed

during clonal expansion through asymmetric segregation of critical transcription factors and protein degradation machinery to the daughter cells (Chang et al. 2011). These studies propose asymmetric cell division (ACD) as driver of early phenotypic dichotomy resulting in either effector or memory cells formation (Arsenio et al. 2014; Kakaradov et al. 2017).

Other research has determined that terminally differentiated cells retain their effector functions during the expansion phase but lose their memory cell properties. This progressive order of differentiation is referred to as the decreasing-potential model (Ahmed et al. 1996). It provides a mechanism for creating a broad spectrum of cells in disparate differentiation states depending on the cumulative signals, such as the repetitive antigen stimulation and the receptions of other signals, that they have experienced during the infection (Ahmed et al. 1996).

A similar developmental pathway is suggested in a study from Buchholz and colleagues (Buchholz et al. 2013a). Although the signal strength or duration was not integrated into their mathematical modelling, they found that naïve CD8⁺ T cells follow a progressive developmental hierarchy with EMP and EFF subsets emerging from multipotent CMP cells (Buchholz et al. 2013a).

Another alternative model implying the opposite order is termed the linear differentiation model and suggests that CM T cells develop from a pool of EM cells that differentiated from effector cells (Wherry et al. 2003b). While the studies that back the ACD or progressive differentiation focused on the early time window between the T cell activation and the peak time point, the latter development model is supported by adoptive transfer experiments in the contraction and memory phase of the response. The absence of cognate antigen and the comparison of dissimilar T cell subsets across different states of differentiation might be the reason for the discrepancies among these three described developmental models.

1.5. Chronic infection and CD8⁺ T cell exhaustion

In contrast to an acute infection that resolves within a few days, a chronic infection lasts for long time periods. It is a consequence of the adaptive immune response failing to contain the infection. The presence of a persisting infection also shapes the CD8⁺ T cell response.

Chronic infection

The development of a chronic infection depends on two conditions: First, the immune evasion of the virus must occur and lead to viral persistence. Second, the immune system must undergo adaptations to adjust the response and limit viral replication, simultaneously avoiding immune-mediated damage of the infected tissues (Virgin et al. 2009). T cell exhaustion is a compromise between keeping the infection at bay and minimising tissue damage.

The effector CD8⁺ T cells with highly potent cytolytic properties could cause immunopathology under the constant stimulation with antigen. Therefore, during chronic infections, the differentiation program of CD8⁺ T cells, including the epigenetic landscape and metabolic and

transcriptional profiles, to develop into classical memory and effector subsets have been modified, resulting in the generation of CD8⁺ T cells with a dysfunctional state, termed exhaustion (Wherry et al. 2015).

Similarly, dysfunctional states have also been described in other experimental infection models, and as well, in chronic human infections such as HIV or HCV and cancer (Gruener et al. 2001; Schietinger et al. 2016; Shankar et al. 2000).

The exhaustion phenotype

T cell exhaustion is a finely controlled mechanism of the immune system to prevent overreaction to the infection. T cell exhaustion does not represent an inactive state but rather a continuous adaptation to the coexistence with the persisting virus.

A successive loss of function occurs during exhaustion, whereby exhausted CD8⁺ T cells tend to lose some properties before losing others (Wherry et al. 2004, 2003a). Features such as IL-2 production, the capacity to proliferate and the *ex vivo* killing abilities are lost first. Other functions are often lost at the later and intermediate stages of exhaustion, including the ability to produce TNF (Wherry et al. 2003a). During a more severe exhaustion state, virus-specific cells ultimately lose the ability to produce IFN- γ or to degranulate (Wherry et al. 2004, 2007). Finally, the terminal stage of exhaustion is the physical deletion of the virus-specific T cells (Wherry et al. 2003a). The severity of exhaustion correlates with high antigen load, as well as with the lack of IL-21 mediated CD4⁺ T cell help (Fröhlich et al. 2009; Wherry et al. 2003a; Zander et al. 2019).

The role of inhibitory receptor expression

The exhausted T cells develop a high surface expression of co-inhibitory molecules (Wherry et al. 2003a). Through the expression of inhibitory molecules, the effectiveness of the CD8⁺ T cell response can be suppressed.

These inhibitory receptors include lymphocyte-activation gene 3 (Lag3) (Workman et al. 2005), CD39 (Chen et al. 2019; Sade-Feldman et al. 2018), cytotoxic T-lymphocyte associated protein 4 (CTLA4) (Parry et al. 2004), T cell immunoglobulin and mucin domain-containing protein 3 (Tim3) (Jin et al. 2010; Jones et al. 2008), and, most importantly, programmed cell death protein 1 (PD1) (Barber et al. 2006). The expression of most of these inhibitory molecules is already induced upon T cell activation, and cumulative co-expression correlates with severity of exhaustion (Blackburn et al. 2009; Verdon et al. 2020).

How the individual inhibitor receptors modulate the T cell response has not been fully elucidated. However, it has been shown that synchronous targeting of two inhibitory receptors compared to single blockade improves the T cell response rates and indicates that each receptor has a specialised function (Blackburn et al. 2009).

Lag3. Lag3 is expressed after priming as a checkpoint to prevent excessive activation (Andrews

et al. 2019). It can cross-link with CD3, part of the TCR complex, on EFF cells and thereby block proliferation and cytokine production (Hannier et al. 1998).

CTLA4. CTLA4 is another checkpoint regulator that is also induced during the early stages of T cell priming. CTLA4 exhibits structural similarity to CD28 and competes with CD80 and CD86 for binding. Blockade of CD28 via CTLA4 inhibits activation, proliferation, IL-2 production, glucose metabolism, and induces cell cycle drop out (Waterhouse et al. 1995).

PD1. Probably the most prominent inhibitory receptor expressed during T cell exhaustion is programmed cell-death 1 (PD1). The expression of PD1 is up-regulated during the later stages of T cell activation and acts as an inhibitor of effector functions. PD1 interacts with its ligands (programmed cell death 1 ligand 1 (PDL1) and PDL2), inhibiting both TCR- and CD28-mediated signalling, and down-regulating the production of cytokines. It also enforces a cell cycle arrest (Sharpe et al. 2018). The expression of PD1 is often associated with T cell exhaustion, although it is also transiently expressed in functional subsets during the expansion phase and therefore not entirely specific to exhaustion (Ahn et al. 2018; Wherry et al. 2007).

CD39. Recently, CD39 has been found to exhibit inhibitory activity. CD39 expression is observed during the late stages of exhaustion, characterising severely exhausted T cells. It inhibits proliferation and the generation of EFF cells (Bastid et al. 2015; Chen et al. 2019; Sade-Feldman et al. 2018).

Tim3. Tim3 is another, relatively newly discovered inhibitory receptor, that interacts with numerous ligands. It is expressed on a subset of exhausted T cells, and its expression is associated with poor disease prognosis in a variety of cancers (Andrews et al. 2019).

Therapeutic targeting of the inhibitors

Pharmacological manipulations through targeting these checkpoint inhibitors can transiently ameliorate the deficits accumulated during exhaustion. Nowadays, immune checkpoint treatment is a proven therapy that demonstrated positive effects in the treatment of several indications. Its development has earned James P. Allison and Tasuku Honjo the 2018 Nobel prize in Physiology and Medicine (Verdon et al. 2020).

The blockade of the PD1 pathway with therapeutic antibodies has been first demonstrated in mouse studies with LCMV clone 13 infection and resulted in the increased proliferation of the exhausted T cells as well as a decreased viraemia in inner organs and blood (Barber et al. 2006). However, the antibody-based PD1 pathway blockade does not target the overall exhausted T cell population but rather a small subset of the exhausted cell pool (Blackburn et al. 2008; He et al. 2016; Im et al. 2016; Utzschneider et al. 2016a).

Memory-like exhausted subset

Exhausted T cell populations are highly heterogeneous, entailing a continuum of phenotypes and intermediate states. However, the pool of cells whose function can be leveraged by therapeutic

interventions has been identified as the exhausted “memory-like” (MEX) subset. The MEX subset is termed memory-like due to the enriched expression of memory signature genes.

For example, MEX cells express IL7R, CD62L, CCR7, T-Box Transcription Factor 21 (T-bet), and T cell factor 1 (TCF1) in addition to their preserved exhausted phenotypic features, but usually express a limited set of inhibitory receptors and lack expression of Tim3 (Blackburn et al. 2008; Im et al. 2016; Pauken et al. 2015; Utzschneider et al. 2016a, 2020).

Moreover, MEX cells have the ability to self-renew and differentiate (He et al. 2016; Im et al. 2016; Utzschneider et al. 2016a). Notably, these cells are observed at an early stage of the exhaustion response (Im et al. 2016; Utzschneider et al. 2020; Yao et al. 2019).

Even when isolating MEX cells from late time-points of chronic infection, the memory-like features are sustained (Hudson et al. 2019; Im et al. 2016; Utzschneider et al. 2016a, 2020). However, despite the possession of the memory-like traits, the exhausted phenotype of the MEX subset is retained upon transfer into more favourable conditions such as naïve hosts or ongoing and resolved acute infections (Hudson et al. 2019; Utzschneider et al. 2020, 2013).

TOX as key driver of exhaustion

Recently a collection of studies identified the expression of the transcription factor TOX, the thymocyte selection-associated high mobility group box, as a critical regulator in the generation of the MEX subset and the maintenance of the antigen-specific CD8⁺ T cell pool during chronic infections and cancer (Alfei et al. 2019; Khan et al. 2019; Scott et al. 2019; Seo et al. 2021; Yao et al. 2019).

Although TOX is also transiently present on marginal expression levels after the response with self-limiting infections, it is redundant for the development of classical MP and EFF subsets.

In contrast, during a chronic infection, already in the expansion phase, TOX is highly expressed in CD8⁺ T cells.

The MEX subset displays its increased expression as well, compared to the terminally exhausted cells (TEX) (Alfei et al. 2019; Khan et al. 2019).

Deficiency in the TOX expression fails to generate MEX cells. Furthermore, the lack of the MEX subset results in the loss of the virus-specific T cell pool throughout the course of infection. Instead, TOX-deficient CD8⁺ T cells developed into a functional KLRG1⁺ subset that exhibited increased cytotoxicity leading to increased weight loss and tissue damage in the infected mice (Alfei et al. 2019).

Developmental order of T cell exhaustion

Single-cell RNA sequencing (scRNA-seq) technologies have massively advanced our understanding in the fields of T cell differentiation and the development of exhaustion. Application of scRNA-seq led to the identification of different CD8⁺ T cell states in the context of exhaustion and shed light into the developmental relationship across these states.

Several studies have collectively placed the MEX subset at the developmental origin of T cell exhaustion. More severely exhausted T cell subsets (early exhausted cells (EEX) and TEX cells) are propagated from the MEX subset (Alfei et al. 2019; Chen et al. 2019; Hudson et al. 2019; Pritykin et al. 2021; Utzschneider et al. 2016a, 2020). During the transition from MEX to EEX, MEX cells acquire a phenotype that is related to classical EFF cells and up-regulate the expression of B lymphocyte-induced maturation protein-1 (Blimp1), Eomesodermin (Eomes) and develop cytolytic properties such as the ability to produce granzyme A and B, and perforin 1 (Chen et al. 2019; Hudson et al. 2019; Pritykin et al. 2021). TEX cells are irreversibly differentiated, and their fate-decisions cannot be reverted upon adoptive transfer into antigen-free hosts, nor can they be rejuvenated upon treatment with immune checkpoint blockades (Andrews et al. 2019).

The effectiveness of reinvigoration ultimately relies on unique epigenetic and genetic changes. For example, the binding of transcription factors as well as gene expression heavily depend on the accessibility of chromatin and the state of DNA methylation (Ghoneim et al. 2017; Khan et al. 2019; Pauken et al. 2016; Sen et al. 2016).

Origin of exhausted T cells

Although several studies have shed light on the process of exhaustion development, it remains unclear when and how exactly exhausted T cells deviate from the classical path and become incapable of generating functional effector and memory cells.

The picture that T cell differentiation in response to chronic infection is fed from the EFF subset progressively that underwent additional transcriptional and epigenetic changes, eventually leading to impaired T cell function (Blank et al. 2019) has been challenged by more recent studies. These studies propose a different developmental order, placing MEX cells at the source of the differentiation, and in addition, they suggest that MP cells develop an exhausted phenotype upon transfer into persisting antigen conditions (Alfei et al. 2019; Chen et al. 2019; Hudson et al. 2019; Utzschneider et al. 2020). Moreover, the new view on the differentiation hierarchy is supported by the inability of KLRG1⁺ EFF cells to exhaust (Angelosanto et al. 2012; Khan et al. 2019),

T cell exhaustion is regarded as a programme that runs parallel to normal T cell differentiation, whereby T cell exhaustion can occur during any stage of differentiation. These cells subsequently give rise to progeny with features of exhaustion. Therefore, in the arrested model of differentiation, it is proposed that the exhausted T cells are generated from memory and effector T cells that have deviated from the normal trajectory of differentiation before developing into a terminal EFF cell (TEF) state (Henning et al. 2018). Several branching points within the canonical differentiation path can hence lead to the exhausted counterpart.

The great heterogeneity in the pool of exhausted T cell reflects the suggested transition to the exhausted phenotype, dependent on the differentiation stage. For example, MEX cells that phenotypically resemble MP cells would have diverted early during exhaustion. Concomitantly,

the more severe exhausted subsets (EEX and TEX) emerge at later time points when further progressed towards the terminal differentiation (Henning et al. 2018). However, so far, it remains unclear if the intermediate functional phenotypes such as EMP can exhaust or if exhaustion is solely MP \rightarrow MEX-driven.

1.6. Mathematical models of T cell responses

The understanding of the kinetics of quantitative T cells remains very scarce because the transition rates, such as the rate of differentiation or apoptosis, are difficult if not impossible to be assessed *in vivo*. These experimental limitations can be overcome by applying mathematical models that can inform on underlying paths not accessible by experiments. However, the complex nature of biological system requires that the mechanisms are simplified in order to develop a mathematical framework.

Nevertheless, mathematical modelling in quantitative biology led to a paradigm shift in how we understand the immune response and the course of a viral infection. They have provided insights into host-virus interactions, population doubling times and cell death.

Lessons learned from mathematical modelling

Most mathematical models to date that describe the population dynamics of T cells have been constructed based on ordinary differential equations (ODEs). They are employed to deduce population turnover rates over time as well as the subset diversification rates of a subset of cells. Mathematical modelling has provided the estimates about the cell proliferation and death, explaining how a population of CD8⁺ T cells grows rapidly after an infection and shrinks as soon as the disease has subsided (Althaus et al. 2007; Homann et al. 2001; Murali-Krishna et al. 1998). Whereby, these models were informed from proliferation measurements data, such as labelling with thymidine analogues 15-bromo-2'-deoxyuridine (BrdU), deuterium, or dye-dilutions methods such as carboxy-fluorescein diacetate succinimidyl ester (CFSE) or CellTrace Violet (De Boer et al. 2003, 2001).

Using elaborate dye-dilution protocols and long-term imaging methods, the group of Philip Hodgkin has performed seminal computational work that contributed to the better understanding of T cell activation and proliferation (Marchingo et al. 2014, 2016; Subramanian et al. 2008). However, their studies rely on direct measurements of the inter-division time distributions and *in vivo* such information is not directly accessible. Therefore, in this section, we focus on the mathematical frameworks applied to real infection situations.

On the example of the LCMV infection, several key biological findings could be uncovered through mathematical modelling. Firstly, thanks to mathematical modelling, it was possible to estimate the initial number of the virus-specific CD8⁺ T cells per mice (Bocharov 1998; Bocharov et al. 2003). The result has been confirmed by experimental measurements (Blattman et al. 2002). Furthermore, data-driven mathematical modelling has made it possible to assess the

threshold number of DCs required to induce an effective anti-viral CD8⁺ T response (Ludewig et al. 2004).

Limitations of mathematical modelling

So far, the understanding of the CD8⁺ T cell kinetics towards LCMV relied predominantly on population-based studies. These studies were limited by the lack of knowledge of the exact initial number of the precursor cells, specific for a particular antigen (antigen-specific naïve T cell pool) (De Boer et al. 2003).

In the applied mathematical models, the initial size of the precursors pool either relied on the estimations from the model fits or the lack thereof was mitigated by collapsing the rate of activation with the precursors' size into one single parameter (Althaus et al. 2007; Blattman et al. 2002). There were further limitations to the studies, resulting from a few additional factors. The lack of information about the initial precursor size hindered the dissections of the response magnitude that is mainly dependent on the degree of the clonal expansion (Heijst et al. 2013). The models also lacked the number of proliferation events undergone by each primed cell. Moreover, the way how cell division depends on the presence of antigen was not sufficiently described. These limitations were overcome by further simplifying the underlying model or using heuristic approaches. For instance, a study by DeBoer and colleagues assumed that cells could undergo an infinite number of divisions (De Boer et al. 2013). This assumption was later disproved by a study which uncovered an upper bound for the number of such events a primed cell experiences (Heinzel et al. 2017).

Misassumptions while constructing the model can lead to deceptive conclusions, such as the reliance on antigen concentration during the whole phase of CD8⁺ T cell expansion (for so-called predator-prey-like models) (De Boer et al. 1995). In fact, this particular assumption has been experimentally disproved, where it has been shown that a short stimulus of only 2 h suffices to induce several rounds of cell division (Kaech et al. 2001; Mercado et al. 2000). Further proof is provided by the studies that show that proliferation continues after antigen clearance and also occurs during homeostasis (Surh et al. 2008). During antigen persistence, CD8⁺ T cells do not continue proliferating infinitely (or until reaching the carrying capacity) but also experience a phase of T cell contraction (Althaus et al. 2007).

The use of mathematical modelling simplified the basis to study the lymphocyte turnover rates and subtype diversification. However, what remained unclear after these studies performed in the late 1990ies and early 2000 in the LCMV infection setting was the developmental order in which memory and effector memory T cells emerge from naïve T cells (Kohler 2007).

Overcoming previous limitations through new experimental designs

Following barcoded or congenically labelled single cells *in vivo* has opened new possibilities to investigate developmental relationships. Mapping of the single-cell fates revealed the hetero-

generality of the responses emerging from one single naïve CD8⁺ T cell. Another learning was that, both MP and EFF cells can be generated from the same progenitor cells (Gerlach et al. 2010; Stemmerger et al. 2007). Single-cell derived responses vary not only in relation to their phenotypic output but also to their clonal size. It has been shown that family sizes originating from a single CD8⁺ T cell clone span up to five orders of magnitude at the peak of the immune response during infection with *L.m.*-OVA. The greater proliferation was positively associated with an increasing frequency of EFF versus MP cells (Buchholz et al. 2013b; Gerlach et al. 2013).

Single-cell derived responses provide information about further statistical quantities, such as the variance and the co-variance. While, population-based responses average over the responses that are elicited from each single cell, masking further statistical information. Therefore, single-cell responses provide additional information to drive the mathematical modelling to describe developmental trajectories.

The lineage relationship of a naïve CD8⁺ T cell could be reconstructed through the application of stochastic mathematical modelling driven by single-cell fate-mapping (Buchholz et al. 2013b). Buchholz and colleagues found that a naïve CD8⁺ T cell diversifies early after activation and it is able to generate slow-proliferating MP progeny that differentiate into fast-dividing effector memory precursors (EMP) and EFF cells (Buchholz et al. 2013b).

The hierarchical order of CD8⁺ T cell differentiation proposed by Buchholz et al. 2013b is also known as the progressive model of differentiation. For the first time in the history of mathematical modelling of CD8⁺ T cell responses, the starting precursor number was known to be a single CD8⁺ T cell. That has allowed obtaining crucial information about the recruitment of cells from *in vivo* studies (Buchholz et al. 2013b).

Moreover, according to the progressive differentiation model, relevant differences in cell cycle speed act as a key driver in the generation of MP and EFF subsets at the peak of the expansion phase (Buchholz et al. 2013b). The developmental relationship proposed by the progressive model of differentiation was later supported by epigenetic studies (Pace et al. 2018) and through the time-resolved tracking of fluorescence-labelled reporter MP cells (Pais Ferreira et al. 2020).

Open questions

The role of cell division, division cessation and their link to the differentiation during the expansion phase of the CD8⁺ T cell response remains incompletely understood. At the same time, only a few studies have applied mathematical modelling to the proliferation and differentiation program during the T cell exhaustion. So far, they were able to uncover only the overall population kinetics (Althaus et al. 2007). The underlying mechanisms of differentiation mechanisms that propagate the different exhausted T cell subsets still remain to be described.

1.7. Regulation of clonal expansion by cell division speed

It was postulated that the cell cycle activity indirectly regulates T cell activity by generating stronger secondary effector cytokine responses when T cells have undergone more cell divisions during primary stimulation (Bird et al. 1998; Gett et al. 1998).

Indeed, proliferation regulates the nature of the immune response by affecting the number of MP and EFF T cells that are generated. Upon priming, the naïve CD8⁺ T cells undergo 14-16 divisions within the first week of infection and expand their population size by several orders of magnitude (Zhou et al. 2012). The expanded CD8⁺ T cell populations consist of a large fraction of EFF cells, mediating the clearance of the pathogen and a minor population of MP cells that provides long-lasting protection to re-infection (Badovinac et al. 2006; Kaech et al. 2012).

Using barcoded or congenically labelled single-cell transfer protocols suggested subset-specific differences in proliferation activity between MP and EFF subsets during the expansion phase (Buchholz et al. 2013b; Gerlach et al. 2013). This finding was further corroborated by the mathematical modelling of such single CD8⁺ T cell-derived responses (Buchholz et al. 2013b). There is evidence that during the acute infection with LCMV, MP cells proliferate less compared to EFF cells (Sarkar et al. 2008).

However, in these studies, it remains unclear whether the difference in the proliferative activity is due to premature cessation of the cell division and/or to the distinct subset-specific speeds of division.

Several *in vitro* studies suggest that the number of divisions a cell can undergo before returning to quiescence (division destiny) strongly depends on the initial stimulation and the cytokine milieu (Hawkins et al. 2009; Marchingo et al. 2014, 2016). In fact, co-stimulation with anti-CD28 (signal 2) as well as triggering IL-2 signalling with exogenous IL-2 stimulation (signal 3) increased the number of divisions a cell undertakes (Marchingo et al. 2014).

Furthermore, additional evidence exists that the time a cell exits the cell cycle is governed by the cell cycle-regulating transcription factor c-Myc (Heinzel et al. 2017). When c-Myc levels fall below a certain threshold, division cessation is enforced (Heinzel et al. 2017). This is in line with previous studies, showing that c-Myc on both protein and mRNA levels is highly induced upon activation and directly regulated by TCR and IL-2 signalling (Guy et al. 2013; Marchingo et al. 2020; Preston et al. 2015). Also, c-Myc plays a role in the metabolic reprogramming of T cells by promoting glycolysis, a bioenergy source that is required in the EFF cells (Windt et al. 2012). However, the role of c-Myc expression during the development of the MP and EFF fates remains an open question.

New outlook on cell division

Most of the studies described in the previous section relied on a *in vitro* experimental settings and whether these findings hold for expanding T cell populations *in vivo* where antigen levels remain high for a minimum of a few days as well as in conditions of persisting infections, remains

unresolved.

Using a cell division reporter system and *ex vivo* continuous imaging, Kinjyo and colleagues discovered that the first few initial divisions are relatively fast with a duration of 6-8 hours (h) and the division times between the sub-populations are comparable (Kinjyo et al. 2015; Yoon et al. 2010). Only after approximately eight divisions do they observe the segregation of a slow-dividing MP subset and fast-cycling EFF cells (Kinjyo et al. 2015).

Contravening these findings, we have recently developed a mathematical framework to directly infer the cell cycle speed *in vivo* from BrdU labelling with subsequent measurements of the total DNA-content. We have demonstrated that even at the early time points after vaccination, the clonal expansion is regulated by the speed of the differential subset-specific division (Kretschmer et al. 2020).

In line with the previous measurements of proliferation *in vivo* (Sarkar et al. 2008) as well as the predictions of the mathematical model (Buchholz et al. 2013b), MP cells display prolonged progression through G1-phase and slower cell cycle speed compared to the EFF subsets (Kretschmer et al. 2020).

In our study using a vaccination method with antigen-pulsed DCs and infection with *L.m.*, division cessation was not observed until the time points close to the peak of the response (Kretschmer et al. 2020).

Open questions

It is certain that after contraction, cell cycle quiescence sets in. However, whether cell cycle arrest plays a role during the initial expansion phase after infections with other pathogens than *L.m.* still needs to be determined. Furthermore, during a persisting infection with the accompanying expression of an exhausted phenotype, the loss of the proliferative capacity is a characteristic attribute. The role of the cell cycle exit as well as the cell cycle activity have not yet been investigated during the expansion phase of the T cell response.

2. Aim of this thesis

CD8⁺ T cells emerging from chronic infections develop an exhausted phenotype that is transcriptionally distinct from that of functional MP and EFF cells. Although many studies extensively investigated the role of transcription factors, epigenetic landscapes, proliferation capacities, and metabolic profiles, the developmental order in which exhausted CD8⁺ T cells emerge still remains incompletely understood. Moreover, the understanding of T cell exhaustion is tied to simultaneous analyses of the functional subsets.

Therefore, the first aim of this study is to understand the diversification order and the underlying processes of the CD8⁺ T cells during the expansion phase of acute viral and bacterial infections. In order to achieve this, we performed scRNA-seq experiments and analysed them together with public data (Chen et al. 2019; Kurd et al. 2020; Yao et al. 2019). We used trajectory inference methods to construct a mathematical model. Furthermore, we worked in close collaboration with the laboratory of Veit Buchholz (Technical University Munich), who conducted the adoptive transfer experiments of single CD8⁺ T cells that were used to constrain the mathematical model. In addition, we developed a mathematical framework to assess division speed *in vivo* and used the output to define the proliferation rates of the mathematical model.

Our second aim was to dissect how exhaustion fits into the proliferation and differentiation program during the expansion phase of infection. To attain this we first compared the single-cell transcriptome at early time points after the acute or chronic LCMV infection and characterised the CD8⁺ T cell subsets emerging over the responses. We then applied the mathematical model that best described the course of the two acute infections to single-cell fate-mapping data from LCMV clone 13 infection. This way, we identified the parameters that needed to be altered to characterise the development of T cell subsets during chronic disease.

Furthermore, we investigated the time-point at which cells from chronic infection remain sufficiently plastic to be deflected towards the functional developmental path.

The third aim was to elucidate how the exhausted T cells deviate from the canonical developmental pathway. To address this, we re-analysed the published scRNA-seq data (Yao et al. 2019) and investigated the role of TOX expression in the development of exhausted subsets by means of mathematical modelling.

3. The CD8⁺ T cell response during the early phase of an acute infection

This chapter establishes a mathematical model to describe the early T cell wave during an acute infection. By combining different data types and interdisciplinary methodological approaches, we aimed at identifying the lineage relationships of CD8⁺ T cell subsets during the acute infection. We are particularly interested in fate decisions and lineage relationships in the transitions between memory and effector T cell formation.

To interrogate the early population dynamics during acute infection and the associated emergence of the memory and effector T cell subsets, we used the infection models of ovalbumin (OVA)-expressing *Listeria monocytogenes* (*L.m.*-OVA) and LCMV Armstrong. These mouse models were already used in numerous studies that have significantly contributed to our understanding of CD8⁺ T cell-mediated immunity.

For both of these infection models, transgenic CD8⁺ T cells with antigen-specific TCR have been engineered. P14 T cells recognise the gp33-peptide expressed on the LCMV, and OTI T cells harbour a TCR designed to detect the SIINFEKL-peptide on the OVA residue.

Upon adoptive T cell transfer of naïve OTI or P14 T cells, following infection with the matching pathogen, the T cell responses were analysed at the early days after infection by flow cytometry and scRNA-seq.

In addition, we discuss in this chapter how a cell's division speed forms a characteristic trait of a T cell subtype. For this purpose we developed a mathematical framework to quantify cell cycle speed *in vivo*. We published the mathematical approach for division length quantification in Kretschmer et al. 2020. Using a unique approach, where we combined experimental data from flow cytometry with bioinformatical analyses and also proliferation measurements, we drove the development of a mathematical model. Furthermore, we re-analysed public scRNA-seq data, combined it with our own and used it to inform and constrain the mathematical model. To this end, we were able to develop a mathematical framework that can disentangle the differentiation hierarchy of CD8⁺ T cells during two types of acute infections.

The experimental data shown in this chapter came either from Lorenz Kretschmer from Veit Buchholz's laboratory or stem from experiments that were performed by myself. Part of the mathematical modelling and bioinformatics analysis was performed by my colleague Jonas Mir, if not indicated differently the results obtained by mathematical modelling and bioinformatics analyses stem from my own investigations.

Dr. med. Veit Buchholz, Lorenz Kretschmer and Jonas Mir are affiliated to the Institute of Medical Microbiology, Immunology and Hygiene at the Technical University of Munich in Munich, Germany.

3.1. Distinct division speed of memory precursors and effector T cell subsets

Testing the prediction of the progressive model of differentiation

Buchholz and colleagues combined single-cell fate-mapping and mathematical modelling to characterise the lineage relationships of CMP, EMP and EFF subsets during the expansion phase of an acute infection (Buchholz et al. 2013b). In their study, Buchholz and colleagues defined the subsets based on the expression of CD62L and CD27: (CMP: CD62L⁺CD27⁺, EMP: CD62L⁻CD27⁺, EFF: CD62L⁻CD27⁻) (Figure 3.1 A). They showed that at the peak of the infection, the differential expansion of memory and effector subsets, comprising of large EFF progenies and a small population of CMP cells is attributed to the distinct division speeds of these subsets. Thus, they propose a hierarchical developmental order where naïve CD8⁺ T cells diversify into slow-cycling CMP cells, that differentiate into a faster-proliferating EMP subset, which then generate fast-dividing EFF cells (Figure 3.1 B). Their model predicted, that in comparison to the CMP cells, the EMP and EFF subsets undergo 1.5 more divisions on average per day (Figure 3.1 B) (Buchholz et al. 2013a).

As first we aimed to test the slow- versus fast-proliferation subset prediction of the model. Therefore, naïve OTI T cells were transferred into congenic wild-type recipients and then infected one day later with *L.m.*-OVA. The OTI T cell response was analysed on day 4.5 p.i. Exactly 3 h before reaching the time of analysis, a dose of BrdU was administered i.p. After that, BrdU incorporation was analysed by flow cytometry in splenic OTI T cells (Figure 3.1 C).

The *in vivo* proliferation measurements were consistent with the model prediction. Namely, the CMP cells incorporated the least amount of BrdU and the EMP, and EFF T cell subsets incorporated significantly more BrdU in 3 h of measurement (Figure 3.1 D, top row and E, left panel).

Slower proliferation of the MP subset is conserved across different infections

We also demonstrated similar results in other animal models, such as after infection with replication-deficient OVA-expressing Modified Vaccinia Ankara Virus (MVA-OVA) or after previous vaccination with chicken ovalbumin (SIINFEKL) peptide-pulsed DCs, subsequent adoptive transfer of OTI T cells and infection with wild-type *L.m.* (Figure 3.1 D-E) (Kretschmer et al. 2020).

The slower division of the CMP compartment was not a characteristic of antigen-specific T cells with high-affinity TCR. We also observed this feature in the polyclonal T cell responses, such as when we examined BrdU incorporation in endogenous H2-*kb*:SIINFEKL⁺CD8⁺ T cells at day 6 after *L.m.*-OVA infection (data not shown).

Based on these findings we expected that during acute infection with LCMV Armstrong MP would incorporate less BrdU than non-MP cells. Therefore, we adoptively transferred naïve

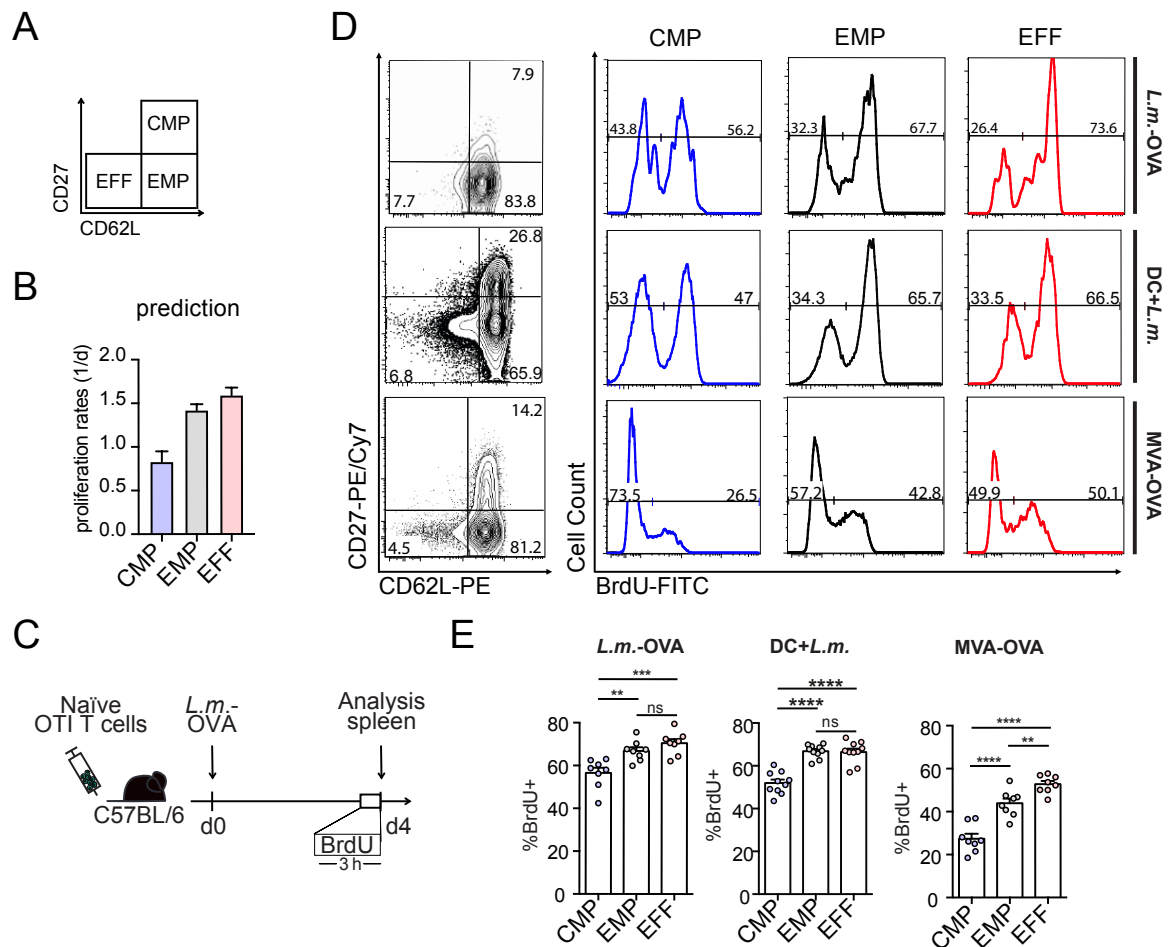


Figure 3.1.: Subset-defining proliferation speed predicted by progressive model of differentiation. **A** Schematic representation of the gating strategy based on expression of CD62L and CD27. **B** Proliferation rates with 95% confidence bounds from the progressive model of differentiations that was fitted to day 8 single-cell fate mapping data (Buchholz et al. 2013a). **C** Experimental setup of single T cell adoptive transfer. 5×10^4 naïve OTI T cells were adoptively transferred into congenic wild-type recipients. The next day, recipients were infected with 5×10^3 cfu *L.m.-OVA*. Minus 3 h before the time point of analysis on day 4, BrdU was administered i.p. to each mouse. **D** Representative contour plot is showing the expression of CD62L and CD27 of transferred OTI T cells, with the corresponding BrdU-profiles for the indicated subsets (top row). Experimental set-up similar to (C), but with SIINFEKL-pulsed DCs and infection with wild-type 2×10^3 *L.m.* (middle row) or after infection with 2×10^8 MVA-OVA (bottom row). **E** Bar graphs depict the percentage of BrdU⁺ OTI T cells at day 4 p.i. after infection with *L.m.-OVA*, DC vaccination and infection with wild-type *L.m.* or MVA-OVA. Mean and std, ns=not significant, ** $p < 0.01$, *** $p < 0.001$, one-way ANOVA. $n = 8 - 10$, and data are pooled from two independent experiments. Data shown in (D-E) has been published in Kretschmer et al. 2020.

P14 T cells into C57BL/6 mice. On the following day, the mice were infected with LCMV Armstrong and 3 h before the endpoint on day 4.5, the mice were given a dose of BrdU i.p. (Figure 3.2 A). Differential expression of TCF1 marked the MP (TCF1⁺) and non-MP (TCF1⁻)

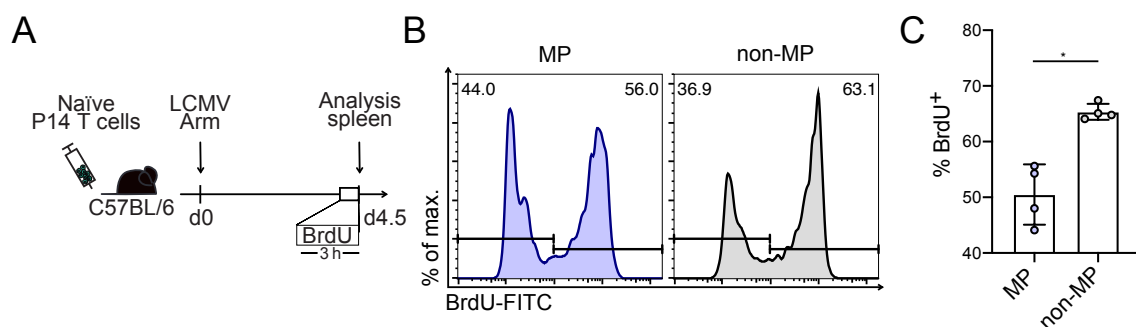


Figure 3.2.: Memory precursor (MP) cells incorporate less BrdU compared to non-memory precursor (non-MP) cells at day 4.5 p.i. **A** Experimental set up for assessing proliferation *in vivo*. C57BL/6 mice were infected with 2×10^5 pfu LCMV Armstrong one day after receiving 5×10^4 naïve P14 T cells i.p. At 3 h before endpoint analysis at day 4.5 p.i., 1 mg/g BrdU was administered i.p. Its incorporation into the DNA was analysed by flow cytometry. **B** Representative histogram depicting the BrdU levels of MP (TCF1⁺) and non-MP (TCF1⁻) P14 T cells. **C** Quantification of BrdU-positive P14 T cells after 3 h of labelling with BrdU. Mean and s.e.m. * $p < 0.05$ Mann-Whitney U test, $n = 4$, data from one out of two similar experiments.

subset. As expected, the distinct proliferation was also observed during the LCMV Armstrong infection. Again, the cells of the MP subset divided less than those of the non-MPs (Figure 3.2 A), suggesting a conserved mechanism resulting in slower (C)MP proliferation.

Investigation of the cell cycle phases

BrdU is a thymidine analogue that is integrated during DNA replication in the S-phase. To understand whether merely a shorter S-phase is responsible for the different BrdU incorporation between the MP and non-MP T cell subsets, we measured the total DNA content using the DNA intercalating agent 7-aminoactinomycin D (7AAD) in addition to BrdU. With the simultaneous measurement of total DNA content and BrdU, we gain the information whether a cells' DNA content is in diploid ($2N$) or tetraploid ($4N$) status and can thereby deduce the distribution of the cells in the cell cycle phases (Figure 3.3 A).

For this purpose, we chose a short BrdU staining window of 0.5 h. Such a short labelling time has previously been used in other *in vitro* and *in vivo* studies to determine the cell cycle state of a cell (G0/G1-(BrdU⁻ $2N$), G2/M-(BrdU⁻ $4N$) and S-phase (BrdU⁺).

Over this measurement, G0 cells are not discriminated from G1 cells. The cells from these two phases are both found in the (BrdU⁻ $2N$)-gate. Therefore, to discern between actively cycling and quiescent cells, we measured the expression of retinoblastoma protein (Rb) with phosphorylation at serine residues Y807/811 (Gookin et al. 2017). During active cell division Rb is present in its phosphorylated form (p-Rb). At day 4.5 p.i. LCMV Armstrong we found that $> 80\%$ of the P14 T cells underwent active cell division, whereas at the same day after infection with *L.m.*-OVA $> 99\%$ of cells were positive for p-Rb (Y807/811) (Figure A.6 A). The vast majority of the cells were actively proliferating i.e. all cells were dividing, and the

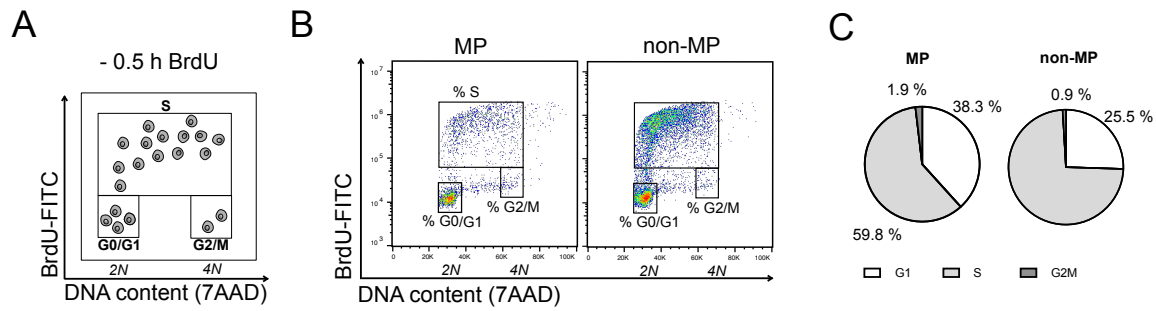


Figure 3.3.: MP and non-MP T cells display differential cell cycle phase distribution after labelling with short BrdU pulses **A** Schematic representation of the cell cycle phase distribution based on BrdU incorporation and DNA content. **B-C** Experimental set-up as in Figure 3.2 A, but with BrdU administration 0.5 h before analysis time point. **B** Representative pseudo-colour plots and **C** pie charts display the phase distribution of the P14 T cells at day 4.5 LCMV Armstrong infection for the MP (TCF1⁺) and non-MP (TCF1⁻) subset. Mean $n = 3$, data from one out of two similar experiments.

(BrdU⁻2N)-gate containing mainly G1 and not G0 cells (Figure A.6 A). On day 4.5, after infection with *L.m.*-OVA or LCMV Armstrong, we detected differences in the cell cycle phase distribution between the CMP and the non-CMP subset (Figure 3.3 B-C, Figure A.6 B).

In both infections, a more significant proportion of MP cells were present in the G1-phase than the non-MP subset (1.5 times in the infection with *L.m.*-OVA and 1.2 times in the infection with LCMV Armstrong) (Figure 3.3 B-C, Figure A.6 B). Approximately 0.8 times fewer MP cells were found in the S-phase compared to the non-MP. Similarly, we observed that approximately 1.5 – 2 times more cells from the MP subset were in the G2M phase (Figure 3.3 B-C, Figure A.6 B). We published similar findings (Kretschmer et al. 2020) for OTI T cells after vaccination with SIINFEKL-pulsed DCs following wild-type *L.m.* infection.

Assessment of cell cycle speed of fast dividing cells *in vivo*

Many approaches exist to distinguish the different cell cycle phases (BrdU/7AAD, FUCCI (Kinjyo et al. 2015)). However, a way to infer cell division speed did not exist. We aimed at inferring the actual cell cycle phase durations and, therefore, required the information about the overall cell cycle length. For the aforementioned reason, we have developed a mathematical framework to quantify the inter-division times of fast-cycling cells *in vivo* (Kretschmer et al. 2020).

In our approach to quantifying cell cycle speed, we made the following assumptions: First, a proportion of cells in the S-phase during the BrdU labelling period divides before the total DNA content is measured. These cells should then appear in the (BrdU⁺2N)-gate and will from here on be referred to as divided cells. The divided gate contains the progeny of cells, whose mother cells were in the S-phase when BrdU was given and divided within the time of BrdU administration and the time point of measurement. The differentiation of these recently divided cells from the entire BrdU⁺ cells is determined by the DNA content of the cells.

The double BrdU and 7AAD labelling approach, therefore, allows us to gain information about the speed of division during the measured time.

We discovered that if we measure the total DNA content after a BrdU labelling window of 3 h, a separation of the divided cells from the overall BrdU-positive cells can be realised. This way, we can easily differentiate the cells that had passed the S-phase when BrdU was available and divided once (Figure 3.4 A, green cells).

Moreover, the half-life of BrdU is relatively short and has a degradation time of about 0.5 h (Matiašová et al. 2014). Thus, the fraction of BrdU⁺ cells remains the same when the time window between BrdU administration and analysis was increased from 0.5 h to 3 h (data not shown).

Therefore, we assumed that the extension of the time window between analysis and BrdU administration from 0.5 h to 3 h, captures only the cells that were in the S-phase in the first 0.5 h after BrdU injection.

Thus, cells with an initial G1-phase status at the time of BrdU administration will not be able to integrate BrdU and remain BrdU-negative (Figure 3.4 A, purple cells).

Second, we slightly underestimate the proportion of dividing cells, as a relatively small percentage of cells that are initially in the G2M-phase (BrdU⁻4N) do not end up in the divided-gate after division, but instead in the (BrdU⁻2N)-gate (Figure 3.4 A, blue cells). Using our measurements after 0.5 h BrdU administration, we obtained the percentage of those initial G2/M cells (0.9 – 7.5%) (Figure 3.3 B-C, Figure A.6 B).

For our mathematical formalism that quantifies the division speed, we used the percentage of cells in the divided gate and subtracted the fraction of cells that are found in the G2M-gate. This subtraction is done to account for the cells that divided between the BrdU administration and measurement but were BrdU-negative.

As next, we performed combinatory BrdU/DNA measurements at day 4.5 after infection with LCMV Armstrong and determined the proportion of P14 T cells that divided within 3 h. As already indicated from the results in Figure 3.2, the percentage of divided cells was different between the MP and non-MP subsets, with a lower fraction of MP cells dividing within the time frame of 3 h.

The mathematical quantification of the cell cycle length durations was performed by my colleague, Jonas Mir. For the quantification, the measurements for the G1- and G2M-phases (Figure 3.2 B-C) and our analyses on the T cells that divided within 3h were used (Figure 3.4 B-C). The detailed calculations used to quantify the division durations as described in chapter 6, subsection 6.4.2.

The T cells from the MP compartment divided on average every 10.6 h and the non-MP subset cell every 6.2 h, respectively, i.e. the MP cells divided approximately twice per day, whereas the non-MP subset underwent on average four cell divisions per day (Figure 3.4 D). A prolonged G1-phase explained a large part of the longer inter-division time of the MP subset (Figure 3.4 D-E). We obtained similar results analysing OTI T cells at day 4.5 after *L.m.*-OVA infection (Figure

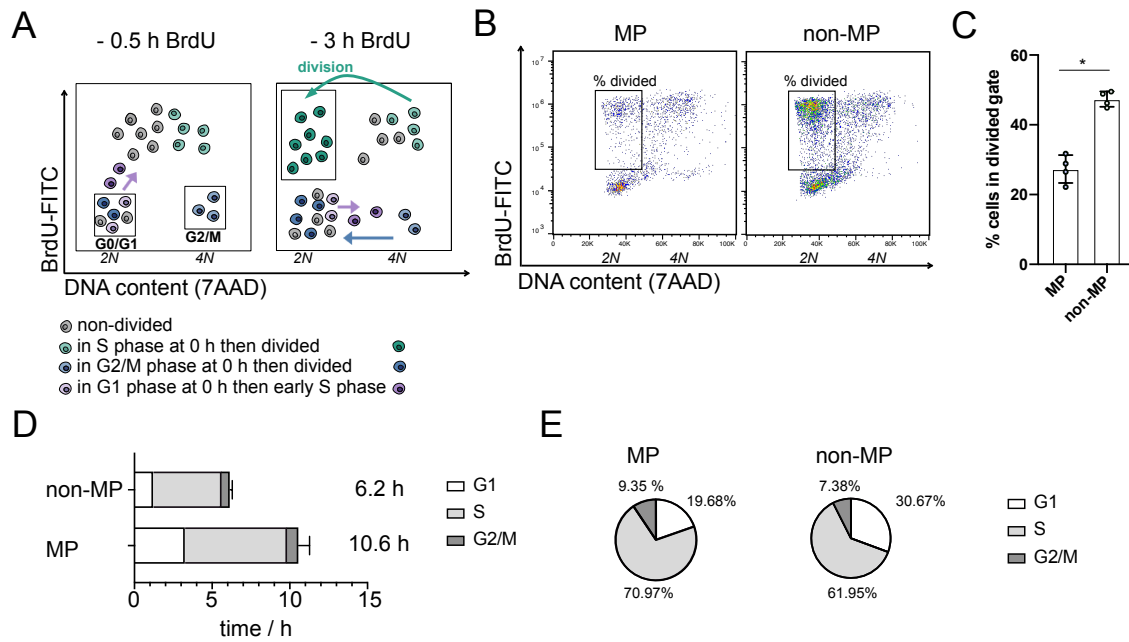


Figure 3.4.: Quantification of the cell cycle speed *in vivo* reveals that memory precursor cells divide slower compared to non-memory precursors. **A** Schematic representation of BrdU incorporation using two different BrdU labelling times. After labelling for 0.5 h, the percentage of cells in the G0/G1- ($2N$ DNA content), G2/M-phase ($4N$ DNA content) as well as the percentage of S-phase cells can be estimated. At the measurement 3 h after BrdU administration, the % divided-gate (BrdU⁺DNA($2N$)) contains all cells that were born in between the time points of BrdU injection and measurement except for the progenies of mother cells that were in the G2/M-phase at the time when BrdU was administered. Figure adapted from Kretschmer et al. 2020. **B** Experimental set up as in Figure 3.2 A. Representative pseudo-colour plots with the gating strategy to estimate the percentage of cells in the divided-gate for the MP (TCF1⁺) and non-MP (TCF1⁻) subset at day 4.5 after LCMV Armstrong infection. **C** Histograms show the percentage of P14 T cells in the divided gate after 3 h. Mean and std, * $p < 0.05$, Man-Whitney U rank test. $n = 4$, data from one of two similar experiments. **D** Bar graph depicts the length of the mean inter-division times of MP and non-MP subsets quantified by the mathematical model as described in Kretschmer et al. 2020. **E** The pie charts display the percentage each cell cycle phase amounts to the total length. mean and s.e.m. $n = 4$.

A.6 D-E). During *L.m.*-OVA infection, CMP cells in comparison to non-CMP cells divided every 8.8 h and 5.8 h, respectively. Furthermore, we demonstrated similar outcomes in OTI T cells after DC immunisation (Kretschmer et al. 2020).

The progressive model of differentiation reflected the proliferation dynamic accurately for the OTI T cells during the acute phase of *L.m.*-OVA infection. As next, we will investigate single-cell responses following the infection with LCMV Armstrong and test if the progressive model of differentiation explains the data.

3.2. High variability of single CD8⁺ T cell responses during LCMV Armstrong infection

Establishment of a murine model to investigate gp33-specific CD8⁺ T cell responses

The laboratory of Dirk Busch came up with an experimental setting that allows the tracking of single T cells *in vivo* (Stemberger et al. 2007). In their protocol, one naïve T cell expressing a distinct congenic marker was adoptively transferred into host mice and followed during the infection. Thus, the descendants that were found after a resolved infection originated from a single progenitor cell. Buchholz and colleagues improved this method and successfully generated CD8⁺ T cells that differ exclusively in their expression of congenic surface markers (Buchholz et al. 2013a). To this end, several naïve CD8⁺ T cells could be transferred into the same host and simultaneously analysed. In this multiplex application, the responses of up to eight single cell progenies can be followed.

To specifically study the fate decisions of individual CD8⁺ T cell progenies, Buchholz and co-workers bred C57BL/6 mice expressing the identical transgenic LCMV-gp33 peptide-specific TCR (P14 T cells) with different congenic backgrounds. The P14 T cell matrix mouse model was established by breeding P14 transgenic C57BL/6 mice expressing CD45.1 and Thy1.1 with CD45.2 and Thy1.2 pairs.

From this crossbreeding, progeny with six different congenic phenotypes were obtained, which are: CD45.1/.1, CD45.1/.2, CD45.2/.2 or Thy1.1/.1, Thy1.1/.2, Thy1.2/.2. These mouse strains were interbred until eight different combinations of those markers were obtained. The eight P14 T cells with unique congenic label are termed the P14 matrix (Figure 3.5 A). This protocol allows the transfer of eight discernible P14 matrix components A-H into CD45.2/.2^{+/+}Thy1.2/.2^{+/+} C57BL/6 recipients.

Investigation of CD8⁺ T cell subset diversification

In the experimental setting, 8 × 1 P14 matrix component A-H were transferred into recipient hosts. One day after P14 matrix transfer, the host mice were infected with LCMV Armstrong, and the recovered progenies from the spleen were analysed at day 8 p.i. by flow cytometry (Figure 3.5 B). To investigate T cell subsets with memory or effector signatures, the differential expression of the following markers was examined: TCF1, Tim3 and CX3CR1.

The expression of transcription factor TCF1 has been found to play a critical role in the formation of CD8⁺ T cell memory during an acute infection (Jeannet et al. 2010; Lin et al. 2016; Pais Ferreira et al. 2020; Zhao et al. 2010).

Further sub-division of the CD8⁺ T cell subsets into a memory and effector compartment, was obtained through the expression of CX3CR1. Depending on the level of CX3CR1 expression, a distinction between effector-memory and terminal effector cells could be made.

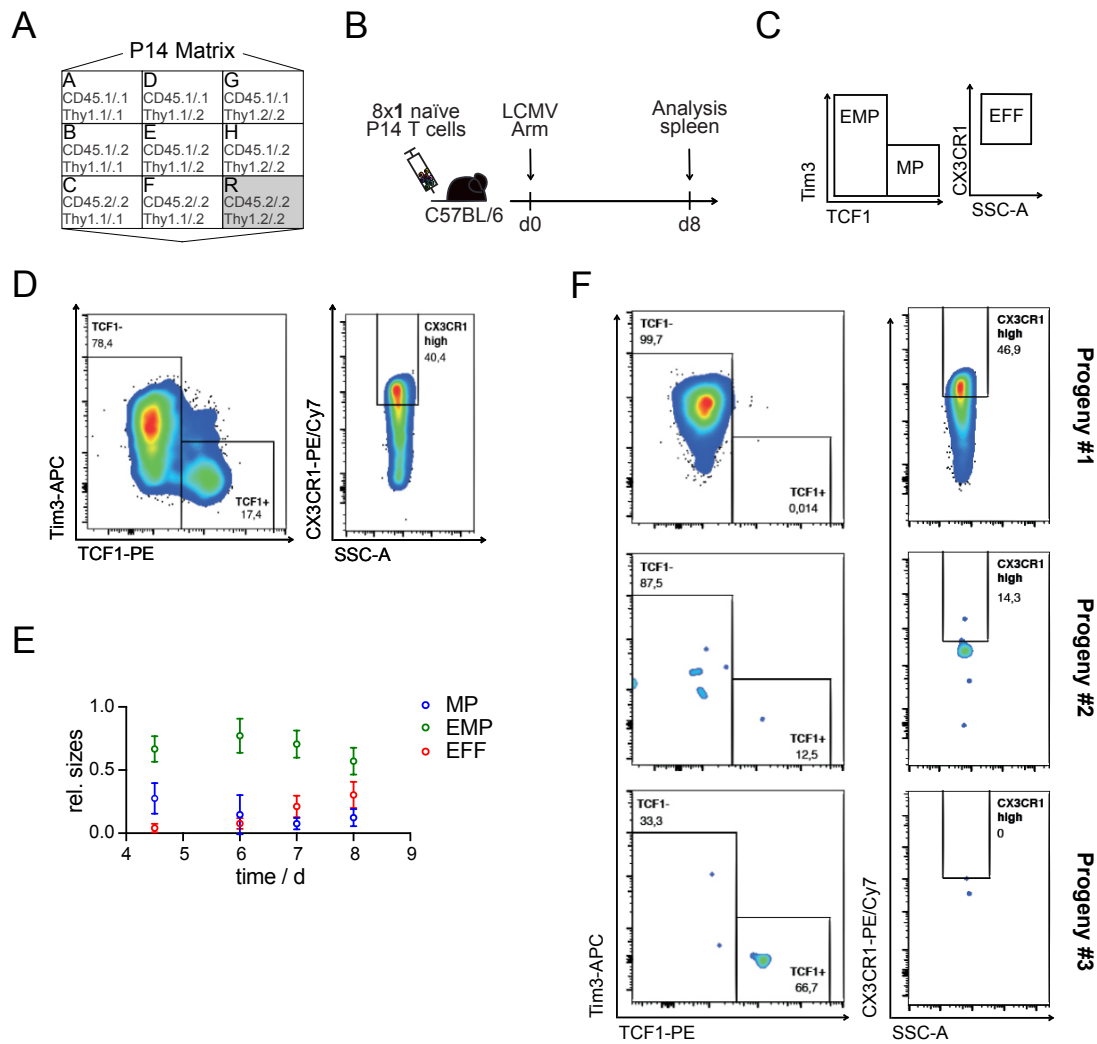


Figure 3.5.: P14 T cells follow diverse fates after LCMV Armstrong infection. **A** Schematic representation of the congenic P14 T cell matrix. **B** Set-up of the single T cell adoptive transfer experiment. 8×1 naïve P14 T cells were adoptively transferred into C57BL/6 mice that were infected with 2×10^5 pfu LCMV Armstrong the next day. On day 8 p.i., the P14 T cell populations in the spleen were analysed. **C** Representative gating strategy based on the expression of TCF1, Tim3 and CX3CR1. **D** Representative pseudo-colour plot of the 5×10^2 -cell derived response on their expression of TCF1, Tim-3 and CX3CR1 at day 8 p.i. **D** Representative pseudo-colour plots of single-cell progenies ordered from large (top) to small (bottom) showing the expression of TCF1, Tim3 and CX3CR1 at day 8 p.i. **E** Experiments were performed as in **B**, but $5 \times 10^2 - 5 \times 10^4$ were adoptively transferred into naïve hosts, and analysed at day 4.5, 6, 7 and 8 p.i. with LCMV Armstrong. The relative population size (mean and s.e.m.) on the markers TCF1, Tim-3 and CX3CR1 was analysed by flow cytometry. Experimental data shown in **C** and **D** was performed by Lorenz Kretschmer and Dr. med. Veit Buchholz, data in **E** stem from own experiments. $n = 6 - 26$ and data are pooled from two to four independent experiments.

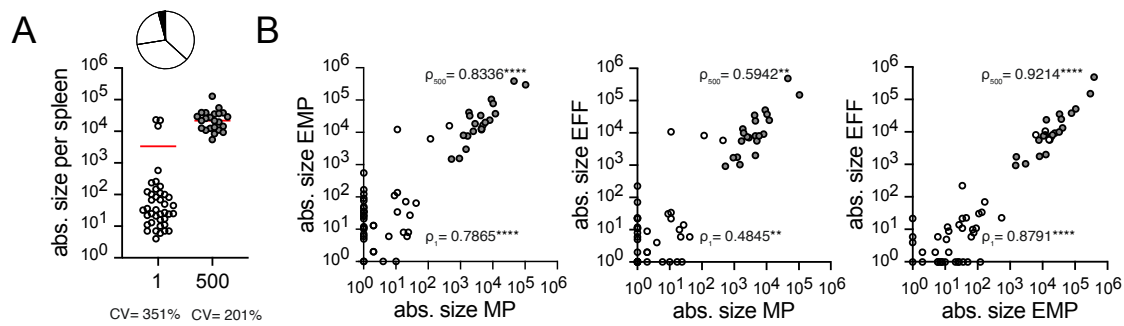


Figure 3.6.: The progeny sizes at day 8 p.i. with LCMV Armstrong range from many small clones to a few dominating giants. Experiments were performed as in Figure 3.5 B. Statistical quantification of the data shown in Figure 3.5 D and F. **A** Absolute population size of the P14 T cell-derived response at 8 p.i. with LCMV Armstrong in the spleen after transfer of 1 or 5×10^2 cells. Pie chart represents the population distribution. **B** Pair-wise Pearson correlations between the absolute population size of a 1- or 5×10^2 cells derived progeny. ρ_1 notes the Pearson correlation coefficient of a 1-cell derived progeny and ρ_{500} of 5×10^2 -cell derived progeny, respectively. Data are pooled from four independent experiments. **** $p < 0.0001$, ** $p < 0.005$. Experiments were performed by Lorenz Kretschmer and Dr. med. Veit Buchholz.

While the $CX3CR1^{\text{high}}$ subset exhibits great cytotoxicity (Böttcher et al. 2015), $CX3CR1^{\text{int/-}}$ cells show high self-renewal capacity (Gerlach et al. 2016). Therefore, $TCF1^+Tim3^-$ T cells were gated to identify memory progenitor T cells (MP).

Further examination of the $TCF1^-$ compartment for the expression of $CX3CR1$, allowed the assignment of $TCF1^-$ cells as EMP and EFF cells, exhibiting high $CX3CR1$ expression levels. A schematic representation of the gating strategy is shown in Figure 3.5 C. First, the P14 T cell response based on these three markers was investigated on a population level. For this purpose, $5 \times 10^2 - 5 \times 10^4$ naïve P14 T cells were adaptively transferred into C57BL/6 recipients. The spleens were analysed between day 4.5 and 8 after LCMV Armstrong infection for their phenotypic composition with respect to the markers $TCF1$, $Tim3$ and $CX3CR1$. A representative pseudo-colour plot of the day 8 population-cell derived response is shown (Figure 3.5 D). We analysed the mean population response for the three T cell subsets (MP, EMP and EFF) in a time-resolved manner. As early as day 4.5 p.i., a small fraction of the EFF subset emerged that grew in size over time, peaking at day 8 p.i. (Figure 3.5 E).

Similar results on the $CX3CR1$ -expression were observed by Böttcher et al. 2015 in an artificial Adenovirus-OVA infection model. Relative size-wise, the MP compartment shrunk over time, while the EMP pool remained comparatively constant in relative size (Figure 3.5 E).

Multiple fates of single $CD8^+$ T cells

From previous studies by Buchholz and colleagues, we observed that single $CD8^+$ T cell responses towards acute infections were very heterogeneous (Buchholz et al. 2013a, Kretschmer et al. 2020). This poses a feature that was all well observed in the P14 T cell response upon infection with

LCMV Armstrong. The single-cell progenies differed not only in their phenotypic composition but also in their total population size (Figure 3.5 F and 3.6 A).

The population size of the single cell-derived progeny spans four orders of magnitude. In comparison, five hundred cell-derived responses following LCMV Armstrong infection do not show such a large spread (Figure 3.6 A).

The diversity of a population can be quantified in different ways. Here, we chose two ways to describe differences and variation in the P14 T cell population distribution. The first of these two measures is the coefficient of variation (CV). The CV determines the standard deviation of the progenies in relation to the mean of the population. The absolute cell size in the spleen at day 8 p.i. LCMV Armstrong has a CV of 351 %.

Interestingly, three giant clones dominated the entire LCMV Armstrong immune response (Figure 3.6 A). However, the CV does not quantify how much each individual clone contributes to the total response. Instead, the Gini index (i_{Gini}) (Gini 1921), can quantify the evenness of a population. The Gini index is widely used in socio-economic studies to represent inequality in the distribution of goods or wealth. A i_{Gini} of zero expresses a total equality, where goods are evenly distributed within a population. In contrast, a i_{Gini} of one represents complete inequality, meaning that one individual owns everything, while the rest of the population owns nothing.

The evenness of the P14 T cell population at day 8 after LCMV Armstrong infection exhibited a i_{Gini} of 0.914. Hence, the Gini coefficient reflected the three dominating clone that account for the majority of the response and depicted the unevenness of the single P14 responses in the population distribution (Pie Chart, Figure 3.6 A).

Determining the Pearson correlation coefficient ρ , we also assessed the linear correlations between the absolute cell number between each subset pair. We observed a strong positive relationship between the absolute size of the MP and EMP subset and the total sizes of the EMP and EFF subset. A weak correlation was present between the absolute sizes of the MP and EMP subsets. A similar relationship between the subsets was observed when quantifying the correlation coefficients for the five hundred-cell derived responses (Figure 3.6 B). All summary statistics can be found in Table A.1.

In the following section, we discuss whether an existing model of T cell differentiation can explain the single-cell fate-mapping responses after the LCMV Armstrong infection.

3.3. Variable recruitment to account for diverse single-cell responses

We were contemplating that the general course of an acute systemic infection, i.e. pathogen elimination and the quality of the associated effector CD8⁺ T cell response, should not differ substantially between different infectious diseases. Therefore, we aimed to explore whether the model of progressive differentiation can also be applied to describe the T cell response during the LCMV Armstrong infection.

As in the original study from Buchholz et al. 2013a we performed least-squares approximation for

parameter estimation and used the mean values, CVs and correlation coefficients to constrain the mathematical model. The best fits to the mean values, the CV of each subset and the correlation coefficients ρ is shown in Figure A.1 B-C. In terms of the means, the variation and the linear relationships between the subsets, as represented by the pairwise Pearson correlation coefficients, the mathematical model supports the data.

However, when we examined the best-fit parameters, we observed that the recruitment rate from the naïve T cell compartment to the MP subset was unrealistically low ($r_0 = 0.11 \text{ d}^{-1}$). We also computed the confidence intervals for the parameters with the profile likelihood method (95 % CI [0.07, 0.18]), meaning that the recruitment parameter can vary between these bounds and still result in a good fit.

A better way to interpret the meaning of this rate is by looking at the inverse value ($1/r_0$): On average, the recruitment of a naïve T cell takes about 9 days (95 % CI [5.6, 14.3]).

Although many naïve T cells differentiated into the MP compartment shortly after activation, a considerable proportion remained in the naïve state even after day 9 p.i. (data not shown). Such a significant fraction of cells being kept in the naïve state after the peak response, which is thought to be around day 7-8 after the infection with LCMV Armstrong (Murali-Krishna et al. 1998), is highly unrealistic. Short differentiation times are backed by a study, showing that even after adoptive transfer of rather high numbers of naïve T cells, the recruitment at the peak of the response was almost complete (Heijst et al. 2013).

Furthermore, even a recruitment time of 5.6 days, which is the lower bound of the inverse parameter value seems rather long. In a previous study, from De Boer et al. 2001 and colleagues, where they modelled endogenous LCMV-specific CD8^+ T cell responses, they found recruitment times of 1.2-1.4 d^{-1} .

We found that the high variability in the data particularly represented by the CV, demanded a large mean recruitment time. Owing to its unrealistically low magnitude and lack of support by published observation (De Boer et al. 2001; Heijst et al. 2013), this model is neglected and further analyses based on the progressive differentiation model were not conducted.

As next, we will analyse the single-cell transcriptomes of CD8^+ T cells during the acute LCMV infection to gain insight into the developmental pathways of the different T cell subsets. Further, we aim to develop a computational framework to describe the fate-decisions of single CD8^+ T cells.

3.4. Time-resolved transcriptional analysis of P14 T cells after acute infection

Investigation of CD8^+ T immunity using scRNA-seq

We used the scRNA-seq approach to interrogate the early population dynamics of antiviral CD8^+ T cells during the acute infection. Therefore, we adoptively transferred naïve P14 T cells

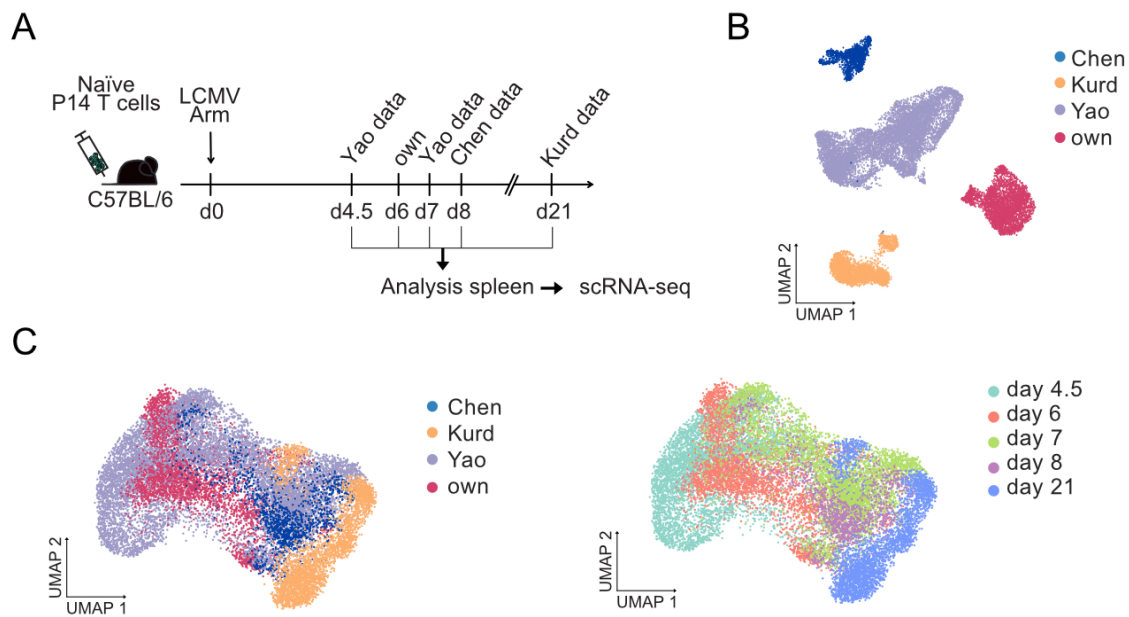


Figure 3.7.: Time-resolved transcriptional analysis of P14 T cells during LCMV Armstrong infection. **A** Schematic representation of the experimental set-up for scRNA-seq. Naïve P14 T cells were adoptively transferred into C57BL/6 hosts one day before infection with 2×10^5 pfu LCMV Armstrong. At days 4.5, 6, 7, 8 and 21 p.i., P14 T cells were re-isolated from the spleens and purified by flow cytometry before performing scRNA-seq using the 10x Chromium technology. The data sets from day 4.5 and 7 p.i. stem from Yao et al. 2019, the day 8 data from Chen et al. 2019 and the data at day 21 p.i. from Kurd et al. 2020, the scRNA-seq data from day 6 stems from own experiments. **B** We analysed the day 6 P14 T cell transcriptome together with the aforementioned published data sets. UMAP representation of the P14 T cell response as at the time points p.i. as in **A**, coloured by the first author of the originating publication. **C** UMAP representation after application of the bbkNN–correction method using the publication as batch key. UMAP coloured by the author of the publication (left) and coloured by the time point p.i. (right).

into wild-type recipients. The mice were then infected with the LCMV Armstrong strain one day later. At 6 day p.i., we isolated splenic CD8⁺ T cells, FACS-enriched CD44^{high} P14 T cells and performed scRNA-seq using the 10× Genomics Chromium platform (Figure A.2).

To understand the CD8⁺ T cell population dynamics over time, we analysed our own dataset together with publicly available datasets (Chen et al. 2019; Kurd et al. 2020; Yao et al. 2019). In the original publications, naïve P14 T cells were transferred into congenic wild-type hosts, that were infected with LCMV Armstrong the next day. At the time points 4.5 and 7 (Yao et al. 2019), 8 (Chen et al. 2019) and 21 (Kurd et al. 2020), CD44^{high} P14 T cells were isolated from the spleen, sorted by flow cytometry and analysed by scRNA-seq (10× Genomics) (Figure 3.7 A).

To relate to changes in the P14 T cell response over time, we merged our own with the public datasets and performed a uniform manifold approximation and projection (UMAP) analysis.

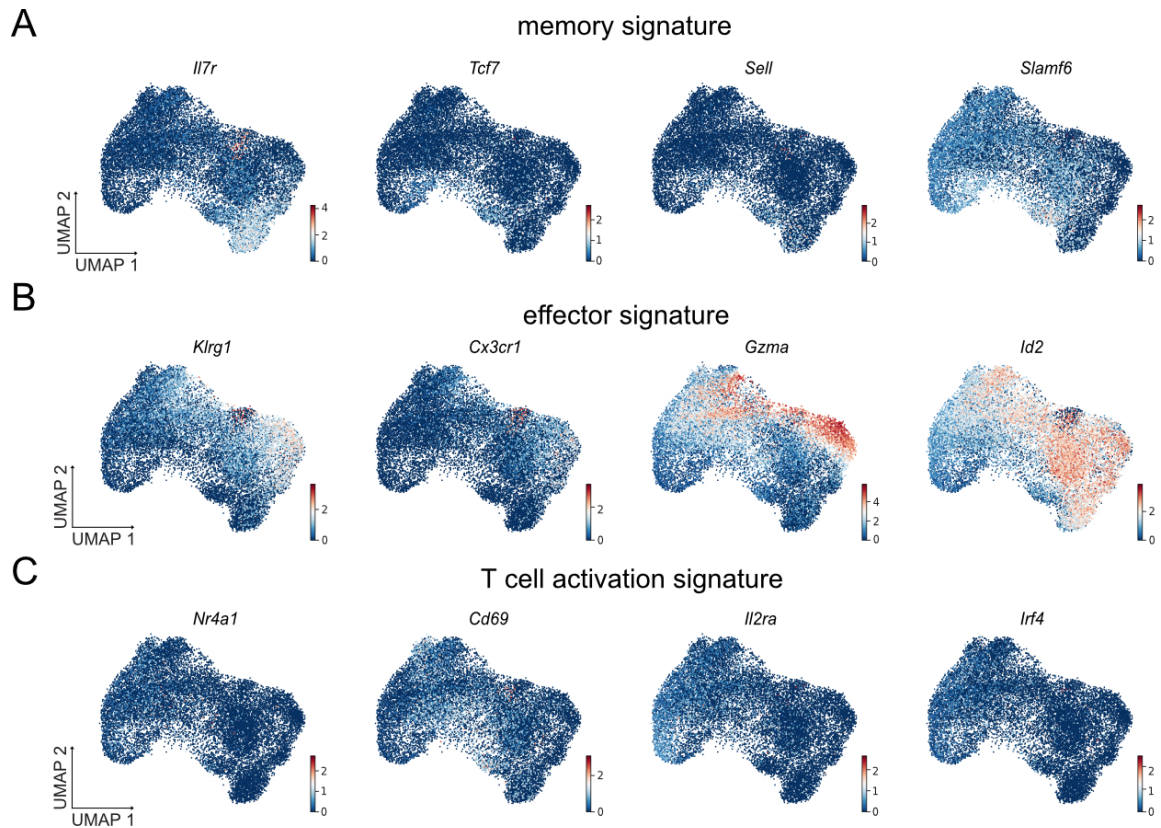


Figure 3.8.: P14 T cells after LCMV Armstrong infection, exhibiting memory signature genes occupy distinct regions in the UMAP compared to P14 T cells expressing effector signature genes. **A** UMAP representation as in Figure 3.7 B showing the expression levels of memory signature, **B** effector signature and **C** T cell activation signature genes at the days 4.5, 6, 7, 8 and 21 p.i. with LCMV Armstrong.

We observed strong batch effects between the different data sets. The data separated based on the laboratory that performed the experiment (Figure 3.7 B), whereas the data from Yao and colleagues that consisted of two different time-points remained together.

We, therefore, assumed that the distinct localisation in the UMAP stem from technical effects caused by the generation in various laboratories, rather than representing actual biological difference.

We addressed these technical effects in the data by applying a batch correction method, the batch-balanced k nearest neighbour correction (bbknn) (Polański et al. 2020), where we considered the original publication as a batch. For the batch corrections analysis the datasets on day 4.5 and 7 p.i. were assigned to the same batch.

Following batch correction, we re-computed the UMAP embedding and reconstructed the time series of LCMV Armstrong infection (Figure 3.7 C).

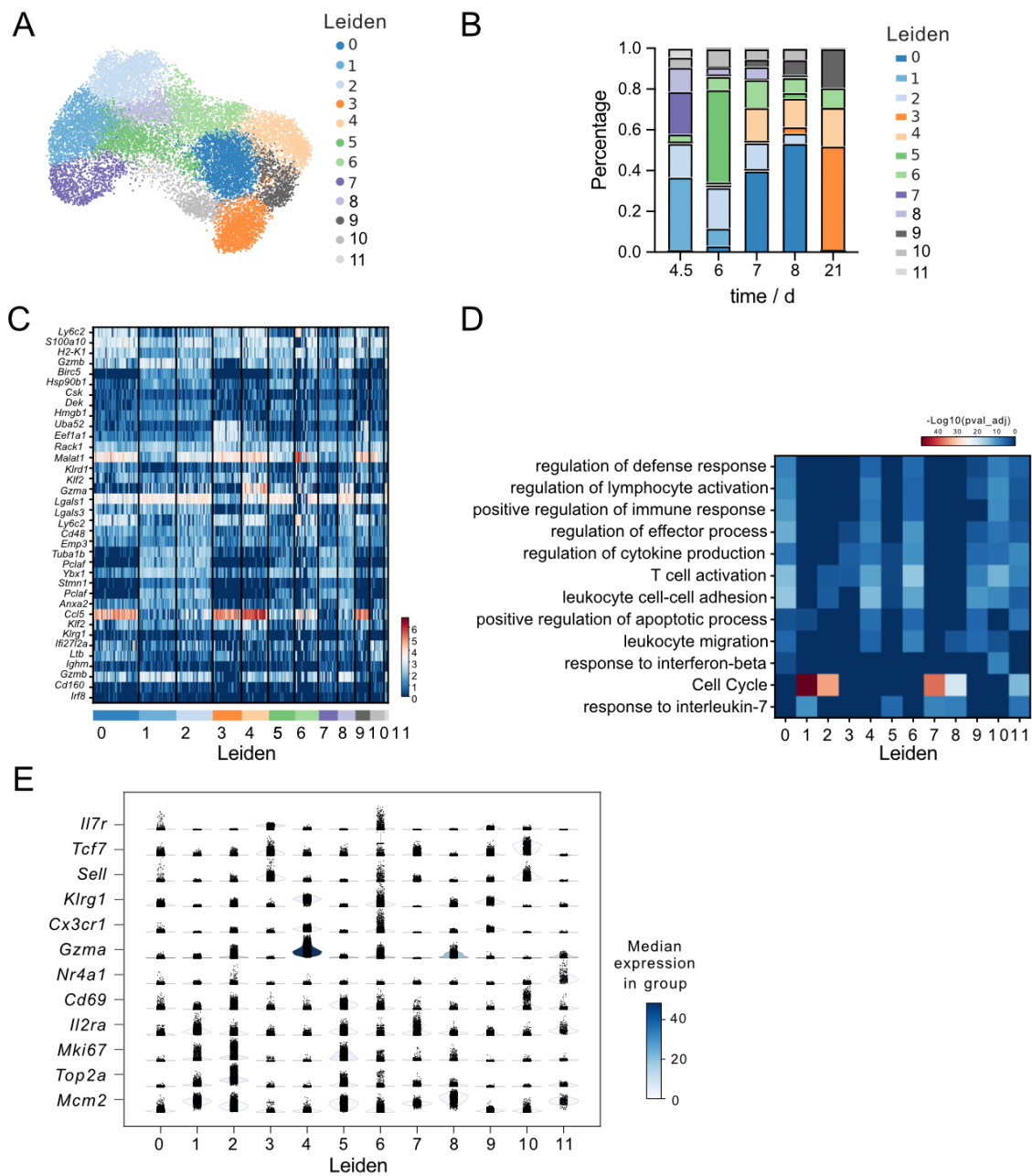


Figure 3.9.: Identification of T cell subsets based on unsupervised clustering. **A** UMAP representation as in Figure 3.7 B is showing Leiden clustering of P14 T cell responses after infection with LCMV Armstrong. **B** Bar plot depicts the percentage of clusters on each time-point. **C** Heatmap showing the expression level of the top 30 differentially expressed genes for each Leiden cluster. **D** Heatmap of gene ontology performed with Metascore 3.0, using only genes with a $\log_2FC > 1.1$ and $p_{adj} < 0.05$. **E** Violin plots with selected marker genes in each cluster. Colour bar indicated the median expression in the cluster.

Identification of T cell subsets in the scRNA-seq data

As next, we examined the gene expression profiles between the splenic P14 T cells at the different time points. Genes that have been previously associated to memory signatures such as *Il7r* (Kaech et al. 2003), *Tcf7* (encoding TCF1) (Jeannet et al. 2010; Zhao et al. 2010), *Sell* (encoding CD62L) (Buchholz et al. 2013a; Graef et al. 2014) and *Slamf6* (encoding Ly108) (Johnnidis et al. 2021) were enriched in the bottom part of the UMAP and were present as early as day 4.5 after infection (Figure 3.8 A).

Whereas, the T cells expressing effector signatures (*Klrg1*, *Cx3cr1*, *Gzma* (Böttcher et al. 2015; Gerlach et al. 2016; Kaech et al. 2003) and *Id2* (Best et al. 2013)) resided in the upper area of the UMAP (Figure 3.8 B).

Nr4a1 (encoding for Nur77) (Best et al. 2013) and other T cell activation markers, such as *Cd69* (Ziegler et al. 1994), *Il2ra* (encoding CD25) (Malek et al. 2010) or *Irf4* (Man et al. 2013) were mainly expressed before the peak of the infection at the days 4.5 and 6 (Figure 3.8 C).

We then used an unsupervised approach to cluster cells based on their transcriptional profiles (Traag et al. 2019) and identified 12 clusters (Figure 3.9 A).

All 12 clusters were already present on day 4.5 p.i. Clusters 1, 2 and 7 were predominantly represented, and clusters 3, 4, 6 and 9 accounted for less than 1% of the day 4.5 data (Figure 3.9 B). Similar to day 4.5 p.i., on day 6 p.i. cluster 3, 6 and 9 were percentage-wise rarely observed, while cluster 5 emerged.

The cells found on day 7 and the later time points contributed substantially to clusters 3, 6, 9, whereas the cells that originated at the time points before the infection peak were no longer found (clusters 1, 5 and 7) (Figure 3.9 B).

Based on the gene signature and gene ontology (GO) analysis, cluster 3 and 7 cells could be identified as CM(P) cells (*Il7r*, *Tcf7* and *Sell*).

Cluster 3 up-regulated genes involved T cell activation (*Rack1*, that is recruited into the immunological synapse after TCR triggering (Ballek et al. 2016)) and cytokine production and cluster 7 expressed cell cycle-related genes and genes involved in response to interleukin-7 (IL-7) (Figure 3.9 C-E). Cluster 0, 1, 5, 9 and 11 were identified as EM(P) subset, expressing high levels of *Il7r*, intermediate levels of *Klrg1* and *Cx3cr1* with differential expression of effector molecules (*Gzma* and/or *Gzmb*) and effector-associated chemokines (*Ccl5*) as well as transcription factors (*Irf8*, Miyagawa et al. 2012) (Figure 3.9 C-D).

Following GO term enrichment analysis, we found elevated expression of cell cycle-related signatures and responses to IL-7 in Leiden cluster 1 and genes involved in regulating defence responses, lymphocyte activation, T cell activation in the clusters 9 and 11.

The clusters 4 and 6 exhibited an EFF phenotype (*Klrd1*, *Klrg1* and *Cx3cr1*) with increased cytolytic potential (*Gzma* for cluster 4 (Figure 3.9 C, E)). Furthermore, these two clusters differentially expressed genes that were enriched in leukocyte cell-cell adhesion, T cell activation and in the regulation of effector processes (Figure 3.9 D-E).

We observed that during the early time points in particular, i.e. the time points before the peak

of the T cell expansion (clusters 1, 2, 5, 7 and 8) a variety of cell cycle genes (*Mki67*, *Top2a* and *Mcm2*) were expressed (Figure 3.9 D-E).

Inference of quiescent cells from transcriptional analysis

As proliferation and differentiation are interlinked mechanisms and we have shown that the T cell subsets exhibit disparate cell cycle speed, we tried to determine what influence the cell cycle and a cell's cell cycle phase have on our analyses.

We inferred a cell's cell cycle status by computing a cell cycle phase score (Satija et al. 2015) based on its transcriptional profile, while using a gene list containing cell cycle phase related genes (Tirosh et al. 2016) (Figure 3.10 A).

Cells with a score greater than 0 were either labelled as S- or G2/M- cell cycle phase. All cells with a S or G2/M score below 0 were assigned to being in G1-phase. With the aim to better understand the role of the cell cycle in our data, we exclusively calculated the UMAP based on the aforementioned cell cycle genes (Tirosh et al. 2016) (Figure 3.10 B, Figure A.3 A).

Additionally, we performed RNA velocity analyses (La Manno et al. 2018) of the data from the different time points in cell cycle gene space (Tirosh et al. 2016), meaning that for the RNA velocity analysis only the cell cycle genes were considered. By taking into account the ratio of spliced to unspliced RNA and projecting the RNA velocities onto the UMAP as well solely computed on the cell cycle genes (Tirosh et al. 2016), this method allowed us in this particular setting to extract the activity and directionality of single-cell division.

The RNA velocities showed a circular flow alongside the cells assigned as S- and G2/M-phase, reflecting the correct order of the cell cycle phases. These streams flew out of the cells assigned to G2/M and found an endpoint in the non-assigned cell subset.

Interestingly, the velocity arrows of the G1-phase assigned cell cluster did not exhibit specific directionality. We, therefore, interpreted this outflow of RNA velocity streams as an exit from the cell cycle, and contemplated that these cells rather represented cells from the G0-phase than from the G1-phase (Figure 3.10 B, Figure A.3 A).

Our results implied that the Seurat classification method (Satija et al. 2015) misclassified G1 and G0-phase cells. In addition, the original list from Tirosh et al. 2016 used for phase scoring in the Seurat method (Satija et al. 2015) contains not only S-phase but G1- and S-phase genes, supporting the G0-phase signature of the G1-assigned cells. Thus, based on these cell cycle genes (Tirosh et al. 2016), we were able to discriminate dividing from cell cycle arrested cells. In line with a previous publication (Bastidas-Ponce et al. 2019), where it was also referred to proliferating and non-proliferating cells instead of distinguishing between the different cell cycle stages following cell cycle phase scoring with the Seurat method. However, Bastidas-Ponce and colleagues did not further comment on why the G1-phase classification on their study was assigned to a non-proliferating subset.

Dividing cells exhibited an enriched signature for the cell cycle genes from Tirosh et al. 2016 (Figure 3.10 C, Figure A.3 B-C).

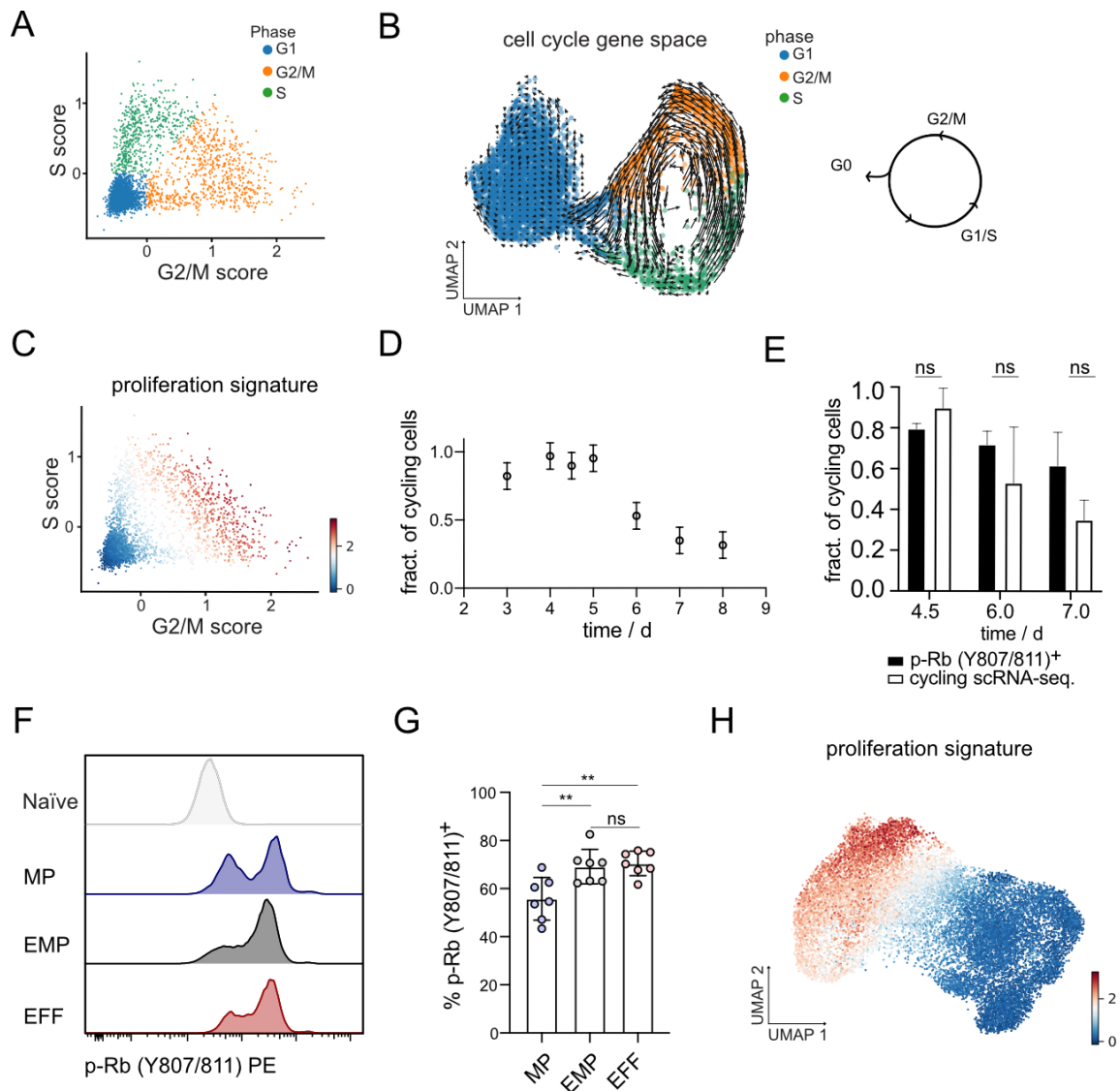


Figure 3.10.: Subset-specific cell cycle drop out with the MP compartment arresting from cell cycle earlier compared to the EMP and EFF subsets. **A** Scatter plot depicting the S and G2/M score for the P14 T cells at day 7 after LCMV Armstrong infection from the scRNA-seq data from Yao et al. 2019. For each cell, a S- or G2/M-phase score was computed based on the gene list from Tirosh et al. 2016 using the Seurat scoring method (Satija et al. 2015). Cells with a score greater than zero for S or G2/M were classified as being in S- or G2/M-phase, respectively. Cells with scores smaller than zero were assigned to the G1-phase. **B** UMAP representation of the scRNA-seq data from P14 T cells at day 7 p.i. with LCMV Armstrong. Computation of the UMAP and assessment of the RNA velocities relied on the cell cycle-related genes from Tirosh et al. 2016. The direction of RNA velocities in the cell cycle gene space indicates cell cycle phase progression. S- or G2/M-phase assigned cells to represent cycling cells, whereas the cells assigned to G1-phase describe the cell cycle arrested cells. **C** Scatter plot as in Figure **A**, proliferation signatures were computed with Vision using the gene list from Tirosh et al. 2016. A high score defines cycling cells, and a low score non-cycling cells.

Next, we inferred the percentage of actively cycling cells from the transcriptional analyses from day 3 till day 8 p.i. with LCMV Armstrong. Therefore, we included additional public available data from an infection with LCMV Armstrong. In addition, to our day 6 data, we also analysed the single-cells in the cell cycle gene space from Yao et al. 2019 (day 4.5 and 7) and Chen et al. 2019 (day 8), as well as from Kurd et al. 2020 (day 3, 4, 5, 7).

Until day 6 p.i. the majority ($> 90\%$) of the cells were actively dividing only then, they stopped and became quiescent (Figure 3.10 D). Of note, the day 21 sample (Kurd et al. 2020) contained only quiescent cells (data not shown).

We then verified the transcriptional cell cycle analyses by comparing the results to the p-Rb expression at the serine residues 807/811. p-Rb expression levels at day 4.5, 6 and 7 p.i. roughly matched the fractions of cycling cells that were assessed from the scRNA-seq datasets (Figure 3.10 E). We probably underestimated the fraction of cycling cells in the transcriptional analyses, as the cells adjacent to the cycling cells in the cell cycle space UMAP still displayed RNA velocity activity in terms of large arrows and distinct directionality.

To better understand the consequence of cell cycle arrest on differentiation, we also examined the expression of p-Rb in our MP, EMP and EFF T cell subsets. For this purpose, naïve P14 T cells were transferred into wild-type recipients, infected with LCMV Armstrong the next day and measured the expression of p-Rb on day 6 after the infection.

We observed that there were already significant differences in the cell cycle activity between the T cell subsets at this time point after infection. Along the progressive differentiation axis, the majority of the MP cell subtype terminated the cell cycle, ahead of the EMP and EFF subtypes (Figure 3.10 F, G).

Figure 3.10 : **D** Fraction of cycling cells inferred from the scRNA-seq analyses as in **B** taking into account only the cells assigned to be in the orange and blue cluster (S- and G2/M-phase according to the Seurat classification). $n = 1 - 4$ data sets per time point, day 4.5 and 7 from Yao et al. 2019, day 3, 4, 5, 6, 7 from Kurd et al. 2020, day 8 from Chen et al. 2019 and day 6 (this study). Depicted is the mean and the pooled variance. Experimental set up as in Figure 3.2 A. In brief, at the days 4.5, 6 and 7 p.i. LCMV Armstrong, P14 T cells were re-isolated from the spleen, and the phosphorylation of the retinoblastoma (p-Rb) protein on the Y807/811 residues was assessed by flow cytometry. **E** Bar graph represents the fraction of cycling P14 T cells measured by the expression of p-Rb and the fraction of cycling P14 T cells inferred from the scRNA-seq data using the approach as in **D**. $n = 2 - 6$, data pooled from two independent experiments. Mean and s.e.m., ns = not significant, $*p > 0.05$ Mann-Whitney U test. **F** Histograms depicting subset-specific phosphorylation of the retinoblastoma protein on the Y807/811 residues and **G** its quantification. The experiment was performed as in **E** with analysis at day 6 p.i. $n = 7$, data pooled from two independent experiments, mean and s.e.m. $**p < 0.005$, ns = not significant, one-way ANOVA with multiple comparisons. **H** UMAP representation of the P14 T cells from day 4.5, 6, 7, 8 and 21 after LCMV Armstrong infection (as in Figure 3.7), displaying proliferation signatures computed using the gene lists from Tirosh et al. 2016.

Division cessation and the concomitant quiescence thus play a significant role in the changes of the CD8⁺ T cell response over time. The proliferation signatures were found to be particularly enriched at the early time points of LCMV Armstrong infection (Figure 3.10 D, H).

Identification of distinct T cell subpopulations based on their gene expression profile

During the acute phase of the LCMV Armstrong infection, the cells demonstrate great heterogeneity, not only based on their gene expression but also concerning their proliferation.

By performing Leiden clustering, we have already been able to identify T cell subgroups and investigated the subtle differences between them (Figure 3.9). In further analyses, we want to focus on the MP, EMP and EFF subgroups as previously identified by flow cytometry (see section 3.2).

Therefore, we have pooled the Leiden clusters based on the differential gene expression analyses (Figure 3.9), the division status (Figure 3.10) and the expression of the memory signature markers such as *Il7r*, *Tcf7*, *Sell* and effector signature genes, exemplified by *Klrg1*, *Cx3cr1*, *Gzma* in addition to the signatures, marking cycling cells (*Mki67*, *Top2a*, *Mcm2*) (Figure 3.11 A-C, Figure A.4 A-B).

From the time point of the peak of the infection and onwards, most of the cells were quiescent, and more mature cells with distinct signature of terminal differentiated cells were detected.

We, therefore, defined the non-cycling (nc) cells based on their transcriptional profile as memory T cells (ncM), effector memory T cells (ncEM) and terminal effector T cells (ncEFF), respectively cycling (c) cells were correspondingly classified as cMP, cEMP and cEFF (Figure 3.11 C).

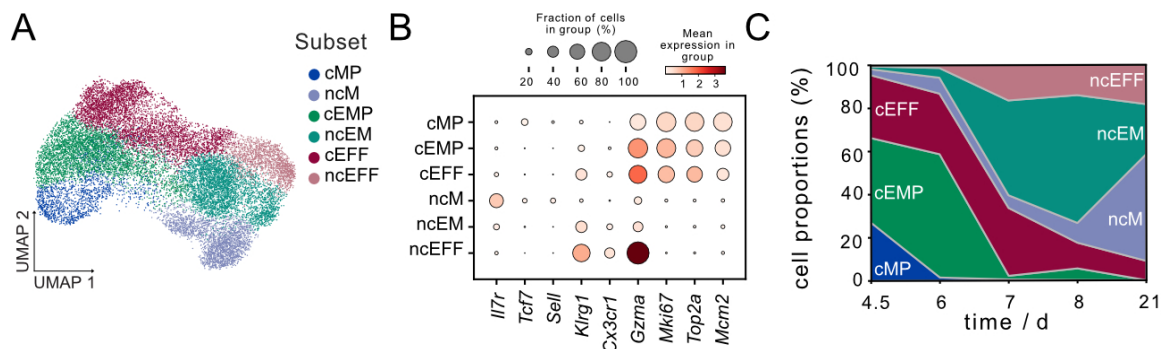


Figure 3.11.: Identification of subsets in the P14 T cell responses after LCMV Armstrong infection based on the expression of maker genes and cell cycle stage. **A** Own grouping based on the combination of the Leiden clusters according to the expression of *Tcf7* and *Cx3cr1* into following subsets: cycling memory precursor (cMP), effector memory precursor (cEMP) and effector (cEFF) cells, or non-cycling memory cells (ncM), effector memory cells (ncEM) and terminal effector cells (ncEFF). **B** Dot plots representing the expression of *Il7r*, *Tcf7*, *Sell* and *Klrg1*, *Cx3cr1*, *Gzma* and *Mki67*, *Top2a*, *Mcm2* in each self-defined T cell subset. Dots are coloured by the mean expression and dot size represents the fraction of cells per group. **C** Stack plot displays the cell proportions in each subset per time point.

The cells from cluster 7 were assigned to the cMP subset, the cEMP subset contained the cells from cluster 1, 5 and 11 and the cEFF subset constituted of a combination from cluster 2, 6 and 8. Cluster 3 and 10 formed the ncM compartment, cluster 0 and 9 the ncEM subset and ncEFF cells contained cells from cluster 4 (Figure A.4 A-B).

Trajectory analysis to delineate the developmental relationship between the subsets

We performed different kinds of trajectory inference analyses to investigate the state transitions of the aforementioned T cell subsets during LCMV Armstrong infection.

We first computed the CytoTRACE score. CytoTRACE is a computational framework that provides an unbiased method to localise the developmental origin based on single-cell transcriptional diversity (Gulati et al. 2019). CytoTRACE pinpointed the cells from the cMP subset as those with the highest developmental potential (Figure 3.12 A). RNA velocity analysis corroborated this finding, when the directionalities were projected onto a 2-D embedding.

The directionality of differentiation originates as well in the cMP subset that diversifies along the progressive axis. The cMP cells fuelled all other subsets. At late time points, the ncM fed the ncEM and ncEFF compartments (Figure 3.12 B). This differentiation pattern is in line with published work from Pais Ferreira et al. 2020 and the Busch laboratory (Buchholz et al. 2013a and Graef et al. 2014). In addition, we have computed the diffusion maps (Figure A.5 A-B) and carried out a diffusion pseudo-time analysis (Haghverdi et al. 2016), designating a cell from the cMP subset with a CytoTRACE value of 1 as the root cell (Figure 3.12 C, Figure A.5 B-C).

Ordering the expression of signature-defining genes in pseudo-time, confirmed the gradual loss of *Myb*, *Slamf6* and *Tcf7* and the later enhancing expression of effector memory and effector gene expression such as *Cd27*, *Il7r* and *Klrg1* as pointers of increasing terminal differentiation (Figure 3.12 D).

Construction of a model structure

With the aid of these trajectory inference analyses, we derived a model topology to describe T cell diversification mechanisms. One approach would be to read the RNA velocity directions, as shown in reduced form in Figure 3.12 E. As in the original UMAP representation, the origin of diversification was the cMP compartment (Figure 3.12 B). The cMP give rise to cEMP and cEFF (perpendicular arrows). When exiting the cell cycle, the cells retain their identity (horizontal arrows). A similar progressive differentiation pathway can be observed after a cell became quiescent (Figure 3.12 B). Further methods have been developed to derive model topologies from transcriptional analyses. One of these methods is the partition-based graph abstraction (PAGA) analysis (Wolf et al. 2019). PAGA extracts interpretable graph-like maps from scRNA-seq data. Through the estimation of the connectivity of manifold partitions a topology-preserving map of the single cells is generated (Wolf et al. 2019) (Figure 3.12 E). PAGA finds up to four connections between two subsets.

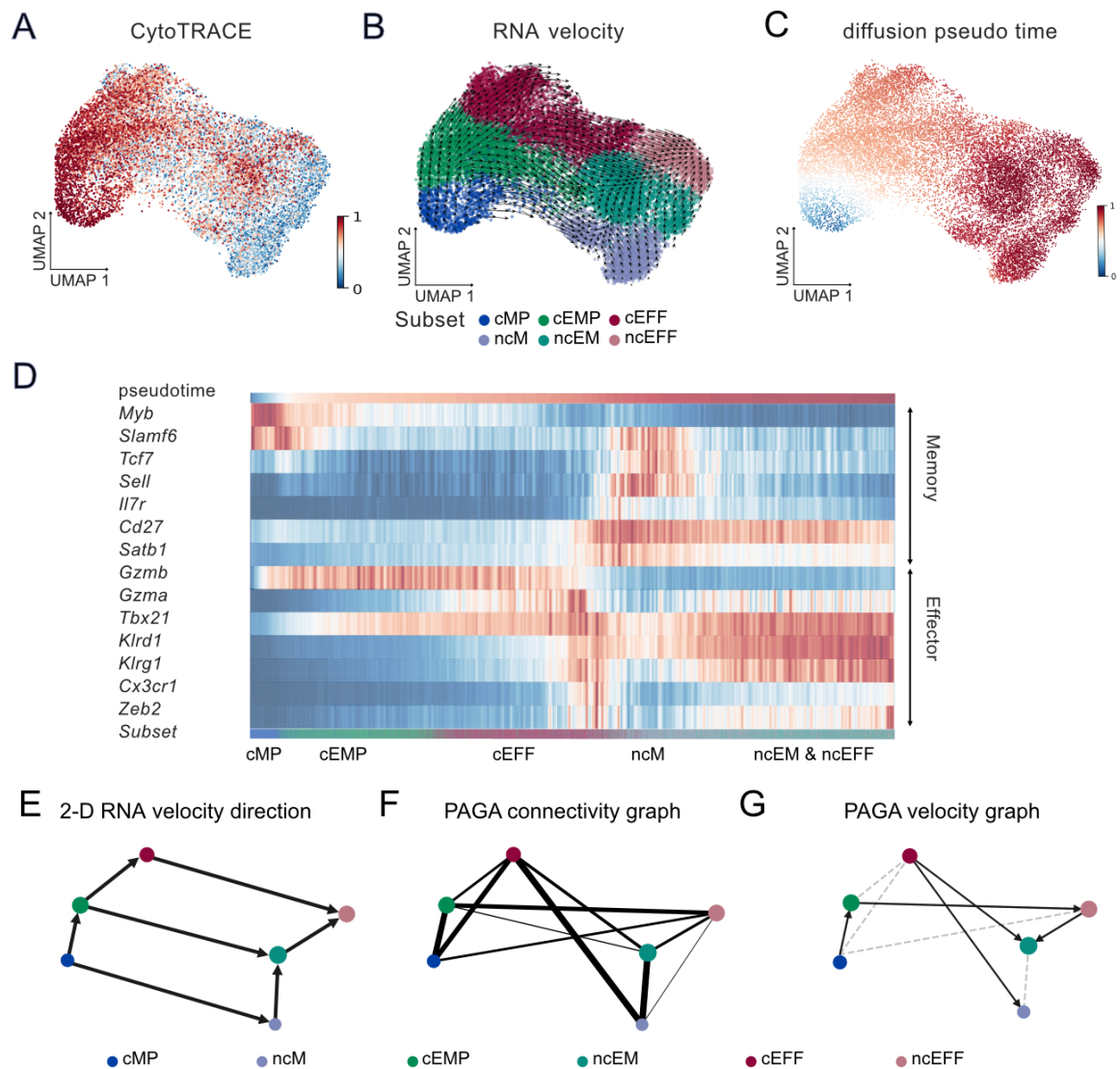


Figure 3.12.: Inference of a descriptive mathematical model for CD8⁺ T cell responses after LCMV Armstrong infection using scRNA-seq trajectory analysis. **A** UMAP representation is displaying the CytoTRACE score. CytoTRACE scoring labels cells according to their degree of differentiation. A score of one represents the most undifferentiated cell state, and a score of zero represents the cell with the highest degree of differentiation. **B** RNA velocities displayed on the 2-D UMAP representation. Directionality originates from the MP subset. **C** UMAP embedding with diffusion pseudo-time. A cell within the cMP subset with a CytoTRACE score of 1 was randomly chosen as root cell for diffusion pseudo-time computation. A low diffusion pseudo-time score identifies undifferentiated cell states, whereas a high score is assigned to cells that have reached a terminal differentiation state. **D** Heat map with selected memory and effector signature genes ordered by diffusion pseudo-time. Normalised marker gene expression of CytoTRACE ordered cells. **E** Reduced visualisation of RNA velocities in a 2-D UMAP embedding with implicated differentiation trajectories based on the subsets defined in **B**. **F** PAGA connectivity graph; Line thickness indicates connectivity strength. **G** PAGA velocity graph. Black arrows represent significantly identified transitions between the subsets. Grey dotted lines indicate non-significant transitions.

Additionally, to gain insight on the directionality of subset transition we included the RNA velocity information in the PAGA analysis (Figure 3.12 F). Many connections found by the connectivity graph computation did not represent significant transitions in the PAGA velocity graph (Figure 3.12 F, grey dashed lines). We observed a significant transition between the cMP and the EMP subsets (cMP \rightarrow cEMP), the cEMP and ncEFF subset (cEMP \rightarrow ncEFF) and the cEFF into the ncM and ncEM subset (cEFF \rightarrow ncM, cEFF \rightarrow ncEM).

This is in contrast to the RNA velocity analysis where the arrows did not indicate the subset conversion from cEFF to ncM. In addition, the PAGA velocity analysis infers a ncEFF to ncEM transformation. The ncEFF \rightarrow ncEM-conversion in the combined PAGA velocity analysis is not only in contradiction to our analyses, in which we evaluated the RNA velocities separately (Figure 3.12 B), but this transition also has been experimentally ruled out (Milner et al. 2020). Furthermore, during the PAGA differentiation scheme predictions, neither connectivity nor a transition between the cMP to the ncM subset was identified, even though this transition has been described in previous studies using TCF1 as phenotypic marker (Johnnidis et al. 2021; Pais Ferreira et al. 2020).

Application of lineage relations methods such as PAGA could be hampered by the analysis of multiple batches. To avoid batch-related misinterpretation and with the aim to deduce the differentiation patterns of CD8⁺ T cells after an acute infection in general, we produced a series of scRNA-seq datasets covering time-points before, at and after the peak response of *L.m.*-OVA infection. We will discuss the transcriptional analysis and derive a mathematical model from the cells after *L.m.*-OVA infection in the following section.

3.5. Towards a uniform model of T cell differentiation during self-limiting infections

CD8⁺ T cell responses mounted after acute infections are alike

Similar to the analyses in the previous section, where we investigated the the CD8⁺ T cell response after the LCMV Armstrong infection, we conducted a time-series scRNA-seq experiment using the *L.m.*-OVA infection model. The bioinformatics analysis shown in this section was performed by my colleague, Jonas Mir, while the experiments was conducted by myself.

To this end, naïve OTI T cells were adoptively transferred into C57BL/6 mice and subsequently analysed at days 4.5, 8 and 12 p.i. OTI T cells were isolated from the spleen and the lymph nodes, CD44^{high} OTI T cells were sorted by flow cytometry and their single-cell transcriptome analysed (10 \times Genomics) (Figure 3.13 A).

Using cellular indexing of transcriptomes and epitopes by sequencing (CITE-seq) (Stoeckius et al. 2017), we performed immunophenotyping of these cells in combination with the transcriptome analysis.

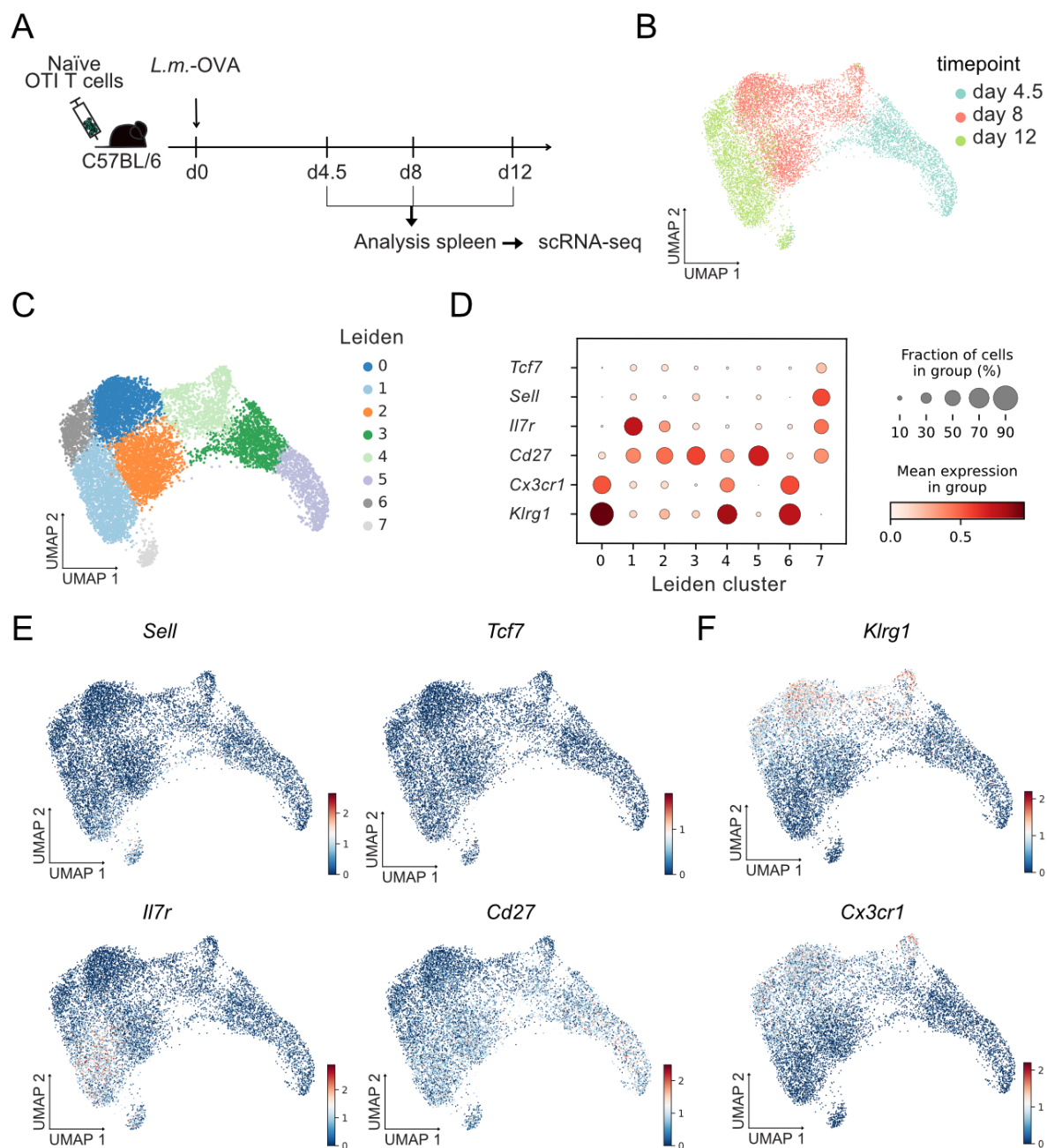


Figure 3.13.: Single-cell transcriptomics analysis of OTI T cells after the infection with *L.m.-OVA*. **A** Schematic overview of the experimental set-up for scRNA-seq. Naïve OTI T cells were adoptively transferred into C57BL/6 mice one day prior to infection with 2×10^3 cfu *L.m.-OVA*. At the days 4.5, 8 and 12 p.i., OTI T cells were re-isolated from the spleen and the lymph nodes, purified by flow cytometry and scRNA-seq was performed using the 10x Chromium technology. **B** UMAP representation of the data sets coloured by the time point p.i. and **C** Leiden clusters. **D** Dot plot depicts the expression of memory and effector signature genes in each Leiden cluster. Colour represents the mean expression and dot size the fraction of cells in each group. **E-F** Gene expression profiles on UMAP depicting **E** the memory signature genes *Sell*, *Tcf7*, *Il7r* and *Cd27*, as well as **D** the effector gene signatures *Klr1* and *Cx3cr1*. Own experiments, bioinformatical data analysis was performed by Jonas Mir.

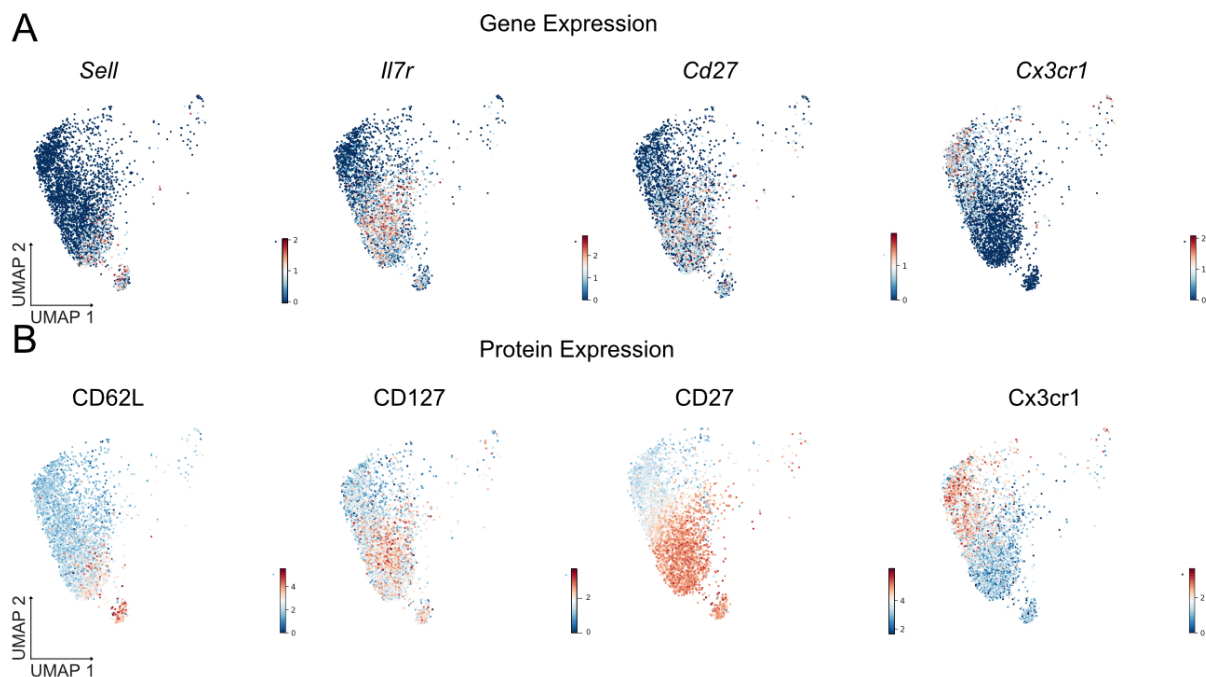


Figure 3.14.: Gene expression in scRNA-seq data coincides with protein expression. **A-B** UMAP representation of the OTI T cell transcriptome at day 12 p.i. with *L.m.*-OVA displaying **A** the gene and **B** protein expression profiles for selected phenotypic markers. Own experiments, bioinformatical data analysis was performed by Jonas Mir.

Transcriptional analysis was performed on the splenic and lymphatic OTI T cells from the three-time points collectively (Figure 3.13 B). The cells from the different time-points aligned based on the day they were retrieved from infection from left to right (Figure 3.13 B).

Unsupervised Leiden clustering (Traag et al. 2019) was applied and 8 clusters were found. Exemplified by a few memory and effector signature genes, subsets expressing *Sell*, *Tcf7*, *Il7r* or *Cd27* were found in the bottom part of the UMAP2 axis, while cells expressing *Klrg1* and *Cx3cr1* covered the upper part of the UMAP (Figure 3.13 C-F). From the comparison of the gene expression levels with the protein expression for the markers CD62L, IL7R, CD27 and CX3CR1 and it was observed that gene and protein expression coincided as representatively shown for the OTI T cells from day 12 p.i. Taking into account the surface expression, the cluster-defining gene expression and the proliferation status of a cell (data not shown), the cells were annotated as cMP, cEMP, cEFF, ncM, ncEM or ncEFF and resting memory subsets.

Next, RNA velocity analyses were performed and very comparable results as in the analyses for the P14 T cells after LCMV Armstrong infection were found. In the same way, as in the LCMV Armstrong scRNA-seq dataset, RNA velocities of OTI T cells during infection with *L.m.*-OVA originated from the cMP subset (Figure 3.15 A).

More extensive analysis with CytoTRACE identified the cMP subset as the most undifferentiated state and corroborated the RNA velocity result (data not shown). These findings suggested that

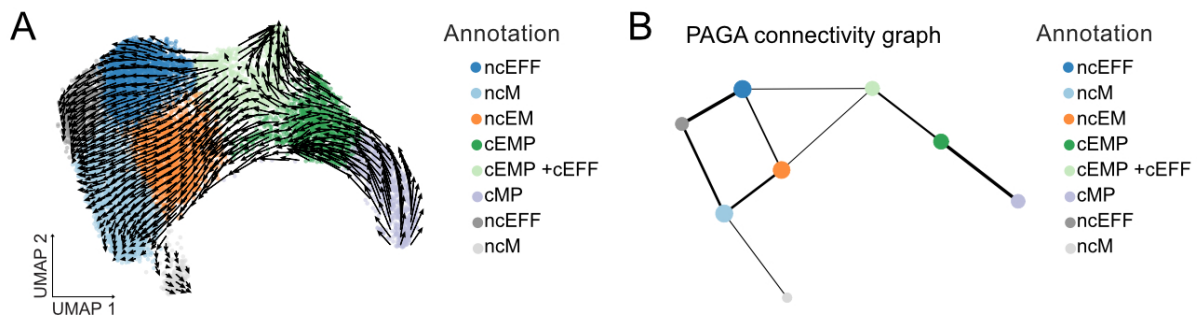


Figure 3.15.: Inference of a mathematical model topology to describe the OTI T cell response after *L.m.*-OVA infection using RNA velocities and PAGA connectivity graphs. **A** Experiment as in Figure 3.13. **F** RNA velocities based on the UMAP representation with Leiden clustering and own annotation. **B** PAGA connectivity graph based on Leiden clusters as in **E**. The thickness of connectivities represents connection strength. Own experiments, bioinformatical data analysis was performed by Jonas Mir.

independent of the pathogen-type that causes the acute infection, multipotent cMP CD8⁺ T cells are found at the developmental root and give rise to any other subsets.

These findings were further validated by the investigation of the connectivities between the T cell clusters with PAGA analysis. The PAGA connectivity graph linked the cMP compartment with the cEMP and cEFF subsets (Figure 3.15 B). At the time cells transitioned from active proliferation to cell cycle quiescence, the cell retained their phenotypic identity. Interestingly, at day 12 p.i. with *L.m.*-OVA a progressive differentiation pattern for the non-dividing cells the way it was detected in the RNA velocity analyses in LCMV Armstrong was not observed (Figure 3.12 B).

During the LCMV Armstrong infection, the progressive stream after division cessation stem mainly from the day 21 p.i. dataset and might indicate that the transition between active cell division and cell cycle quiescence masked the effects of differentiation accessible by the applied methods.

In these transcriptomic analyses we identified the same T cell subsets for both, bacterial and viral infections.

In both infection models, the differentiation origin pinpointed to the MP subset and followed a strikingly similar pattern with a transition to terminally differentiated states through cell cycle exit. PAGA analysis reflected some of these trajectories. However, the RNA velocity directionalities were supported by experimental data. In the next section, we will construct a mathematical model based on the structure suggested from the RNA velocity analyses and test it on the LCMV Armstrong single-cell fate-mapping data.

3.6. Mathematical modelling corroborates the MP to EFF subset lineage relationship

In the previous section, we performed lineage tracing with the scRNA-seq data and found possible differentiation patterns. In line with published research using animal models of early acute infection (Buchholz et al. 2013a; Kretschmer et al. 2020; Pace et al. 2018; Pais Ferreira et al. 2020), our analyses pinpointed the MP compartment as the origin of differentiation that fed the other, EMP and EFF, subsets.

For model construction, we then translated the results from the lineage analyses of the scRNA-seq data into a mathematical model, where the RNA-velocity analyses in the 2-D UMAP representation formed the core structure (Figure 3.12).

The dynamics of differentiation were initiated starting from one single naïve $CD8^+$ T cells. The naïve T cell is recruited following the infection and reaches the MP compartment. Cells in the MP compartment can either divide and self-renew, exit the cell cycle to become a cell of the ncM type, or differentiate and end up in the EMP compartment.

A cell with an EMP subset identification can either proliferate, stop dividing and become a ncEMP cell or differentiate into an cEFF T cell. cEFF T cells are terminally differentiated and have the ability to increase their subset size by proliferation or accumulate in a non-dividing state. Non-dividing T cells and exit their state and start to differentiate along the progressive axis and advance from memory (M) T cells to EM T cells, and eventually become EFF T cells. We call this model the full differentiation model (Figure 3.16 A). The preceding part on the mathematical modelling was performed by my colleague Jonas Mir.

The full differentiation model comprises of 11 subsets and 14 parameters. In this mathematical framework, differentiation, proliferation and cell cycle exit are stochastic processes that follow an exponential waiting time. The waiting time for the recruitment was constructed to follow a gamma-distribution

However, for the mathematical modelling the lowest layer, as indicated by the box (Figure 3.16, A) was omitted, as it was only observed in the data after day 8 p.i. The data that is used for the following mathematical description covers the time points from the expansion phase.

Therefore, the model structure as in Figure 3.16 A without the boxed layer was used. It contains 7 compartments and 9 parameters, whereby the proliferation rates of the EMPs and EFFs posed a combined rate and the time at which cells stop proliferating was the 9th parameter. Based on these 7 compartments and 9 parameters, equations to describe the time dependence of the means, variances and covariances were derived. These equations were solved and their solution used to fit the data and to find parameters that reflect the underlying measurements realistically. For the mathematical modelling, the means, CVs and correlation coefficients from the single-cell fate-mapping data from day 8 after LCMV Armstrong infection was used (summary of data in Appendix I Table A.1).

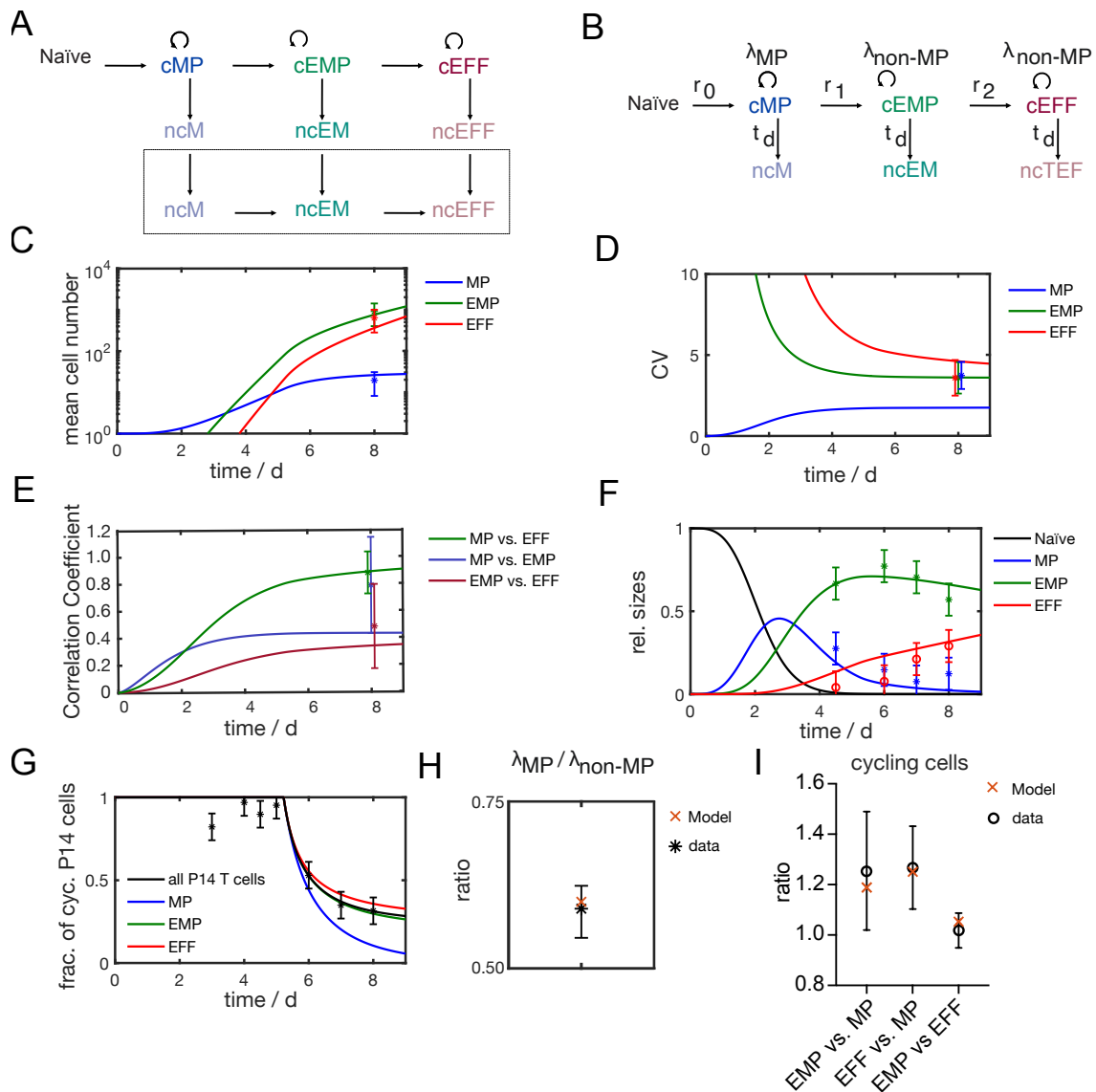


Figure 3.16.: A by cell cycle drop-out extended progressive model supports the fate decision of P14 T cells during LCMV Armstrong infection. **A** The full model of progressive differentiation. The boxed layer is only observed after the peak of the response during the contraction and memory phase. **B** Mathematical model that best represents the data. **C** Fit to the mean value of the MP, EMP and EFF progenies, also to the **D** coefficient of variation (CV) and to the **E** three pair-wise Pearson correlation coefficients (ρ) and **F** the relative subset sizes. **G** Cell cycle drop out dynamics over time predicted by the mathematical model and data, containing the fraction of cycling cells, data as in Figure 3.10 D. **H** The proliferation rate ratio of the MP versus the non-MP subset. **I** Ratio of each cycling subset with one another and s.e.m. Asterisks (*) indicate data points used in the model fitting routine, open circles (o) represent predicted data. Jonas Mir has developed the mathematical model and identified the best supporting model for the data. Experimental data shown in **C-E** were generated by Lorenz Kretschmer and Dr. med. Veit Buchholz. Data depicted in **F-I** stem from own experimental and bioinformatics analysis.

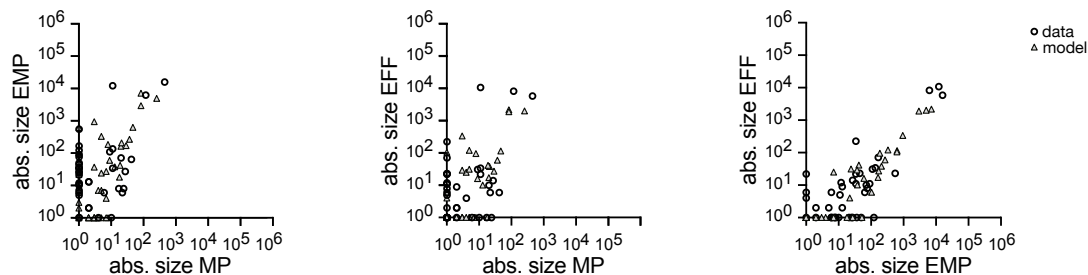


Figure 3.17.: Verification of cell cycle arrest progressive model using the Markov stochastic simulation. Pair-wise correlation of the single-cell fate-mapping data at day 8 p.i. with LCMV Armstrong as in Figure 3.6. Open circles (o) represent the data, and grey triangles (Δ) the model simulation. Jonas Mir generated the simulated data shown in this figure. Experimental data stems from Lorenz Kretschmer and Dr. med. Veit Buchholz.

The model was further informed using the relative subset sizes from day 4.5, 6, 7 and 8 after LCMV Armstrong infection. Furthermore, the cell cycle exit kinetics of the P14 T cell response provided information on the non-dividing compartment, using the analyses from the scRNA-seq data from day 3 to 8.

The cell cycle speed quantifications were used to constrain the proliferation rates of the model. For this, the cell cycle durations were converted into division rates (using equation 6.3) and the ratio of these rates between the MP and non-MP subset taken to fit the model. The parameters were estimated by minimising the sum of squared residuals.

The best-describing model for the LCMV Armstrong P14 response up to day 8 is shown in Figure 3.16 B. This model is, in essence, the progressive model as published in Buchholz et al. 2013a, which has been extended with a cell cycle exit process and we will call from here on as extended progressive model of differentiation.

The resulting fit of this model is shown in Figure 3.16 C-I. This model can accurately describe the mean values, variability and correlations, and the evolution of subset sizes over time, cell cycle rates and division arrest.

In terms of AICc, the extended progressive model outperformed the full model of differentiation, in which the processes in last layer were omitted (Figure 3.16 A, model structure without the boxed layer). Therefore, the full model of differentiation was rejected given the provided data. Compared to the full differentiation model, the best model was reduced in such a way, that it used only 7 parameters to describe the data, demanding the same cell cycle drop out rate (t_d) for the three subsets.

Six out of the seven parameters explained the transition processes between or within the compartments, such as the recruitment (r_0), the differentiation (r_1 , the differentiation rate from cMP to cEMP and r_2 , the differentiation rate from cEMP to cEFF), the cell division (λ_{MP} and λ_{non-MP} and the transition to the non-cycling subset (t_d).

The additional parameter τ represented the time at which cells can stop dividing. The pa-

Table 3.1.: Best fit parameters to the by cell cycle drop out extended progressive model of differentiation. Parameter estimation and identification of their 95 % interval confidence bounds were done by Jonas Mir.

parameter	value	95 % CI
naïve \rightarrow cMP rate (r_0)	1.1 d ⁻¹	(0.8, 2.5) d ⁻¹
cMP \rightarrow cEMP rate (r_1)	0.3 d ⁻¹	(0.2, 0.5) d ⁻¹
cEMP \rightarrow cEFF rate (r_1)	0.082 d ⁻¹	(0.045, 0.124) d ⁻¹
MP proliferation rate (λ_{MP})	1.1 d ⁻¹	(0.9, 1.3) d ⁻¹
non-MP proliferation rate (λ_{non-MP})	1.8 d ⁻¹	(1.5, 2.0) d ⁻¹
drop out rate (t_d)	1.3 d ⁻¹	(1.0, 1.8) d ⁻¹
drop out time (τ)	5.2 d	(4.7, 5.7) d

parameters from the best fit and the parameter uncertainties that were estimated by the profile likelihood method are listed in Table 3.1.

In the extended progressive differentiation model the recruitment rate reflected a realistic value and was found to lie in the range of published recruitment times (De Boer et al. 2001).

Using Markov’s stochastic simulation algorithm, the results from the mathematical modelling were tested and corroborated (Figure 3.17). Also, the dispersion of the T cell response size was correctly reflected when the single-cell responses were simulated based on the parameters from the extended progressive model. This was further confirmed by the comparison of the evenness index of the data ($i_{Gini,d} = 0.914$) to the modelled response ($i_{Gini,m} = 0.876$).

Furthermore, the simulations showed that the model described the dichotomy between a few large clones (giants) and many small clones (dwarfs) adequately.

It was further tested whether the extended progressive model could recreate the OTI response up to day 12 after L.m.-OVA infection. Using similar input data as when modelling the LCMV Armstrong P14 T cell response (mean, CV, ρ , proliferation rate, cell cycle drop out kinetics), this model also accurately reproduced the OTI T cell dynamics and when including the lower layer (Figure 3.16 A, including the processes in the box) and applying it to data at later time points, it described the CD8⁺ T cell responses during the contraction and memory phase as well (unpublished observations by Jonas Mir, data not shown).

Finally, we have established a differentiation model that quantitatively describes the differentiation dynamics of CD8⁺ T cells during the expansion phase of a bacterial and viral infection.

4. Developmental plasticity and the commitment to T cell exhaustion

Following the detailed investigation of the T cell dynamics during the acute infection with two different pathogens, both viral and bacterial, in the last chapter, we investigate how exhausted T cells develop in this chapter.

We use the animal model for LCMV, which, depending on the strain, leads to either an acute, self-clearing LCMV infection (Armstrong) or a chronic one (clone 13 strain) with concomitant T cell exhaustion.

In particular, we focus in this chapter on the early time points of the expansion phase and investigate the antigen-specific T cell responses before the peak of the infections.

Our aim is to scrutinize the role of progenitor T cells in the development of T cell exhaustion. Also, we want to understand which modulators lead to a divergence between functional and exhausted T cell subsets at these early stages of the infection.

As in the previous chapter, we employ an interdisciplinary approach: First, we use single-cell transcriptomics to investigate the heterogeneity of the T cell responses after the two infections. Through scRNAseq analyses, we aim to understand the processes during differentiation that differ between the acute and chronic infection and those that are shared between both.

Differential gene expression analyses, allowed us to find markers that identify the different sub-populations of these T cells and we verified the expression of these markers by flow cytometric analysis.

Furthermore, we test the extended progressive model on data from both LCMV Armstrong and clone 13 infection using the same phenotypic marker combination. Thereby, we intend to understand which parameters need to be different in the chronic infection setting compared to the acute infection.

To understand the role of exhausted progenitor cells and their branching from canonical differentiation trajectories we also mathematically examine the arrested model of T cell exhaustion. Among other things, we also investigate the role of TOX, a hallmark of T cell exhaustion. Therefore, we re-analyse a published scRNA-seq dataset obtained from wild-type and *Tox*^{-/-} T cells at day 7 of LCMV clone 13 infection with the aim to understand how its expression hampers the differentiation into effector subsets in a persisting infection setting.

This chapter contains experimental data collected by Lorenz Kretschmer from Dr. med. Veit Buchholz's laboratory and data from experiments that were performed by myself. I performed mathematical modelling and bioinformatics analyses. Jonas Mir quantified the duration of the cell cycle length. Dr. med. Veit Buchholz, Lorenz Kretschmer and Jonas Mir are affiliated to the Institute of Medical Microbiology, Immunology and Hygiene at the Technical University of Munich in Munich, Germany.

4.1. Early divergence of T cell transcriptomes following acute and chronic infection

Integration of time series data to study acute and chronic infection

CD8⁺ T cell responses are highly diversified in the early phase of the infection and heterogeneous in an acute and chronic infection setting. To investigate early differentiation dynamics during both infections, we analysed the single-cell transcriptome of P14 T cells at day 4.5, 6 and 7 and 8 p.i. with LCMV Armstrong and clone 13 using previously published datasets and generating own scRNA-seq data.

For both the published data and our own data sets, naïve P14 T cells were adoptively transferred

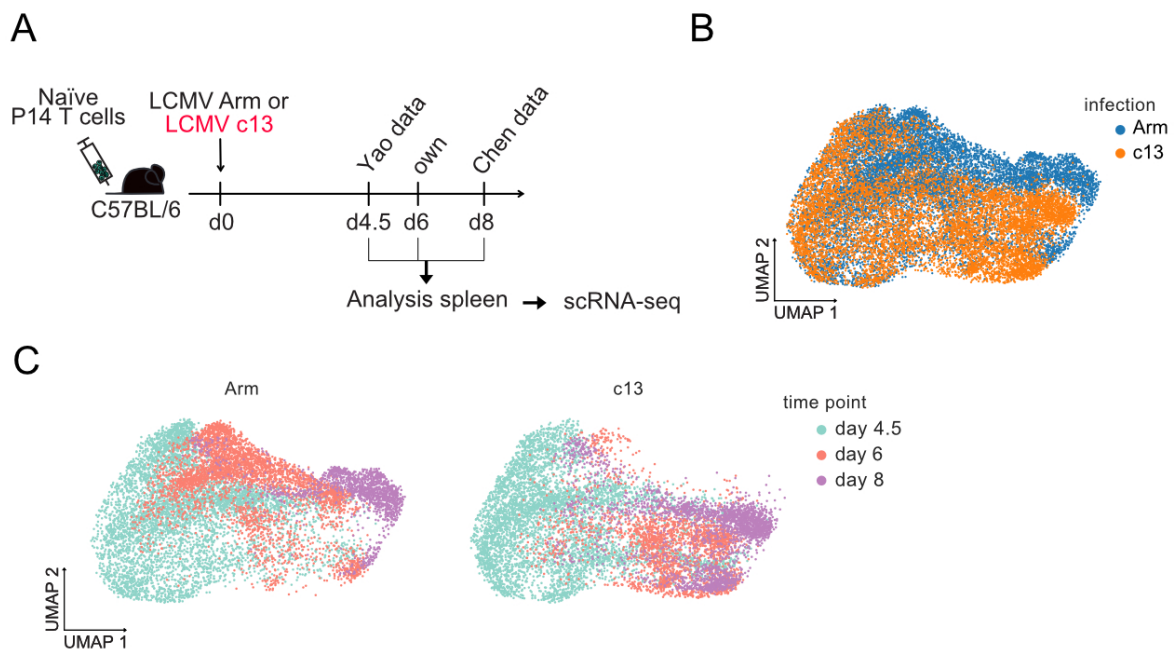


Figure 4.1.: Transcriptomic comparison of the P14 response during the acute phase of LCMV Armstrong and LCMV clone 13 infection. **A** Schematic representation of the experimental set up for scRNA-seq. Data stem from different sources (day 4.5 from Yao et al. 2019, day 6 own and day 8 Chen et al. 2019). For the generation of all data sets, naïve P14 T cells were adoptively transferred into C57BL/6 mice, and their progenies from the spleens were re-covered by flow cytometric sorting. Single-cell transcriptomes from purified P14 T cells from day 4.5, 6 or 8 after LCMV Armstrong or clone 13 infections were generated using the 10× Genomics protocol. **B** UMAP representation of the day 4.5, 6 and 8 p.i. samples infected with either LCMV Armstrong or clone 13 after applying the batch-balanced k nearest neighbour (bbknn) batch correction method using the originating publication as batch key is shown. **C** UMAP embedding was computed on both infections at the time points indicated in A. UMAP plots show the P14 T cells from either LCMV Armstrong (left) or LCMV clone 13 infection (right) coloured by the day p.i.

into congenic recipients infected with LCMV Armstrong or clone 13 on the following day (Figure B.1 A). At time points day 4.5, 6, 7 and 8 after infection, P14 T cells were isolated from the spleen and enriched by flow cytometric sorting. Afterwards, scRNA-seq was performed using the 10× Genomics method.

To perform a time-resolved analysis of the P14 T cell responses, we analysed the published and our datasets together. Without batch correction, the different datasets were separated in the UMAP embedding (Figure B.1 B), while both the data sets from the two infections, stemming from our laboratory overlap.

An overlap of the cells from both infections in the data from Chen et al. 2019's publication was also observed. This was also the case for the data sets from Yao et al. 2019 at day 4.5 p.i. The separation between the laboratories in which the data was created, suggested the presence of a technical effect. However, the day 7 LCMV clone 13 infection sample was separated from the other datasets generated by Yao and colleagues (Figure B.1 B). It remained unclear whether the observed partitioning was due to technical or biological source.

We then attempted to merge the data sets and applied different batch corrections to account for the technical differences.

After application of two batch corrections methods batch-balanced k nearest neighbour (bbknn) correction (Polański et al. 2020) and Harmony (Korsunsky et al. 2019) batch correction methods, integration of the day 7 clone 13 sample remained unsuccessful. While the other data were arranged in their logical time series, the day 7 data set remained detached (Figure B.1 C).

To this end, we excluded the day 7 samples and only considered the day 4.5, 6 and 8 p.i. data for all subsequent analyses (Figure 4.2 A).

Heterogeneous antiviral T cell responses after acute and chronic infections

We computed a joint UMAP of the remaining time points and observed a substantial overlap between the infections at day 4.5 (Figure 4.1 B, C). From day 6 on, the cells from the two infections began to diverge, and the separation between the P14 T cells from the Armstrong and the clone 13 infection became even more significant at day 8 (Figure 4.1 B, C).

Next, we looked at various marker genes associated with either memory, effector and exhausted T cells (Figure 4.2). A pronounced expression of T cell memory genes, such as *Tcf7* (encoding TCF1) (Jeannet et al. 2010; Zhao et al. 2010), *Il7r* (Kaech et al. 2003) and *Sell* (encoding CD62L) (Buchholz et al. 2013a; Graef et al. 2014) were found in both infections in the lower section of the UMAP2 axis with enhanced enrichment along UMAP1 (Figure 4.2 A-B).

We observed that over time fewer cells expressed the above mentioned memory genes, while a slightly stronger expression was detected in the LCMV clone 13 sample.

Effector signatures, exemplified by the expression of *Cx3cr1* (Böttcher et al. 2015), *Klrg1* (Kaech et al. 2003) and *Gzma* were mainly found in the P14 T cells from the LCMV Armstrong infection and showed a stronger expression already from day 4.5 compared to the cells from the clone 13 infection (Figure 4.2 C-D). In the UMAP plot, the cells with an effector signature were located

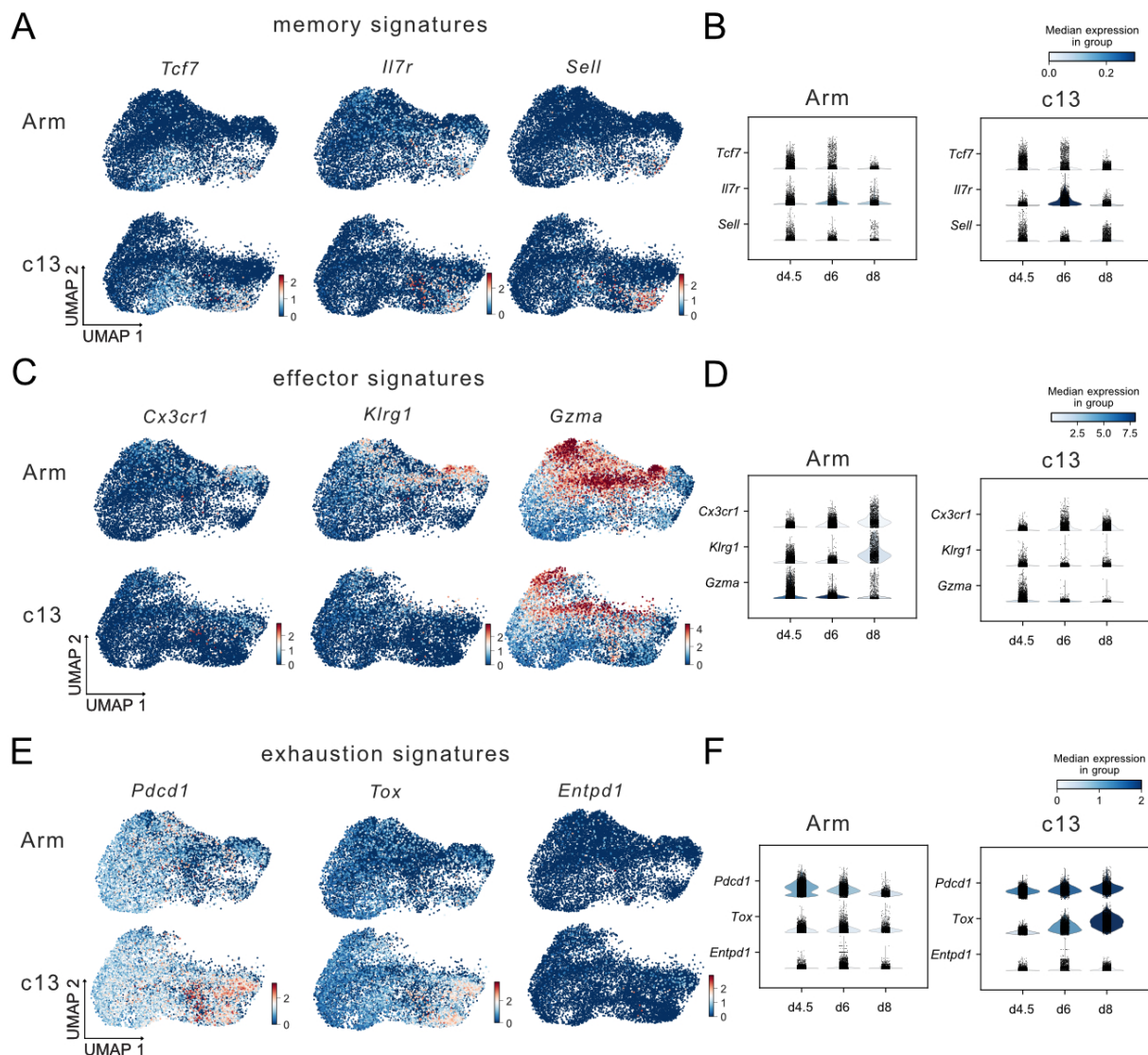


Figure 4.2.: Distinct T cell exhaustion signatures detectable early during LCMV clone 13 infection. **A** UMAP representation of the P14 T cell transcriptomes after LCMV Armstrong or LCMV clone 13 infection (as in Figure 4.1) A and B showing the expression profiles of the memory signature genes *Tcf7*, *Il7r* and *Sell*. **B** To the memory signature genes corresponding violin plots per time point and infection are shown. **C** UMAP as in A showing the effector signature genes *Cx3cr1*, *Klr1* and *Gzma* and **D** violin plots depicting the expression of the effector signature genes from B for each infection per time-point. **E** UMAP showing selected exhaustion signature genes *Pdc1*, *Tox* and *Entpd1* for LCMV Armstrong (top row) and LCMV clone 13 (bottom row). **F** Violin plots displaying the expression of the exhausted genes as in E for LCMV Armstrong (left) and LCMV clone 13 (right) per time point.

in the upper section of the UMAP2 axis.

In agreement with the literature, looking at single exhaustion-associated signature genes, we saw, as expected, that the inhibitory receptor PD1 (*Pdc1*) (Wherry et al. 2007) and the thymocyte

In LCMV Armstrong, the expression of *Pdcd1* and *Tox* was also observed at day 4.5 p.i., albeit to a lower level (Figure 4.2 E-F).

However, in the acute infection *Pdcd1* and *Tox* expression was down-regulated from day 4.5 onwards (Figure 4.2 C). *Entpd1*, a gene found in terminally exhausted T cells, encoding for the CD39 protein (Chen et al. 2019) was lowly expressed during the early time points, with slightly higher expression at day 8 in the clone 13 infection (Figure 4.2 E-F).

To assign the cells to specific clusters, we used the Leiden algorithm (Traag et al. 2019) and found 8 different clusters (Figure 4.3 A). Among them were 5 clusters (clusters 0, 1, 2, 4 and 7) from both samples of the day 4.5 time point.

On day 6, all clusters were represented, although cluster 0, 1 and 2 had shrunk in size and contributed only minimally to the total cells present at day 6 p.i. Cluster 5 was strongly represented on day 6. On day 8 after infection, clusters 0, 5 and 7 diminished in size and contributed marginally to the total number of the day 8 samples.

Instead, a large proportion of the clusters 3, 4 and 6 formed the main cell types on day 8 after infection (Figure 4.3 B). In comparison, we saw that in the LCMV clone 13 infection, clusters 3 and 4 were stronger represented, and in the Armstrong infection sample, consisted of clusters 5 and 6 instead (Figure 4.3 C).

To define the clusters, we performed differential gene expression analysis. We found that in the clusters 0, 1, 2, 5 and 7, cell cycle genes were differentially expressed (*Tuba1b*, *Birc5*, *Mcm5* and *Tubb5*) (Figure 4.3 D, G). Leiden clusters 1, 2 and 5 additionally differentially expressed effector molecules such as *Gzmb* and *Gzma*. In contrast to cluster 7 which, according to differential gene expression analysis, was assigned to a proliferating memory T cell subset (*Sell*, *Slamf6* and *Batf*) (Figure 4.3 D,G). Likewise, in cluster 4, differential gene expression analysis revealed that memory T cell markers such as *Sell* were up-regulated.

Cluster 3, mainly composing the T cell responses from day 6, up-regulated in comparison to the remaining clusters encoding for inhibitory receptor genes such as *Lag3*, *Pdcd1* and also for *Tox*. In addition, cluster 3 was defined by the increased expression of chemokines such as *Ccl3*, *Ccl4*, *Ccl5* (Figure 4.3 D). Genes down-regulated in cluster 3 are mainly cell cycle-associated (*Mki67*, *Top2a*, *Birc5*) and effector-phenotype associated genes (*Klrg1*, *Ehz2*) (Figure 4.3 C, E and G). In contrast, cluster 6 was defined by the up-regulation of effector signature genes and the down-regulation of inhibitory receptors in comparison to the cells in the other clusters (Figure 4.3 C, F-G).

The clone 13 infection samples completely lacked the cells in cluster 6, indicating that effector cells were absent during persisting infection. This finding was shown in previous studies (Wherry et al. 2003a, 2007) and, suggests that exhaustion develops early during infection and is further propagated with time.

In the next sections we analyse how the responses to the two infections differ at the time points before the peak.

4.2. Cessation of cell division halfway before reaching peak response

So far, it has been described that MP cells (Buchholz et al. 2013a) and MEX cells (Alfei et al. 2019; Chen et al. 2019; Utschneider et al. 2020) develop early during infection.

Therefore, we compared the transcriptomes before the responses in the acute infection setting culminate.

The differentially expressed genes in the Armstrong versus clone 13 comparison at day 6 after infection showed that distinctive phenotypes were present at this time point.

In the clone 13 infection, the cells showed an up-regulation of the inflammatory chemokines *Ccl3* and *Ccl4* (Figure 4.4 A). The expression of *Ccl3* and *Ccl4* was already reported in other studies that investigated exhausted T cells (Wherry et al. 2007), but their role not followed up.

Similarly, in the cells from clone 13 infection, we found an up-regulation of *Xcl1* (Figure 4.4 A). *Xcl1* is expressed in activated T cells and leads to the recruitment of DCs, expressing the associated receptor XCR1. During an established clone 13 infection, XCL1-producing T cells were thought to be involved in keeping the virus under control (Argilaguet et al. 2019).

In addition, we also found an elevated expression of *Cd200* in the cells from the clone 13 infection (Figure 4.4 A, B). We examined the protein levels of CD200 seen at day 6 after LCMV Armstrong and clone 13 infection and found that in the clone 13 infection more cells were positive for CD200 and that Tim3-negative T cells have a slightly higher CD200 MFI (Figure 4.4 C).

Studies using an Influenza infection model implicated that CD200 up-regulation is crucial to prevent CD8⁺ T cell mediated immunopathology (Rygiel et al. 2009). However, the exact function of CD200 in CD8⁺ T cells under persisting infection conditions remains unclear and will not be further investigated in this thesis.

Tnfrsf4 (coding for OX40) was up-regulated in the T cells from clone 13 infection compared to the acute infection with LCMV Armstrong (Figure 4.4 A, B). OX40 is a co-stimulatory protein known for the maintenance and memory formation of anti-viral T cells, whose role is essential for containing the virus during chronic LCMV infection (Boettler et al. 2012).

We used flow cytometry to monitor the surface expression of OX40 and observed similar levels in both infections at day 4.5. On day 6, after the infection with LCMV clone 13, as already indicated in the differential gene expression analysis, we observed higher OX40 levels in the P14 T cells from the persistent infection (Figure 4.4 A, B and D).

This is consistent with data from Boettler et al. 2012, where they showed that by the peak of the acute immune response in LCMV Armstrong OX40 is completely down-regulated. However, in clone 13 infection, OX40 remains expressed well beyond the peak of chronic infection. *Tnfrsf4* is increasingly expressed in T cells from cluster 7, which contains T cells with a distinct memory T cell signature (Figure 4.3 and Figure 4.4 B).

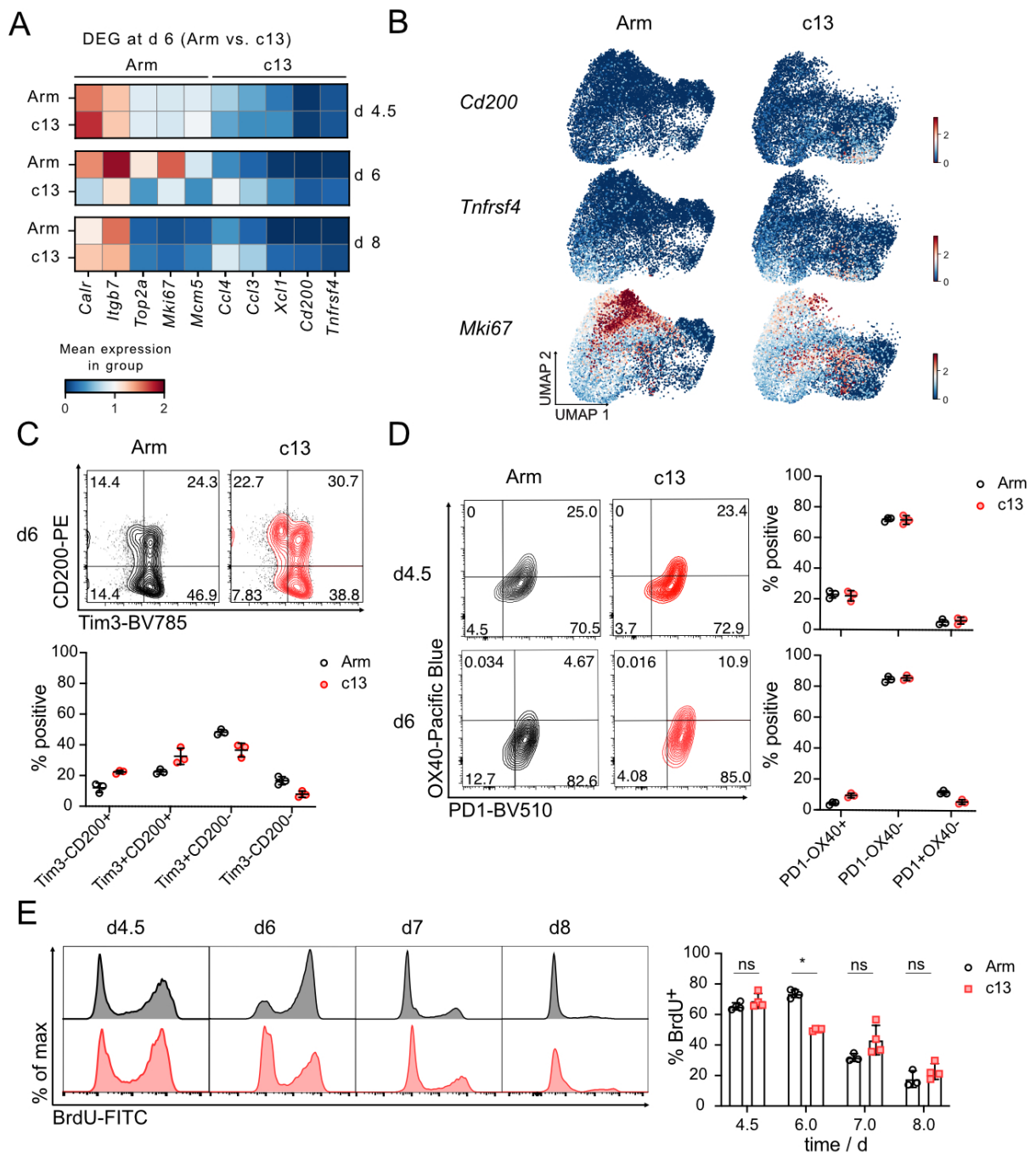


Figure 4.4.: Changes in the proliferation activity among the most distinctive drivers between LCMV Armstrong and clone 13 at day 6 p.i. **A** Matrix plot depicting the mean gene expression at day 4.5, 6 and 8 p.i. of significantly up-regulated differentially expressed genes in P14 T cells in LCMV Armstrong versus clone 13 at day 6. **B** UMAP visualisation as in Figure 4.2 showing the expression of *Cd200*, *Tnfrsf4* and *Mki67*. **C-D** After adoptive transfer of 5×10^2 or 5×10^3 naïve P14 T cells to C57BL/6 mice. Mice were infected with either 2×10^5 LCMV Armstrong or 2×10^6 LCMV clone 13 and analysed by flow cytometry. **C** Representative contour plot displaying the expression of CD200 and Tim-3 and the quantification of the relative subset size at day 6 p.i. $n = 3$, data from one experiment.

This is indicative that OX40 is responsible for the maintenance of the T cell pool and thus has a role in virus control. This is in line with the compromised secondary response that is exhibited in OX40 deficiency (Hendriks et al. 2005). The more specific properties of OX40 in this context will not be further investigated.

We also determined the differentially expressed genes in the T cells from the LCMV Armstrong infection. In contrast to the T cells from clone 13 infection, in the Armstrong infection, calreticulin *Calr7*, a protein that binds free calcium ions, and the adhesion molecule *Itgb7* were both differentially expressed transcripts (Figure 4.4 A). In addition, cell cycle-related genes (*Top2a*, *Mki67*, *Mcm5*) were differentially expressed (Figure 4.4 A, B), suggesting distinct division dynamics between the two infections.

The role of the cell cycle during the development of exhaustion

To this end, we tested whether the T cells from the two infections exhibit different proliferation activities. To investigate this, we infected wild-type C57BL/6 mice that received P14 T cells by adoptive transfer the day before infection with LCMV Armstrong or clone 13. We analysed the splenic P14 T cell response at the time points 4.5, 6, 7 and 8 days after infection. Exactly 3 h before the time of analysis, the mice were administered a dose of BrdU i.p. and the incorporation of BrdU was measured by flow cytometry.

While on day 4.5 after infection, the P14 T cells from both infections took up the same amount of BrdU within 3 h, on day 6 after infection with LCMV clone 13 a 1.5 times smaller fraction of P14 T cells incorporated BrdU than the P14 T cells from the LCMV Armstrong infection (Figure 4.3 E). While a smaller percentage of T cells became BrdU⁺ towards the peak of the acute response, more T cells from the clone 13 infection remained in division and incorporated BrdU (Figure 4.3 E).

We also inferred the cell cycle activity in the transcriptome data. For this, we have used the cell cycle gene list of Tirosh et al. 2016, which contains genes, whose expression enables us to distinguish proliferating and non-proliferating cells.

We applied the Vision method, a tool that allows to display gene signature to describe variation between cells. In other words, a list of signature gene is provided and the tool box computes a score, determining a positive or negative correlation to that signature. Here we applied the Vision method (DeTomaso et al. 2019) on the cell cycle gene list, a score is calculated for each cell.

Figure 4.4 : D Representative contour plots depicting the OX40 (*Tnfrsf4* gene) and PD1 expression at 4.5 or 6 p.i. Mean and std, $n = 3$, data from one experiment. **E** Experimental set up similar as in **C-D**, with analysis at days 4.5, 6, 7 and 8 p.i. 3 h after i.p. BrdU administration, the incorporation of BrdU was analysed by flow cytometry. Representative histograms with BrdU profiles and the quantification for each time point. Mean and std, $n = 3 - 4$, data from one experiment. Mann-Whitney U test, ns= not significant, $*p < 0.05$

The higher the value of the score, the more pronounced is the proliferation signature in the cells in this case (Figure 4.5 A). As already described with by BrdU measurements at this time point after infection (Figure 4.4 E), we observed that in both infections at day 4.5 p.i. the majority of the cells showed a pronounced proliferation signature (Figure 4.5 A). For both infections, the proliferation signature weakened from day 6 onwards. While in the LCMV Armstrong infection day 6 sample a large fraction of cells showed a distinct proliferation signature, the signature was lost on day 8 (Figure 4.5 A).

The cells from the clone 13 infection displayed a weaker pronounced proliferation signature on day 6 (Figure 4.5 A), while the signature remained at similar levels between day 6 and day 8. In comparison to the infection with LCMV Armstrong, the LCMV clone 13 derived P14 T cells exhibited a much weaker proliferation signature.

Based on our own method to infer division drop out from scRNA-seq data (the method is in detail described in section 3.4.), we derived the percentage of actively proliferating T cells for all time points (Figure 4.5 B).

While at day 4.5 p.i., approximately 90 % of P14 T cells actively divided, over time, the fraction of T cells exiting the cell cycle increased. On day 6 after infection with LCMV clone 13, slightly more cells stopped dividing (Figure 4.5 B), resulting that at mid peak 50 % of the virus-specific T cells terminated their proliferation. It is of common understanding that during persisting infection the loss of proliferative activity is observed among the activated T cells.

Quantification of cell division duration

As next, we quantified the duration of the cell cycle length. Therefore, we measured BrdU incorporation and total DNA content with 7AAD at different time points between day 4.5 and the peak of chronic infection at day 12. Based on the gating strategy, that was described in detail under section 3.1, we inferred the division speed of the cells to be analysed by simultaneously measuring BrdU and total DNA content.

In the comparison of the ratios of the divided P14 T cells at day 4.5, 6, 7, 8 and 12 after infection, the P14 T cells from the LCMV Armstrong infection proliferated faster at day 6 than the T cells from the clone 13 infection (Figure 4.5 C). Towards the peak of the acute phase, the cell division times equalised, whereas towards the peak of the chronic infection on day 12, the P14 T cells from the LCMV Armstrong infection divided very slowly relative to the cells isolated from the infection with LCMV clone 13 (Figure 4.5 C).

A discrimination between considerable deceleration and cell cycle exit, or a combination of both could only be inferred through the assessment of the cell cycle status for each cell (Figure 4.5 C). Therefore, we first investigated the division cessation by flow cytometric measurement of the p-Rb protein. Upon exit from the cell cycle and thus entry into the G₀-phase, the Rb protein is de-phosphorylated. Thus, it provides good evidence of whether a cell performs active cell division or has stopped dividing.

For this, we transferred P14 T cells into wild-type mice and infected the recipients the next day

with either LCMV Armstrong or clone13. On day 6 after infection, we detected the proportion of P14 T cells that were p-Rb positive.

When we examined the overall P14 response to p-Rb expression, in the clone 13 infection at day 6 p.i., approximately half of the P14 T cells had already stopped actively dividing, while in LCMV Armstrong, approximately 70 % of the P14 T cells were still actively proliferating (data not shown). Further differentiation between the phenotypes using the markers TCF1 and CX3CR1 revealed that in both infections, the TCF1⁺CX3CR1⁻ subset had the lowest p-Rb levels and stopped proliferating to a significantly greater extent compared to the other two subsets (Figure 4.5 D).

The P14 T cells of the TCF1⁻CX3CR1⁻ and TCF1⁻CX3CR1⁺ subsets each had similar p-Rb⁺ proportions within the same infection, although, for all subsets, the P14 T cells stemming from the infection with LCMV clone 13 exhibited a lower fraction of p-Rb⁺ P14 T cells (Figure 4.5 D). As indicated in the transcriptomic data, we observed an increased division drop out on day 6 in the P14 T cells following LCMV clone 13 infection than in the T cell responses after infection with LCMV Armstrong. The observed division drop out was subset specific.

To find out whether the P14 T cells from the clone 13 infection divide at different rates compared to the cells from the LCMV Armstrong infection, we quantified the cell cycle duration using our mathematical formalism (see under section 3.1, Kretschmer et al. 2020). The cell cycle length quantification, was done by my colleague Jonas Mir, and the fraction of cells in the divided-gate at the respective time points after infection and the percentages of the T cell fractions in the G1- and G2M-phases were used.

As described in subsection 3.1, the different cell cycle stages were extracted by simultaneous measurements of BrdU and total DNA content. The fraction of cells in the G1- and G2/M-phases were obtained through a measurement using a short BrdU labelling time of 0.5 h (Figure 3.4 A, left).

Since the BrdU-negative gate with diploid DNA content contained T cells from both G0- and G1-phase, the fraction of G0-phase cells was subtracted from the G0/G1-gate and only the cells in the G1-phase were considered for the cell cycle speed quantification. The proportion of G0-phase cells was obtained by inferring the quiescent cells from the scRNAseq data or by the p-Rb measurement using flow cytometry.

On day 4.5, after infection with LCMV Armstrong or clone 13, the P14 T cells divided at a speed of 5.8 h and 6.0 h, respectively, and thus at the same rate (Figure 4.5 E). While on day 6, the P14 T cells from the LCMV Armstrong infection divided at similar speed as on day 4.5 p.i. (5.1 h on day 6 to 5.8 h on day 4.5), the P14 T cells from the clone 13 infection decelerated and divided 1.3 times slower than on day 4.5 p.i. (Figure 4.5 E).

Consequently, on day 6 after the infection with LCMV clone 13, the virus-specific T cells exited the cell cycle at a higher proportion and displayed a prolonged average division speed.

From day 7 after both infections, the P14 T cells slowed down to 13.3 h per division following LCMV Armstrong infection and to 11.7 h for P14 T cells from LCMV clone 13 infection. Thus,

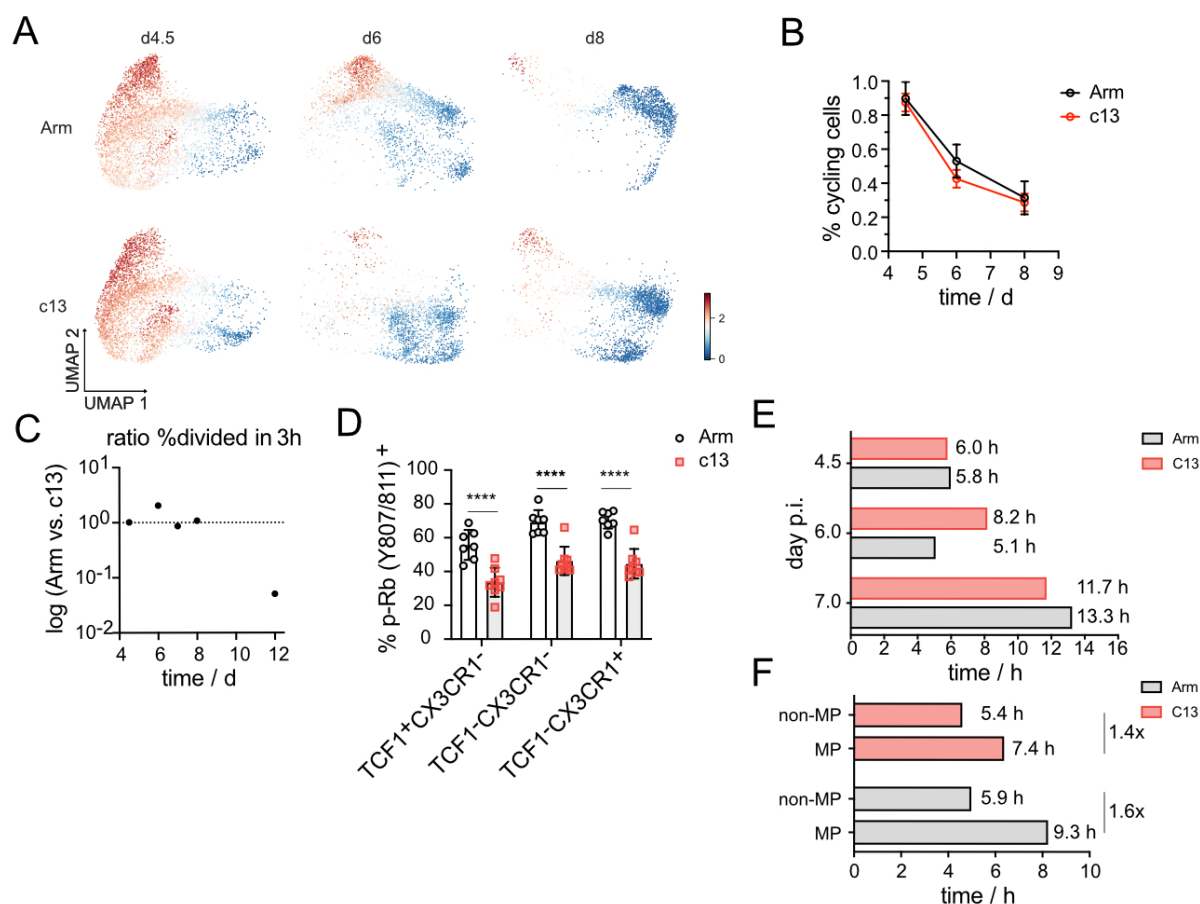


Figure 4.5.: A greater extent of cell cycle arrest is observed in clone 13-derived P14 T cells. **A** UMAP representation is visualised for each time point individually for LCMV Armstrong (upper row) and LCMV clone 13 (lower row) showing the proliferation score computed with Vision based on the gene list from Tirosch et al. 2016 **B** Estimate of the fraction of cycling cells from the scRNA-seq analysis as in Figure 3.10. Mean and pooled variance, $n = 1 - 2$. **C** Similar experimental set up as in Figure 4.4 **E**. In addition to BrdU, we also measured the total DNA content with 7AAD. Based on the gating strategy as in Figure 3.4, the fraction of P14 T cells in the divided gate was quantified. Dot plot depicts the log ratio of the in 3 h-divided P14 T cells in c13 versus Armstrong at the days 4.5, 6, 7, 8 and 12 p.i. **D** Bar graph depicted the fraction of p-Rb on the Y807/811 residues at day 6 p.i. with LCMV Armstrong or clone 13. $n = 6 - 7$, data from two independent experiments. One-way ANOVA, **** $p < 0.0001$. **E** Bar plots depict the quantified mean inter-division times of cycling P14 T cells at the days 4.5, 6 and 7 after infection with LCMV Armstrong or clone 13. **F** Bar plots display the quantified mean inter-division time of cycling MP (TCF1⁺) and non-MP (TCF1⁻) P14 T cells at the day 4.5 p.i. Data is own, Jonas Mir quantified the cell cycle speed.

the duration of cell division aligned between the infections towards the peak (Figure 4.5 E).

For day 4.5 after the infection with Armstrong and clone 13, we also quantified the mean division times for the MP (TCF1⁺) and non-MP (TCF1⁻) subsets. Consistent with the data from other bacterial and viral infection models (see Section 3.1), the cell cycle duration for the MP subset

was longer than for the non-MP subset, for P14 T cells from both viral infections. The ratios between the mean division time of the MP to non-MP subsets were slightly different in the respective infections. In LCMV clone 13, the ratio of division between the MP subset to the non-MP subset was 1.4, and in the Armstrong infection, the MP divided 1.6 times slower than the non-MP T cells (Figure 4.5 F).

The slightly, but not significantly different relative sizes for the TCF1⁺ and TCF1⁻ subsets at day 4.5 (Figure 4.10 C) might have compensated for the distinct infection-specific speeds of the subsets, resulting in the similar cell cycle durations for the total P14 T cell response (Figure 4.5 E, F).

It seemed that already at day 6 following the persisting infection, the CD8⁺ T cells committed towards an exhausted phenotype. After the LCMV clone 13 infection, the T cells already differ strongly from the P14 T cells from the LCMV Armstrong infection regarding their cell cycle activity and gene expression. Using mathematical modelling we want to further elucidate how the trajectories of P14 T cells differ between both these infections.

4.3. The extended progressive model of differentiation describes the mechanisms of CD8⁺ T cells during the onset of the chronic infection

As we have described in the previous chapter, the extended progressive differentiation model that includes cell cycle arrest described the data from two different types of acute infections, including the P14 T cell response following infection with LCMV Armstrong until day 8.

Therefore, our data implies that for acute systemic infections differentiation follows a conserved patterns that is independent of the infectious pathogen.

To determine the differences and similarities between the acute and chronic infection by mathematical modelling, the Buchholz laboratory followed single P14 T cells during LCMV Armstrong and clone 13 infection with readout at day 8 p.i. Therefore, the naïve P14 T cell-matrix was adoptively transferred into recipient mice that were infected with LCMV Armstrong or clone 13 the next day. On day 8 p.i., the single-cell progenies in the spleen were analysed for their expression of TCF1, Tim3 and CX3CR1 by flow cytometry.

While we discussed in detail the responses to the LCMV Armstrong infection in the previous chapter, we will focus on the differences between LCMV Armstrong and clone 13 in this section. The mean P14 T cell response at day 8 p.i. with LCMV clone 13 was smaller than the response after the LCMV Armstrong infection (Figure B.2 B). An expected finding, regarding that at day 8 the peak response in the Armstrong infection is reached while, the response to the clone 13 infection culminates around day 12 (single-cell fate-mapping data at day 12 not shown).

On day 8 p.i., the single-cell progenies from the LCMV clone 13 infection showed less variation in the total population size than the P14 T cell responses after the LCMV Armstrong infection

($CV_{\text{Arm}} = 3.58$, $CV_{\text{c13}} = 1.78$) (Figure B.2 B). Notably, the three giant clones that accounted for 94 % of the variability in the response toward LCMV Armstrong were missing entirely in the clone 13 infection (Figure B.2 B). In consistence with experiments after population transfer, the progeny of individual P14 T cells do not propagate a $\text{CX3CR1}^{\text{high}}$ subset after the LCMV clone 13 infection (Figure B.2 A, C).

Several mechanisms could play in concert to limit the formation of a $\text{CX3CR1}^{\text{high}}$ compartment in the clone 13 infection. On the one hand, the T cells might be forced out of the cell cycle before they reach an effector differentiation state. Alternatively, the differentiation process from an EMP ($\text{TCF1}^-\text{CX3CR1}^-$) cell into a terminal EFF ($\text{TCF1}^-\text{CX3CR1}^{\text{high}}$) cell is prolonged, and exhaustion mechanisms as suggested by the elevated expression of TOX and hence its regulation of the exhausted epigenetics landscape (Alfei et al. 2019; Khan et al. 2019) intervene before the T cell terminally differentiates.

Due to the lack of available experimental data to identify cells that have stopped dividing and also have committed towards an exhausted phenotype, we will focus solely on the role of division drop out during the expansion phase of the infection with LCMV clone 13 in this section.

Quantitative comparison of the LCMV Armstrong versus clone 13 mediated CD8^+ T cell immunity

Application of the extended model of progressive differentiation, we aimed to disentangle the differentiation pathways and discover which mechanistic differences are required to describe the course of a chronic infection.

For the mathematical modelling, we used the mean values and the CVs of the subsets and also the pairwise Pearson correlation coefficients between the subsets within an infection. For both infections, we also used the ratio between the cell cycle duration of the TCF1^+ - and TCF1^- -subsets to inform the mathematical model.

Furthermore, the cell cycle drop out kinetics for both infections, which were inferred from the transcriptome data were used. For the clone 13 infection, we also used the fraction of dividing cells from the p-Rb flow cytometric measurement at day 6. Furthermore, the model was also informed by the relative subset sizes for both infections at the time points, day 4.5, 6, 7 and 8 after infection.

We performed simultaneous fitting and chose the same parameters for both infections (Figure 4.6 A). However, having the same parameter set for both infections did not reflect the data (data not shown). We then performed a forward selection to identify which infection-specific parameter sets were required.

We started the model selection from a model in which all rates were the same for both infections (model as in Figure 4.6 A). In the first round of the forward selection, all parameters were fixed except for one that was allowed to be infection-specific (6 fixed parameters, 1 infection-specific, total 8 parameters). We then performed non-linear least-squares fitting and calculated the χ^2 for each model. This process was repeated until we iterated through all the parameters. We

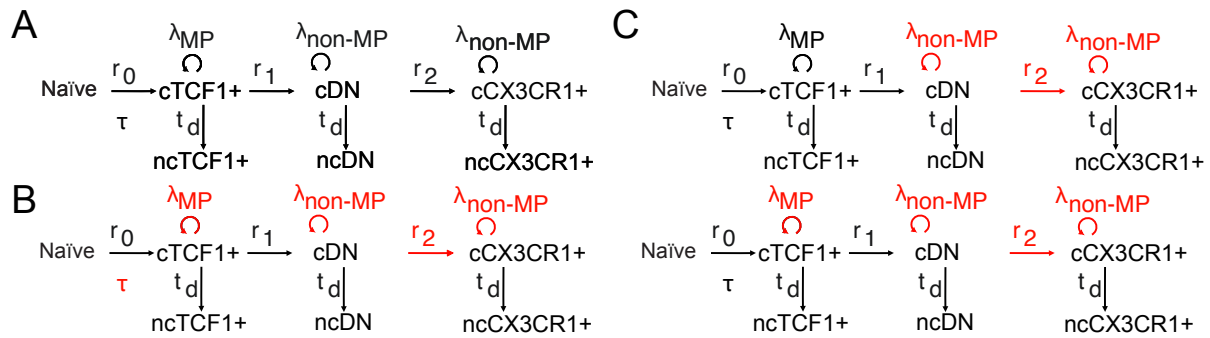


Figure 4.6.: Mathematical models tested by forward selection to explain the fate-decision of P14 T cells during LCMV Armstrong and clone 13 infection. **A** Topology of the cell cycle arrest progressive model of differentiation. For both infections the data was fitted simultaneously and all parameters were forced to be equal. **B** Best-fitting model found by forward selection after simultaneous fitting was performed. The following processes differed between infections: the proliferation rates for the MP and the non-MP (λ_{MP} and λ_{non-MP}), the differentiation rate from the cycling DN to cycling CX3CR1⁺ subset and, the time-point from which cell cycle drop out is initiated (τ). **C** The two other models, performing better than the model shown in (A) with an $\Delta AICc \leq 10$ than the model depicted in (B). In black transitions where the same parameter was used for both infections are indicated, the red colour marks the processes where the parameters differ between the two infections.

found that the model with pathogen-distinct r_2 rate to exhibit the lowest χ^2 -value.

Starting from the latter model, we proceeded with the second step of model selection. This time five parameters were fixed. Again, one parameter was allowed to be different for the infection (5 fixed parameters, 2 that could be infection-unique, total 9 parameters). It was iterated through all parameters until the model with the lowest χ^2 -value was found.

We continued performing the forward selection until the introduction of additional pathogen-dependent rates led to an increase in the χ^2 -value. At that point, we stopped the forward selection.

Based on the χ^2 values and the number of parameters, the AICc was calculated for each model. The AICc-differences ($\Delta AICc$) between the individual models were determined, and the models with a $\Delta AICc$ greater than 10 were rejected.

The best-performing model compared to the simple model with 7 equal rates is shown in Figure 4.6 B. It contains 11 parameters, 3 of which are shared between the two infections, and 4 are infection-specific rates. The models shown in Figure 4.6 C were more favourable than the simple model in Figure 4.6 A, but could not be ruled out given the data (a $\Delta AICc$ smaller than 10 compared to the best model was determined).

For the following analyses we focused on the model in Figure 4.6 B. In the best-performing model (Figure 4.6 B), the following parameters must be different so that the data from both infections was adequately described.

On the one hand, different proliferation rates were required for the MP and non-MP subsets

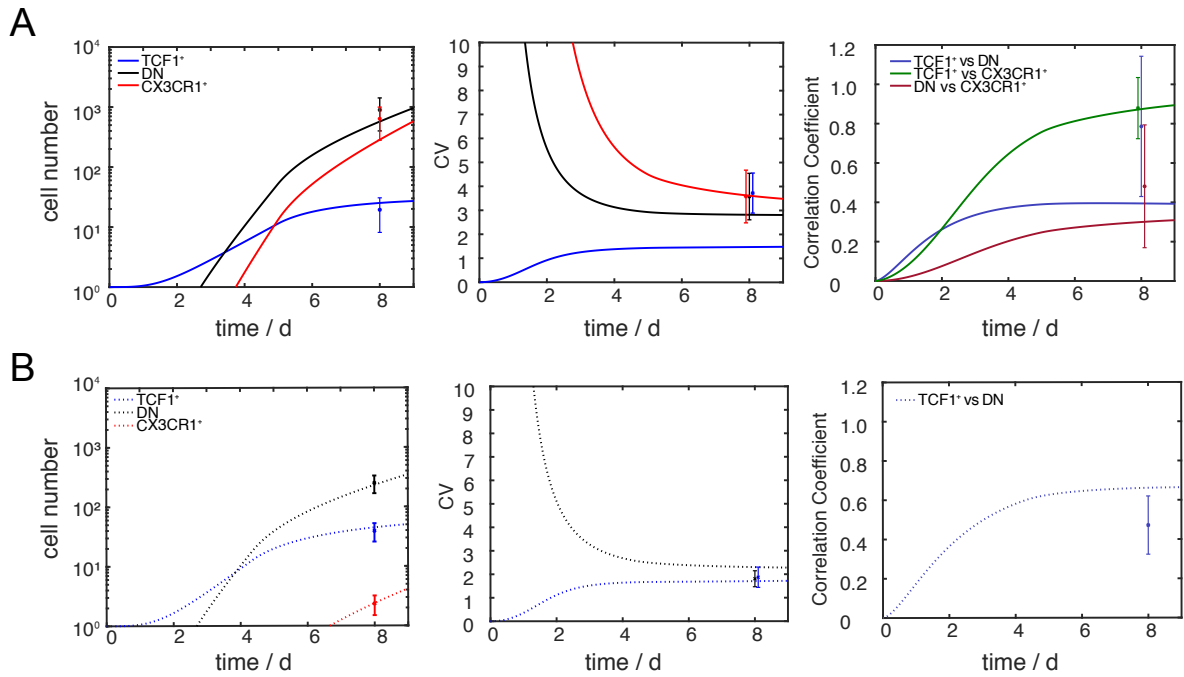


Figure 4.7.: Results after simultaneous fitting to the P14 T cell responses after the infection with LCMV Armstrong and clone 13. Best-fit results of the extended progressive model of differentiation to the means, the coefficient of variation and the three pairwise Pearson correlation coefficients for **A** LCMV Armstrong and **B** LCMV clone 13. Data from Lorenz Kretschmer and Dr. med. Veit Buchholz, mathematical modelling was performed by myself.

depending on the infection. Since the ratio of the proliferation rates entered into the modelling, and we have previously demonstrated, that the MP T cells divided slower in the LCMV Armstrong infection than in the one with the clone 13 variant (Figure 4.5 F), it was evident that the model demanded different division rates. In addition, the rate of differentiation from the DN-subset into the CX3CR1^{high} subset must be different in both infections. Consistent with the experimental data, the time point at which drop out of the cell cycle was observed, was different in the LCMV Armstrong and the clone 13 infection.

Using this mathematical model we were able to explain the response until day 8 p.i. for the P14 T cell response after LCMV Armstrong and clone 13 infection. Although, the models in Figure 4.6 C generated comparable fits (data not shown).

The best fit to the means, the CV and pairwise correlation coefficients is shown in Figure 4.7. The fit to the cell cycle drop out kinetics also described that the TCF1⁺ subset stopped proliferating first, followed by the other two subsets (Figure 4.8 B and E), for both infections. Furthermore, the rates at which the cells exited the cell cycle were found to be the same for the T cell responses of both infections. Finally, Figure 4.8 C and F show the best fit result for the ratio of the proliferation rates.

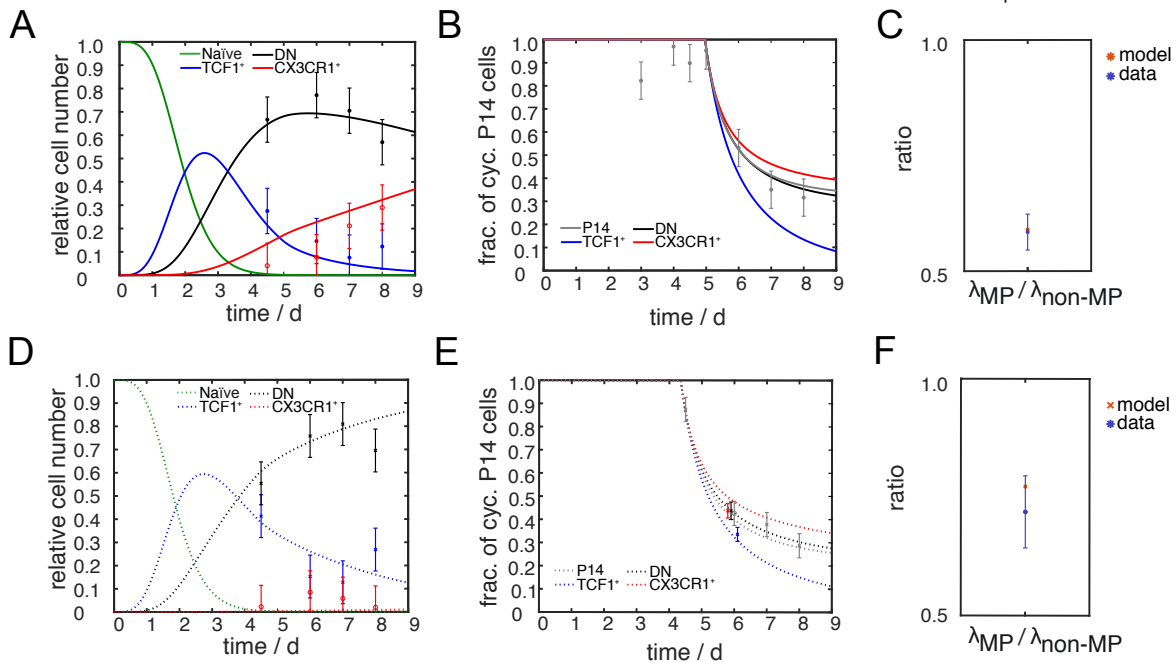


Figure 4.8.: A uniform model correctly depicts the population dynamics for the P14 T cell subsets and their proliferation and cell cycle exit kinetics. Best-fit results to the relative subset sizes, the cell cycle drop out kinetics from the ratio of the proliferation rates of the MP and non-MP subset following infection with LCMV Armstrong or LCMV clone 13.

Validation of the mathematical model using stochastic simulations

Next, we corroborated the best-fitting model by performing simulations. We generated *in silico* P14 responses using the Gillespie simulation algorithm (Gillespie 1976). With the given parameter set from the best fitting model (Figure 4.6 B), our simulations reproduced the data accurately (Figure 4.9). Even fine subtleties, such as large clones with missing TCF1 expression, were reproduced with this model (Figure 4.9 A, middle column). In addition, the variability of the absolute P14 response was also correctly modelled (Figure 4.9 B and D). Of note, the upper model from Figure 4.6 C failed to reproduce the distribution between the subsets, while the lower model was unable to reproduce fine differences in the marker expression (data not shown). We computed 95 % confidence bounds parameter estimates using the profile likelihood method (Venzon et al. 1988). All parameters are listed in Table 4.1. The recruitment rate from naïve T cells to TCF1⁺ T cells was found to take on average 1.2 d⁻¹, a value similar to findings by De Boer et al. 2001 where they mathematically modelled virus-specific CD8⁺ T cell responses during LCMV Armstrong infection.

Interestingly, the differentiation rate between the DN-subset and the CX3CR1^{high} compartment was forty times smaller during the response to LCMV clone 13 than to LCMV Armstrong. The small value of the DN → CX3CR1⁺-transition rate indicated that during the LCMV clone 13 infection, the formation of CX3CR1⁺ T cells was prevented.

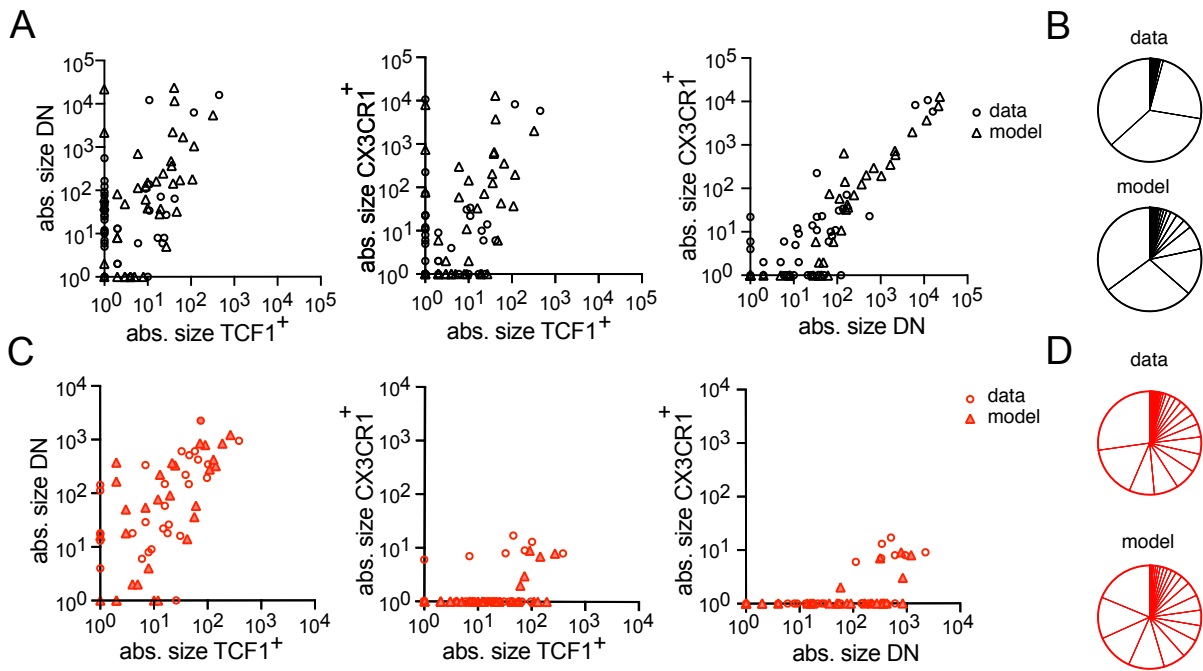


Figure 4.9.: Verification of the mathematical model by simulating the single CD8⁺ T cell responses after LCMV Armstrong and clone 13 infection. **A** Pair-wise correlations of the three subsets showing the data and the model simulations performed with the Gillespie stochastic simulation algorithm at day 8 after LCMV Armstrong infection. **B** Pie chart depicting the distribution of the population size each clone has contributed to at day 8 p.i. with LCMV Armstrong for the data (top) and the model simulations (bottom). **C** As in (A), but for P14 T cells after LCMV clone 13 infection. **D** As is (B), but shows the distribution of the total P14 T cell response at day 8 following LCMV clone 13 infection. Data stems from Lorenz Kretschmer and Dr. med. Veit Buchholz, mathematical modelling was performed by myself.

Furthermore, the cells from the two infections also stopped proliferating at different time-points. While the majority of the P14 T cells from the clone 13 infection stopped dividing at an earlier time. On average P14 T cells from clone 13 infection ceased to proliferate around day 4.3 p.i., whereas P14 T cells from Armstrong infection kept dividing until day 4.9 p.i. However, as indicated by the increased division speed measured in the clone 13-derived P14 T cells (Figure 4.5 C), the fraction of these cells that remained actively cycling after day 8 infection divided faster until the peak of the infection with clone 13 was reached.

Thus, several mechanisms are acting on T cell development in chronic infection. Different proliferation activity and reduced differentiation into the effector compartment were two of the processes that we could identify with the help of this mathematical model.

However, what role inhibitory receptor expression and exhaustion-driving transcription factors play at the onset of the chronic response remains elusive and requires further investigation.

Therefore, we test as next, how similar the response between the infection with LCMV Armstrong and clone 13 is at an earlier time point.

Table 4.1.: Best fit parameters to the by cell cycle drop out extended progressive model of differentiation where the model was fitted to the data for LCMV Armstrong and clone 13 simultaneously. Identification of the 95 % interval confidence bounds of the parameters was performed using the profile likelihood method.

parameter	value	95 % CI
shared parameters		
naïve \rightarrow TCF1 ⁺ rate (r_0)	1.2 d ⁻¹	(1.1, 1.5) d ⁻¹
TCF1 ⁺ \rightarrow DN rate (r_1)	0.25 d ⁻¹	(0.21, 0.31) d ⁻¹
drop out rate (t_d)	1.1 d ⁻¹	(1.0, 1.2) d ⁻¹
parameters specific for LCMV Armstrong		
TCF1 ⁺ proliferation rate (λ_{TCF1^+})	0.95 d ⁻¹	(0.99, 1.04) d ⁻¹
TCF1 ⁻ proliferation rate (λ_{TCF1^-})	1.6 d ⁻¹	(1.5, 1.7) d ⁻¹
DN \rightarrow CX3CR1 ⁺ rate (r_1)	0.08 d ⁻¹	(0.05, 0.12) d ⁻¹
drop out time (τ)	4.9 d	(4.8, 5.3) d
parameters specific for LCMV clone 13		
TCF1 ⁺ proliferation rate (λ_{TCF1^+})	1.18 d ⁻¹	(1.12, 1.24) d ⁻¹
TCF1 ⁻ proliferation rate (λ_{TCF1^-})	1.4 d ⁻¹	(1.3, 1.5) d ⁻¹
DN \rightarrow CX3CR1 ⁺ rate (r_1)	0.002 d ⁻¹	(0.0008, 0.0045) d ⁻¹
drop out time (τ)	4.3 d	(4.2, 4.5) d

4.4. Early fate plasticity at the onset of a persisting infection

Early divergence of T cell fates

In the previous section we identified distinct division drop out kinetics as differential mechanism in the best fitting model during T cell diversification after LCMV Armstrong and clone 13 infection.

The time point of division cessation was different in either infection and clone 13-derived T cells arrested from proliferation half a day earlier than the Armstrong-derived counterparts. P14 T cells after the LCMV Armstrong infection stopped proliferating around 4.9 days p.i., while P14 T cells following a clone 13 infection exited from cell cycle around 4.3 day p.i.

Furthermore, we showed that the recruitment rate and the differentiation rate between MP to the non-MP (DN + CX3CR1⁺) subset could be explained using the same parameter for both infections. As the MP subset has formed early during the infection, and at day 4.5 p.i. all subsets of interest (MP, non-MP) were readily present, we will focus our analyses in this section to the

single-cell transcriptomic data from day 4.5 p.i.

At day 4.5 p.i. the majority of cells were actively dividing at similar speed, even though in the clone 13 infection the division drop out of the P14 T cells was initiated. This time point was of particular interest, as the overlap of the P14 T cells on day 4.5 following infection with LCMV Armstrong or clone 13 that was observed in the UMAP plot and indicated some degree of similarity in expression of gene transcripts.

Indeed, the overlap of the day 4.5 samples in the UMAP embedding could therefore also be attributed to a high expression of proliferation signatures. Nevertheless, we investigated if diverging events were taking place and, therefore, analysed the differentially expressed genes in LCMV Armstrong versus clone 13.

In the LCMV Armstrong infection, effector genes were already differentially up-regulated at day 4.5. Among the differentially expressed genes were the transcription factor *Id2*, and genes related to cytotoxic effector function (*Klrg1*, *Gzmb* and *Gzma*) (Figure 4.10 A, B).

Furthermore, compared to the day 4.5 P14 T cells from the infection with LCMV clone 13, *Satb1* was up-regulated in LCMV Armstrong-derived cells. *Satb1* is thought to play a role in regulating PD1 during T cell activation (Stephen et al. 2017). It is also down-regulated in exhausted T cells compared to naïve CD8⁺ T cells (Wherry et al. 2007) (Figure 4.10 A). These five genes exhibited a stronger expression in the P14 T cells from the LCMV Armstrong infection at all time points. Although, the expression levels of *Gzmb* and *Gzma* decreased towards the peak of acute infection, starting to diminish from a time point where the virus reduced viral titers are observed (Moskophidis et al. 1995; Wherry et al. 2003a).

In the P14 T cells from the clone 13 infection, the inhibitory receptors *Pdcd1* and *Lag3* were differentially up-regulated compared to the P14 T cells from the infection with LCMV Armstrong.

Similarly, *Tox*, which has been identified as a key driver of T cell exhaustion (Alfei et al. 2019; Khan et al. 2019; Yao et al. 2019), was already up-regulated at day 4.5 after chronic infection (Figure 4.10 A, B). We also found that *Slamf6* (encoding Ly108), a progenitor-associated gene, was up-regulated compared to the LCMV Armstrong infection (Figure 4.10 A, B).

Also *Batf*, a TCR-regulated transcription factor, has been shown to promote the transcription of inhibitory PD1 (Kallies et al. 2020; Quigley et al. 2010). Furthermore, high expression of *Batf* coincided with impaired T cell function (Kallies et al. 2020; Kurachi et al. 2014; Man et al. 2017; Quigley et al. 2010). BATF was differentially up-regulated on day 4.5 following the LCMV clone 13 infection (Figure 4.10 A). Furthermore, it has been shown that BATF counteracts the formation of exhausted memory-like precursor cells by repressing TCF1 (Man et al. 2017; Utzschneider et al. 2020).

The surface expression of some of these marker genes was analysed by the Buchholz laboratory. They performed a flow cytometry staining for day 4.5 and day 8 after infection.

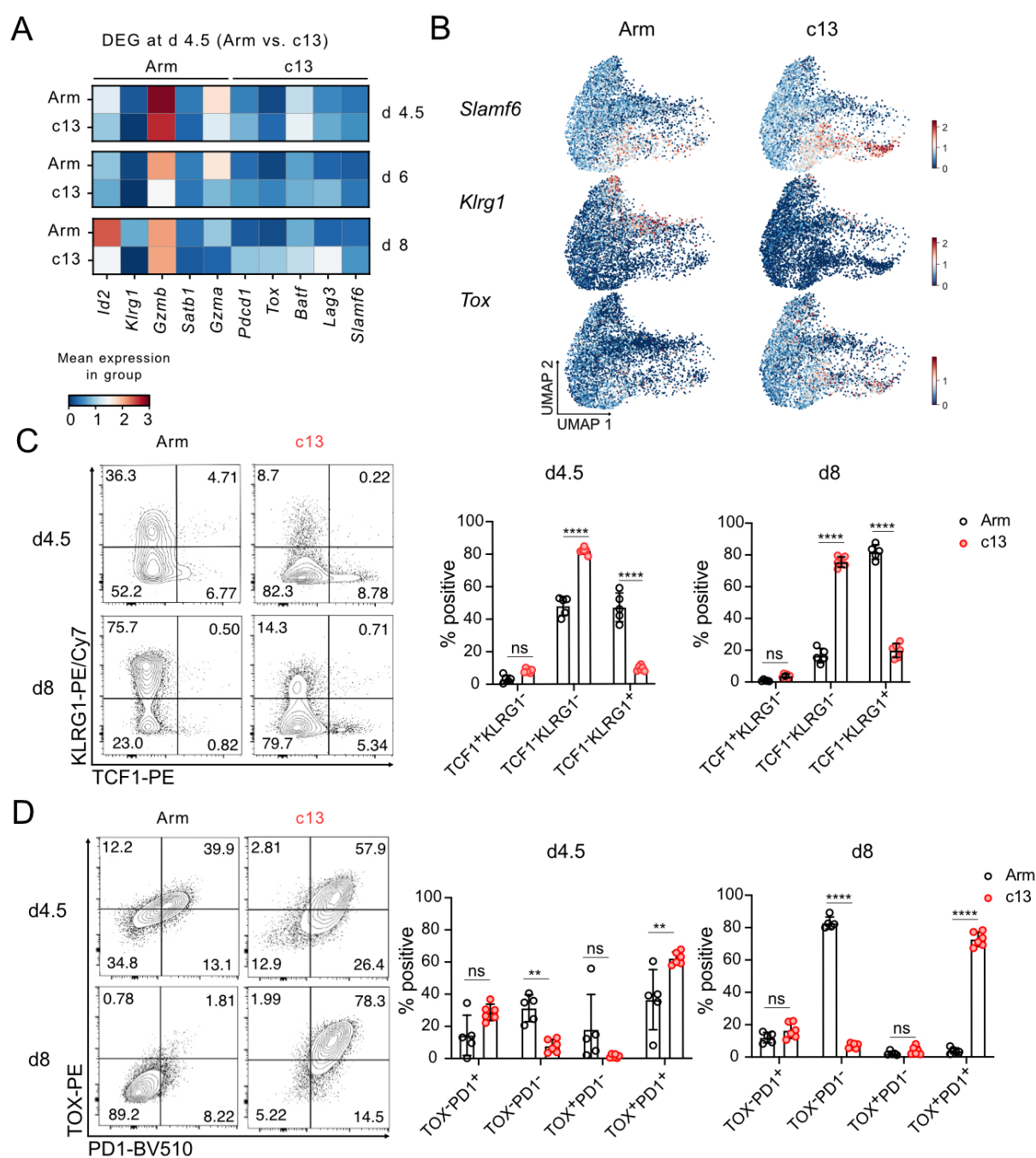


Figure 4.10.: Differential gene expression analysis suggests that the fate of P14 T cells during clone 13 LCMV infection is decided as early as day 4.5. **A** Matrix plot depicting the mean gene expression at day 4.5, 6 and 8 p.i. of significantly up-regulated differentially expressed genes in P14 T cells in LCMV Armstrong vs. clone 13 at day 4.5. **B** UMAP visualisation as in Figure 4.2 depicting only the cells from day 4.5 p.i. and their expression of *Slamf6*, *Tcf7* and *Tox*. **C-D** 5×10^2 or 5×10^4 naïve P14 T cells were adoptively transferred into C57BL/6 mice. The mice were infected with either 2×10^5 LCMV Armstrong or 2×10^6 LCMV clone 13. **C** Representative contour plot showing the expression of TCF1 and KLRG1 at day 6 p.i. and **D** representative contour plot depicting the PD1 and TOX expression at 4.5 or 8 p.i. by flow cytometry. Mean and std, $n = 5 - 6$, data from two independent experiments. One-way ANOVA with multiple-comparison testing, ns= not significant, $**p < 0.05$, $****p < 0.0001$. Experiments for the data shown in **C-D** were performed by Lorenz Kretschmer and Dr. med. Veit Buchholz.

First, by staining for KLRG1 and TCF1 (as surrogate for the surface protein Ly108), the precursors and effector subtypes were examined (Figure 4.10 C). Already at day 4.5 after infection, differences in expression between these two markers were observed. This was further manifested at this early stage of the chronic LCMV infection, 5 times less KLRG1⁺TCF1⁻ P 14 T cells were formed compared to the infection with LCMV Armstrong (Figure 4.10 D). In return, there were 2 times more KLRG1⁻TCF1⁻ P 14 T cells in the clone 13 infection, and slightly but not significantly more KLRG1⁻TCF1⁺ P 14 T cells (Figure 4.10 C).

Between day 4.5 and day 8, these differences in the subset distributions mentioned above intensified (Figure 4.10 D). Second, the expression of TOX and PD1 was measured. As early as day 4.5 p.i., the P14 T cells from clone 13 infection had a higher PD1 and TOX MFI (data not shown) and, percentage-wise, more cells were positive for the expression of both markers (Figure 4.10 D) than during infection with LCMV Armstrong.

While in the P14 T cells from LCMV Armstrong infection, the expression of PD1 and TOX was transient and both markers were down-regulated until the peak response at day 8, the P14 T cells in the clone 13 infection maintained their high expression for PD1 and TOX (Figure 4.10 D). The TOX expression was highest in the TCF1⁺-subset in both infections, with the percentage of TOX-expressing cells decreasing with progressing effector phenotype (Figure B.4 B). The enriched expression of TOX in TCF1⁺ T cells fits the current opinion that TOX is responsible for maintaining the exhausted T cell pool during chronic infection (Alfei et al. 2019; Khan et al. 2019; Yao et al. 2019).

Developmental flexibility of P14 T cells early during the LCMV clone 13 infection

It has been previously described that TCF1⁺ T cells and, therefore, also MEX precursor T cells, possess self-renewing properties (Chen et al. 2019; Im et al. 2016; Utzschneider et al. 2013). Furthermore, it was shown that even after antigen removal, the exhausted imprint is retained, and only exhausted progeny can be formed when MEX subset cells were adoptively transferred (Im et al. 2016; Utzschneider et al. 2013). Therefore, we wondered whether during early time points, e.g. at day 4.5 after infection, the exhausted fate remained plastic and the TCF1⁺ P14 T cells still retained the ability to generate functional effector progeny.

Even though several differences were observed on the transcriptional level on day 4.5, co-localisation in the UMAP embedding and comparable proliferative speeds suggested a certain degree of similarity. The Buchholz laboratory performed the following experiments to test our hypothesis.

Therefore, naïve *Tcf7*-GFP P14 T cells were transferred into wild-type C57BL/6 mice. The mouse recipients were subsequently infected with LCMV clone 13. At day 4.5 p.i., the P14 T cells from the spleen were isolated, and enriched based on their *Tcf7* expression by flow cytometric sorting (Figure 4.11 A, B). *Tcf7*-GFP⁺ and *Tcf7*-GFP⁻ P14 T cells were then transferred into mice infected with LCMV Armstrong or LCMV clone 13 4.5 days ago.

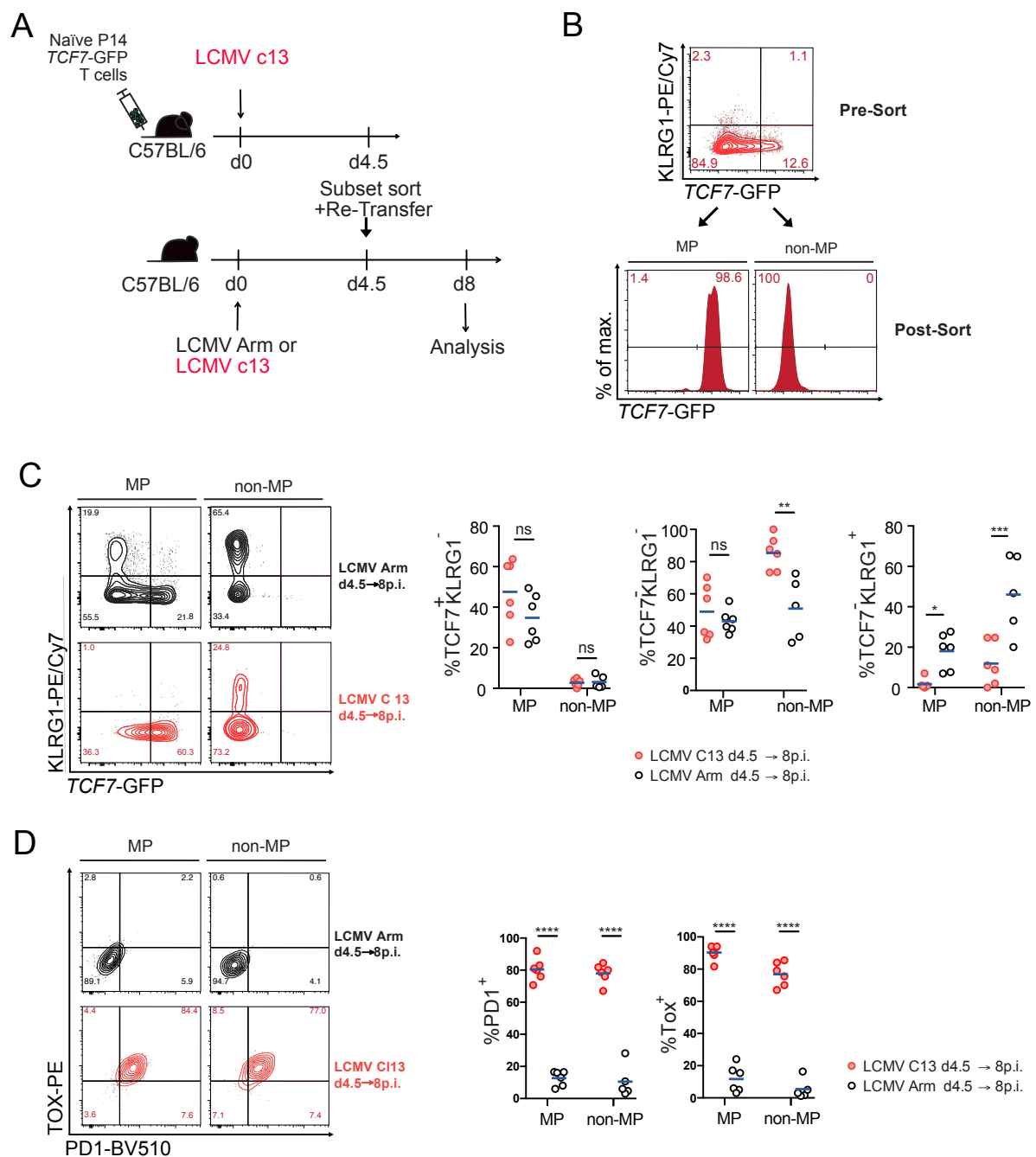


Figure 4.11.: P14 T cells from day 4.5 LCMV clone 13 p.i. retain the potential to become functional effector cells. **A** Scheme of experimental setup. C57BL/6 mice received naïve *Tcf7*-GFP reporter P14 T cells i.p. and were infected with LCMV clone 13 the next day. On day 4.5 p.i. MP (*TCF7*⁺) and non-MP (*TCF7*⁻) subsets were re-isolated by flow cytometric sorting and re-transferred into infection matched or time point matched LCMV Armstrong infected hosts. On day 8 p.i., the P14 T cells from the spleens were analysed. **B** Contour colour plot depicting the gating strategy for FACS-purification of MP and non-MP subsets based on the expression of *Tcf7*-GFP (top) and representative histograms of the *Tcf7*-GFP profiles of the purity control (bottom). **C** Representative contour colour plots of the *Tcf7*-GFP and KLRG1 expression at day 8 p.i. with LCMV Armstrong (top row, left) or LCMV clone 13 (bottom row, left) and the quantification of the subset sizes (right).

At day 8 p.i., or 3.5 days post re-transfer, the progeny of *Tcf7*-GFP⁺ and *Tcf7*-GFP⁻ P14 T cell subsets were examined for their expression of *Tcf7* and KLRG1 (Figure 4.11 A-C). MP cells, when re-transferred into infection-matched recipients, could self-renew or down-regulate TCF1 and generated TCF1⁻KLRG1⁻ progeny (Figure 4.11 C). Non-MP subsets, after re-transfer into clone 13, retained their phenotype and produced only few KLRG1⁺ progeny (< 5 %) (Figure 4.11 C). After re-transfer into time point-matched but LCMV Armstrong-infected recipients, the TCF1⁺ subset retained the ability of self-renewal, but at the same time differentiated into TCF1⁻KLRG1⁻ and TCF1⁻KLRG1⁺ terminal EFF progeny (Figure 4.11 C).

Nevertheless, after re-transfer into clone 13, non-MP subsets retained their phenotype and produced only few KLRG1⁺ progeny (Figure 4.11 C). Whereas, non-MP precursors failed up-regulate TCF1 expression and were, therefore, unable to form TCF1⁺KLRG1⁻ MP T cells (Figure 4.11 C).

These results were in agreement with data from Utzschneider et al. 2020. Utzschneider and colleagues investigated the role of ID3⁺ P14 T cells during the development of T cell exhaustion. ID3⁺ P14 T cells essentially map to the TCF1⁺ T subset, and accordingly also express other memory precursor cell markers such as Ly108, and CXCR5 (Kallies et al. 2020; Utzschneider et al. 2020). In their study, Utzschneider and colleagues used an *Id3*-GFP reporter system and isolated ID3⁺ P14 T cells at day 5 after persistent LCMV infection. After re-transfer of ID3⁺ P14 T cells into time-matched and LCMV Armstrong infected recipients with subsequent analysis at day 7 post-infection (day 2.5 after re-transfer), they showed that ID3⁺ P14 T cells were able to generate effector T cells, albeit to a lesser extent.

Furthermore, it was further investigated whether the P14 T cells retained their PD1 and TOX imprint after transfer from clone 13 infection into LCMV Armstrong. On day 4.5, after infection with LCMV Armstrong and clone 13, all progenies were PD1 and TOX double-positive (Figure 4.10 D). After the isolation from clone 13-infected donors and subsequent re-transfer into recipients with ongoing LCMV Armstrong infection, both MP and non-MP subset T cells lost their expression for the two markers PD1 and TOX (Figure 4.11 D). However, when the P14 T cells remained in an ongoing chronic infection (Figure 4.10 D, bottom row) or were transferred to infection-matched recipients, the high expression of PD1 and TOX lasted (Figure 4.11 D).

The findings imply that at the early stages of infection with LCMV clone 13, the fate of a CD8⁺ T cell has not yet been entirely decided, and the remaining fate-flexibility can be used to rescue the exhaustion phenotype when removing the antigen.

As next, we aim to reconstruct the differentiation trajectories in the scRNA-seq data to identify

Figure 4.11 : D Representative pseudocolour plots showing the expression of PD1 and TOX at day 8 p.i. with LCMV Armstrong (top row, left) or LCMV clone 13 (bottom row, left) and the quantification of the subset sizes (right). $n = 6$, data from two independent experiments. One-way ANOVA, ns= not significant, $**p < 0.05$, $***p < 0.005$, $****p < 0.0001$. Lorenz Kretschmer and Dr. med. Veit Buchholz generated experimental data.

additional mechanisms preventing the formation of EFF T cells in the infection with LCMV clone 13.

4.5. An early differentiation program drives the acquisition of an exhausted phenotype

Deflection of memory-like progenitor cells during the course of differentiation

It is assumed that during a persisting infection, inhibitory receptors influence the transcription of effector genes. Thus, the formation of functional effector T cells is prevented and thereby also the consequences of an immune pathology during persistent infection. However, it is still unclear how the differentiation pathways between the CD8⁺ T cell subsets are related during the acute or chronic LCMV infection.

Therefore, we performed trajectory analyses of time-resolved splenic transcriptomes from day 4.5 to 8 to unravel the differentiation relationships between functional or exhausted precursors to more terminal differentiated subsets.

First, we computed the RNA velocities based on the relative abundance between spliced and unspliced mRNA to predict the future status of a cell (La Manno et al. 2018). We calculated the RNA velocities for the infections separately and visualised them in the jointly determined UMAP embedding (Figure 4.12 A). We have analysed the RNA velocities during LCMV Armstrong infection in more detail in section 3.4. Considering only the early time points up to the peak of the immune response the directionalities in the LCMV Armstrong data set were equivalent to the analysis, including the time point from the contraction phase.

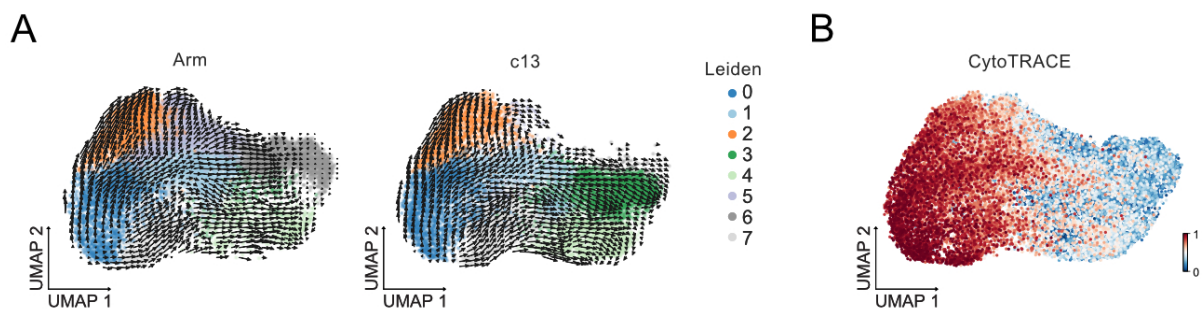


Figure 4.12.: According to RNA velocity analysis EFF subset cells are not formed during the infection with LCMV clone 13.

A UMAP representation with Leiden clustering is showing the RNA velocities for the P14 T cells after LCMV Armstrong (left) or LCMV clone 13 infection (right). RNA velocities were computed individually per infection and projected into the same UMAP embedding. **B** UMAP is showing the CytoTRACE score for LCMV Armstrong and clone 13. The CytoTRACE score displays the degree of differentiation, where a score of one represents cells in the most undifferentiated state and a score of zero represents cells with terminal differentiation.

The cells were flowing from the proliferating state to the non-proliferating state, keeping their phenotypic identity (Figure 4.5, Figure 4.12 A, left). Meaning, that the differentiation started from the P14 T cells with a proliferating memory T cell phenotype, following the arrows follow from the cells in cluster 7 (MP) into the cells in cluster 4 (non-proliferating MP cells). We also observed that from the junction area between clusters 0 (proliferating EMP) and 7 (cycling MP), there is a bifurcation from which cells either migrate through cluster 7 into cluster 4 (cMP → ncMP), or via cluster 0, through cluster 1 (cMP → cEMP) into the highly proliferative effector-like cluster 5 into cluster 6 (cEMP → cEFF → ncEFF) (Figure 4.12 A). Cluster 6 contained the cells with a characteristic terminal effector signature (Figure 4.3 F). These findings are in line with published observations (Pritykin et al. 2021).

In the clone 13 infection, the arrow directions in the UMAP embedding for the common clusters were very similar. Here too, clusters 0 and 7 were the first clusters from which the arrows emerged (Figure 4.12 A, left). By calculating the CytoTRACE score (Gulati et al. 2019) we identified which cells were most advanced in their differentiation path and which ones still retained stem cell-like properties. The cells that were embedded between clusters 0 and 7 received the highest CytoTRACE score and represented the least differentiated cells in both infections (Figure 4.12 B).

Starting from cluster 7, cells with a memory-like signature ended up in cluster 4 (cTCF1⁺ → ncTCF1⁺). And as from cluster 0 (pendant to cEMPs), the cells in clone 13 also passed over cluster 1 (transitioning cEMPs to ncEMPs) and were then directly diverted into cluster 3, the cluster with a pronounced exhaustion signature (Figure 4.3 E, Figure 4.12 A).

Based on the increased cell cycle exit at day 6 after clone 13 infection (Figure 4.5) and the associated absence of the highly proliferative cluster 5, the P14 T cells from clone 13 failed to reach the terminal EFF compartment. It has been described that the formation of functional MP and EFF subsets is possible during acute infection in absence of TOX (Alfei et al. 2019; Khan et al. 2019). That the EFF population is not generated during the infection with LCMV clone 13 is possibly due to the lack of TCF1 and TOX expression (Angelosanto et al. 2012; Khan et al. 2019).

4.6. TOX limits differentiation into the terminal effector subtype

Supporting previous findings

The expression of TOX inhibits the manifestation of the effector phenotype (Alfei et al. 2019; Khan et al. 2019; Yao et al. 2019). Therefore, we wanted to investigate whether the deletion of TOX altered the differentiation streams during clone 13 infection and therefore, re-analysed the scRNA-seq data set from Yao et al. 2019. Yao et al. 2019 generated scRNA-seq data from H-2D^b:gp33 tetramer⁺ wild-type and *Tox*^{-/-} CD8⁺ T cells.

For this, the authors infected wild-type and *Tox*^{-/-} reconstituted bone marrow chimeras with LCMV clone 13 following analysis on day 7 p.i. Splenic wild-type and *Tox*^{-/-} CD8⁺ T cells

were isolated, purified and enriched by flow cytometric sorting and scRNA-seq using the 10× Genomics technology was performed.

As in the original publication, we pooled the wild-type with the *Tox*^{-/-} sample for the bioinformatics analysis.

In the UMAP embedding little overlap between the wild-type and *Tox*^{-/-} T cells was observed. The segregated localisation indicated that the cells from either condition were at different stages of differentiation (Figure 4.13 A).

After clustering with the Leiden algorithm (Traag et al. 2019), we obtained 7 different clusters (Figure 4.13 B). Cluster 5 was not represented in the *Tox*^{-/-} T cells, and cluster 3 to a lesser extent. In the original analysis of the publication by Yao et al. 2019 it was shown that *Tox*^{-/-} cells generated less TCF1⁺ (Figure 4.13 C, E and F). The reduced representation of the TCF1⁺ subset was also in line with findings from Alfei et al. 2019.

Moreover, we found that cluster 0 was five times larger in the *Tox*^{-/-} CD8⁺ T cells. In this cluster, terminal effector-signature genes were expressed and the cluster comprised *Klrg1*-positive cells with cytolytic properties (Figure 4.13 C, E and F). Comparing the differentially expressed genes between wild-type and *Tox*^{-/-} T cells in cluster 0, we observed that in the wild-type T cells, exhaustion-associated genes such as *Tox* and *Pdcd1* were up-regulated, while the genes that were up-regulated in the *Tox*^{-/-} T cells resembled effector-associated signatures (*Gzma*, *Ccl5*, *Klrg1*) (Figure 4.13 D-F).

The expression of the cytotoxic effector signature in *Tox*^{-/-} cells was probably associated with the enhanced immunopathology observed by Alfei et al. 2019. However, how much alike to effector T cells formed during acute infection the *Tox*^{-/-} cells are, remains unclear.

TOX expression and proliferation

In our comparison between Armstrong and clone 13, we observed that the fraction of dividing cells was different. In clone 13, the cells were forced out of active cell division at mid-peak, while a small fraction kept on proliferating. During acute infection with LCMV Armstrong cell cycle arrest was observed closer to the peak time. Most likely this was due to the viral clearance and accompanied by the on-set of cell death of the highly proliferative effector compartment with the starting contraction phase. Therefore, we wondered whether the proliferative activity in the *Tox*^{-/-} CD8⁺ T cells was different from wild-type CD8⁺ T cells.

We calculated a signature score based on the cell cycle gene list of Tirosh et al. 2016 and thus identified the proliferating cells. A low proliferation score marks cells that are in the G0-phase of the cell cycle.

Approximately 40 % of the *Tox*^{-/-} cells on day 7 after infection were still actively proliferating, a proportion that is very similar to the fraction of dividing T cells from Armstrong infection (Figure 4.13 G-H, Figure 3.10 D-E). In contrast, a more significant proportion of cell proliferated in the presence of TOX (Figure 4.13 G-H).

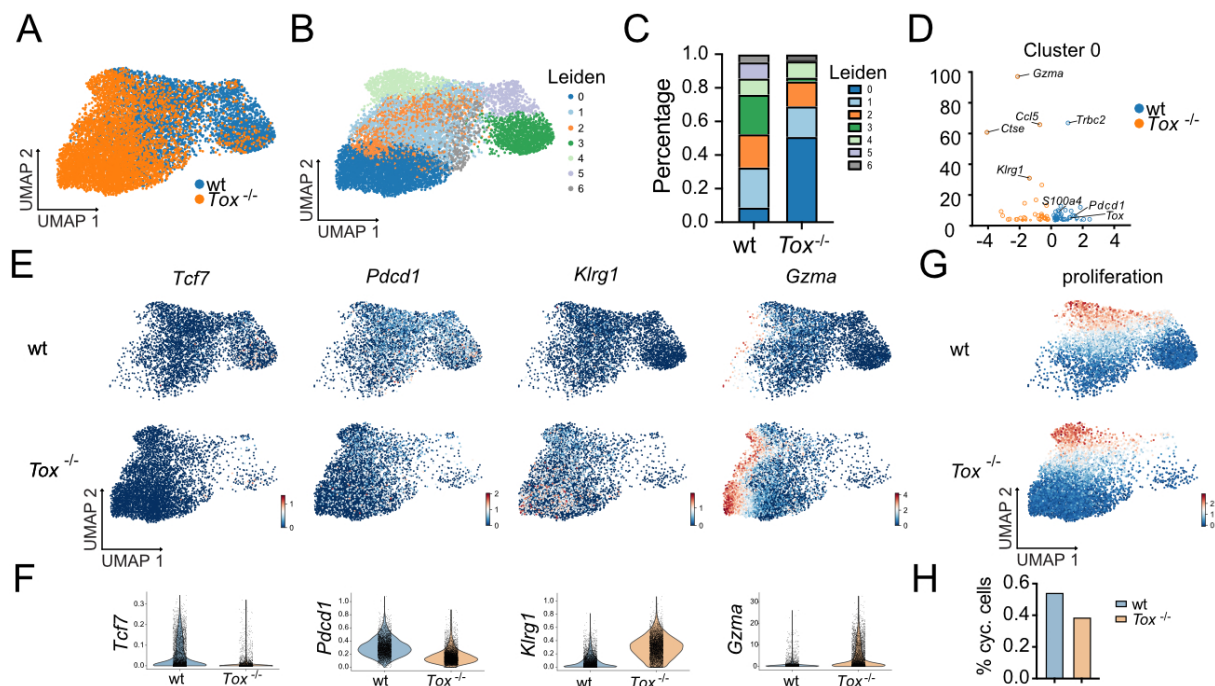


Figure 4.13.: *Tox*^{-/-} P14 T cells during LCMV clone 13 infection develop into terminal effector subsets. **A** Mixed bone marrow chimeras that received wild-type and *Tox*^{-/-} cells were infected with LCMV clone 13. H-2D^b:gp33 tetramer⁺ wild-type and *Tox*^{-/-} CD8⁺ T cells from mixed bone marrow chimeras on day 7 p.i. were isolated from the spleen and analysed by scRNA-seq. UMAP with wild-type and *Tox*^{-/-} CD8⁺ T cells. **B** UMAP representation as in (A) showing Leiden clustering. **C** Bar graph depicts the fraction of cells in each Leiden cluster for wild-type or *Tox*^{-/-} transcriptional data. **D** Volcano plot showing the differentially expressed genes in cluster 0 for wild-type and *Tox*^{-/-}. Selected genes with a fold change > 1.1 and *p*_{adj} < 0.05 are shown (blue: up-regulated in wild-type, orange: up-regulated in *Tox*^{-/-}). **E** UMAP representation using the same embedding showing the expression of *Tcf7*, *Pdc1*, *Klr1* and *Gzma* in wild-type or *Tox*^{-/-} responses. **F** Violin plots display the expression of *Tcf7*, *Pdc1*, *Klr1* and *Gzma* for wild-type and *Tox*^{-/-} CD8⁺ T cells. **G** UMAP depicting the proliferation score. The signature scoring was computed in Vision using the cell cycle gene list from Tirosh et al. 2016. **H** Bar graph shows the fraction of cycling cells inferred from the scRNA-seq data. Data from Yao et al. 2019 with own analysis.

How TOX deficiency alters differentiation

One study suggested that the effector function of T cells was not affected by TOX. They proposed that TOX rather acted by regulating inhibitory receptor expression in exhausted T cells (Scott et al. 2019). We, therefore, wondered whether the differentiation dynamics in *Tox*^{-/-} T cells more closely resembled that of CD8⁺ T cells during acute LCMV infection, in contrast to classical exhaustion differentiation.

We performed RNA velocity analyses on the *Tox*^{-/-} and wild-type data (Figure 4.14). Indeed, the arrow directionalities in wild-type CD8⁺ T cells pointed from the proliferating TCF1⁺ cluster (Cluster 5) to the non-proliferating TCF1⁺ cluster 3.

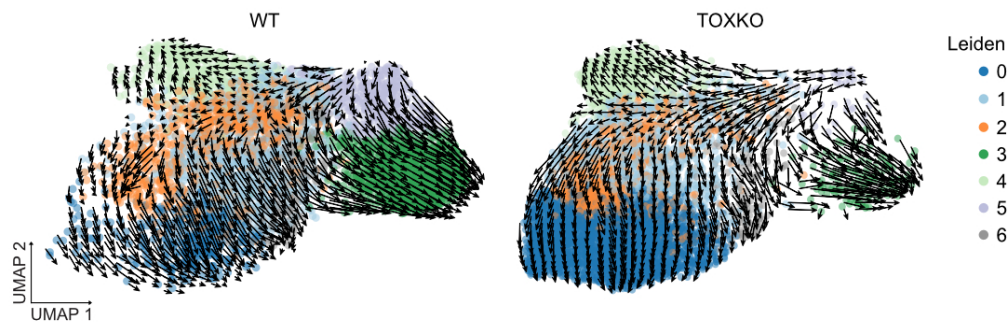


Figure 4.14.: Deflection in the progressive direction of differentiation during a clone 13 infection prevents the formation of effector cells. RNA velocity analysis of wild-type (left) or *Tox*^{-/-} (right) CD8⁺ T cells on day 7 p.i. LCMV clone 13. RNA velocities were computed separately and projected into the same UMAP embedding. Data from Yao et al. 2019 with own analysis.

Thus, we observed such a differentiation pattern in all the RNA velocities that were analysed in this thesis (Figure 4.14 left). The differentiation along the proliferation axis (horizontal arrows in the upper part of the UMAP image), starting from the TCF1-positive cluster and moving over to the TCF1-negative cluster 5 (Figure 4.14 left). Furthermore, the differentiation was deflected to the right side of the UMAP, allowing the cells to rarely reach the areas where *Klrg1* and *Gzma* were expressed.

In the *Tox*^{-/-} T cells, this deflection was abrogated, and the cells gained access to the KLRG1-positive EFF subset of cluster 0 (Figure 4.14, right).

Thus, expression of TOX prevented the formation of a large EFF subset pool.

In the following section, we aim to discern the differentiation relationships during chronic LCMV infection and determine the branch points from canonical diversification paths leading to T cell exhaustion. We, therefore, perform mathematical modelling based on a differentiation framework described in the literature as the arrested model of T cell exhaustion.

4.7. MP and non-MP subsets exhaust independently

The arrested model of T cell exhaustion states that at some point during the differentiation process, the T cells deviate from their default differentiation path, arrest, and become ultimately exhausted (Henning et al. 2018). Since the pool of exhausted T cells is very diverse, it is assumed in this model that different subtypes emerge depending on the differentiation stage at which the cells leave their standard path and start the exhaustion program. That is, MP T cells give rise to MEX T cells, and EFF T cells give rise to TEX cells. Experimental evidence exists that the formation of a terminal exhausted T cell pool is driven solely by the exhaustion of the MP subset to MEX T cells (Alfei et al. 2019; Angelosanto et al. 2012; Pritykin et al. 2021; Utzschneider et al. 2020) and that the exhaustion imprint is passed on to the progeny. The MEX subset has similar characteristics as the MP subset. MEX T cells are identifiable by the expression of

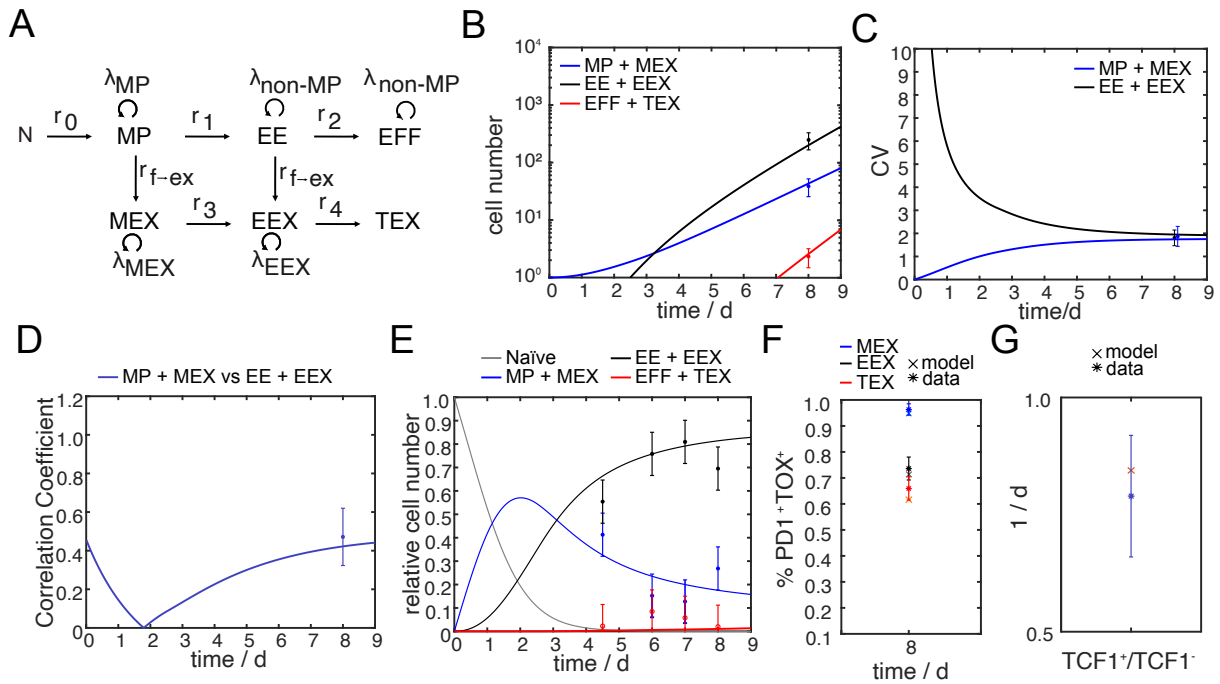


Figure 4.15.: Exhaustion driven only by the MP and non-MP subset explains the single cell transfer responses to LCMV clone 13. **A** Mathematical model topology. **B** Best fit to the mean, **C** the CV and **D** the correlation coefficient of the single CD8⁺ T cell responses at day 8 following the infection with LCMV clone 13. As well as the best fit of the model shown in **A** **E** to the relative cell number in each subset, **F** the fraction of PD1⁺TOX⁺ MEX, EEX or TEX subset and **G** to the relative proliferation rate. Data used for the modelling and shown in **B-D** and **F** stem from Dr. med. Veit Buchholz and Lorenz Kretschmer. Data shown in **E** and **G** stem from own experiments. Mathematical modelling was performed by myself.

memory markers such as TCF1, CXCR5 and CD62L and exhibit similar stem-like properties (Alfei et al. 2019; Im et al. 2016; Utzschneider et al. 2016a, 2020). The T cells from the MEX subset, however, also express high levels of several inhibitory receptors (PD1, Lag3) and are positive for TOX, a transcription factor that plays a key role in the regulation and promotion of T cell exhaustion (Alfei et al. 2019; Khan et al. 2019; Yao et al. 2019).

Modelling T cell exhaustion using the arrested differentiation model

Using mathematical modelling, we investigated which functional subsets can exhaust. We build a topology based on the blueprint of the arrested T cell exhaustion model.

Angelosanto et al. 2012 showed that KLRG1^{high} T cells cannot exhaust after isolation during the peak response in LCMV Armstrong and upon re-transfer into clone 13 infected recipient mice. Therefore, the mathematical model was simplified in such a way, that the transition between KLRG1^{high} EFF T cells and TEX T cells was prevented. This was achieved by setting the transition rate from the EFF to the TEX subset to zero. Furthermore, as in the arrested exhaustion model (Henning et al. 2018) the ability to proliferate decreases with the accumulation

of exhaustion traits. Therefore, we further simplified the mathematical model by assuming that TEX T cells were unable to proliferate (Figure 4.15 A). Thus, the first model we tested followed a scheme where naïve T cells linearly differentiated from MP to early effector (EE) T cells to EEF T cells. In this process, the functional (f) subsets were allowed to deviate from their canonical pathway starting at a particular time point after infection and to differentiate at the rate $r_{f \rightarrow ex}$ to feed the exhausted (ex) subsets. The time point at which the branching into the exhausted compartment started was estimated by the mathematical model (Figure 4.15 A).

We informed the mathematical modelling, using the single-cell fate-mapping data, that was also used in the preceding chapters. The Buchholz laboratory conducted experiments in which mice received individual congenic P14 T cells by adoptive transfer. These mice were then infected with LCMV clone 13. On day 8 after LCMV clone 13 infection, the P14 T cells were isolated from the spleens and analysed based on the expression of TCF1, Tim3 and CX3CR1. Because T cells with an exhausted phenotype emerge early (Philip et al. 2017; Schietinger et al. 2016), using the aforementioned marker combination, we were unable distinguish which cell was already exhausted and which not. Unfortunately, further single-cell fate-mapping data, providing a segregation between functional and exhausted subsets was unavailable to date.

We have worked around this problem by assuming the following: We observed that on day 8 p.i. KLRG1 and CX3CR1 were co-expressed (data not shown), and therefore, assumed that the fraction of KLRG1-positive subset was similar to the CX3CR1-positive one. This way we could use the data from Figure B.3 A-B to identify the exhausted subsets based on the expression of PD1⁺TOX⁺ on day 8 p.i. with LCMV clone 13. We are aware, that this posed a drastic simplification because exhausted T cells are difficult to be identified by solely two markers. Ideally, for each subset (functional and exhausted) the expression of distinct inhibitory receptors and the information about cytotoxic properties would have been used. However, even when such data had existed, the characterisation by multiple markers would reveal many heterogeneous subsets that hitherto would complicate the mathematical model.

Furthermore, the proliferation measurements as well comprised of a mixture of functional and exhausted cells. Due to lack of data to distinguish the speed between the both, we weighted the proliferation rates according to the functional and exhausted subset sizes. This poses of a heuristic assumptions that requires experimental validation.

For the mathematical modelling, we used least-squares fitting and determined the best fit based on χ^2 -minimisation. The best fit to the means, CVs and correlation coefficients between MP + MEX and EE + EEX subsets is shown (Figure 4.15 B-D). Similarly, the best fit to the relative subset sizes at time points 4.5, 6, 7 and 8, to the day 8 PD1⁺TOX⁺ percentages and to the ratios of proliferation rates between TCF1⁺ and TCF1⁻ is shown (Figure 4.15 F-G). The model where the MP and the TCF1⁻CX3CR1^{low} non-MP (here denoted as EE) subset can exhaust individually described the data well.

We also tested the model that has been described in the literature, i.e. allowing only the MP subset to arrest (Utzschneider et al. 2020). This way, we aimed at investigating whether the

MP subset acted as the sole source for the formation of the exhausted pool and was sufficient to explain the single-cell fate-mapping data. Thus, we set the rate $r_{f \rightarrow ex}$ between the EE and the EEX subset to zero (Figure B.4 A).

We re-run the model fitting and saw that a model that allowed the transition into the exhausted compartments only via the MP subset was also able to describe the data equally well. The best fit for the MP-driven exhaustion model only is shown in Figure B.4 B-F. To discriminate which of the two models performs best, we conducted model selection by comparing the AICc values between the two models. By determining the difference in the AIC score, we found that the difference between the two models is 4.11 ($\Delta AIC = 4.11$). While the MP and EE independent exhaustion model was favoured over the MP-driven exhaustion model.

We are aware that the classification of the exhausted subsets by the expression of PD1 and TOX solely is ambiguous. With regard that both TOX and PD1 are expressed, albeit transiently, in acute infection (Figure 4.10 D) (Alfei et al. 2019). Also, on day 8 after the infection with LCMV Armstrong, on average, about 50 % of the MP subset and approximately 10 % of the EE subset remained positive in their expression for PD1 and TOX (Figure B.3 C). Solely the EFF cells completely down-regulated TOX and PD1 until day 8 (Figure B.3 C).

Hence, assignment of the exhausted subsets based on these two markers provided a rough estimate and an approximation of how many cells were exhausted. The sizes of the MEX, EEX and TEX subsets were probably overestimated using the classification based on TOX and PD1. Furthermore, the estimation of the cell cycle rate relied on a heuristic assumption. Whether this represented a valid hypothesis has yet to be tested.

Given this set of data both models were unidentifiable and the CI bounds for several parameters could not be determined. Therefore, the parameters values are not listed.

Even though the mathematical modelling was drastically simplified due to limited available experimental data resulting in non-identifiable parameter confidence regions, we wanted to experimentally test whether a discrimination between the two exhaustion models could be made. Therefore, the Buchholz laboratory performed experiments where the MP, EE and EFF subsets after canonical differentiation during acute infection were isolated and re-transferred into hosts, previously infected with LCMV clone 13.

MP and EE subset cells fuel the exhausted T cell pool

To this end, naïve *Tcf7*-GFP P14 T cells were transferred into wild-type C57BL/6 mice. On day 8, after infection with LCMV Armstrong, the P14 T cells were isolated from the spleen and enriched according to their expression for KLRG1 and *Tcf7* by flow cytometric sorting (Figure 4.16 A, B).

KLRG1⁺ *Tcf7*⁻ EFF, KLRG1⁻ *Tcf7*⁻ EE T cells and KLRG1⁻ *Tcf7*⁺ MP T cells were adaptively re-transferred into ongoing LCMV Armstrong or clone 13 infection at day 4.5 adaptively re-transferred, 3.5 day after the re-transfer respectively on day 8 of the infection the P14 T cells from the spleen were analysed (Figure 4.16 A, B).

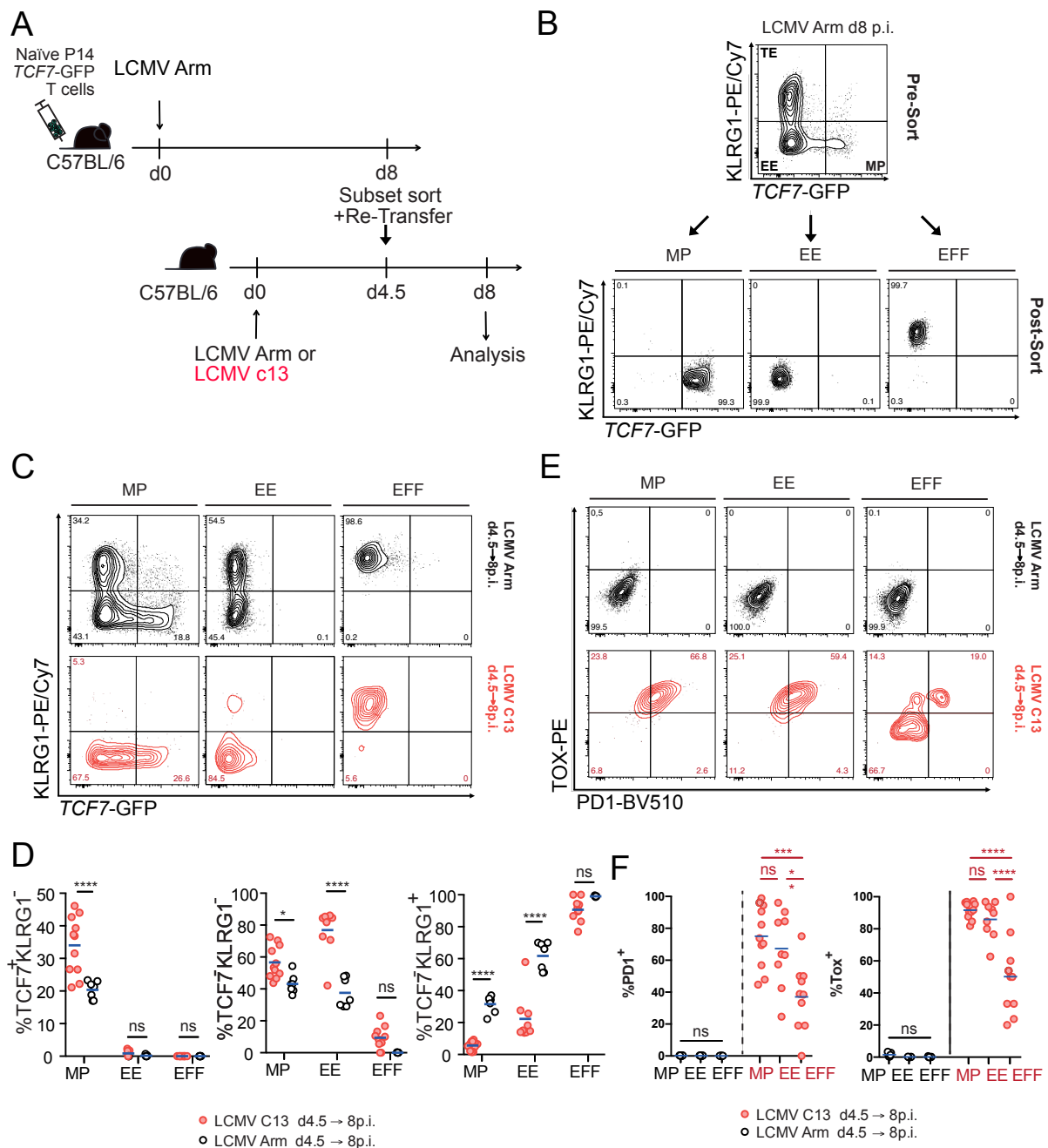


Figure 4.16.: EFF T cells do not exhaust upon re-transfer into chronic LCMV infection. **A** Experimental set-up for re-transfer of functional subsets. Naïve *TCF7*-GFP were adoptively transferred into wild-type C57BL/6 mice and infected with LCMV Armstrong. On day 8 p.i. the subsets were sorted based on their expression of KLRG1 and *TCF7*-GFP. Subsets were re-transferred into LCMV Armstrong- or LCMV clone 13-infected mice and were analysed at day 8 p.i. (3.5 days after re-transfer). **B** Representative contour plot shows the gating strategy for the KLRG1 and *TCF7*-GFP expression and the post-sorting control. **C** On day 8 p.i. LCMV Armstrong (upper row) and LCMV clone 13 (bottom row) the three subsets were analysed on their expression of KLRG1 and *TCF7*-GFP and **F** TOX and PD1. **D** Quantification of **C** **F** and **D**. $n = 7 - 10$, mean, data from two independent experiment. ns, not significant. $*p < 0.5$, $***p < 0.001$, $****p < 0.0001$ One-way ANOVA. Data stems from Lorenz Kretschmer and Dr. med. Veit Buchholz.

After re-transfer into the acute LCMV infection, we observed that MP T cells formed all subsets, whereas EE T cells only regenerated themselves and produced EFF progeny (Figure 4.16 C, D, top row). EFF cells maintained their T cell pool and retained their KLRG1-positive phenotype (Figure 4.16 C, D).

After the re-transfer into an ongoing clone 13 infection, the MP T cells gave rise to the EE subset. Furthermore, the MP subset also differentiated to EFF T cells, even though this differentiation path was limited and only a few KLRG1-positive cells developed (Figure 4.16 C, bottom row, D).

EE T cells proliferated and differentiated into EFF T cells. Upon re-transfer of EFF T cells into clone 13 infection, the EFF T cells retained their original phenotype, similar to re-transfer into an acute infection (Figure 4.16 C, bottom row, D).

As expected, all subtypes did not express TOX or PD1 after re-transfer from LCMV Armstrong into infection with LCMV Armstrong (Figure 4.16 E, top row, F). However, interestingly, TOX and PD1 were expressed after re-transfer into LCMV clone 13 from MP and EE subsets (Figure 4.16 E, bottom row, F). These results suggest that not only the MP subset was the driving component of T cell exhaustion, but that the EE subset can be exhausted independently of the MP subset and thus, generated exhausted progeny. These findings validate the model prediction (Figure 4.15 A).

Furthermore, we found that EFF T cells no longer up-regulated TOX and PD1 after re-transfer into a clone 13 infection, indicating that their terminal effector state prevented them from acquiring an exhausted phenotype (Figure 4.16 E, bottom row, F). Moreover, the adoptive transfer of functional EFF T cells caused more severe immunopathology in the lungs of clone 13 infected mice than the other two subsets, in which the exhaustion phenotype still could be imposed (data not shown).

Epigenetic factors such as open loci that allow rewiring could potentially play a role in the flexibility of phenotypic emergence. However, further work is needed to understand the role of TOX during CD8⁺ T cell differentiation in the suppression of effector phenotypes during the expansion phase of infection.

5. Discussion

In this thesis, we investigated the developmental relationship between functional CD8⁺ T cell subsets emerging during self-limiting infections and exhausted T cell subsets that develop during chronic diseases. Using a unique approach that combined experimental methods, bioinformatical analyses and mathematical modelling, we dissected the mechanisms that lead to these heterogeneous populations during the expansion phase of acute and chronic infections.

5.1. Subset-dependent cell cycle speed is conserved between different infections

The peak of the immune response is dominated by the EFF subset, while the MP subset comprises of a minor population (Buchholz et al. 2013b; Gerlach et al. 2013; Kretschmer et al. 2020). Thus, the number of divisions an activated CD8⁺ T cell undergoes strongly correlates with its expansion size and phenotype, both of which are dependent of the division speed.

The progressive model of differentiation predicted that the differential progeny size measured at the peak is due to the subset-specific proliferation (Buchholz et al. 2013b). In this thesis we tested and validated the model prediction, using a recently published mathematical framework (Kretschmer et al. 2020).

Cell cycle speed CD8⁺ T cell in different infection systems

We have recently developed a computational method to quantify the duration of the cell cycle (Kretschmer et al. 2020). The quantification relies on the *in vivo* measurements of the fraction of cells that divide within a certain time window.

In contrast to dye-dilution methods or the FUCCI-reporter system, our approach is able to extract the actual mean division speed. Division dye-dilutions such as CFSE or CellTrace Violet (Marchingo et al. 2014; Yoon et al. 2010) can only detect up to 9 divisions, and reflect the number of undergone proliferations at the generation level over multiple days without accessible information on the division speed. Or, the FUCCI-reporter (Kinjyo et al. 2015) reliably informs about the cell cycle stage of the dividing CD8⁺ T cells, however the speed at which cells progress through these stages cannot be determined.

Our method is based on the simultaneous assessment of DNA and BrdU incorporation at an explicitly specified time frame. The time window between DNA analysis and BrdU administration is chosen as such, that within all BrdU⁺ cells recently divided cells are segregated from those in the S-phase cell. The distinction between the two populations of BrdU⁺ cells is made through their DNA content.

In line with the progressive differentiation model (Buchholz et al. 2013b), experimental measurements of the fraction of cells that divided within a certain time window showed that MP T

cells cycle at a slower speed than cells from the non-MP subset.

Interestingly, we noticed comparable inter-division times in all the infection models analysed. While at the day 4.5 p.i. time point the MP subset was consistently slower proliferating with an average speed of approximately 7.5-9 hours, the cells of the non-MP subset divided every 5.5-6 h. Thus, the MP subset divides on average 1.5 time slower than the non-MP subset. The ratio between the subset-specific division speeds is maintained during the expansion and early contraction phase (data not shown). Extrapolating from the day 4.5 inter-division times, the non-MP subset undergoes one more division per day, and consequently becomes more numerous than the MP subset at the peak.

In the comparison of the infection with LCMV Armstrong with the one of the clone 13, we found that the division speed of the overall cycling CD8⁺ T cell population from the clone 13 infection decelerated around day 6 and continued to proliferate at a slower pace until day 12 p.i. It is noteworthy to mention here that we did not investigate time points beyond day 12. Therefore, it is likely that after this particular time point, a small fraction of cells continues proliferating. The reduction in the division speed at day 6 p.i. might be explained through the phenotype-specific attributes of the subsets. I.e. during the LCMV clone 13 infection, the fast-proliferating EFF subset is not formed. Thus, the lack of this fast-cycling population would on average decrease the overall speed of division.

In contrast, the P14 T cells from infection with LCMV Armstrong cycle very rapidly until time points before the peak. Around the peak, they significantly reduce their division rate.

The initiating contraction phase, accompanied by shifts in the cytokine environment and the increase of pro-apoptotic signals could affect the division speed and promote cell cycle exit (Heinzel et al. 2017; Pucci et al. 2003; Schluns et al. 2003). However, it requires further research to discern the molecular drivers of division time elongations during an infection setting.

5.2. A uniform model describes CD8⁺ T cell responses

With the emergence of single-cell omics technologies and the development of computational methods to infer lineage dynamics from such data, considerable progress has been made in the understanding of the mechanisms regulating the commitment to effector and memory lineages (Johnnidis et al. 2021; Kurd et al. 2020; Pace et al. 2018). The use of scRNAseq has drastically improved our knowledge on how exhaustion fits into the developmental program of T cell differentiation (Cerletti et al. 2020; Chen et al. 2019; Hudson et al. 2019; Yao et al. 2019) and how key modulators tailor the response to contain a persisting infection (Yao et al. 2021, 2019). Also, the tracking of individual cells *in vivo* has shown that the eliciting responses within the same host are remarkably heterogeneous, and the underlying stochastic pattern was observed for T cell responses against a variety of pathogens (Buchholz et al. 2013b; Cho et al. 2017; Gerlach et al. 2013; Grassmann et al. 2020; Kretschmer et al. 2020). The application of mathematical modelling on such data have discerned the developmental order of T cell responses (Buchholz

et al. 2013b; Cho et al. 2017; Kretschmer et al. 2020). Therefore, we use these highly informative single-cell responses to build a powerful investigative framework for determining the differentiation relationships between different cell populations when combined with mathematical models.

Inferring differentiation dynamics from single cells

We have studied the single-cell transcriptomes following two acute infections, a viral and bacterial one. Therefore, we have analysed tightly paced time points during the expansion phase of these two infections. Although the CD8⁺ T cell responses that were elicited from these two infections were separately investigated, the same subpopulations were found in both infection settings.

Furthermore, we performed dimensional reduction methods that relied on features related to the cell cycle and were thereby able to distinguish cycling (c) from non-cycling (nc) cells. This way, the proliferative status of a cell could be inferred and allowed us to investigate the mechanistic role of proliferation in the developmental path.

Strikingly, for both infections, the trajectory inference analyses revealed similar developmental patterns. For both infections, a proliferating subset of TCF1⁺CD62L⁺ MP cells formed the starting point of the developmental path. The MP subset gave rise to proliferating TCF1⁻CD62L⁻ progeny (EMP subset). The EMP cells gradually increased their expression of effector cytokines such as granzymes and perforins, and correlated with the increased expression of effector signature genes (*Klrg1* and *Cx3cr1*), marking the EFF subset.

Within these subsets of proliferating cells, we observed a developmental order previously described as the progressive model of differentiation: cMP → cEMP → cEFF.

However, when the cells transitioned from active proliferation to quiescence, each subset kept the phenotypic identity it had while it was still proliferating: cMP → ncMP, cEMP → ncEMP, cEFF → ncEFF.

At the later time points of the contraction phase, when the cells ceased to divide, the progressive differentiation pattern was repeated: ncMP → ncEMP → ncEFF.

The ncMP → ncEMP → ncEFF progression at a late time point was observed during the infection with LCMV Armstrong but not following the infection with *L.m.*-OVA. We speculate that this could pose a time-point related effect, caused by the intrinsic nature of the pathogen. Although the clearance of these two pathogens strongly depends on robust CD8⁺ T cell immunity, distinct pathogen replication kinetics as well as the route of inoculation could affect the time frame of the immune response (Dangi et al. 2020; Kernbauer et al. 2013). Also, a pathogen-unique cytokine milieu drives the responses towards these two pathogens (Curtsinger et al. 2010; Keppler et al. 2009) that influence the speed of recruitment and differentiation (Badovinac et al. 2007; Wherry et al. 2003a).

Nevertheless, we identified that until day 8 p.i., the responses to both these pathogens followed the equivalent developmental order, suggesting that the mechanisms on how CD8⁺ T cell differentiate are conserved.

The extended progressive model of CD8⁺ T cell differentiation

The developmental trajectories from the scRNAseq data were translated into a construct that served as a base for the mathematical modelling. The states in the model were defined by the distinct subsets, characterised by the expression profiles of TCF1 and CX3CR1 (and additional gene that hallmark memory and effector subsets). The transitions between the states were determined through the observed connectivities within these subsets and also included the arrest from the cell cycle.

Our results show that the extended progressive model of differentiation accurately reflects the total CD8⁺ T cell response. In addition, it correctly depicts the subset sizes, the correlation between the individual subsets as well as the modelled cell cycle drop out kinetics.

These results are in line with the proposed biological model of the decreasing developmental potential: A naïve CD8⁺ T cell that receives little stimulation differentiates into a memory cell, while those that receive cumulative stimuli differentiate into effector cells. In this setting a cumulative stimulation comprises of TCR signalling, co-stimulatory- and cytokine signals (Ahmed et al. 1996). The model proposed in this thesis adds to the decreasing potential model by including a quiescent state to each subset. Interestingly, EFF cells are identified as the population that arrested from cell cycle the latest. Their increased responsiveness to IL-2 signalling through the expression of CD25 impacts the proliferation of effector cells (Kretschmer et al. 2020) could hold them from dropping out of the cell cycle.

However, the picture that emerges from our analyses contradicts the effector-first model that proposes an opposite path of differentiation, in which CM cells originate from the EFF subset (Wherry et al. 2003b). Wherry and colleagues performed adoptive transfer experiments during the contraction and memory phase of the infection. In our analyses the EFF → EM → CM transition was not observed. The reasons resulting in these discrepancies remain unresolved.

Moreover, we have not investigated the importance of the first cell division to be asymmetric on the differentiation pattern during the expansion phase. So far, ACD has mainly been studied *in vitro* or *ex vivo* (Borsa et al. 2019; Chang et al. 2007), and it remains unclear to what extent the first cell division is asymmetric during an *in vivo* infection. These percentages are not inferable from the scRNAseq data. Therefore, such a question requires further mathematical investigation.

Comparison of the T cells kinetics following an acute and chronic viral infection

After having identified a mathematical model that explains the lineage paths of CD8⁺ T cells during two different kinds of acute infections, we tested if the same model is able to describe the responses within a chronic infection setting.

It is unlikely for a naïve CD8⁺ T cells to have a predetermined fate before the first encounter with antigen (Gerlach et al. 2010; Stemmerger et al. 2007). In addition, the increasing viral titres and the shift from a pro-inflammatory to an immunosuppressive milieu at the onset of a

persisting infection, drive the progressive exhaustion of CD8⁺ T cells (Wherry et al. 2003b).

We, therefore, assumed that the initial phase of the CD8⁺ T cell differentiation in developing chronic conditions must be similar to those during acute infections. Thus, the immune response would follow a normal differentiation pathway in the first stages of the chronic infection. External influences, such as the persistence of the antigen, interfere with the canonical differentiation path and induce T cell exhaustion. This theory would support of the arrested model of T cell exhaustion, where T cells would deviate from the normal pathway of differentiation and become incapacitated (Henning et al. 2018).

At first, we aimed to compare the gross differences between the two infections of LCMV Armstrong and clone 13 without discriminating the exhausted from the non-exhausted subsets.

Therefore, the subsets were defined by their expression of TCF1, Tim3 and CX3CR1.

The use of the same phenotypic markers allowed us to quantitatively compare the responses by simultaneously fitting LCMV Armstrong and clone 13-derived progenies to the extended progressive differentiation model. Through systematic forward selection, we identified the parameters that were common to both infections and those that differed in the immune response to LCMV clone 13.

The recruitment rate of a naïve cell to the TCF1⁺ subset was described using the same parameter for both infections. This finding is rather surprising because LCMV clone 13 is transmitted i.v. and uses a higher infectious dose, suggesting a higher transmission rate and faster systemic spread compared to the i.p.-inoculated LCMV Armstrong. Furthermore, it is supported by the study that compared the viral loads at 24 h following the infections and found higher viraemia in the spleen of LCMV clone 13 infected mice (Snell et al. 2018).

The same recruitment rate could be attributed to the properties of the model topology. The waiting time for recruitment rate in this model follows a gamma-distribution. This long-tailed distribution is required to explain the large variability in the total response to the infection with LCMV Armstrong (a waiting time for the recruitment that is exponentially distributed does not describe the data, data not shown). However, if the clone 13 data is fitted separately to the extended model of progressive differentiation the recruitment parameter unique to the LCMV clone 13 infection (data not shown) lies within the confidence bounds of the shared parameter. The transition rate between TCF1⁺ \rightarrow Tim3⁺CX3CR1^{low} and the rate at which cells drop out of cell cycle were as well described by the same parameters. The latter indicates that cell-intrinsic processes regulate cell cycle exit. Division cessation is suggested to be governed by the expression of c-myc and the phosphorylation state of Rb (Gookin et al. 2017). Therefore, it seems to be independent of the infection-causing pathogen.

The proliferation parameters were informed from the cell cycle speed measurements. Even though the ratios between the cell cycle speed of the TCF1⁺ and TCF1⁻ subsets were comparable in both infections, distinct parameters were required to account for the disparity in the fate-mapping data. This indicates that next to division cessation, during the time window of the expansion, proliferation is substantially different between the two infections, supported through

the significantly distinct cell division speeds on day 6.

As already described in the literature, during LCMV clone 13 infection, a KLRG1⁺ and CX3CR1⁺ EFF cannot be formed (Wherry et al. 2007). Our model predicts that the transition rate that propagates the formation of CX3CR1^{high} cells is forty times lower in the infection with clone 13 than in the infection with LCMV Armstrong. Hence, the TCF1⁻CX3CR1^{low} \rightarrow CX3CR1^{high} transitions occur rarely. Limiting the development of functional EFF cells during a persisting infection constitutes a protection mechanism to prevent cell-induced tissue destruction. It has also been shown that the accumulated expression of TOX in the TCF1⁺ subset during a persisting infection minimises further diversification into cytolytic effector subsets (Alfei et al. 2019; Khan et al. 2019; Yao et al. 2019).

In addition, the high expression of inhibitory receptors, manipulating cell cycle progression, further retrain the proliferation-linked differentiation (Sharpe et al. 2018; Waterhouse et al. 1995). This is supported by the model, predicting distinct division drop out times between the two infections. We will discuss the effect of division cessation in detail in section 5.3.

To our knowledge, the modelling introduced in this thesis is the first to describe the CD8⁺ T cell response to acute and chronic LCMV infection, driven by single-cell data and without relying on any assumptions of extrinsic signals.

From a modelling point of view

Many mathematical frameworks exist that describe the diversification of lymphocytes during T cell expansion (Crauste et al. 2017; Ganusov 2007; Gossel et al. 2017; Pandit et al. 2019). However, most of these models require additional parameters to account for the cytokine environment, the pathogen replication kinetics, proliferation and cell death (Crauste et al. 2017; Gossel et al. 2017; Pandit et al. 2019). Some of them were solely applied on the total number of cells without information on the subpopulations (Ganusov 2007).

Other studies have also concentrated on dissecting the mechanisms of T cell exhaustion. These studies have applied mathematical modelling to characterise the immune responses towards these two infections and heavily relied on population data as well, did not further explore the relationship between the different subsets (Althaus et al. 2007; Bocharov 1998; Bolouri et al. 2020).

The study by Althaus and colleagues was limited by the unknown initial precursor frequency, which had to be estimated through combining the activation parameter with the precursor size. Bolouri et al. 2020 investigated the molecular network during the development of exhaustion, including transcription factor interactions and antigen stimulation. While experimental data informed the underlying network (serving as a construct for the model topology), the outcomes stem from model simulations without fitting to data.

A mathematical model that includes the effects of global and internal factors to describe the outcome is complex and comprises numerous parameters, representing the interactions between the virus, immune cells, and cytokines and even transcription factor networks (Baral et al. 2019;

Bocharov 1998; Bolouri et al. 2020).

The mathematical modelling we present in this thesis is independent on any intrinsic or extrinsic cues, such as the pathogen replication or cytokine signalling and merely relies on the sizes of the subsets, their relative fractions, the total number of cycling cells and the proliferation rate. Furthermore, since we only model the expansion phase of the infection, we simplified the model by neglecting the role of cell death. This poses a valid assumption, a study using an apoptosis-reporter system has shown that the impact of cell death during the expansion phase is marginal (Garrod et al. 2012).

Also, the type of data that we use for fitting is much richer in information as compared to the above mentioned studies. In addition to the mean, the variances and co-variances of the response are determined. In contrast, the variance and co-variance cannot be extracted from population-derived responses because the bulk transfer of cells averages over the response, emerging from each single cell.

This model contributes to the understanding on how the different population of memory and effectors cells emerge during the expansion phase of infection and how subset-specific proliferations and division cessation result in the magnitude of heterogeneity.

5.3. Cell cycle quiescence dictates the course of T cell exhaustion

The processes leading to T cell exhaustion occur in an hierarchical manner. The loss of effector functions, the IL-2 production and a decreased proliferative capacity are among the features that are observed during the early stages of exhaustion. However, these are processes that happen as well during canonical differentiation. Here, we observed that already early during the expansion phase of the infection, the cells can become quiescent. Whereas in the clone 13 infection, division drop out occurs earlier and is probably driven by the different inflammation and the increased expression of inhibitory receptors.

Inhibitory receptors regulate cell cycle activity

Mathematical analysis of the response to the acute LCMV infection, using the extended progressive model of differentiation, predicted that cell cycle drop out commences before the peak of the response is reached, with roughly 60% of the cells remaining in the cell cycle at day 6 p.i. Interestingly, at this time point during infection with the persisting LCMV variant, only 40% actively divided.

During acute infection, the exit out from the cell cycle might be mediated through the decreasing viral loads upon resolution of the infection. It is accompanied by alterations in the inflammatory environment and the increasing apoptotic signals (Pucci et al. 2003; Schluns et al. 2003). In contrast, during a chronic infection, the expression of inhibitory receptors play a crucial role in regulating the proliferation activity.

Several inhibitory receptors have been implicated to control and inhibit cell cycle activities. For example, in comparison to the infection with LCMV Armstrong, *Pdcd1* was differentially up-regulated at day 4.5 in the cells stemming from the infection with LCMV clone 13. Even though PD1 expression is transient in the acute infection (Ahn et al. 2018), under persisting conditions, its expression levels remain high with strong inhibitory consequences. The interaction of PD1 with its ligands (PDL1 or PDL2) forms a control mechanism that blocks proliferation under persistent antigen stimulation. By acting downstream of the TCR and CD28 signalling, PD1 regulates the cell cycle activity and, inhibits the mammalian target of rapamycin (mTOR) and c-Myc (Barber et al. 2006; Sharpe et al. 2018). While the inhibition of mTOR has been described to block the G1-phase progression, the levels of expressed c-Myc regulate the cell cycle exit: c-Myc values below a certain threshold promote cell cycle quiescence (Heinzel et al. 2017).

Next to PD1, *Lag3* and *Batf* were as well differentially expressed in the cells from the LCMV clone 13 infection at day 4.5. While Lag3 blocks proliferation and cytokine production through cross-linkage with CD3 (Waterhouse et al. 1995), Batf signalling up-regulates CTLA4 expression that blocks IL-2 pathways (Parry et al. 2004; Quigley et al. 2010).

Our findings suggest that many inhibitory receptors interplay very early during the onset of chronic infection and regulate cell division at different levels.

Interestingly, the TCF1⁺ subset was the first one affected from the cell cycle drop out, with a significant fraction of cells being quiescent at day 6 p.i. (40 % quiescence in the LCMV Armstrong infection and 70 % in the infection with the clone 13 variant). We speculate, that the immune system locks these cells in the quiescent state early in the infection to avoid full differentiation into other subsets, to thereby ensure the maintenance of their pool when the antigen is gone. This speculation finds support in our RNA velocity analyses where further differentiation is only observed again during the phases of late contraction and the mathematical modelling, that does not support differentiation within the quiescent states. However, follow on investigation is required to back this hypothesis.

Furthermore, one of the top differentially expressed genes at day 4.5 p.i. with LCMV clone 13 was TOX. TOX is required for the generation and the maintenance of this subset and its induction has been described to be dependent on NFAT (Khan et al. 2019; Scott et al. 2019). Interestingly, NFAT has been implicated in influencing the cell cycle activity probably through its involvement in promoting exhaustion by playing a crucial role in the regulation of PD1, CTLA4 and also Tim3 (Martinez et al. 2015; Oestreich et al. 2008). Additionally, it has been described that TOX is responsible for the maintenance of high PD1 levels (Wang et al. 2019). Several studies showed that on a proliferation level CD8⁺ T cells deficient of TOX and TOX-competent counterparts during the clone 13 infection were similar (Alfei et al. 2019; Khan et al. 2019; Scott et al. 2019). These studies employed dye-dilution methods to compare cell division at early time points before the peak or measured the 5-Ethynyl-2'-deoxyuridine (EdU) incorporation (integrates into the DNA similar to BrdU) and the Ki67 expression for time points after the peak response (Alfei et al. 2019; Khan et al. 2019; Scott et al. 2019). While division

cessation cannot be extracted directly from dye-dilution and/or BrdU/EdU measurements, Ki67 is commonly used to distinguish between cycling and non-cycling cells. However, the long lag time of Ki67 down-regulation might mask subtle differences occurring at these time points (Gossel et al. 2017). Thus, only measurements of c-Myc or p-Rb would reliably identify the quiescent subsets of these cells.

Furthermore, it was recently found, that TOX directly inhibits mTOR in colorectal cancer cells, and thereby also the cell cycle progression (Yang et al. 2021). However, if these findings also mimic the mode of action of TOX in activated T cells requires further research.

Summarising, there are implications on how TOX expression could regulate cell division. However, its role in the intricate network of inhibitory receptors, antigenic stimulus and cytokine environment regulating division drop out is incompletely understood.

We also observed that CX3CR1⁺ (or EFF) subsets cycled longer before they returned to the quiescent state. A possible explanation could be that a faster cell cycle progression prevents premature division cessation.

5.4. The fate of the CD8⁺ T cells from early time points of persisting infection remains plastic

TCF1⁺ MEX and memory (or MP) CD8⁺ T cells have a shared transcriptional profile, attributing the MEX subset to sustain the pool of exhausted cells through their ability to self-renew (Chen et al. 2019; He et al. 2016; Hudson et al. 2019; Im et al. 2016; Utzschneider et al. 2016a, 2020). However, their epigenetic landscapes are significantly different, suggesting an antigen-driven transcriptional regulation that results in the production of exclusively exhausted progeny (Ghoneim et al. 2017; Jadhav et al. 2019; Pauken et al. 2016; Sen et al. 2016).

However, the mechanisms leading to the formation of precursor cells during chronic infection remain an open question.

Before the exhaustion fate is sealed

Despite the retained proliferative capacity and the ability to self-renew, the progeny that is propagated from the MEX subset retains the exhaustion imprint (Pritykin et al. 2021; Utzschneider et al. 2016a, 2020).

In this thesis, we show that the fate of TCF1⁺ CD8⁺ T cells from the onset of a persisting infection is reverted upon transfer into an ongoing acute infection. Moreover, TCF1⁻ CD8⁺ T cells can as well be rescued from their exhaustion imprint when changing from persisting to resolving infection conditions. Both of these subpopulations followed the canonical differentiation path and down-regulated the expression of TOX and PD1 upon transfer into an acute infection. However, when the cells were transferred into the same chronic environment, PD1 and TOX expression remained high and the formation of an EFF subset was limited.

In contrast to the current picture that suggests a unique epigenetic profiling to counteract the rescue from the exhaustion imprint (Ghoneim et al. 2017; Jadhav et al. 2019; Pauken et al. 2016; Sen et al. 2016). However, these studies investigated MEX subset cells at late stages of the chronic infection.

A recent study by Utzschneider and colleagues investigated at early time points of infection the plasticity of the MEX precursor (and non-MEX precursors) subset and detected that both subsets remained high in their expression of TOX upon re-transfer into an LCMV Armstrong infection, resulting as a consequence of their imprinted epigenetic landscape (Utzschneider et al. 2020).

However, in their investigation Utzschneider et al. 2020 used the LCMV docile infection. The LCMV docile variant replicates faster than clone 13, and additionally causes a life-long persisting infection, while the clone 13 strain is cleared in the mouse after approximately two months (Moskophidis et al. 1995).

It is therefore possible, that in the LCMV docile infection model the exhaustion is further progressed and that these MEX precursor resemble MEX cells from later stages, where the imprint of exhaustion is fixed (Pritykin et al. 2021). Along with this, also the developmental flexibility is lost, preventing the reversion to the canonical path of differentiation.

Non-peer reviewed observations from the Oxenius and Claassen laboratories showed that the re-transfer of the TCF1⁺ subset from the wild-type LCMV clone 13 infection into LCMV clone 13 P14-escape mutant infected hosts, did not develop exhausted progeny (Cerletti et al. 2020).

The LCMV clone 13 escape mutant used in their study has alterations in the gp33 epitope, making it unrecognisable to P14 T cells, yet resulting in the same inflammatory environment as the wild-type clone 13 strain. They suggest that a continuous TCR stimulations is required to drive exhaustion and that differentiation is halted when the stimuli is removed (Cerletti et al. 2020). While their findings concerning the presence of antigen are in line with the observations from Utzschneider et al. 2020, Cerletti and colleagues did not examine other attributes to account for an exhausted phenotype, such as the expression of inhibitory receptors.

It was shown that during the acute infection antigen levels are declining around day 5 (this is the time point at which the transfer experiments by Utzschneider and Cerletti were performed) (Moskophidis et al. 1995; Wherry et al. 2003a). In comparison to our results, that were obtained upon re-transfer into the setting of the LCMV Armstrong infection setting, the full differentiation was observed in spite of antigen presence. Although, the abundance of the antigen regulates the chances of its encounter, implicating that a certain threshold level of stimulation is required to drive exhaustion.

Thus, at early time points of infection the fate of the subsets are flexible, suggesting that the initial molecular pathways are conserved between the two infection settings.

5.5. The arrested model of T cell exhaustion

T cell exhaustion is considered a parallel programme to the normal T cell differentiation, which can occur at any stage of development. As a result, the arrested model of differentiation proposes that exhausted T cells arise from memory and effector T cells that have branched from the normal differentiation pathway before progressing to a terminal EFF cell stage (TEF). Multiple branching points within the canonical differentiation pathway can thus lead to the exhausted counterpart, reflecting the large heterogeneity of the exhausted T cell pool (Henning et al. 2018).

Exhausted progeny originates from the MP and non-MP subsets

Many studies have concentrated on dissecting the developmental relationships of exhausted T cell subsets. While there is large consensus on the developmental order within the exhausted subsets, suggesting a propagation of the exhausted progenies originating from TCF1⁺ MEX progenitor cell (Alfei et al. 2019; Chen et al. 2019; He et al. 2016; Hudson et al. 2019; Im et al. 2016; Utzschneider et al. 2016a, 2020), the origin of exhausted progenitor cells remains unclear.

In the joint RNA velocity analyses, where we examined the differentiation of cells during acute and chronic infections, we observed two endpoints of settling in an exhausted state, marked by the two subsets of exhausted cells, MEX and TEX. While the initial branch arose from the TCF1⁺ subset ended in the cluster containing the MEX cells, the other branch was directed through an effector-like cluster to the TEX cluster. Interestingly, the source that fed the exhausted progenies co-localised with the cells fuelling the functional subsets, suggesting that at the onset of a persisting infection the progression is initiated towards a functional phenotype. This is in line with the afore-discussed flexibility in the developmental fates and the arrested model of T cell exhaustion.

We performed mathematical modelling, taking the arrested model of T cell exhaustion as blueprint for the model structure.

The facts that the parametrisation of the model relied on scarce data, rendered the model unidentifiable. Nevertheless, it predicted that the individual exhaustion of the MP subset is insufficient to drive the exhausted T cell pool. Instead, the independent exhaustion of the non-MP subset is required. This prediction was experimentally validated.

Our results are in consent with the current picture, that exhaustion is driven through the exhaustion of MP cells, leading to MEX precursors (Alfei et al. 2019; Utzschneider et al. 2020). Additionally, the EFF subset is prevented from exhaustion due to their terminal differentiation state (Angelosanto et al. 2012). Moreover, we add to this picture of the exhaustion program by showing that EE subset cells exhaust separately, as suggested in the arrested model of T cell exhaustion.

5.6. Significance

Viral infections can lead to various outcomes. They can be acute with a short-term illness, become chronic and sometimes co-exist as a latent infection or cause significant damage to the immune system and tissue. T cell immunity has a significant role in protecting against viral infection and in determining their outcome. Therefore, understanding the mechanisms that lead to the failure of a viral clearance is essential for finding ways to prevent it.

In this study, we have examined the lineage relationships of CD8⁺ T cells using the mouse models of acute and chronic lymphocytic choriomeningitis virus infection. We show that the CD8⁺ T cell development follows a core motif that is conserved among different infectious diseases. Alterations in the environmental conditions, such as antigen persistence and immunosuppressive cytokine milieu, mediate branching from the canonical differentiation path, rendering the T cells incapacitated. These results provide important insights into the differentiation hierarchy during the onset of persisting infections and offer novel opportunities to identify interventions to prevent such diseases.

6. Materials and Methods

6.1. Materials

All materials, reagents and equipment used in this thesis are listed in alphabetical order in the Tables 6.1, 6.2 and 6.3. Antibodies and primers are summarised in the Tables 6.4, 6.5 and 6.6. All antibodies used in this study are directed towards mouse epitopes and were titrated to optimal dilutions for the use in flow cytometry stainings.

Table 6.1.: List of experimental equipment used in this study.

Device	Model	Manufacturer
analytical balance	ACJ/ACS	Kern & Sohn GmbH
biosafety cabinets	HSL 12	Heraeus
centrifuges	Megastar 3.0R	VWR
	Fresco 21 Microcentrifuge	Thermo Fisher Scientific
flow cytometer	CytoFlex LX	Beckman Coulter
	MoFlow XPD	Beckman Coulter
	MoFlow Astrios EQ	Beckman Coulter
	Aria III Sorter	BD Bioscience
GEM generator	Chromium Controller	10x Genomics
hemocytometer	Neubauer	Superior Marienfeld
incubator	Heracell 240i CO ₂ Incubator	Thermo Fisher Scientific
microscope	Axiovert S100	Carl Zeiss
pH-Meter	766 Calimatic	Knick
photometer	BioPhotometer	Eppendorf
QC & quantification	Bioanalyzer	Agilent
	QuBit 4.0 Fluorometer	Thermo Fisher Scientific
sequencer	NovaSeq 6000 S2	Illumina
thermal cycler	Biometra TAdvanced 96S	Analytik Jena
thermoblock	Thermomixer C	Eppendorf
vortex mixer	Vortex Genie 2	VWR
water bath	1003	GFL

Table 6.2.: List of chemical compounds and reagents used in this study.

Compound	Manufacturer
Ammonium chloride (NH ₄ Cl)	Roth
Ampure XP beads	Beckman Coulter
Brain heart infusion medium	TUM
Brain heart infusion agar plates	TUM
Bovine serum albumine	Sigma
Bromodeoxyuridine	Sigma
Buffer EB	Qiagen
Chromium Chip B Single Cell Kit	10x Genomics
Chromium i7 Multiplex Kit	10x Genomics
Chromium Single Cell 3'Reagent Kit v3	10x Genomics
Dimethyl sulfoxide	Sigma
DNAse I	Sigma
Ethanol	Merck
Fetal Calf Serum	Biochrome
FITC BrdU Flow Kit	BD Bioscience
Foxp3/Transcription Factor Staining Buffer Set	eBioscience
Gentamicin	Gibco
L-glutamine	Gibco
Glycerol	Merck
Heparin-Sodium-25000	RatiophArmstrong
HEPES	Roth
High Sensitivity DNA Kit	Agilent
Hydrochloric acid	Roth
KAPA Hifi Master Mix	Roche
Low TE buffer	Thermo Fisher Scientific
β-mercaptoethanol	Gibco
nuclease-free water	Thermo Fisher Scientific
Paraformaldehyde	Sigma
Penicilline/Streptomycin	Gibco
Phosphate buffered saline	Gibco

Continued on next page

Table 6.2 – *Continued from previous page*

Compound	Manufacturer
Propodium Iodide	Thermo Fisher Scientific
Qubit dsDNA HS Assay Kit	Gibco
RPMI-1640	PAA
Transcription Factor Phospho Buffer Set	BD Bioscience
Tris-Hydroxychloride (Tris-HCl)	Roth
Triton-X	Roth
Trypan blue	Roth
Trypsin-EDTA	Gibco
Tween-20	Bio-Rad
Zombie UV TM Fixable Viability Kit	Biolegend

Table 6.3.: List of buffers and media used in this study.

Buffer	Composition
ACT solution	0.17 M NH ₄ Cl 0.3 M Tris-HCl, pH 7.5
cell culture medium	500 mL RPMI-1640 10 % (v/v) FCS 5 % (v/v) SC ⁺
flow cytometry buffer	500 mL PBS, pH 7.5 0.5 % (w/v) BSA 2 mM EDTA
SC ⁺ medium	1 mL β-mercaptoethanol 10 mL Gentamicin 11.9 g HEPES 2 g L-Glutamine 100 mL Penicillin/Streptomycin

Table 6.4.: List of antibodies used for analyses by flow cytometry.

Antibody	Label	Clone	Provider
α CD4	APC-Cy7	GK1.5	Biolegend
	PE/Dazzle	GK1.5	Biolegend
α CD8a	BV510	53-6.7	Biolegend
	Pacific Blue	53-6.7	Biolegend
	Pacific Orange	5H10	Life Technologies
α CD16/CD32	unlabelled	93	Biolegend
α CD19	APC-Cy7	6D5	Biolegend
	PE/Dazzle	6D5	Biolegend
α CD25	APC	PC61.5	Life Technologies
α CD27	BV421	LG.3A10	Biolegend
	PE/Cy7	LG.7F9	Life Technologies
α CD44	APC	IM7	Biolegend
	FITC	IM7	Biolegend
α CD45.1	BV785	A20	Biolegend
	FITC	A20	Biolegend
	Pacific Blue	A20	Biolegend
α CD45.2	BV650	102	Biolegend
α CD62L	BV421	MEL-14	Biolegend
	APC	MEL-14	Biolegend
α CD200	APC	OX-90	Biolegend
α CX3CR1	BV785	SAO11F11	Biolegend
	PE/Cy7	SAO11F11	Biolegend
α KLRG1	PE/Cy7	2F1	Biolegend
α OX-40	BV421	OX-86	Biolegend
α PD-1 (CD279)	BV510	29F.1A12.7	Biolegend
α p-Rb(Y807/811)	PE	D20B12	Cell Signaling
α TCF-7/TCF-1	BV421	S33-966	BD Bioscience
	PE	S33-966	BD Bioscience
α Thy1.1	FITC	HIS51	Life Technologies
	eF450	HIS51	Life Technologies
α Thy1.2	BV785	H30-H12	Biolegend
α Tim-3 (CD366)	APC	RTM3-23	Biolegend
	BV421	RTM3-23	Biolegend
α TOX	PE	TXRX10	Life Technologies

Table 6.5.: List of oligonucleotide-conjugated antibodies used for protein expression analyses in combination with scRNA-seq.

Antibody	Label	Clone	Provider
α CD27	CAAGGTATGTCACTG	LGA.3A10	Biologend
α CD62L	TGGGCCTAAGTCATC	MEL-14	Biologend
α CD127 (IL7R)	GTGTGAGGCACTCTT	A7R34	Biologend
α CX3CR1	CACTCTCAGTCCTAT	SAO11F11	Biologend
Hashtag 1	ACCCACCAGTAAGAC	M1/42,30-F12	Biologend
Hashtag 2	GGTGCAGAGCATTCA	M1/42,30-F12	Biologend

Table 6.6.: List of primers used in this study.

Name	Sequence
ADT additive primer 0.2 μ M	5' CCTTGGCACCCGAGAATT*C*C 3'
D702_s	5' CAAGCAGAAGACGGCATAACGAGATTCTCCG- GAGTGACTGGAGTTCAGACGTGTGCTCTTC- CGAT*C*T 3'
D703_s	5' CAAGCAGAAGACGGCATAACGAGATAAT- GAGCGGTGACTGGAGTTCAGACGTGT- GCTCTTCCGAT*C*T 3'
D704_s	5' CAAGCAGAAGACGGCATAACGAGATG- GAATCTCGTGACTGGAGTTCAGACGTGT- GCTCTTCCGAT*C*T 3'
D705_s	5' CAAGCAGAAGACGGCATAACGAGATTTCT- GAATGTGACTGGAGTTCAGACGTGTGCTCTTC- CGAT*C*T 3'
D706_s	5' CAAGCAGAAGACGGCATAACGAGATAC- GAATTCGTGACTGGAGTTCAGACGTGT- GCTCTTCCGAT*C*T 3'
HTO additive primer 0.2 μ M	5' GTGACTGGAGTTCAGACGTGTGCTCTTCC- GAT*C*T 3'
RPI2	5' CAAGCAGAAGACGGCATAACGAGATA- CATCGGTGACTGGAGTTCCTTGGCACCCGA- GAATTC*C*A 3'
RPI3	5' CAAGCAGAAGACGGCATAACGAGATGCC- TAAGTGACTGGAGTTCCTTGGCACCCGA- GAATTC*C*A 3'
RPI4	5' CAAGCAGAAGACGGCATAACGAGATTG- GTCAGTGACTGGAGTTCCTTGGCACCCGA- GAATTC*C*A 3'
SI-PCR primer	5' AATGATACGGCGACCACCGAGATCTA- CACTCTTCCCTACACGACGC*T*C 3'

* indicate phosphorylated bonds.

6.2. Experimental Methods

6.2.1. Mice

Female C57BL/6 wild-type mice were purchased from Envigo (Germany) and housed in individually ventilated cages under specific pathogen free conditions at the animal facility at the Technische Universität München. Rag1^{-/-} OTI-transgenic T cells recognizing the SIINFEKL peptide as well as P14-transgenic C57BL/6 mice expressing a T cell receptor specific for the LCMV gp33-41 peptide were crossed to C57BL/6 mice that express distinct combinations of the congenic markers CD45.1, CD45.2, Thy1.1 and Thy1.2 and held in-house under specific pathogen free conditions. Wild-type C57BL/6 mice entered the experiments at 6 to 8 weeks of age, OTI T cell-transgenic and P14 T cell-transgenic female mice were used at an age of 6 to 20 weeks. All animal experiments were performed in accordance with the ethics committee and approved by the Regierung von Oberbayern in Germany.

6.2.2. Infections with LCMV

Viral stocks for LCMV Armstrong and LCMV clone 13 were generated in-house and kept in frozen vials at -80°C . The LCMV stocks were thawed on ice and diluted in PBS to a final infectious concentration of 2×10^5 phage forming units (pfu) for LCMV Armstrong and 2×10^5 pfu for LCMV clone 13. LCMV Armstrong was administered intraperitoneally (i.p.), LCMV clone 13 intravenously (i.v.) by tail vein injection. Both infections were performed using a 26-gauge needle (BD Plastipak 1 mL Sub-Q).

6.2.3. Infections with *L.m.-OVA*

The infections with OVA-expressing *Listeria monocytogenes* species (*L.m.-OVA*) were performed as previously described in Buchholz et al. 2013a. In brief, frozen glycerol cultures of recombinant *L.m.-OVA* were stored at -80°C , thawed at room temperature and 12.5 μL of the liquid culture were incubated for 4 h in 4 mL brain-heart-infusion (BHI) medium in a shaking incubator at 37°C and with 90 rpm. After a 4 h incubation, the optical density at 600 nm ($\text{OD}_{600\text{nm}}$) of the culture was measured using a photometer. When an $\text{OD}_{600\text{nm}}$ between 0.05 and 0.1 was reached, the number of colony forming units (cfu) was determined by $\# \text{ cfu/ml} = 1.1 \times 10^9 \text{OD}_{600\text{nm}}$. The culture was then serially diluted in PBS to a final dose of 5×10^3 cfu in 200 μL . The infections dose was verified by colony counting after plating 20 μL on BHI agar plates and incubating over night at 37°C . *L.m.-OVA* were administered i.v. using a 26-gauge needle (BD Plastipak 1 mL Sub-Q).

6.2.4. Infections with MVA-OVA

Ready-to-infect MVA-OVA aliquots containing 2×10^8 PFU were a generous gift from Andreas Muschaweckh from the Korn laboratory (Institute for Experimental Neuroimmunology at the

Technical University of Munich). Each mouse received a dose of 200 μL 2×10^8 PFU MVA-OVA one day after the adoptive transfer of OTI T cells. For the infection a 26-gauge needle (BD Plastipak 1 mL Sub-Q) was used.

6.2.5. Purification of T cells from the blood

For blood sample collection, the vena facialis was punctured with a lancet and 100-200 μL blood was directly collected in 1.5 mL Eppendorf tubes containing 20 μL Heparin. The blood samples were transferred into 15 mL Falcon tubes, diluted in ACT solution for erythrocyte lysis to a final volume of 10 mL and incubated at room temperature for 10 min. After centrifugation at 1500 rpm at room temperature (VWR Megastar 3.0R), the supernatant was discarded and the pellet was re-suspended in 5 mL ACT solution. After a second incubation for 5 min, the lysis was stopped by the addition of 5 mL cell culture medium and the samples was centrifuged at 1500 rpm at room temperature for 6 min. The supernatant was discarded and the pellet re-suspended in flow cytometry buffer.

6.2.6. Purification of T cells from the spleen and lymph nodes

The spleen and the cervical, axillary, cubital, mesenteric, inguinal and popliteal lymph nodes were harvested from sacrificed mice and collected in 5 mL cell culture medium. Using a syringe stamp, the tissue was mechanically disrupted and pressed through a 70 μm cell strainer (Falcon). The single-cell suspension was centrifuged at 1500 rpm at 4 $^{\circ}\text{C}$ for 6 min and the supernatant was discarded. For the removal of the remaining erythrocytes, the cell pellets were re-suspended in 3 mL ACT solution and incubated for 3 min at room temperature. The further erythrocyte lysis was blocked by the addition of 7 mL cell culture medium. After centrifugation (1500 rpm, 4 $^{\circ}\text{C}$, 6 min) the cells were collected, counted using a Neubauer hemocytometer and diluted to 1×10^7 cells per 100 μL flow cytometry buffer.

6.2.7. Adoptive T cell transfers

Naïve $\text{CD8}^+\text{CD44}^{\text{low}}$ P14-transgenic T cells from the peripheral blood or from the spleen were purified to $> 99\%$ by flow cytometric cell sorting. After isolation of the leukocytes from the blood or spleen (as described in section 6.2.5 and 6.2.6), the cells were stained with CD44-FITC and CD8-eF450 for 30 min on ice in the dark. The cells were then washed 2.5 times and re-suspended in flow cytometry buffer and filtered through a 30 μm syringe filter (BD Bioscience). For the exclusion of dead cells, propidium iodide (PI) was added immediately before sorting. 1×10^3 , 1×10^4 or 5×10^4 P14-transgenic cells were sorted into V-bottom plates (VWR), containing 5×10^5 wild-type C57BL/6 splenocytes in 200 μL fetal calf serum (FCS). The purified naïve P14 T cells were adoptively transferred into naïve C57BL/6 hosts via i.p.-injection on day prior to infection.

6.2.8. Cell surface staining for flow cytometry

For the staining of surface epitopes, 1×10^7 leukocytes were collected in 96- well V-bottom plates. If not stated differently, all steps were performed on ice using ice cold flow cytometry medium, and with centrifugation at 1500 rpm at 4 °C for 3 min. To block unspecific binding sites, α CD16/CD32 antibodies (Fc-block) were incubated with fixable viability dye for 20 min. The cells were washed 1.5 times before addition of the cell surface staining mix. The cell surface staining was performed for 30 min in flow cytometry buffer, containing the appropriate dilution of a combination of the antibodies listed in Table 6.4 The cells were then washed 2.5 times and either fixed in 1 % PFA in PBS for 20 min, filtered and analysed by flow cytometry, or intracellular staining steps were performed.

6.2.9. Intracellular staining of transcription factors

The intracellular staining was performed after the surface staining using the Foxp3/Transcription Factor Staining Kit according to manufacturer's instructions. The cells were stained for 45 min at 4 °C using a combination of the intracellular antibodies listed in Table 6.4. After filtration and re-suspension in flow cytometry buffer, cells were acquired by flow cytometry.

6.2.10. Intracellular staining of phosphorylated proteins and transcription factors

The staining of phosphorylated proteins in combinations with transcription factors was performed using the Transcription Factor Phospho Buffer Set. After the surface staining, the cells were fixed according to manufacturer's instructions and incubated over night at 4 °C. After the intracellular staining, the cells were filtered and the retinoblastoma protein signal was measured by flow cytometry.

6.2.11. BrdU staining for cell cycle phase quantification

Mice received a single dose of bromodeoxyuridine (BrdU, 1 mg/mL) i.p. 3 h respectively 0.5 h before end point analysis. For BrdU analysis, cells were first stained with surface markers and transcriptions factors as indicated in the sections 6.2.8 and 6.2.9, then stained and fixed according to the BrdU FITC Flow Kit protocol. To stain for total DNA content, the cells were filtered and 20 μ L 7AAD was added to 180 μ L cell suspension in flow cytometry buffer. After an incubation period of 20 min at 4 °C the samples were directly measured by flow cytometry. Apoptotic and sub-G1 cells were excluded from the analysis.

6.2.12. Single-cell fate-mapping

The single-cell fate-mapping experiments were performed by Lorenz Kretschmer and Dr. med. Veit Buchholz at the Institute for Medical Microbiology, Immunology and Hygiene at the Technical University Munich. For the fate-mapping experiments, a matrix of single congenic P14-

transgenic T cells was adoptively transferred into naïve C57BL/6 female hosts that were infected with LCMV Armstrong or clone 13 the next day. At day 8 post infection, the P14 T cells in the spleen were analysed by flow cytometry.

6.2.13. Re-transfer experiments

The experiments where functional subsets were re-transfer into time-point or infection-matched mice were conducted by Lorenz Kretschmer and Dr. med. Veit Buchholz at the Institute for Medical Microbiology, Immunology and Hygiene at the Technical University Munich.

Frozen spleen samples from *TCF7-GFP*-reporter P14 transgenic wild-type mice were generously provided by Prof. Dr. med. Dietmar Zehn (Division of Animal Physiology and Immunology at the Technical University Munich, mice were generated as described in (Utzschneider et al. 2016a)). The frozen spleens were thawed, re-suspended in culture medium and prepared for flow cytometric sorting as described in section 6.2.7 except that CD44-APC was used to determine the naïve *TCF7-GFP*-reporter P14 T cells.

One day prior to the infection with LCMV Armstrong or clone 13, the naïve *TCF7-GFP*-reporter P14 T cells were transferred into wild-type C57BL/6 mice. At day 4.5 after infection with LCMV Armstrong or clone 13, adoptively transferred *TCF7-GFP*-reporter P14 T cells were re-isolated, purified and enriched based on their expression of *TCF7-GFP* by flow cytometric sorting and re-transferred into infection-matched or time-point matched hosts (LCMV clone 13 derived into LCMV Armstrong transferred or transfer from LCMV clone 13 to LCMV clone 13). The final readout was performed by flow cytometry at day 8 after infection.

For the re-transfer experiments from LCMV Armstrong infected mice into Armstrong or clone 13 infected, naïve *TCF7-GFP*-reporter P14 T cells were adoptively transferred into wild-type C57BL/6 mice and infected with LCMV Armstrong the next day. On day 8 p.i. P14 T cells were isolated from the spleens and sorted by flow cytometry based on the expression on *TCF7* and KLRG1. *TCF7*⁺KLRG1⁻, *TCF7*⁻KLRG1⁻ and *TCF7*⁻KLRG1⁺ subsets were sorted and re-transferred into recipients that were infected 4.5 days before with either LCMV Armstrong or clone 13. Exactly 3.5 days after re-transfer, the progeny of the subsets in the spleens was analysed by flow cytometry.

6.2.14. Analysis of flow cytometry data

The measurements performed by flow cytometry were analysed by the CyExpert software v2.4 (Beckman Coulter) and FlowJo v10 (Treestar).

6.2.15. Re-isolation of T cell populations for single cell RNA sequencing

At day 6 post infection (p.i.) with LCMV Armstrong or LCMV clone13 or at day 4.5, 8 and 12 p.i. with L.m.OVA, the spleen and the lymph nodes were collected from sacrificed mice. The cervical, axillary, cubital, mesenteric, inguinal and popliteal lymph nodes were pooled

for further processing. After generation of a single cell suspension as described in section 6.2.6, the cells were counted and $2 - 4 \times 10^7$ cells were used for the proceeding steps. Un-specific binding sites were blocked using unlabelled α CD16/CD32 antibodies for 15 min on ice. The master mix containing the fluorescent antibodies for sorting (α CD44-FITC, α CD8-PE, α CD4-PE/Dazzle, α CD19-PE/Dazzle, α CD45.1-APC, α Thy1.1-APC, α CD45.1-Pacific Blue, α Thy1.1 eF450) and oligonucleotide-conjugated antibodies to detect surface proteins as used here for sample discrimination after sequencing (hashtag 1 for the spleens and hashtag 2 for the lymph nodes) and for immune-profiling (see Table 6.5) were added and incubated for additional 30 min on ice. The cells were then washed trice in EDTA-poor flow cytometry buffer and filtered using a 30 μ m syringe filcon (BD Bioscience). Immediately before enrichment by flow cytometric sorting, PI was added to the samples. For either infection, $1 - 1.2 \times 10^4$ live CD4⁻CD19⁻CD8a⁺CD44^{high}CD45.1⁺Thy1.1⁺ P14 or OTI T cells, respectively, were enriched from the spleen and the lymph nodes and sorted into the same well of a 96-well V bottom plate (VWR) containing PBS supplemented with 2 % BSA.

6.2.16. Single cell RNA sequencing

After cell sorting, the cells were centrifuged at 1500 rpm for 3 min at 4 °C and the supernatant was removed without disturbing the pellet. The total cell pellet was re-suspended in the master mix with 46.6 μ L nuclease-free water and 75 μ L of the cell suspension was directly loaded on the chip (Chromium Single Cell 3'GEM v3 user guide, instead of step 1.1. and 1.2a). From step 1.2.c to step 2.1, the experimental procedures were performed as in the manufacturers instructions. During the cDNA amplification step (original protocol step 2.2) supplementary primers to recover the proteogenomic information were added, that were 1 μ L ADT additive primer and 1 μ L HTO additive primer. In total, 11 amplification cycles were performed. The cDNA-clean up step was performed according to manufacturers protocol Feature Barcode Technology for Cell Surface Protein RevD.

For the preparation of the mRNA libraries, the original protocol has been followed. For the cell surface library construction, 5 μ L of the purified supernatant fraction of the sample were mixed with 2.5 μ L of the SI-PCR primer, and either 2.5 μ L TrueSeq D702_s (TrueSeq D703_s, TrueSeq D704_s, TrueSeq D705_s or TrueSeq D706_s), RPI2 (or RPI3, RPI4, RPI5 or RPI6) primer, together with 50 μ L KAPA Hifi Master Mix and 40 μ L nuclease-free water was incubated with protocol in Table 6.7 for D70x_s and according to the protocol in Table 6.8 for the RPI primers. After cell surface library construction, 120 μ L of Ampure XP beads were added to each sample. The samples were well re-suspended and incubated for 5 min at room temperature. The beads were magnet-enriched and while on the magnet, washed twice with fresh 80 % Ethanol. After removal of the Ethanol, the tubes with the beads were removed from the magnet, the sample was re-suspended in 40.5 μ L buffer EB and incubated at room temperature for 2 min. The tubes with the eluted library and beads mixture was placed back on the magnet and the supernatant containing the cell surface library was collected. All libraries were quantified with the Qubit

dsDNA HS assay kit and sample size and quality was assessed with the high sensitivity DNA-Kit on a Bioanalyzer 2100. All libraries were pooled according to the required reads (2×10^4 for the 3'libraries and 5×10^3 for the cell surface libraries). The pooled libraries were sequenced on a Illumina Novaseq 6000 S2 (paired-end, 28+94 bp).

Table 6.7.: Thermocycle protocol for hashtags

temperature	time	cycles
98 °C	2 min	
98 °C	20 s	
64 °C	30 s	15
72 °C	20 s	
72 °C	5 min	
4 °C	hold	

Table 6.8.: Thermocycle protocol for antibody-derived tags

temperature	time	cycles
98 °C	2 min	
98 °C	20 s	
60 °C	30 s	18
72 °C	20 s	
72 °C	5 min	
4 °C	hold	

6.3. Bioinformatics methods

6.3.1. Generation of gene expression count matrices

The alignment of the single cell RNA sequencing data to the mouse reference genome (GRCm38, release 8.4) including filtering were performed using the 10x Genomics Cell Ranger software (v3.1.0). The resulting .bam-files were used as input for further analysis with velocity (v0.17.17) (La Manno et al. 2018) to generate the count matrices for the spliced and unspliced RNA counts.

6.3.2. Data processing and quality control

The Python software package SCANPY (v1.6.0) was used for all further analyses (Wolf et al. 2019). Cells that expressed less than 200 genes, had less than 20 counts and more than 7.5 % mitochondrial gene counts have been excluded from the analysis. Gene counts were per-cell-normalised and (log + 1)-transformed. Highly variable genes were computed using the first 4000 most highly variable genes for all samples.

6.3.3. De-multiplexing of samples

As the cells from spleen and lymph nodes were pooled into one well during the preparation of the gel-beads emulsion (Step 1 of Chromium Single Cell 3'GEM v3 user guide), the samples were first de-multiplexed. Separation of spleen from lymph node samples based on the expression of the oligonucleotide-antibody label (spleen: hashtag 1, lymph nodes: hashtag 2).

The expression of the hashtags was $(\log+1)$ -transformed and an expression threshold of 4 was set for both hashtags. The cells with a hashtag 1 expression count ≥ 4 were assigned to be spleen-derived, and cells with a hashtag 2 expression count ≥ 4 as derived from the lymph nodes. The cells expressing both, hashtag 1 and 2 were classified as doublets and removed before the downstream analysis.

6.3.4. Proteogenomics analysis

For the surface immune-phenotyping, the counts for the antibody derived tags (ADTs) were per-cell- normalised and $(\log + 1)$ -transformed. Expression levels of the surface markers were visualised in the UMAP representation.

6.3.5. Removal of doublets

For data sets containing $n > 5000$ cells, doublet cells were identified and removed using the solo doublet detection tool (Bernstein et al. 2020). Solo was run using the standard parameter settings. Using the hashtag label information, a list containing the known doublets was passed when running solo. For the LCMV Armstrong day 6 samples 935 doublets and for the LCMV Armstrong day 7 data set 126 doublets were detected and excluded from the analysis. In the LCMV clone 13 data sets at day 6 and day 7, 889 cells and 133 cells were classified as doublets and as well removed before further analyses.

6.3.6. LCMV data integration and batch correction

Our own day 6 spleen single cell RNA sequencing data sets were combined with previously published data from (Chen et al. 2019, Kurd et al. 2020, Yao et al. 2019). By integrating these data sets, we were able to investigate the T cell differentiation dynamics during LCMV infection in a time-resolved manner. Therefore, the .fastq- or .bam- files of the published data sets were downloaded from the genesetomnibus or ENA data base and aligned with the 10x Genomics Cell Ranger Software (v3.1.0.). The .bam-file were first converted to .fastq-files using the 10x Genomics bam2fastq (v1.2.0) command. Then the count matrices for the spliced and unspliced reads were generated with velocity (v0.17.17) (La Manno et al. 2018). All count matrices were combined by concatenation in SCANPY (v1.6.0) before initial filtering for cells with more than 200 expressed genes, more than 20 spliced and 10 unspliced counts and lower than 7.5 % mitochondrial genes. The top 4000 highly variable genes (flavor="Seurat") were selected for the combined data set. As the different data sets exhibited up to a 10 fold variance in their expression of mitochondrial genes, the percentage of mitochondrial genes was regressed out with a linear model using the scanpy.pp.regress_out command. The batch-corrected neighbourhood graph was computed using the SCANPY implementation of batch-balanced k nearest neighbour method (bbknn, v1.3.7) (Polański et al. 2020) based on $n = 30$ principal components, $k = 30$ neighbours. Data sets from the same publication were considered as the same batch.

6.3.7. Cell cycle scoring

To assign cell cycle phases the spliced count matrix of the combined data set was first filtered for genes that were minimally expressed in 3 cells, then per-cell-normalised, $(\log + 1)$ -transformed and scaled to unit variance and zero mean. The cell cycle stage scoring was performed as by (Satija et al. 2015) given two lists of genes associated to S phase and G2M phase (Kowalczyk et al. 2015). Cells assigned a G2M-phase score > 0.5 were classified as being in G2M stage, cells with a S phase score > 0.5 to S-phase respectively. Cells with S-phase and G2M-phase scores < 0.5 were labelled as G1.

6.3.8. Dimensionality reduction and clustering

The principal component analysis (PCA) was performed only on the highly variable genes. The Leiden algorithm (Traag et al. 2019) with a resolution $r = 0.8$ was used for the clustering. The neighbourhood graph for the combined data sets was computed as described in section 6.3.6. For analysis of single datasets, the neighbourhood graph was computed based on $n = 30$ principal components and $k = 30$ neighbours. The uniform manifold approximation and projection (UMAP) and the diffusion map projections were calculated on the default parameters in SCANPY (v1.6.0).

6.3.9. Differential gene expression testing and GO term analysis

The marker genes were identified by computing a ranking for highly differentially genes in SCANPY (v1.6.0). The `scanpy.tl.rank_genes_group` command was used and the differentially expressed genes were obtained by the comparison between Armstrong versus clone 13 per time-point. The differential gene expression analysis to compare the Leiden clusters with each other, was performed using the MAST R package (v 1.10.0) (Finak et al. 2015). Gene Ontology analyses were performed with Metascape 3.0 using the list differential gene expression analysis from MAST and visualised in Python using matplotlib (v 3.3.1). A cut-off of 0.05 for the adjusted p-value and a Log2-fold change of bigger than 1.1 was chosen.

6.3.10. T cell signature scoring

The signature scores were calculated using the R package VISION (v.2.1.0) (DeTomaso et al. 2019). Therefore, the count matrices were normalised to total counts per cell and scaled to the median of total counts per sample. Genes with high expression contributed positively to the signature, while genes with low expression conversely contributed negatively.

6.3.11. Trajectory inference analysis

The RNA velocities within a stochastic model (Bergen et al. 2020) were computed for each time point individually using the scVelo Python tool (v.0.2.2). Partition-based graph abstraction

(PAGA) (Wolf et al. 2019) connectivities within cell clusters were computed taking into account the RNA velocity information. Using the R package CytoTRACE (v.0.3.3) (Gulati et al. 2019) and running iCytoTRACE on multiple data sets, where data from the same publications were considered as the same batch, a differentiation score was computed for each cell. For diffusion pseudo-time analysis (Angerer et al. 2016) with SCANPY (v.1.6.0), a cell with a CytoTRACE score of 1.0 within the cMP-subset was randomly chosen as root cell and $n = 10$ diffusion components were used.

6.3.12. Inferring cell cycle drop out from scRNA-seq data

RNA velocities using the stochastic method were computed only on genes related to cell cycle using scVelo (v.0.2.2) (Bergen et al. 2020). Firstly, the count matrices for each individual time point were filtered for the genes on the cell cycle gene list (Kowalczyk et al. 2015) and genes that were expressed in less than 3 cells were excluded.

Next, the count matrices were normalised to total counts per cell, $(\log + 1)$ -transformed and scaled to zero mean and unit variance. As described in section 6.3.7 the cell cycle phases were calculated based on the S- and G2M-phase score of a cell. Then, the principal component analysis was performed on all the cell cycle genes, the neighbourhood graph was obtained using $n = 2 - 5$ principal components and $k = 30$ neighbours and the UMAP in cell cycle gene space was computed. Based on $k = 30$ neighbours and $n = 30$ principal components the first and second order moments were computed for each cell. Then the velocities were estimated and the velocity graph was computed. The single cell velocities were then projected in the UMAP embedding. Areas with high velocity activity (large arrows) indicate movement along cell cycle gene space and represent cycling cells. The fraction of cycling cells was used to fit the mathematical model.

6.3.13. Bioinformatics analysis of OTI T cells derived from *L.m.*-OVA infection

The analyses of the OTI T cells at the days 4.5, 8 and 12 p.i. with *L.m.*-OVA were performed by my colleague Jonas Mir in a similar fashion as described before in detail for the P14 T cells during LCMV infection.

Briefly, the gene expression count matrices were generated as described in section 6.3.1. The Python software packages SCANPY (v1.4.6) and scVelo (v0.1.25) were used for all further analyses (Wolf et al. 2019). Basic filtering was performed the same way as aforementioned. Highly variable genes were determined using the R package scater (v1.12.2) (McCarthy et al. 2017). Data sets were demultiplexed similarly as described in section 6.3.3 but without performing $(\log + 1)$ - transformation and a threshold between 20-120 was used for the hashtags 1-4. Then, the percentage of mitochondrial gene counts was regressed using a linear model. For the principal component analysis (PCA) the default parameter set was used. Clustering based on the Leiden algorithm (Traag et al. 2019) with a resolution $r = 0.8$. The neighbourhood graph for

combined data sets was computed using $n = 30$ PC and $k = 50$ neighbours. The UMAP was calculated on the default parameters in SCANPY (v1.4.6). The trajectory inference analyses were performed as described in section 6.3.11, except that the RNA velocities were computed using the deterministic model.

6.3.14. Bioinformatics analysis of LCMV-specific CD8⁺ TOX knock-out and wild-type T cells responses during LCMV clone 13 infection

The scRNA-seq data for the *Tox* knock-out (*Tox*^{-/-}) and wild-type CD8⁺ T cells responses at day 7 after infection with LCMV clone 13 stem from Yao et al. 2019. The gene expression count matrices were generated as previously described in section 6.3.1. The Python software packages SCANPY (v1.4.6) and scVelo (v0.1.25) were used for all further analyses (Wolf et al. 2019). We performed basic filtering the same way as aforementioned and selected the $n = 3000$ top highly variable genes (flavor="Seurat"). The UMAP was computed for the pooled cells from wild-type and *Tox*^{-/-} progenies. Leiden clustering was performed with a resolution $r = 0.6$ (Traag et al. 2019). The differential gene expression analysis was performed as described in section 6.3.9. The RNA velocities were determined for each condition separately using the stochastic method (La Manno et al. 2018).

6.4. Mathematical and statistical methods

6.4.1. Summary statistics

For comparison between two groups a Mann-Whitney U test was used (GraphPad Prism v8). We tested for normality using the D'Agostino Pearson omnibus normality test (GraphPad Prism v8) to identify if values come from a Gaussian distribution. For normally distributed data and comparison of the group mean over time a one-way ANOVA was performed.

For stochastic modelling, the mean values, the coefficient of variations (CV), as well as the Pearson correlation between the subsets were used. The errors for the means, the CVs and the Pearson correlation between the subsets were determined by repetitive sampling using non-parametric bootstrapping. The errors for the relative subset sizes and the fraction of cycling P14 T cells at day 4.5, 6, 7 and 8 that were inferred from the scRNA-seq data, were assessed by taking the square root of the pooled variance. The uncertainties of the fraction of cycling subsets at day 6 post infection with LCMV Armstrong or c13 were obtained by calculation of the standard error of the mean (s.e.m.). The uncertainties for the proliferation rates, that were informed by the cell cycle length measurements, were unknown and therefore set to 10 %. The evenness of the single T cell-derived population at day 8 was quantified using the Gini index (Gini 1921). The data used for the mathematical modelling, along with an reference to their origin, are summarised in Table C.1 in the appendix C.

6.4.2. Quantification of cell cycle speed and the length of cell cycle phases

Cell cycle length was quantified as previously described by Kretschmer et al. 2020. In brief, a system of the following three equations has to be solved in order to estimate the duration of the cell cycle:

$$p(\text{BrdU}^+\text{DNA}(2N)) = 2(1 - e^{c(t_{\text{Ml}} - \langle T_{\text{G2M}} \rangle)}) \quad (6.1)$$

and

$$p(\text{BrdU}^-\text{DNA}(4N)) = e^{c(\langle T_{\text{G2M}} \rangle - t_{\text{Ms}})} - 1, \quad (6.2)$$

where $p(\text{BrdU}^+\text{DNA}(2N))$ is the probability of a cell to appear inside the $\text{BrdU}^+\text{DNA}(2N)$ divided-gate at time t_{Ml} with $t_{\text{Ml}} = 3$ h. In other words, the mother cells of divided progenies passed through S-phase during the time window when BrdU was available and divided within the time of measurement t_{Ml} . $\langle T_{\text{G2M}} \rangle$ denotes the expected mean duration of the G2M-phase. Furthermore, the fraction of cells not having undergone cell division during the measurement is captured by $p(\text{BrdU}^-\text{DNA}(4N))$, the probability of cells that are in the G2M-phase after a short labelling time t_{Ms} with $t_{\text{Ms}} = 0.5$ h. The exponential growth rate c is approximated by

$$c \approx \frac{\log(2)}{\langle D(T_{\text{Div}}) \rangle}, \quad (6.3)$$

where $\langle D(T_{\text{Div}}) \rangle$ represents the inter-division time distribution. By substitution of equation (6.2) to equation (6.1), we can solve for c . Further substitution of c into equation (6.3) gives us the duration of the cell cycle. In order to quantify the mean length for the G1- and G2M-phase, the following equations (6.4) and (6.5) were evaluated together with equations (6.1) and (6.3).

$$p(\text{BrdU}^-\text{DNA}(2N)) = 2(e^{-c(t_{\text{Ms}} - \langle T_{\text{G2M}} \rangle)} - e^{c(\langle T_{\text{G1}} \rangle)}) \quad (6.4)$$

$$p(\text{BrdU}^-\text{DNA}(4N)) = e^{c(\langle T_{\text{G2M}} \rangle - t_{\text{Ms}})} - 1 \quad (6.5)$$

6.4.3. Mathematical modelling

The mathematical model describing the P14 T cell response after LCMV Armstrong infection as well as mathematical model for the OTI T cell dynamics after *L.m.*-OVA infection were both developed and investigated by Jonas Mir. The mathematical for the LCMV clone 13 infection and the combined modelling of LCMV Armstrong and clone 13 P14 T cell response was based on the best-fitting model Jonas Mir found in the LCMV Armstrong and *L.m.*-OVA infection setting and was performed by myself. The identification of the model topology underlies the findings from the RNA velocity analyses of the scRNA-seq data following LCMV Armstrong or

L.m.-OVA infection and is discussed in detail in section 3.4 and 3.5. The mathematical model fitting routine to the single cell progenies derived from *L.m.*-OVA infection and to the LCMV Armstrong infection was performed by Jonas Mir as described here. The model topology was defined as described in Chapter 3 in Figure 3.12 H.

Starting from a naïve state, cells diversified and generated offspring associated to three different subsets (TCF1⁺, TCF1⁻CX3CR1^{low} and CX3CR1^{high} for LCMV infection and CD62L⁺CD27⁺, CD62L⁻CD27⁺ and CD62L⁻CD27⁻ for *L.m.*-OVA infection). These three subsets were further subdivided into a cycling and a non-cycling compartment.

In this diversification system, the state vector consists of the species ($N_{1-5}, C_A, C_B, C_C, NC_A, NC_B, NC_C$) with the number of naïve (N_{1-5}), cycling TCF1⁺ (or CD62L⁺CD27⁺) (C_A), cycling TCF1⁻CX3CR1^{low} or CD62L⁻,CD27⁺ (C_B), cycling CX3CR1^{high} or CD62L⁻,CD27⁻ (C_C) and the corresponding non-cycling TCF1⁺ (or CD62L⁺CD27⁺) (NC_A), non-cycling TCF1⁻CX3CR1^{low} (or CD62L⁺CD27⁻) (NC_B), non-cycling CX3CR1^{high} (or CD62L⁻CD27⁻) (NC_C) cells.

All reactions in our mathematical model, recruitment, proliferation, differentiation and transitions between cycling and non-cycling compartments, were assumed to be Markov processes. In a Markov system, transitions between states follow an exponential distribution. To introduce a long-tailed distribution for the recruitment process, several naïve compartments were sequentially linked, as the addition of several exponential distributions with equal rates results in a gamma distribution.

The ordinary differential equations (ODE) for the first and second cell number moments of the differentiation model can easily be derived by solving the master equations as in Lestas et al. 2008. Thus, the first order moments are defined as $\frac{d\langle x(t) \rangle}{dt} := \sum_i r_i W_i(x)$ with r_i representing the replacement vector and W_i the species propensity.

In the linear case, the equation above can be written as $\frac{d\langle x(t) \rangle}{dt} = A\langle x(t) \rangle + f_0$, $A \in \mathbb{R}^{n \times n}$ $f_0 \in \mathbb{R}^n$ where $\langle x(t) \rangle$ denotes the expected mean of the state x at time t , A is the stoichiometric matrix multiplied with the reaction rate vector $\vec{\theta}$ and the constant f_0 . In this case, $\vec{x}(t) = (N_1 N_2 N_3 N_4 N_5 C_A C_B C_C NC_A NC_B NC_C)^T$,

$\vec{\theta} = (r_{N_1 N_2} r_{N_2 N_3} r_{N_3 N_4} r_{N_4 N_5} r_{N_5 C_A} r_{C_A C_B} r_{C_B C_C} r_{C_A NC_A} r_{C_B NC_B} r_{C_C NC_C} \lambda_{C_A} \lambda_{C_B} \lambda_{C_C})^T$ and $f_0 = 0$. The moments equations for the evolution of the states' means can be derived according to equation $\frac{d\langle x(t) \rangle}{dt} = A\langle x(t) \rangle$ and are summarised in Appendix C.

Similarly, in a linear case, the second order moments are defined as in Lestas et al. 2008: $\frac{d\Sigma(t)}{dt} = A\Sigma(t) + \Sigma(t)A^T + \sum_i r_i W_i(\langle x(t) \rangle) r_i^T$. Where, W_i is the species propensity that was introduced in the equation for the first order moments.

Solving the equation for the second order moments, we obtain the ODEs for the variances and covariances (Appendix C, equations (C.1),(C.2) and (C.3)).

Accordingly, we derived the moments for the model of T cell exhaustion. For the arrested model of T cell exhaustion, we also used the single-cell responses after LCMV clone 13 infection. The TCF1⁺ subset constituted the MP and MEX T cells, the TCF1⁻CX3CR1^{low} the EE and EEX T cells and the CX3CR1^{high} subset the TEF and TEX T cells. For moments equation

derivation of the arrested T cell model, we used $\vec{x}(t) = (N A_f B_f C_f A_{ex} B_{ex} C_{ex})^T$ and $\vec{\theta} = (r_{N A_f} r_{A_f B_f} r_{B_f C_f} r_{A_f A_{ex}} r_{B_f B_{ex}} r_{C_f C_{ex}} \lambda_{A_f} \lambda_{B_f} \lambda_{A_{ex}} \lambda_{B_{ex}})^T$. The equations for the arrested model of exhaustion are listed in Appendix C, equations (C.4),(C.5) and (C.6)).

6.4.4. Fitting the model to the data

Parameter estimation was performed by solving the non-linear least-squares problem in Matlab (v2020a). All models were fit to the mean values, and the coefficients of variation (CV) and the Pearson correlation coefficients (ρ) of the single-cell descendants at day 8 p.i.

For modelling the LCMV Armstrong infection, we used all three correlation coefficients between the subsets, but for LCMV clone 13 infection, only a few single-cell progenies were found in the CX3CR1^{high} compartment, therefore only the correlation coefficient between the TCF1⁺ and TCF1⁻CX3CR1^{low} was used.

In addition, the fraction of cycling cells inferred from the scRNA-seq data at the day 4.5, 6, 7 and 8 (as described in section 6.3.12, the fraction of cycling cells in each subset at day 6 (flow cytometric measurements of the phospho-Rb protein) and the ratio of the cell cycle length between the TCF1⁺ vs. TCF1⁻ subsets. The uncertainties of those quantities were used as described in section 6.4.1.

In the division drop out model we have 11 compartments, whereas from the experimental single cell fate-mapping data we have only the information for the population distribution in terms of their expression of TCF1⁺, TCF1⁻CX3CR1^{low} and CX3CR1^{high} and not if a cell was yet arrested or still progressing through cell cycle at the time point of measurement. Therefore, to describe the first and second order moments, we combined the cycling and non-cycling TCF1⁺, as well as the naïve compartments to the one subset named TCF1⁺. The same was as well done for the TCF1⁻CX3CR1^{low} and CX3CR1^{high} subsets, that comprised of the cycling and non-cycling TCF1⁻CX3CR1^{low} and cycling and non-cycling CX3CR1^{high} cells, respectively.

For the evaluation of the solution, the means of each sub-compartment were added and for the coefficients of variation and correlation coefficients, the variance sum law for the dependent variable was applied. This means, for the variances were added to two times the co-variance of each sub-compartment to the other.

The combination of the T cell compartments was as well employed for the arrested model of T cell exhaustion. However, in the latter model only one naïve compartment and instead of cycling and non-cycling, the grouping of the subsets was performed based on the functional (f) and exhausted (ex) states.

The best fit was determined by a local optimisation based algorithm with 1000 different random starting values, sampling from a Latin hypercube with an edge length of 7 (7, for the extended model of differentiation and 8 for the arrested model of T cell exhaustion) with random initial values.

We performed χ^2 - minimisation with the above mentioned summary statistics for the objective

function: $\chi^2 = \sum_{i=1}^n \left(\frac{\langle Y_i \rangle - \bar{Y}_i^d}{\sigma_{Y_i}} \right)^2$. With $\langle Y_i \rangle$ denoting the model prediction, \bar{Y}_i^d standing for the data and error of the data point σ_{Y_i} .

In cases where the model was fit to the LCMV Armstrong data, we used the mean and the CV for each subset from day 8 p.i. after LCMV Armstrong infection, the pair-wise Pearson correlation coefficients, the relative subset sizes at day 4.5, 6, 7 and 8 p.i. for the TCF1⁺ and TCF1⁻CX3CR1^{low} subset, and the fractions of cycling cells inferred from the scRNA-seq on day 3, 4, 4.5, 5, 6, 7 and 8 p.i. Also, the ratio of the proliferation rate between the TCF1⁺ and TCF1⁻ subset from the day 4.5 p.i. measurement was used in the objective function.

For parameter estimation to describe the LCMV clone 13 infection, the objective function contained the mean values for the three subsets, the CV for the TCF1⁺ and TCF1⁻CX3CR1^{low} subset and the pair-wise Pearson correlation coefficient for TCF1⁻ and TCF1⁻CX3CR1^{low}. In addition, the relative subset sizes as previously described for the LCMV Armstrong infection, the fraction of dividing cells inferred from the scRNA-seq on the days 4.5, 7 and 8 as well as the fraction of p-Rb-positive P14 T cells for each subset at day 6 was used. Furthermore, we also included the ratio of measured division rate between the TCF1⁺ and TCF1⁻ subset from the day 4.5 p.i. measurement. To estimate the parameter in a model where both infections were fit together, we used $\chi^2 = \chi_{\text{Arm}}^2 + \chi_{\text{c13}}^2$ for the objective function.

For parameter estimation to describe the LCMV clone 13 infection using the arrested model of T cell exhaustion, the mean values for the three subsets, the CV for the TCF1⁺ and TCF1⁻CX3CR1^{low} subset and the pair-wise Pearson correlation coefficient for TCF1⁻ and TCF1⁻CX3CR1^{low} were included in the cost function. In addition, the cost function also included the relative subset sizes, the fraction of exhausted T cells based on the expression of PD1 and TOX on day 8 p.i. Furthermore, we also included the ratio of measured division rate between the TCF1⁺ and TCF1⁻ subset from the day 4.5 p.i. measurement. Due to lack of experimental data on the division speed of the exhausted subset, we weighted the measured proliferation rate using the subset sizes.

Under the assumptions that the errors in our linear models are independent and normally distributed, then $\hat{\beta} := \arg \min_{\beta} \chi^2(\beta) = \arg \max_{\beta} \log L(\beta)$ with $\beta = (\theta, y)$. Minimising χ^2 with respect to a set of parameters θ and a set of data y is equivalent to maximisation of the log-likelihood $\log L$.

6.4.5. Model comparison and selection

The different models were ranked according to the corrected Akaike information criterion for small sample sizes (Cavanaugh 1997),

$$\text{AICc} = 2k - 2\log L + \frac{2k(k+1)}{(n-k-1)}. \quad (6.6)$$

Where k denotes the number of parameters used in the model and n number of data points at day 4.5, 6, 7 and 8. Given that $\log L = -\frac{1}{2}\chi_{\min}^2 + \text{constant}$,

$$\text{AICc} = \chi_{\min}^2 + 2k + \frac{2k(k+1)}{(n-k-1)} + \text{constant}. \quad (6.7)$$

We used equation (6.7) to evaluate the models. We therefore calculated the AICc for each model and compared the difference of each tested model i to the best fitting model AICc_{\min} , $\Delta\text{AICc}_i = \text{AICc}_i - \text{AICc}_{\min}$. Models with a $\Delta\text{AICc} \geq 10$ did not support the data and were omitted from further consideration.

For the combined analysis of the LCMV Armstrong and LCMV clone 13 derived P14 T cell responses, forward selection (Friedman et al. 2014) was employed to identify the mathematical model providing best support for both of the data sets. When performing forward selection, we started with the simplest model that contained $k = 7$ parameters, i.e. the parameters were set to be the same for both infections. In the first round of the model selection process, 6 out of 7 parameters were kept the same for both infections, except for one that was iteratively allowed to differ. Thus, during the first round of model selection a total of 8 parameters were fit (6 fixed, and 2 infection-specific). After the first selection round, the model with the lowest χ^2 was chosen and additional parameter was iteratively altered. This way, the number of parameters were successively increased during each new round of the fitting routine until the χ^2 -value did not decrease any further. Then, the AICc was calculated for each model

6.4.6. Confidence intervals for the model parameters

For the best performing model, we computed the confidence intervals (CI) of each parameter using the profile likelihood method (Venzon et al. 1988). Briefly, in this method each parameter θ_i is fixed to its best fit value and χ^2 is minimised over the remaining parameters. Then, to obtain the 95 % confidence region of each parameter, the parameter values at $\Delta\chi_{\min}^2(\theta_i) = \chi_{\min}^2(\theta_i) - \chi_{\min}^2 = 3.84$ were taken.

6.4.7. Model simulations

All the simulations were based on Gillespie's stochastic simulation algorithm (Gillespie 1976).

7. Abbreviations

7AAD	7-aminoactinomycin D
ACD	asymmetric cell division
ACT	Ammonium chloride-Tris
APC	Allophycocyanin
APCs	antigen-presenting cells
Arm	Armstrong
AIC	Akaike information criterion
bbknn	batch-balanced k nearest neighbour
BHI	brain heart infusion growth medium
BrdU	5-Bromo-2'-deoxyuridine
BSA	bovine serum albumin
BV	brilliant violet
c13	clone 13
CCL3	C-C Motif Chemokine Ligand 3
CCL4	C-C Motif Chemokine Ligand 4
CCL5	C-C Motif Chemokine Ligand 5
CD	cluster of differentiation
CFU	colony forming units
CI	confidence interval
CMP	central memory precursor T cell
CV	coefficient of variation
CX3CR1	C-X3-C motif chemokine receptor 1
d	days
DC	dendritic cell
DMSO	Dimethyl sulfoxide
DNA	Deoxyribonucleic acid
EDTA	Ethylenediaminetetraacetic acid
EdU	5-Ethynyl-2'-deoxyuridine
EMP	effector memory precursor T cell
EE	early effector T cell
EFF	effector T cell
FCS	fetal calf serum
FITC	Fluorescein-isothiocyanat
FUCCI	Fluorescent ubiquitination-based cell cycle indicator
G0	gap 0
G1	gap 1

G2/M	gap 2/ mitosis
GEM	gel bead in emulsion
GFP	green fluorescent protein
gp	glycoprotein
Gzma	Granzyme a
Gzmb	Granzyme b
h	hours
IL	Interleukin
IL2Rα	Interleukin 2 receptor alpha
IL7R	Interleukin 7 receptor
i.p.	intraperitoneal
Irf4	Interferon Regulatory Factor 4
Irf8	Interferon Regulatory Factor 8
i.v.	intravenous
KLRD1	Killer Cell Lectin Like Receptor D1
KLRG1	Killer Cell Lectin Like Receptor G1
LCMV	Lymphocytic Choriomeningitis Virus
<i>L.m.</i>	<i>Listeria monocytogenes</i>
<i>L.m.-OVA</i>	<i>Listeria monocytogenes</i> expressing ovalbumin
MFI	median fluorescent intensity
MKI67	Marker Of Proliferation Ki-67
MP	memory precursor T cell
MVA	Modified vaccinia virus Ankara
MVA-OVA	ovalbumin-expressing Modified vaccinia virus Ankara
N	Naïve
Nur77	Nuclear Receptor Subfamily 4 Group A Member 1
OVA	ovalbumin
OX40	TNF Receptor Superfamily Member 4
p_{adj}	adjusted p -value
PAGA	Partition-based graph abstraction
PBS	phage forming units
PD1	Programmed Cell Death 1
PE	phycoerythrin
PFA	paraformaldehyde
PFU	phage forming units
p.i.	post infection
PI	propidium iodide

p-Rb	phosphorylated Retinoblastoma protein
QC	quality control
Rack1	Receptor For Activated C Kinase 1
Rag	Recombination activating gene
RNA	Ribonucleic acid
RPM	rotations per minute
S	synthesis
scRNA-seq	single cell RNA-sequencing
Sell	L-selectin (CD62L)
s.e.m.	standard error of the mean
TCF1	T cell factor 1
TCR	T cell receptor
Tim3	T-cell immunoglobulin and mucin-domain containing-3
TOX	Thymocyte selection associated high mobility group box
<i>Tox</i>^{-/-}	Tox knock-out
UMAP	uniform manifold approximation and projection
WT	wild-type

Bibliography

- Abdel-Hakeem, Mohamed S. (2019). “Viruses teaching immunology: Role of LCMV model and human viral infections in immunological discoveries”. In: *Viruses* 11.2. ISSN: 19994915. DOI: 10.3390/v11020106.
- Ahmed, Rafi, Salmi Aimo, Larry D. Buttler, Jacques M. Chiller, and Michael B. A. Oldstone (1984). “Selection of genetic variants of lymphocytic choriomeningitis virus in spleens of persistently infected mice”. In: *Journal of Experimental Medicine* 60. August, pp. 521–540.
- Ahmed, Rafi and David Gray (1996). “Immunological Memory and Protective Immunity: Understanding Their Relation”. In: *Science* 272. April, pp. 54–61.
- Ahn, Eunseon, Koichi Araki, Masao Hashimoto, Weiyang Li, James L. Riley, Jeanne Cheung, Arlene H. Sharpe, Gordon J. Freeman, Bryan A. Irving, and Rafi Ahmed (2018). “Role of PD-1 during effector CD8 T cell differentiation”. In: *Proceedings of the National Academy of Sciences of the United States of America* 115.18, pp. 4749–4754. ISSN: 10916490. DOI: 10.1073/pnas.1718217115.
- Alfei, Francesca, Kristiyan Kanev, Maike Hofmann, Ming Wu, Hazem E. Ghoneim, Patrick Roelli, Daniel T. Utzschneider, Madlaina von Hoesslin, Jolie G. Cullen, Yiping Fan, Vasyil Eisenberg, Dirk Wohlleber, Katja Steiger, Doron Merkler, Mauro Delorenzi, Percy A. Knolle, Cyrille J. Cohen, Robert Thimme, Benjamin Youngblood, and Dietmar Zehn (2019). “TOX reinforces the phenotype and longevity of exhausted T cells in chronic viral infection”. In: *Nature* 571.7764, pp. 265–269. ISSN: 14764687. DOI: 10.1038/s41586-019-1326-9.
- Althaus, Christian L., Vitaly V. Ganusov, and Rob J. De Boer (2007). “Dynamics of CD8+ T cell responses during acute and chronic lymphocytic choriomeningitis virus infection.” In: *The Journal of Immunology* 179.5, pp. 2944–2951. ISSN: 0022-1767. DOI: 10.4049/jimmunol.179.5.2944.
- Andrews, Lawrence P., Hiroshi Yano, and Dario A.A. Vignali (2019). “Inhibitory receptors and ligands beyond PD-1, PD-L1 and CTLA-4: breakthroughs or backups”. In: *Nature Immunology* 20.11, pp. 1425–1434. ISSN: 15292916. DOI: 10.1038/s41590-019-0512-0.
- Angelosanto, Jill M., Shawn D. Blackburn, Alison Crawford, and E. John Wherry (2012). “Progressive loss of memory T cell potential and commitment to exhaustion during chronic viral infection.” In: *Journal of Virology* 86.15, pp. 8161–70. ISSN: 1098-5514. DOI: 10.1128/JVI.00889-12.
- Angerer, Philipp, Laleh Haghverdi, Maren Büttner, Fabian J. Theis, Carsten Marr, and Florian Büttner (2016). “Destiny: Diffusion maps for large-scale single-cell data in R”. In: *Bioinformatics* 32.8, pp. 1241–1243. ISSN: 14602059. DOI: 10.1093/bioinformatics/btv715.
- Argilaguuet, Jordi, Mireia Pedragosa, Anna Esteve-Codina, Graciela Riera, Enric Vidal, Cristina Peligero-Cruz, Valentina Casella, David Andreu, Tsuneyasu Kaisho, Gennady Bocharov, Burkhard Ludewig, Simon Heath, and Andreas Meyerhans (2019). “Systems analysis reveals complex biological processes during virus infection fate decisions”. In: *Genome Research* 29.6, pp. 907–919. ISSN: 15495469. DOI: 10.1101/gr.241372.118.
- Arsenio, Janilyn, Boyko Kakaradov, Patrick J. Metz, Stephanie H. Kim, Gene W. Yeo, and John T. Chang (2014). “Early specification of CD8+ T lymphocyte fates during adaptive immunity revealed by single-cell gene-expression analyses”. In: *Nature Immunology* 15.4, pp. 365–372. ISSN: 1529-2908. DOI: 10.1038/ni.2842. arXiv: NIHMS150003.

- Badovinac, Vladimir P. and John T. Harty (2006). “Programming, demarcating, and manipulating CD8+ T-cell memory”. In: *Immunological Reviews* 211, pp. 67–80. ISSN: 01052896. DOI: 10.1111/j.0105-2896.2006.00384.x.
- (2007). “Manipulating the Rate of Memory CD8 + T Cell Generation after Acute Infection”. In: *The Journal of Immunology* 179.1, pp. 53–63. ISSN: 0022-1767. DOI: 10.4049/jimmunol.179.1.53.
- Ballek, Ondrej, Jan Valecka, Martina Dobešová, Adéla Broucková, Jasper Manning, Pavel Rehulka, Jirí Stulík, and Dominik Filipp (2016). “TCR triggering induces the formation of Lck-RACK1-actinin-1 multiprotein network affecting Lck redistribution”. In: *Frontiers in Immunology* 7.OCT. ISSN: 16643224. DOI: 10.3389/fimmu.2016.00449.
- Baral, Subhasish, Rustom Antia, and Narendra M. Dixit (2019). “A dynamical motif comprising the interactions between antigens and CD8 T cells may underlie the outcomes of viral infections”. In: *Proceedings of the National Academy of Sciences of the United States of America* 116.35, pp. 17393–17398. ISSN: 10916490. DOI: 10.1073/pnas.1902178116.
- Barber, Daniel L., E. John Wherry, David Masopust, Baogong Zhu, James P. Allison, Arlene H. Sharpe, Gordon J. Freeman, and Rafi Ahmed (2006). “Restoring function in exhausted CD8 T cells during chronic viral infection”. In: *Nature* 439.7077, pp. 682–687. ISSN: 00280836. DOI: 10.1038/nature04444.
- Bastid, Jeremy, Anne Regairaz, Nathalie Bonnefoy, Cecile Dejou, Jerome Giustiniani, Caroline Laheurte, Stephanie Cochaud, Emilie Laprevotte, Elisa Funck-Brentano, Patrice Hemon, Laurent Gros, Nicole Bec, Christian Larroque, Gilles Alberici, Armand Bensussan, and Jean Francois Eliaou (2015). “Inhibition of CD39 enzymatic function at the surface of tumor cells alleviates their immunosuppressive activity”. In: *Cancer Immunology Research* 3.3, pp. 254–265. ISSN: 23266074. DOI: 10.1158/2326-6066.CIR-14-0018.
- Bastidas-Ponce, Aimée, Sophie Tritschler, Leander Dony, Katharina Scheibner, Marta Tarquis-Medina, Ciro Salinno, Silvia Schirge, Ingo Burtscher, Anika Böttcher, Fabian J. Theis, Heiko Lickert, and Mostafa Bakhti (2019). “Comprehensive single cell mRNA profiling reveals a detailed roadmap for pancreatic endocrinogenesis”. In: *Development (Cambridge)* 146.12. ISSN: 14779129. DOI: 10.1242/dev.173849.
- Bergen, Volker, Marius Lange, Stefan Peidli, F. Alexander Wolf, and Fabian J. Theis (2020). “Generalizing RNA velocity to transient cell states through dynamical modeling”. In: *Nature Biotechnology* 38.12, pp. 1408–1414. ISSN: 15461696. DOI: 10.1038/s41587-020-0591-3.
- Bernstein, Nicholas J., Nicole L. Fong, Irene Lam, Margaret A. Roy, David G. Hendrickson, and David R. Kelley (2020). “Solo: Doublet Identification in Single-Cell RNA-Seq via Semi-Supervised Deep Learning”. In: *Cell Systems* 11.1, 95–101.e5. ISSN: 24054720. DOI: 10.1016/j.cels.2020.05.010.
- Best, J. Adam, David A. Blair, Jamie Knell, Edward Yang, Viveka Mayya, Andrew Doedens, Michael L. Dustin, Ananda W. Goldrath, Paul Monach, Susan A. Shinton, Richard R. Hardy, Radu Jianu, David Koller, Jim Collins, Roi Gazit, Brian S. Garrison, Derrick J. Rossi, Kavitha Narayan, Katelyn Sylvia, Joonsoo Kang, Anne Fletcher, Kutlu Elpek, Angelique Bellemare-Pelletier, Deepali Malhotra, Shannon Turley, J. Adam Best, Vladimir Jovic, Daphne Koller, Tal Shay, Aviv Regev, Nadia Cohen, Patrick Brennan, Michael Brenner, Taras Kreslavsky, Natalie A. Bezman, Joseph C. Sun, Charlie C. Kim, Lewis L. Lanier, Jennifer Miller, Brian Brown, Miriam Merad, Emmanuel L. Gautier, Claudia Jakubzick, Gwendalyn J. Randolph, Francis Kim, Tata Nageswara Rao, Amy Wagers, Tracy Heng, Michio Painter, Jeffrey Ericson, Scott Davis, Ayla Ergun, Michael Mingueneau, Diane Mathis, and Christophe Benoist (2013). “Transcriptional insights into the CD8 + T cell response to infection

- and memory T cell formation". In: *Nature Immunology* 14.4, pp. 404–412. ISSN: 15292908. DOI: 10.1038/ni.2536.
- Bird, Jennifer J., Daniel R. Brown, Alan C. Mullen, Naomi H. Moskowitz, Michael A. Mahowald, Jenny R. Sider, Thomas F. Gajewski, Chyung Ru Wang, and Steven L. Reiner (1998). "Helper T cell differentiation is controlled by the cell cycle". In: *Immunity* 9.2, pp. 229–237. ISSN: 10747613. DOI: 10.1016/S1074-7613(00)80605-6.
- Blackburn, Shawn D., Haina Shin, Gordon J. Freeman, and E. John Wherry (2008). "Selective expansion of a subset of exhausted CD8 T cells by α PD-L1 blockade". In: *Proceedings of the National Academy of Sciences of the United States of America* 105.39, pp. 15016–15021. ISSN: 00278424. DOI: 10.1073/pnas.0801497105.
- Blackburn, Shawn D., Haina Shin, W. Nicholas Haining, Tao Zou, Creg J. Workman, Antonio Polley, Michael R. Betts, Gordon J. Freeman, Dario A.A. Vignali, and E. John Wherry (2009). "Coregulation of CD8+ T cell exhaustion by multiple inhibitory receptors during chronic viral infection". In: *Nature Immunology* 10.1, pp. 29–37. ISSN: 15292908. DOI: 10.1038/ni.1679.
- Blank, Christian U., W. Nicholas Haining, Werner Held, Patrick G. Hogan, Axel Kallies, Enrico Lugli, Rachel C. Lynn, Mary Philip, Anjana Rao, Nicholas P. Restifo, Andrea Schietinger, Ton N.M. Schumacher, Pamela L. Schwartzberg, Arlene H. Sharpe, Daniel E. Speiser, E. John Wherry, Benjamin A. Youngblood, and Dietmar Zehn (2019). "Defining 'T cell exhaustion'". In: *Nature Reviews Immunology* 19.11, pp. 665–674. ISSN: 14741741. DOI: 10.1038/s41577-019-0221-9.
- Blattman, Joseph N., Rustom Antia, David J.D. Sourdive, Xiaochi Wang, Susan M. Kaech, Kaja Murali-Krishna, John D. Altman, and Rafi Ahmed (2002). "Estimating the precursor frequency of naive antigen-specific CD8 T cells". In: *Journal of Experimental Medicine* 195.5, pp. 657–664. ISSN: 00221007. DOI: 10.1084/jem.20001021.
- Bocharov, G. A. (1998). "Modelling the dynamics of LCMV infection in mice: Conventional and exhaustive CTL responses". In: *Journal of Theoretical Biology* 192.3, pp. 283–308. ISSN: 00225193. DOI: 10.1006/jtbi.1997.0612.
- Bocharov, Gennady, Paul Klenerman, and Stephan Ehl (2003). "Modelling the dynamics of LCMV infection in mice: II. Compartmental structure and immunopathology". In: *Journal of Theoretical Biology* 221.3, pp. 349–378. ISSN: 00225193. DOI: 10.1006/jtbi.2003.3180.
- Boehm, U. T., M. Klamp, and J. C. Howard Groot (2013). "Cellular responses to Interferon- γ ". In: *Annual Review of Immunology* 13.1978, pp. 618–634.
- Boettler, Tobias, Friedrich Moeckel, Yang Cheng, Maximilian Heeg, Shahram Salek-Ardakani, Shane Crotty, Michael Croft, and Matthias G. von Herrath (2012). "OX40 Facilitates Control of a Persistent Virus Infection". In: *PLoS Pathogens* 8.9. ISSN: 15537366. DOI: 10.1371/journal.ppat.1002913.
- Bolouri, Hamid, Mary Young, Joshua Beilke, Rebecca Johnson, Brian Fox, Lu Huang, Cristina Costa Santini, Christopher Mark Hill, Anne Renee van der Vuurst de Vries, Paul T. Shannon, Andrew Dervan, Pallavur Sivakumar, Matthew Trotter, Douglas Bassett, and Alexander Ratushny (2020). "Integrative network modeling reveals mechanisms underlying T cell exhaustion". In: *Scientific Reports* 10.1, pp. 1–15. ISSN: 20452322. DOI: 10.1038/s41598-020-58600-8.
- Borsa, Mariana, Isabel Barnstorf, Nicolas S. Baumann, Katharina Pallmer, Alexander Yermanos, Fabienne Gräbnitz, Niculò Barandun, Annika Hausmann, Ioana Sandu, Yves Barral, and Annette Oxenius (2019). "Modulation of asymmetric cell division as a mechanism to boost CD8+ T cell memory". In: *Science Immunology* 4.34. ISSN: 24709468. DOI: 10.1126/sciimmunol.aav1730.

- Böttcher, Jan P., Marc Beyer, Felix Meissner, Zeinab Abdullah, Jil Sander, Bastian Höchst, Sarah Eickhoff, Jan C. Rieckmann, Caroline Russo, Tanja Bauer, Tobias Flecken, Dominik Giesen, Daniel Engel, Steffen Jung, Dirk H. Busch, Ulrike Protzer, Robert Thimme, Matthias Mann, Christian Kurts, Joachim L. Schultze, Wolfgang Kastenmüller, and Percy A. Knolle (2015). “Functional classification of memory CD8 + T cells by CX 3 CR1 expression”. In: *Nature Communications* 6. ISSN: 20411723. DOI: 10.1038/ncomms9306.
- Buchholz, Veit R., Michael Flossdorf, Inge Hensel, Lorenz Kretschmer, B. Weissbrich, Patricia Graf, Admar Verschoor, Matthias Schiemann, Thomas Hofer, and Dirk H. Busch (2013a). “Disparate Individual Fates Compose Robust CD8+ T Cell Immunity”. In: *Science* 340.6132, pp. 630–635. ISSN: 0036-8075. DOI: 10.1126/science.1235454. arXiv: 20.
- Buchholz, Veit R., Patricia Gräf, and Dirk H. Busch (2013b). “The smallest unit: Effector and memory CD8+ T cell differentiation on the single cell level”. In: *Frontiers in Immunology* 4.FRB, pp. 1–10. ISSN: 16643224. DOI: 10.3389/fimmu.2013.00031.
- Buck, Michael D D., David O’Sullivan, Ramon I I. Klein Geltink, Jonathan D D. Curtis, Chih Hao Chang, David E E. Sanin, Jing Qiu, Oliver Kretz, Daniel Braas, Gerritje J J.W. van der Windt, Qiongyu Chen, Stanley Ching Cheng Huang, Christina M M. O’Neill, Brian T T. Edelson, Edward J J. Pearce, Hiromi Sesaki, Tobias B B. Huber, Angelika S S. Rambold, and Erika L L. Pearce (2016). “Mitochondrial Dynamics Controls T Cell Fate through Metabolic Programming”. In: *Cell* 166.1, pp. 63–76. ISSN: 10974172. DOI: 10.1016/j.cell.2016.05.035.
- Cavanaugh, Joseph E. (1997). “Unifying the derivations for the Akaike and corrected Akaike information criteria”. In: *Statistics and Probability Letters* 33.2, pp. 201–208. ISSN: 01677152. DOI: 10.1016/s0167-7152(96)00128-9.
- Cerletti, Dario, Ioana Sandu, Revant Gupta, Annette Oxenius, and Manfred Claassen (2020). “Fate Trajectories of CD8 + T Cells in Chronic LCMV Infection a Preprint”. In: *bioRxiv*, p. 2020.12.22.423929.
- Chang, John T., Maria L. Ciocca, Ichiko Kinjyo, Vikram R. Palanivel, Courtney E. McClurkin, Caitlin S. DeJong, Erin C. Mooney, Jiyeon S. Kim, Natalie C. Steinel, Jane Oliaro, Catherine C. Yin, Bogdan I. Florea, Herman S. Overkleeft, Leslie J. Berg, Sarah M. Russell, Gary A. Koretzky, Martha S. Jordan, and Steven L. Reiner (2011). “Asymmetric Proteasome Segregation as a Mechanism for Unequal Partitioning of the Transcription Factor T-bet during T Lymphocyte Division”. In: *Immunity* 34.4, pp. 492–504. ISSN: 10747613. DOI: 10.1016/j.immuni.2011.03.017.
- Chang, John T., Vikram. R. Palanivel, Ichiko. Kinjyo, Felix Schambach, Andrew M. Intlekofer, Arnob Banerjee, Sarah A. Longworth, Kristine E. Vinup, Paul Mrass, Jane Oliaro, Nigel Killeen, Jordan S. Orange, Sarah M. Russell, Wolfgang Weninger, and Steven L. Reiner (2007). “Asymmetric T Lymphocyte Division in the Initiation of Adaptive Immune Responses”. In: *Science* 315.5819, pp. 1687–1691. ISSN: 0036-8075. DOI: 10.1126/science.1139393.
- Chaplin, David D. (2010). “Overview of the immune response”. In: *Journal of Allergy and Clinical Immunology* 125.2, S345. ISSN: 10976825. DOI: 10.1016/j.jaci.2010.01.002.
- Chen, Zeyu, Zhicheng Ji, Shin Foong Ngiew, Sasikanth Manne, Zhangying Cai, Alexander C. Huang, John Johnson, Ryan P. Staupe, Bertram Bengsch, Caiyue Xu, Sixiang Yu, Makoto Kurachi, Ramin S. Herati, Laura A. Vella, Amy E. Baxter, Jennifer E. Wu, Omar Khan, Jean Christophe Beltra, Josephine R. Giles, Erietta Stelekati, Laura M. McLane, Chi Wai Lau, Xiaolu Yang, Shelley L. Berger, Golnaz Vahedi, Hongkai Ji, and E. John Wherry (2019). “TCF-1-Centered Transcriptional Network Drives an Effector versus Exhausted CD8 T Cell-Fate Decision”. In: *Immunity* 51.5, pp. 840–855. ISSN: 10974180. DOI: 10.1016/j.immuni.2019.09.013.

- Cho, Yi Li, Michael Flossdorf, Lorenz Kretschmer, Thomas Höfer, Dirk H. Busch, and Veit R. Buchholz (2017). “TCR Signal Quality Modulates Fate Decisions of Single CD4+ T Cells in a Probabilistic Manner”. In: *Cell Reports* 20.4, pp. 806–818. ISSN: 22111247. DOI: 10.1016/j.celrep.2017.07.005.
- Crauste, Fabien, Julien Mafille, Lilia Boucinha, Sophia Djebali, Olivier Gandrillon, Jacqueline Marvel, and Christophe Arpin (2017). “Identification of Nascent Memory CD8 T Cells and Modeling of Their Ontogeny”. In: *Cell Systems* 4.3, 306–317.e4. ISSN: 24054720. DOI: 10.1016/j.cels.2017.01.014.
- Croft, Michael (2003). “Co-stimulatory members of the TNFR family: Keys to effective T-cell immunity?” In: *Nature Reviews Immunology* 3.8, pp. 609–620. ISSN: 14741733. DOI: 10.1038/nri1148.
- Curtsinger, Julie M. and Matthew F. Mescher (2010). “Inflammatory cytokines as a third signal for T cell activation”. In: *Current Opinion in Immunology* 22.3, pp. 333–340. ISSN: 09527915. DOI: 10.1016/j.coi.2010.02.013.
- Dangi, Tanushree, Young Rock Chung, Nicole Palacio, and Pablo Penaloza-MacMaster (2020). “Interrogating Adaptive Immunity Using LCMV”. In: *Current Protocols in Immunology* 130.1, pp. 1–37. ISSN: 1934368X. DOI: 10.1002/cpim.99.
- De Boer, Rob J., Dirk Homann, and Alan S. Perelson (2003). “Different Dynamics of CD4+ and CD8+ T Cell Responses During and After Acute Lymphocytic Choriomeningitis Virus Infection”. In: *The Journal of Immunology* 171.8, pp. 3928–3935. ISSN: 0022-1767. DOI: 10.4049/jimmuno1.171.8.3928.
- De Boer, Rob J., Mihaela Oprea, Rustom Antia, Kaja Murali-Krishna, Rafi Ahmed, and Alan S. Perelson (2001). “Recruitment Times, Proliferation, and Apoptosis Rates during the CD8+ T-Cell Response to Lymphocytic Choriomeningitis Virus”. In: *Journal of Virology* 75.22, pp. 10663–10669. ISSN: 0022-538X. DOI: 10.1128/jvi.75.22.10663-10669.2001.
- De Boer, Rob J. and A. S. Perelson (1995). “Towards a general function describing t cell proliferation”. In: *Journal of Theoretical Biology* 175.4, pp. 567–576. ISSN: 00225193. DOI: 10.1006/jtbi.1995.0165.
- De Boer, Rob J. and Alan S. Perelson (2013). “Quantifying T lymphocyte turnover”. In: *Journal of Theoretical Biology* 327, pp. 45–87. ISSN: 00225193. DOI: 10.1016/j.jtbi.2012.12.025.
- DeTomaso, David, Matthew G. Jones, Meena Subramaniam, Tal Ashuach, Chun J. Ye, and Nir Yosef (2019). “Functional interpretation of single cell similarity maps”. In: *Nature Communications* 10.1. ISSN: 20411723. DOI: 10.1038/s41467-019-12235-0.
- Farber, Donna L., Mihai G. Netea, Andreas Radbruch, Klaus Rajewsky, and Rolf M. Zinkernagel (2016). “Immunological memory: Lessons from the past and a look to the future”. In: *Nature Reviews Immunology* 16.2, pp. 124–128. ISSN: 14741741. DOI: 10.1038/nri.2016.13.
- Finak, Greg, Andrew McDavid, Masanao Yajima, Jingyuan Deng, Vivian Gersuk, Alex K. Shalek, Chloe K. Slichter, Hannah W. Miller, M. Juliana McElrath, Martin Prlic, Peter S. Linsley, and Raphael Gottardo (2015). “MAST: A flexible statistical framework for assessing transcriptional changes and characterizing heterogeneity in single-cell RNA sequencing data”. In: *Genome Biology* 16.1, pp. 1–13. ISSN: 1474760X. DOI: 10.1186/s13059-015-0844-5.
- Friedman, Trevor, Robert Hastie, and Jerome Tibshirani (2014). *The Elements of Statistical Learning*, pp. 58–60. DOI: 10.1057/9780230355033.0018.
- Fröhlich, A, Jan Kisielow, Iwana Schmitz, Stefan Freigang, Abdijapar T Shamshiev, Jacqueline Weber, Benjamin J Marsland, Annette Oxenius, and Manfred Kopf (2009). “IL-21R on T Cells Is Critical”. In: *Science* June, pp. 1576–1580.
- Gallimore, By Awen, Ann Glithero, Andrew Godkin, Alain C Tissot, Andreas Plückthun, Tim Elliott, Hans Hengartner, and Rolf Zinkernagel (1998). “Induction and Exhaustion of Lymphocytic Chori-

- omeningitis Virus – specific Cytotoxic T Lymphocytes Visualized Using Class I – Peptide Complexes”. In: *Journal of Experimental Medicine* 187.9, pp. 1383–1393.
- Ganusov, Vitaly V (2007). “Discriminating between different pathways of memory CD8+ T cell differentiation.” In: *Journal of Immunology* 179.8, pp. 5006–5013. ISSN: 0022-1767. DOI: 179/8/5006[pii].
- Garrod, Kym R., Hélène D. Moreau, Zacarias Garcia, Fabrice Lemaître, Isabelle Bouvier, Matthew L. Albert, and Philippe Bousso (2012). “Dissecting T Cell Contraction In Vivo Using a Genetically Encoded Reporter of Apoptosis”. In: *Cell Reports* 2.5, pp. 1438–1447. ISSN: 22111247. DOI: 10.1016/j.celrep.2012.10.015.
- Gerlach, Carmen, Jan C. Rohr, Leila Perie, Nienke van Rooij, Joeren W.J. van Heijst, Arno Velds, Jos Urbanus, Shaling H. Naik, Heinz Jacobs, Joost B. Beltman, Rob J. de Boer, and Ton N. M. Schumacher (2013). “Heterogeneous differentiation patterns of individual CD8+ T cells”. In: *Science* 340.6132, pp. 635–639. ISSN: 0036-8075. DOI: 10.1126/science.1235487.
- Gerlach, Carmen, Jeroen W.J. van Heijst, Erwin Swart, Daoud Sie, Nicola Armstrong, Ron M. Kerkhoven, Dietmar Zehn, Michael J. Bevan, Koen Schepers, and Ton N.M. Schumacher (2010). “One naive T cell, multiple fates in CD8+ T cell differentiation”. In: *Journal of Experimental Medicine* 207.6, pp. 1235–1246. ISSN: 00221007. DOI: 10.1084/jem.20091175.
- Gerlach, Carmen, E. Ashley Moseman, Scott M. Loughhead, David Alvarez, Anthonie J. Zwijnenburg, Lisette Waanders, Rohit Garg, Juan C. de la Torre, and Ulrich H. von Andrian (2016). “The Chemokine Receptor CX3CR1 Defines Three Antigen-Experienced CD8 T Cell Subsets with Distinct Roles in Immune Surveillance and Homeostasis”. In: *Immunity* 45.6, pp. 1270–1284. ISSN: 10974180. DOI: 10.1016/j.immuni.2016.10.018.
- Gett, Amanda V. and Philip D. Hodgkin (1998). “Cell division regulates the T cell cytokine repertoire, revealing a mechanism underlying immune class regulation”. In: *Proceedings of the National Academy of Sciences of the United States of America* 95.16, pp. 9488–9493. ISSN: 00278424. DOI: 10.1073/pnas.95.16.9488.
- Ghoneim, Hazem E., Yiping Fan, Ardiana Moustaki, Hossam A. Abdelsamed, Pradyot Dash, Pranay Dogra, Robert Carter, Walid Awad, Geoff Neale, Paul G. Thomas, and Ben Youngblood (2017). “De Novo Epigenetic Programs Inhibit PD-1 Blockade-Mediated T Cell Rejuvenation”. In: *Cell* 170.1, 142–157.e19. ISSN: 10974172. DOI: 10.1016/j.cell.2017.06.007.
- Gillespie, Daniel T. (1976). “A general method for numerically simulating the stochastic time evolution of coupled chemical reactions”. In: *Journal of Computational Physics* 22.4, pp. 403–434. ISSN: 10902716. DOI: 10.1016/0021-9991(76)90041-3.
- Gini, Corrado (1921). “Measurement of Inequality of Incomes”. In: *The Economic Journal* 31.121, pp. 124–126.
- Gookin, Sara, Mingwei Min, Harsha Phadke, Mingyu Chung, Justin Moser, Iain Miller, Dylan Carter, and Sabrina L. Spencer (2017). “A map of protein dynamics during cell-cycle progression and cell-cycle exit”. In: *PLoS Biology* 15.9, pp. 1–25. ISSN: 15457885. DOI: 10.1371/journal.pbio.2003268.
- Gossel, Graeme, Thea Hogan, Daniel Cownden, Benedict Seddon, and Andrew J. Yates (2017). “Memory CD4 T cell subsets are kinetically heterogeneous and replenished from naive T cells at high levels”. In: *eLife* 6, pp. 1–29. ISSN: 2050084X. DOI: 10.7554/eLife.23013.
- Graef, Patricia, Veit R. Buchholz, Christian Stemmerger, Michael Flossdorf, Lynette Henkel, Matthias Schiemann, Ingo Drexler, Thomas Höfer, Stanley R. Riddell, and Dirk H. Busch (2014). “Serial Transfer of Single-Cell-Derived Immunocompetence Reveals Stemness of CD8+ Central Memory T Cells”. In: *Immunity* 41.1, pp. 116–126. ISSN: 10974180. DOI: 10.1016/j.immuni.2014.05.018.

- Grassmann, Simon, Lorenz Mihatsch, Jonas Mir, Atefeh Kazeroonian, Roza Rahimi, Sophie Flommersfeld, Kilian Schober, Inge Hensel, Justin Leube, Ludwig O. Pachmayr, Lorenz Kretschmer, Qin Zhang, Adrien Jolly, M. Zeeshan Chaudhry, Matthias Schiemann, Luka Cicin-Sain, Thomas Höfer, Dirk H. Busch, Michael Flossdorf, and Veit R. Buchholz (2020). “Early emergence of T central memory precursors programs clonal dominance during chronic viral infection”. In: *Nature Immunology* 21.12, pp. 1563–1573. ISSN: 15292916. DOI: 10.1038/s41590-020-00807-y.
- Gruener, Norbert H., Franziska Lechner, Maria-Christina Jung, Helmut Diepolder, Tilman Gerlach, Georg Lauer, Bruce Walker, John Sullivan, Rodney Phillips, Gerd R. Pape, and Paul Klenerman (2001). “Sustained Dysfunction of Antiviral CD8 + T Lymphocytes after Infection with Hepatitis C Virus”. In: *Journal of Virology* 75.12, pp. 5550–5558. ISSN: 0022-538X. DOI: 10.1128/jvi.75.12.5550-5558.2001.
- Gulati, Gungsagar S., Shaheen S. Sikandar, Daniel J. Wesche, Anoop Manjunath, Anjan Bharadwaj, Mark J. Berger, Francisco Ilagan, Angera H. Kuo, Robert W. Hsieh, Shang Cai, Maider Zabala, Ferenc A. Scheeren, Neethan A. Lobo, Dalong Qian, Feiqiao B. Yu, Frederick M. Dirbas, Michael F. Clarke, and Aaron M. Newman (2019). “Single-cell transcriptional diversity is a hallmark of developmental potential”. In: *bioRxiv* 411.January, pp. 405–411. DOI: 10.1101/649848.
- Guy, Clifford S., Kate M. Vignali, Jamshid Temirov, Matthew L. Bettini, Abigail E. Overacre, Matthew Smeltzer, Hui Zhang, Johannes B. Huppa, Yu Hwai Tsai, Camille Lobry, Jianming Xie, Peter J. Dempsey, Howard C. Crawford, Iannis Aifantis, Mark M. Davis, and Dario A.A. Vignali (2013). “Distinct TCR signaling pathways drive proliferation and cytokine production in T cells”. In: *Nature Immunology* 14.3, pp. 262–270. ISSN: 15292916. DOI: 10.1038/ni.2538.
- Haghverdi, Laleh, Maren Büttner, F. Alexander Wolf, Florian Büttner, and Fabian J. Theis (2016). “Diffusion pseudotime robustly reconstructs lineage branching”. In: *Nature Methods* 13.10, pp. 845–848. ISSN: 15487105. DOI: 10.1038/nmeth.3971.
- Hannier, S, M Tournier, G Bismuth, and F Triebel (1998). “CD3/TCR complex-associated lymphocyte activation gene-3 molecules inhibit CD3/TCR signaling.” In: *Journal of immunology (Baltimore, Md. : 1950)* 161.8, pp. 4058–65. ISSN: 0022-1767.
- Hawkins, E D, J F Markham, L P McGuinness, and P D Hodgkin (2009). “A single-cell pedigree analysis of alternative stochastic lymphocyte fates.” In: *Proceedings of the National Academy of Sciences of the United States of America* 106.32, pp. 13457–13462. ISSN: 0027-8424. DOI: 10.1073/pnas.0905629106.
- He, Ran, Shiyue Hou, Cheng Liu, Anli Zhang, Qiang Bai, Miao Han, Yu Yang, Gang Wei, Ting Shen, Xinxin Yang, Lifan Xu, Xiangyu Chen, Yaxing Hao, Pengcheng Wang, Chuhong Zhu, Juanjuan Ou, Houjie Liang, Ting Ni, Xiaoyan Zhang, Xinyuan Zhou, Kai Deng, Yaokai Chen, Yadong Luo, Jianqing Xu, Hai Qi, Yuzhang Wu, and Lilin Ye (2016). “Follicular CXCR5-expressing CD8+ T cells curtail chronic viral infection”. In: *Nature* 537.7620, pp. 412–416. ISSN: 14764687. DOI: 10.1038/nature19317.
- Heijst, Jeroen W. J. van, Carmen Gerlach, Erwin Swart, Daoud Sie, Cláudio Nunes-Alves, Ron M. Kerkhoven, Ramon Arens, Margarida Correia-Neves, Koen Schepers, and Ton N. M. Schumacher (2013). “Recruitment of Antigen-Specific CD8+ T Cells in Response to Infection is Markedly Efficient”. In: *Science* 325.9, pp. 1265–1269. ISSN: 1098-6596. arXiv: arXiv:1011.1669v3.
- Heinzel, Susanne, Tran Binh Giang, Andrey Kan, Julia M. Marchingo, Bryan K. Lye, Lynn M. Corcoran, and Philip D. Hodgkin (2017). “A Myc-dependent division timer complements a cell-death timer to regulate T cell and B cell responses”. In: *Nature Immunology* 18.1, pp. 96–103. ISSN: 15292916. DOI: 10.1038/ni.3598.

- Hendriks, Jenny, Loes A. Gravesteyn, Kiki Tesselaar, René A.W. Van Lier, Ton N.M. Schumacher, and Jannie Borst (2000). “CD27 is required for generation and long-term maintenance of T cell immunity”. In: *Nature Immunology* 1.5, pp. 433–440. ISSN: 15292908. DOI: 10.1038/80877.
- Hendriks, Jenny, Yanling Xiao, John W. A. Rossen, Koenraad F. van der Sluijs, Kazuo Sugamura, Naoto Ishii, and Jannie Borst (2005). “ During Viral Infection of the Respiratory Tract, CD27, 4-1BB, and OX40 Collectively Determine Formation of CD8 + Memory T Cells and Their Capacity for Secondary Expansion ”. In: *The Journal of Immunology* 175.3, pp. 1665–1676. ISSN: 0022-1767. DOI: 10.4049/jimmunol.175.3.1665.
- Henning, Amanda N., Rahul Roychoudhuri, and Nicholas P. Restifo (2018). “Epigenetic control of CD8+ T’cell differentiation”. In: *Nature Reviews Immunology* 18.5, pp. 340–356. ISSN: 14741741. DOI: 10.1038/nri.2017.146.
- Homann, Dirk, Luc Teyton, and Michael B.A. Oldstone (2001). “Differential regulation of antiviral T-cell immunity results in stable CD8+ but declining CD4+ T-cell memory”. In: *Nature Medicine* 7.8, pp. 913–919. ISSN: 10788956. DOI: 10.1038/90950.
- Hudson, William H., Julia Gensheimer, Masao Hashimoto, Andreas Wieland, Rajesh M. Valanparambil, Peng Li, Jian Xin Lin, Bogumila T. Konieczny, Se Jin Im, Gordon J. Freeman, Warren J. Leonard, Haydn T. Kissick, and Rafi Ahmed (2019). “Proliferating Transitory T Cells with an Effector-like Transcriptional Signature Emerge from PD-1+ Stem-like CD8+ T Cells during Chronic Infection”. In: *Immunity* 51.6, 1043–1058.e4. ISSN: 10974180. DOI: 10.1016/j.immuni.2019.11.002.
- Im, Se Jin, Masao Hashimoto, Michael Y. Gerner, Junghwa Lee, Haydn T. Kissick, Matheus C. Burger, Qiang Shan, J. Scott Hale, Judong Lee, Tahseen H. Nasti, Arlene H. Sharpe, Gordon J. Freeman, Ronald N. Germain, Helder I. Nakaya, Hai-Hui Xue, and Rafi Ahmed (2016). “Defining CD8+ T cells that provide the proliferative burst after PD-1 therapy”. In: *Nature* 537.7620, pp. 417–421. ISSN: 0028-0836. DOI: 10.1038/nature19330. arXiv: 15334406.
- Iwasaki, Akiko and Ruslan Medzhitov (2015). “Control of adaptive immunity by the innate immune system”. In: *Nature Immunology* 16.4, pp. 343–353. ISSN: 15292916. DOI: 10.1038/ni.3123.
- Jadhav, Rohit R., Se Jin Im, Bin Hu, Masao Hashimoto, Peng Li, Jian Xin Lin, Warren J. Leonard, William J. Greenleaf, Rafi Ahmed, and Jorg J. Goronzy (2019). “Epigenetic signature of PD-1+ TCF1+ CD8 T cells that act as resource cells during chronic viral infection and respond to PD-1 blockade”. In: *Proceedings of the National Academy of Sciences of the United States of America* 116.28, pp. 14113–14118. ISSN: 10916490. DOI: 10.1073/pnas.1903520116.
- Jeannot, Grégoire, Caroline Boudousquié, Noémie Gardiol, Joonsoo Kang, Joerg Huelsken, and Werner Held (2010). “Essential role of the Wnt pathway effector Tcf-1 for the establishment of functional CD8 T cell memory”. In: *Proceedings of the National Academy of Sciences of the United States of America* 107.21, pp. 9777–9782. ISSN: 00278424. DOI: 10.1073/pnas.0914127107.
- Jin, Hyun Tak, Ana C. Anderson, Wendy G. Tan, Erin E. West, Sang Jun Ha, Koichi Araki, Gordon J. Freeman, Vijay K. Kuchroo, and Rafi Ahmed (2010). “Cooperation of Tim-3 and PD-1 in CD8 T-cell exhaustion during chronic viral infection”. In: *Proceedings of the National Academy of Sciences of the United States of America* 107.33, pp. 14733–14738. ISSN: 00278424. DOI: 10.1073/pnas.1009731107.
- Johnnidis, Jonathan B., Yuki Muroyama, Shin Foong Ngiow, Zeyu Chen, Sasikanth Manne, Zhangying Cai, Shufei Song, Jesse M. Platt, Jason M. Schenkel, Mohamed Abdel-Hakeem, Jean Christophe Beltra, Allison R. Greenplate, Mohammed Alkhatim A. Ali, Kito Nzingha, Josephine R. Giles, Christelle Harly, John Attanasio, Kristen E. Pauken, Bertram Bengsch, Michael A. Paley, Vesselin T. Tomov, Makoto Kurachi, Dario A.A. Vignali, Arlene H. Sharpe, Steven L. Reiner, Avinash Bhandoola, F.

- Bradley Johnson, and E. John Wherry (2021). “Inhibitory signaling sustains a distinct early memory CD8+ T cell precursor that is resistant to DNA damage”. In: *Science immunology* 6.55. ISSN: 24709468. DOI: 10.1126/sciimmunol.abe3702.
- Jones, R. Brad, Lishomwa C. Ndhlovu, Jason D. Barbour, Prameet M. Sheth, Aashish R. Jha, Brian R. Long, Jessica C. Wong, Malathy Satkunarajah, Marc Schweneker, Joan M. Chapman, Gabor Gyenes, Bahareh Vali, Martin D. Hycza, Feng Yun Yue, Colin Kovacs, Aref Sassi, Mona Loutfy, Roberta Halpenny, Desmond Persad, Gerald Spotts, Frederick M. Hecht, Tae Wook Chun, Joseph M. McCune, Rupert Kaul, James M. Rini, Douglas F. Nixon, and Mario A. Ostrowski (2008). “Tim-3 expression defines a novel population of dysfunctional T cells with highly elevated frequencies in progressive HIV-1 infection”. In: *Journal of Experimental Medicine* 205.12, pp. 2763–2779. ISSN: 15409538. DOI: 10.1084/jem.20081398.
- Kaech, Susan M. and Rafi Ahmed (2001). “Memory CD8+ T cell differentiation: Initial antigen encounter triggers a developmental program in naïve cells”. In: *Nature Immunology* 2.5, pp. 415–422. ISSN: 15292908. DOI: 10.1038/87720.
- Kaech, Susan M. and Weiguo Cui (2012). “Transcriptional control of effector and memory CD8+ T cell differentiation”. In: *Nature Reviews Immunology* 12.11, pp. 749–761. ISSN: 14741733. DOI: 10.1038/nri3307.
- Kaech, Susan M., Joyce T. Tan, E. John Wherry, Bogumila T. Konieczny, Charles D. Surh, and Rafi Ahmed (2003). “Selective expression of the interleukin 7 receptor identifies effector CD8 T cells that give rise to long-lived memory cells”. In: *Nature Immunology* 4.12, pp. 1191–1198. ISSN: 15292908. DOI: 10.1038/ni1009.
- Kakaradov, Boyko, Janilyn Arsenio, Christella E. Widjaja, Zhaoren He, Stefan Aigner, Patrick J. Metz, Bingfei Yu, Ellen J. Wehrens, Justine Lopez, Stephanie H. Kim, Elina I. Zuniga, Ananda W. Gol-drath, John T. Chang, and Gene W. Yeo (2017). “Early transcriptional and epigenetic regulation of CD8+ T cell differentiation revealed by single-cell RNA sequencing”. In: *Nature Immunology* 18.4, pp. 422–432. ISSN: 1529-2908. DOI: 10.1038/ni.3688.
- Kallies, Axel, Dietmar Zehn, and Daniel T. Utzschneider (2020). “Precursor exhausted T cells: key to successful immunotherapy?” In: *Nature Reviews Immunology* 20.2, pp. 128–136. ISSN: 14741741. DOI: 10.1038/s41577-019-0223-7.
- Keppler, Selina J., Kerstin Theil, Smiljka Vucikujka, and Peter Aichele (2009). “Effector T-cell differentiation during viral and bacterial infections: Role of direct IL-12 signals for cell fate decision of CD8+ T cells”. In: *European Journal of Immunology* 39.7, pp. 1774–1783. ISSN: 00142980. DOI: 10.1002/eji.200839093.
- Kernbauer, Elisabeth, Verena Maier, Isabella Rauch, Mathias Müller, and Thomas Decker (2013). “Route of Infection Determines the Impact of Type I Interferons on Innate Immunity to *Listeria monocytogenes*”. In: *PLoS ONE* 8.6. ISSN: 19326203. DOI: 10.1371/journal.pone.0065007.
- Khan, Omar, Josephine R. Giles, Sierra McDonald, Sasikanth Manne, Shin Foong Ngiow, Kunal P. Patel, Michael T. Werner, Alexander C. Huang, Katherine A. Alexander, Jennifer E. Wu, John Attanasio, Patrick Yan, Sangeeth M. George, Bertram Bengsch, Ryan P. Staupé, Greg Donahue, Wei Xu, Ravi K. Amaravadi, Xiaowei Xu, Giorgos C. Karakousis, Tara C. Mitchell, Lynn M. Schuchter, Jonathan Kaye, Shelley L. Berger, and E. John Wherry (2019). “TOX transcriptionally and epigenetically programs CD8+ T cell exhaustion”. In: *Nature* 571.7764, pp. 211–218. ISSN: 14764687. DOI: 10.1038/s41586-019-1325-x.

- Khan, Shaniya H. and Vladimir P. Badovinac (2015). “Listeria monocytogenes: a model pathogen to study antigen-specific memory CD8 T cell responses”. In: *Seminars in Immunopathology* 37.3, pp. 301–310. ISSN: 18632300. DOI: 10.1007/s00281-015-0477-5. arXiv: 15334406.
- Kinjyo, Ichiko, Jim Qin, Sioh-Yang Tan, Cameron J. Wellard, Paulus Mrass, William Ritchie, Atsushi Doi, Lois L. Cavanagh, Michio Tomura, Asako Sakaue-Sawano, Osami Kanagawa, Atsushi Miyawaki, Philip D. Hodgkin, and Wolfgang Weninger (2015). “Real-time tracking of cell cycle progression during CD8+ effector and memory T-cell differentiation”. In: *Nature Communications* 6.May 2014, p. 6301. ISSN: 2041-1723. DOI: 10.1038/ncomms7301.
- Kohler, Brynja (2007). “Mathematically modeling dynamics of T cell responses: Predictions concerning the generation of memory cells”. In: *Journal of Theoretical Biology* 245.4, pp. 669–676. ISSN: 00225193. DOI: 10.1016/j.jtbi.2006.10.017.
- Korsunsky, Ilya, Nghia Millard, Jean Fan, Kamil Slowikowski, Fan Zhang, Kevin Wei, Yuriy Baglaenko, Michael Brenner, Po ru Loh, and Soumya Raychaudhuri (2019). “Fast, sensitive and accurate integration of single-cell data with Harmony”. In: *Nature Methods* 16.12, pp. 1289–1296. ISSN: 15487105. DOI: 10.1038/s41592-019-0619-0.
- Kowalczyk, Monika S., Itay Tirosh, Dirk Heckl, Tata Nageswara Rao, Atray Dixit, Brian J. Haas, Rebekka K. Schneider, Amy J. Wagers, Benjamin L. Ebert, and Aviv Regev (2015). “Single-cell RNA-seq reveals changes in cell cycle and differentiation programs upon aging of hematopoietic stem cells”. In: *Genome Research* 25.12, pp. 1860–1872. ISSN: 15495469. DOI: 10.1101/gr.192237.115.
- Kretschmer, Lorenz, Michael Flossdorf, Jonas Mir, Yi-Li Cho, Marten Plambeck, Irina Treise, Albulena Toska, Susanne Heinzel, Matthias Schiemann, Dirk H. Busch, and Veit R. Buchholz (2020). “Differential expansion of T central memory precursor and effector subsets is regulated by division speed”. In: *Nature Communications* 11.1. ISSN: 20411723. DOI: 10.1038/s41467-019-13788-w.
- Kurachi, Makoto, R. Anthony Barnitz, Nir Yosef, Pamela M. Odorizzi, Michael A. Diiorio, Madeleine E. Lemieux, Kathleen Yates, Jernej Godec, Martin G. Klatt, Aviv Regev, E. John Wherry, and W. Nicholas Haining (2014). “The transcription factor BATF operates as an essential differentiation checkpoint in early effector CD8 + T cells”. In: *Nature Immunology* 15.4, pp. 373–383. ISSN: 15292916. DOI: 10.1038/ni.2834.
- Kurd, Nadia S., Zhaoren He, Tiani L. Louis, J. Justin Milner, Kyla D. Omilusik, Wenhao Jin, Matthew S. Tsai, Christella E. Widjaja, Jad N. Kanbar, Jocelyn G. Olvera, Tiffani Tysl, Lauren K. Quezada, Brigid S. Boland, Wendy J. Huang, Cornelis Murre, Ananda W. Goldrath, Gene W. Yeo, and John T. Chang (2020). “Early precursors and molecular determinants of tissue-resident memory CD8 + T lymphocytes revealed by single-cell RNA sequencing”. In: *Science Immunology* 5.47. ISSN: 24709468. DOI: 10.1126/sciimmunol.aaz6894.
- La Manno, Gioele, Ruslan Soldatov, Amit Zeisel, Emelie Braun, Hannah Hochgerner, Viktor Petukhov, Katja Lidschreiber, Maria E. Kastriiti, Peter Lönnerberg, Alessandro Furlan, Jean Fan, Lars E. Borm, Zehua Liu, David van Bruggen, Jimin Guo, Xiaoling He, Roger Barker, Erik Sundström, Gonçalo Castelo-Branco, Patrick Cramer, Igor Adameyko, Sten Linnarsson, and Peter V. Kharchenko (2018). “RNA velocity of single cells”. In: *Nature* 560.7719, pp. 494–498. ISSN: 14764687. DOI: 10.1038/s41586-018-0414-6.
- Laidlaw, Brian J., Joseph E. Craft, and Susan M. Kaech (2016). “The multifaceted role of CD4+ T cells in CD8+ T cell memory”. In: *Nature Reviews Immunology* 16.2, pp. 102–111. ISSN: 14741741. DOI: 10.1038/nri.2015.10.

- Lestas, Ioannis, Johan Paulsson, Nicholas E Ross, and Glenn Vinnicombe (2008). “Noise in Gene Regulatory Networks”. In: *Special Issue on Systems Biology* January, pp. 189–200. ISSN: 0018-9286. DOI: 10.1109/TAC.2007.911347.
- Lin, Wen Hsuan W., Simone A. Nish, Bonnie Yen, Yen Hua Chen, William C. Adams, Radomir Kratchmarov, Nyanza J. Rothman, Avinash Bhandoola, Hai Hui Xue, and Steven L. Reiner (2016). “CD8+ T Lymphocyte Self-Renewal during Effector Cell Determination”. In: *Cell Reports* 17.7, pp. 1773–1782. ISSN: 22111247. DOI: 10.1016/j.celrep.2016.10.032.
- Ludewig, Burkhard, Philippe Krebs, Tobias Junt, Helen Metters, Neville J. Ford, Roy M. Anderson, and Gennady Bocharov (2004). “Determining control parameters for dendritic cell-cytotoxic T lymphocyte interaction”. In: *European Journal of Immunology* 34.9, pp. 2407–2418. ISSN: 00142980. DOI: 10.1002/eji.200425085.
- Mackanness, George B. (1964). “The Immunological Basis of Acquired Cellular resistance”. In: *Journal of Geotechnical and Geoenvironmental Engineering ASCE* 137.84 m, pp. 105–120.
- Malek, Thomas R. and Iris Castro (2010). “Interleukin-2 Receptor Signaling: At the Interface between Tolerance and Immunity”. In: *Immunity* 33.2, pp. 153–165. ISSN: 10747613. DOI: 10.1016/j.immuni.2010.08.004.
- Man, Kevin, Sarah S. Gabriel, Yang Liao, Renee Gloury, Simon Preston, Darren C. Henstridge, Marc Pellegrini, Dietmar Zehn, Friederike Berberich-Siebelt, Mark A. Febbraio, Wei Shi, and Axel Kallies (2017). “Transcription Factor IRF4 Promotes CD8+ T Cell Exhaustion and Limits the Development of Memory-like T Cells during Chronic Infection”. In: *Immunity* 47.6, 1129–1141.e5. ISSN: 10974180. DOI: 10.1016/j.immuni.2017.11.021.
- Man, Kevin, Maria Miasari, Wei Shi, Annie Xin, Darren C. Henstridge, Simon Preston, Marc Pellegrini, Gabrielle T. Belz, Gordon K. Smyth, Mark A. Febbraio, Stephen L. Nutt, and Axel Kallies (2013). “The transcription factor IRF4 is essential for TCR affinity-mediated metabolic programming and clonal expansion of T cells”. In: *Nature Immunology* 14.11, pp. 1155–1165. ISSN: 15292908. DOI: 10.1038/ni.2710.
- Marchingo, Julia M., Andrey Kan, Robyn M. Sutherland, Ken R. Duffy, Cameron J. Wellard, Gabrielle T. Belz, Andrew M. Lew, Mark R. Dowling, Susanne Heinzl, and Philipp D. Hodgkin (2014). “Antigen affinity, costimulation, and cytokine inputs sum linearly to amplify T cell expansion”. In: *Science* 346.6213, pp. 1123–1127. ISSN: 0036-8075. DOI: 10.1126/science.1260044.
- Marchingo, Julia M., Giulio Prevedello, Andrey Kan, Suzanne Heinzl, Philipp D. Hodgkin, and Ken R. Duffy (2016). “T-cell stimuli independently sum to regulate an inherited clonal division fate”. In: *Nature Communications* 7, p. 13540. ISSN: 2041-1723. DOI: 10.1038/ncomms13540.
- Marchingo, Julia M., Linda V. Sinclair, Andrew Jm Howden, and Doreen A. Cantrell (2020). “Quantitative analysis of how myc controls t cell proteomes and metabolic pathways during t cell activation”. In: *eLife* 9, pp. 1–23. ISSN: 2050084X. DOI: 10.7554/eLife.53725.
- Martinez, Gustavo J., Renata M. Pereira, Tarmo Äijö, Edward Y. Kim, Francesco Marangoni, Matthew E. Pipkin, Susan Togher, Vigo Heissmeyer, Yi Chen Zhang, Shane Crotty, Edward D. Lamperti, K. Mark Ansel, Thorsten R. Mempel, Harri Lähdesmäki, Patrick G. Hogan, and Anjana Rao (2015). “The Transcription Factor NFAT Promotes Exhaustion of Activated CD8+ T Cells”. In: *Immunity* 42.2, pp. 265–278. ISSN: 10974180. DOI: 10.1016/j.immuni.2015.01.006.
- Masopust, David and Jason M. Schenkel (2013). “The integration of T cell migration, differentiation and function”. In: *Nature Reviews Immunology* 13.5, pp. 309–320. ISSN: 14741733. DOI: 10.1038/nri3442.

- Matiašová, Anna, Juraj Ševc, Jaromír Mikeš, Rastislav Jendželovský, Zuzana Daxnerová, and Peter Fedoročko (2014). “Flow cytometric determination of 5-bromo-2-deoxyuridine pharmacokinetics in blood serum after intraperitoneal administration to rats and mice”. In: *Histochemistry and Cell Biology* 142.6, pp. 703–712. ISSN: 1432119X. DOI: 10.1007/s00418-014-1253-7.
- Matloubian, By Mehrdad, T Somasundaram, Suhas R Kolhekar, R Selvakumar, and Rafi Ahmed (1990). “From the Department of Microbiology and Immunology, UCLA School of Medicine, Los Angeles, California 90024”. In: *October* 172.October, pp. 1043–1048.
- McCarthy, Davis J., Kieran R. Campbell, Aaron T.L. Lun, and Quin F. Wills (2017). “Scater: Pre-processing, quality control, normalization and visualization of single-cell RNA-seq data in R”. In: *Bioinformatics* 33.8, pp. 1179–1186. ISSN: 14602059. DOI: 10.1093/bioinformatics/btw777.
- McGregor, D. D., F. T. Koster, and G. B. Mackaness (1970). “Biological sciences: The short lived small lymphocyte as a mediator of cellular immunity”. In: *Nature* 228.5274, pp. 855–856. ISSN: 00280836. DOI: 10.1038/228855a0.
- Mercado, Roberto, Sujata Vijh, S. Elise Allen, Kristen Kerksiek, Ingrid M. Pilip, and Eric G. Pamer (2000). “Early Programming of T Cell Populations Responding to Bacterial Infection”. In: *The Journal of Immunology* 165.12, pp. 6833–6839. ISSN: 0022-1767. DOI: 10.4049/jimmunol.165.12.6833.
- Milner, J. Justin, Hongtuyet Nguyen, Kyla Omilusik, Miguel Reina-Campos, Matthew Tsai, Clara Toma, Arnaud Delpoux, Brigid S. Boland, Stephen M. Hedrick, John T. Chang, and Ananda W. Goldrath (2020). “Delineation of a molecularly distinct terminally differentiated memory CD8 T cell population”. In: *Proceedings of the National Academy of Sciences of the United States of America* 117.41, pp. 25667–25678. ISSN: 10916490. DOI: 10.1073/pnas.2008571117.
- Miyagawa, Fumi, Hong Zhang, Atshushi Terunuma, Keiko Ozato, Yutaka Tagaya, and Stephen I. Katz (2012). “Interferon regulatory factor 8 integrates T-cell receptor and cytokine-signaling pathways and drives effector differentiation of CD8 T cells”. In: *Proceedings of the National Academy of Sciences of the United States of America* 109.30, pp. 12123–12128. ISSN: 00278424. DOI: 10.1073/pnas.1201453109.
- Moskophidis, D., M. Battagay, M. Van den Broek, E. Laine, U. Hoffmann-Rohrer, and R. M. Zinkernagel (1995). “Role of virus and host variables in virus persistence or immunopathological disease caused by a non-cytolytic virus”. In: *Journal of General Virology* 76.2, pp. 381–391. ISSN: 00221317. DOI: 10.1099/0022-1317-76-2-381.
- Muckenfuss, Ralph S, Charles Armstrong, and L.T. Webster (1933). “Only Species”. In: *The Journal of the American Medical Association*, 103.10, pp. 15–17.
- Murali-Krishna, Kaja, John D. Altman, M. Suresh, David J.D. Sourdive, Allan J. Zajac, Joseph D. Miller, Jill Slansky, and Rafi Ahmed (1998). “Counting antigen-specific CD8 T cells: A reevaluation of bystander activation during viral infection”. In: *Immunity* 8.2, pp. 177–187. ISSN: 10747613. DOI: 10.1016/S1074-7613(00)80470-7.
- Murali-Krishna, Kaja, Lisa L. Lau, Suryaprakash Sambhara, Francois Lemonnier, John D. Altman, and Rafi Ahmed (1999). “Persistence of memory CD8 T cells in MHC class I-deficient mice”. In: *Science* 286.5443, pp. 1377–1381. ISSN: 00368075. DOI: 10.1126/science.286.5443.1377.
- Oestreich, Kenneth J., Hyesuk Yoon, Rafi Ahmed, and Jeremy M. Boss (2008). “NFATc1 Regulates PD-1 Expression upon T Cell Activation”. In: *The Journal of Immunology* 181.7, pp. 4832–4839. ISSN: 0022-1767. DOI: 10.4049/jimmunol.181.7.4832.

- Pace, Luigia, Christel Goudot, Elina Zueva, Paul Gueguen, Nina Burgdorf, Joshua J. Waterfall, Jean Pierre Quivy, Geneviève Almouzni, and Sebastian Amigorena (2018). “The epigenetic control of stemness in CD8+ T cell fate commitment”. In: *Science* 359.6372, pp. 177–186. ISSN: 10959203. DOI: 10.1126/science.aah6499.
- Pais Ferreira, Daniela, Joana Gomes Silva, Tania Wyss, Silvia A. Fuertes Marraco, Leonardo Scarpellino, Mélanie Charmoy, Roeltje Maas, Imran Siddiqui, Li Tang, Johanna A. Joyce, Mauro Delorenzi, Sanjiv A. Luther, Daniel E. Speiser, and Werner Held (2020). “Central memory CD8+ T cells derive from stem-like Tcf7hi effector cells in the absence of cytotoxic differentiation”. In: *Immunity* 53.5, 985–1000.e11. ISSN: 10974180. DOI: 10.1016/j.immuni.2020.09.005.
- Pandit, Aridaman and Rob J. De Boer (2019). “Stochastic inheritance of division and death times determines the size and phenotype of CD8+ T cell families”. In: *Frontiers in Immunology* 10.MAR, pp. 1–12. ISSN: 16643224. DOI: 10.3389/fimmu.2019.00436.
- Parry, Richard V., Jens M. Chemnitz, James L. Riley, Kenneth A. Frauwirth, Inbal Braunstein, Sumire V. Kobayashi, Peter S. Linsley, and Craig B. Thompson (2004). “CTLA-4 and PD-1 Receptors Inhibit T-Cell Activation by Distinct Mechanisms.” In: *Blood* 104.11, pp. 2657–2657. ISSN: 0006-4971. DOI: 10.1182/blood.v104.11.2657.2657.
- Pauken, Kristen E., Morgan A. Sammons, Pamela M. Odorizzi, Sasikanth Manne, Jernej Godec, Omar Khan, Adam M. Drake, Zeyu Chen, Debattama R. Sen, Makoto Kurachi, R. Anthony Barnitz, Caroline Bartman, Bertram Bengsch, Alexander C. Huang, Jason M. Schenkel, Golnaz Vahedi, W. Nicholas Haining, Shelley L. Berger, E. John Wherry, Sasikanth Manne, Jernej Godec, Omar Khan, Adam M. Drake, Zeyu Chen, Debattama R. Sen, Makoto Kurachi, R. Anthony Barnitz, Caroline Bartman, Bertram Bengsch, Alexander C. Huang, Jason M. Schenkel, Golnaz Vahedi, W. Nicholas Haining, Shelley L. Berger, and E. John Wherry (2016). “Epigenetic stability of exhausted T cells limits durability of reinvigoration by PD-1 blockade”. In: *Science* 354.6316, pp. 1160–1164. ISSN: 1095-9203. DOI: 10.1126/science.aaf5530.
- Pauken, Kristen E. and E. John Wherry (2015). “Overcoming T cell exhaustion in infection and cancer”. In: *Trends in Immunology* 36.4, pp. 265–276. ISSN: 14714981. DOI: 10.1016/j.it.2015.02.008. arXiv: NIHMS150003.
- Philip, Mary, Lauren Fairchild, Liping Sun, Ellen L. Horste, Steven Camara, Mojdeh Shakiba, Andrew C. Scott, Agnes Viale, Peter Lauer, Taha Merghoub, Matthew D. Hellmann, Jedd D. Wolchok, Christina S. Leslie, and Andrea Schietinger (2017). “Chromatin states define tumour-specific T cell dysfunction and reprogramming”. In: *Nature* 545.7655, pp. 452–456. ISSN: 14764687. DOI: 10.1038/nature22367.
- Polański, Krzysztof, Matthew D. Young, Zhichao Miao, Kerstin B. Meyer, Sarah A. Teichmann, and Jong Eun Park (2020). “BBKNN: Fast batch alignment of single cell transcriptomes”. In: *Bioinformatics* 36.3, pp. 964–965. ISSN: 14602059. DOI: 10.1093/bioinformatics/btz625.
- Preston, Gavin C., Linda V. Sinclair, Aneesa Kaskar, Jens L. Hukelmann, Maria N. Navarro, Isabel Ferrero, H. Robson MacDonald, Victoria H. Cowling, and Doreen A. Cantrell (2015). “Single cell tuning of Myc expression by antigen receptor signal strength and interleukin-2 in T lymphocytes”. In: *The EMBO Journal* 34.15, pp. 2008–2024. ISSN: 0261-4189. DOI: 10.15252/embj.201490252.
- Pritykin, Yuri, Joris van der Veeke, Allison R. Pine, Yi Zhong, Merve Sahin, Linas Mazutis, Dana Pe’er, Alexander Y. Rudensky, and Christina S. Leslie (2021). “A unified atlas of CD8 T cell dysfunctional states in cancer and infection”. In: *Molecular Cell* 81.11, 2477–2493.e10. ISSN: 10972765. DOI: 10.1016/j.molcel.2021.03.045.

- Pucci, Bruna, Margaret Kasten, and Antonio Giordano (2003). “Cell cycle and apoptosis”. In: *Cell Proliferation* 36.3, pp. 165–175. ISSN: 09607722. DOI: 10.1046/j.1365-2184.2003.00267.x.
- Punt, Jenni, Sharon A. Stranford, Patricia P. Jones, and Judith A. Owen (2009). *Immunology*. 7th. W.H. Freeman, pp. 385–415. ISBN: 978-1319267223.
- Quigley, Michael, Florencia Pereyra, Björn Nilsson, Filippos Porichis, Catia Fonseca, Quentin Eichbaum, Boris Julg, Jonathan L. Jesneck, Kathleen Brosnahan, Sabrina Imam, Kate Russell, Ildiko Toth, Alicja Piechocka-Trocha, Douglas Dolfi, Jill M. Angelosanto, Alison Crawford, Haina Shin, Douglas S. Kwon, Jennifer Zupkosky, Loise Francisco, Gordon J. Freeman, E. John Wherry, Daniel E. Kaufmann, Bruce D. Walker, Benjamin Ebert, and W. Nicholas Haining (2010). “Transcriptional analysis of HIV-specific CD8+ T cells shows that PD-1 inhibits T cell function by upregulating BATF”. In: *Nature Medicine* 16.10, pp. 1147–1151. ISSN: 10788956. DOI: 10.1038/nm.2232.
- Reiner, Steven L. (2007). “Development in Motion: Helper T Cells at Work”. In: *Cell* 129.1, pp. 33–36. ISSN: 00928674. DOI: 10.1016/j.cell.2007.03.019.
- Russell, John H. and Timothy J. Ley (2002). “Lymphocyte-mediated cytotoxicity”. In: *Annual Review of Immunology* 20.6, pp. 323–370. ISSN: 07320582. DOI: 10.1146/annurev.immunol.20.100201.131730.
- Rygiel, Tomasz P., Eva S. K. Rijkers, Talitha de Ruiter, Ellen H. Stolte, Martin van der Valk, Guus F. Rimmelzwaan, Louis Boon, Anton M. van Loon, Frank E. Coenjaerts, Robert M. Hoek, Kiki Tesselaar, and Linde Meyaard (2009). “Lack of CD200 Enhances Pathological T Cell Responses during Influenza Infection”. In: *The Journal of Immunology* 183.3, pp. 1990–1996. ISSN: 0022-1767. DOI: 10.4049/jimmunol.0900252.
- Sade-Feldman, Moshe, Keren Yizhak, Stacey L. Bjorgaard, John P. Ray, Carl G. de Boer, Russell W. Jenkins, David J. Lieb, Jonathan H. Chen, Dennie T. Frederick, Michal Barzily-Rokni, Samuel S. Freeman, Alexandre Reuben, Paul J. Hoover, Alexandra Chloé Villani, Elena Ivanova, Andrew Portell, Patrick H. Lizotte, Amir R. Aref, Jean Pierre Eliane, Marc R. Hammond, Hans Vitzthum, Shauna M. Blackmon, Bo Li, Vancheswaran Gopalakrishnan, Sangeetha M. Reddy, Zachary A. Cooper, Cloud P. Paweletz, David A. Barbie, Anat Stemmer-Rachamimov, Keith T. Flaherty, Jennifer A. Wargo, Genevieve M. Boland, Ryan J. Sullivan, Gad Getz, and Nir Hacohen (2018). “Defining T Cell States Associated with Response to Checkpoint Immunotherapy in Melanoma”. In: *Cell* 175.4, 998–1013.e20. ISSN: 10974172. DOI: 10.1016/j.cell.2018.10.038.
- Sallusto, Federica, Danielle Lenig, Reinhold Förster, Martin Lipp, and Antonio Lanzavecchia (1999). “Two subsets of memory T lymphocytes with distinct homing potentials and effector functions”. In: *Nature* 401.6754, pp. 708–712. ISSN: 00280836. DOI: 10.1038/44385.
- Sarkar, Surojit, Vandana Kalia, W. Nicholas Haining, Bogumila T. Konieczny, Shruti Subramaniam, and Rafi Ahmed (2008). “Functional and genomic profiling of effector CD8 T cell subsets with distinct memory fates”. In: *Journal of Experimental Medicine* 205.3, pp. 625–640. ISSN: 00221007. DOI: 10.1084/jem.20071641.
- Satija, Rahul, Jeffrey A. Farrell, David Gennert, Alexander F. Schier, and Aviv Regev (2015). “Spatial reconstruction of single-cell gene expression data”. In: *Nature Biotechnology* 33.5, pp. 495–502. ISSN: 15461696. DOI: 10.1038/nbt.3192.
- Schietinger, Andrea, Mary Philip, Varintra E. Krisnawan, Edison Y. Chiu, Jeffrey J. Delrow, Ryan S. Basom, Peter Lauer, Dirk G. Brockstedt, Sue E. Knoblaugh, Günter J. Hämmerling, Todd D. Schell, Natalio Garbi, and Philip D. Greenberg (2016). “Tumor-Specific T Cell Dysfunction Is a Dynamic

- Antigen-Driven Differentiation Program Initiated Early during Tumorigenesis”. In: *Immunity* 45.2, pp. 389–401. ISSN: 10974180. DOI: 10.1016/j.immuni.2016.07.011.
- Schluns, Kimberly S., William C. Kieper, Stephen C. Jameson, and Leo Lefrançois (2000). “Interleukin-7 mediates the homeostasis of naïve and memory CD8 T cells in vivo”. In: *Nature Immunology* 1.5, pp. 426–432. ISSN: 15292908. DOI: 10.1038/80868.
- Schluns, Kimberly S. and Leo Lefrançois (2003). “Cytokine control of memory T-cell development and survival”. In: *Nature Reviews Immunology* 3.4, pp. 269–279. ISSN: 14741733. DOI: 10.1038/nri1052.
- Schwartz, Ronald H. (2003). “T cell anergy”. In: *Annual Review of Immunology* 21, pp. 305–334. ISSN: 07320582. DOI: 10.1146/annurev.immunol.21.120601.141110.
- Scott, Andrew C., Friederike Dündar, Paul Zumbo, Smita S. Chandran, Christopher A. Klebanoff, Mojdeh Shakiba, Prerak Trivedi, Laura Menocal, Heather Appleby, Steven Camara, Dmitriy Zamarin, Tyler Walther, Alexandra Snyder, Matthew R. Femia, Elizabeth A. Comen, Hannah Y. Wen, Matthew D. Hellmann, Niroshana Anandasabapathy, Yong Liu, Nasser K. Altorki, Peter Lauer, Olivier Levy, Michael S. Glickman, Jonathan Kaye, Doron Betel, Mary Philip, and Andrea Schietinger (2019). “TOX is a critical regulator of tumour-specific T cell differentiation”. In: *Nature* 571.7764, pp. 270–274. ISSN: 14764687. DOI: 10.1038/s41586-019-1324-y.
- Sen, Debattama R., James Kaminski, R. Anthony Barnitz, Makoto Kurachi, Ulrike Gerdemann, Kathleen B. Yates, Hsiao-Wei Tsao, Jernej Godec, Martin W. LaFleur, Flavian D. Brown, Pierre Tonnerre, Raymond T. Chung, Damien C. Tully, Todd M. Allen, Nicole Frahm, Goerg M. Lauer, E. John Wherry, Nir Yosef, and W. Nicholas Haining (2016). “The epigenetic landscape of T cell exhaustion”. In: *Science* 354.6316, pp. 1165–1169. ISSN: 0036-8075. DOI: 10.1126/science.aae0491.
- Seo, Wooseok, Chandsultana Jerin, and Hiroyoshi Nishikawa (2021). “Transcriptional regulatory network for the establishment of CD8+ T cell exhaustion”. In: *Experimental and Molecular Medicine* 53.2, pp. 202–209. ISSN: 20926413. DOI: 10.1038/s12276-021-00568-0.
- Shankar, P., M. Russo, B. Harnisch, M. Patterson, P. Skolnik, and J. Lieberman (2000). “Impaired function of circulating HIV-specific CD8+ T cells in chronic human immunodeficiency virus infection”. In: *Blood* 96.9, pp. 3094–3101. ISSN: 00064971. DOI: 10.1182/blood.v96.9.3094.
- Sharpe, Arlene H. and Kristen E. Pauken (2018). “The diverse functions of the PD1 inhibitory pathway”. In: *Nature Reviews Immunology* 18.3, pp. 153–167. ISSN: 14741741. DOI: 10.1038/nri.2017.108.
- Sinclair, Linda V., Julia Rolf, Elizabeth Emslie, Yun Bo Shi, Peter M. Taylor, and Doreen A. Cantrell (2013). “Control of amino-acid transport by antigen receptors coordinates the metabolic reprogramming essential for T cell differentiation”. In: *Nature Immunology* 14.5, pp. 500–508. ISSN: 15292908. DOI: 10.1038/ni.2556.
- Smith-Garvin, Jennifer E., Gary A. Koretzky, and Martha S. Jordan (2009). “T cell activation”. In: *Annual Review of Immunology* 27, pp. 591–619. ISSN: 07320582. DOI: 10.1146/annurev.immunol.021908.132706.
- Snell, Laura M., Bethany L. MacLeod, Jaclyn C. Law, Ivan Osokine, Heidi J. Elsaesser, Kebria Hezaveh, Russell J. Dickson, Marc A. Gavin, Cynthia J. Guidos, Tracy L. McGaha, and David G. Brooks (2018). “CD8+ T Cell Priming in Established Chronic Viral Infection Preferentially Directs Differentiation of Memory-like Cells for Sustained Immunity”. In: *Immunity* 49.4, 678–694.e5. ISSN: 10974180. DOI: 10.1016/j.immuni.2018.08.002.
- Stemberger, Christian, Katharina M. Huster, Martina Koffler, Florian Anderl, Matthias Schiemann, Hermann Wagner, and Dirk H. Busch (2007). “A Single Naive CD8+ T Cell Precursor Can Develop

- into Diverse Effector and Memory Subsets”. In: *Immunity* 27.6, pp. 985–997. ISSN: 10747613. DOI: 10.1016/j.immuni.2007.10.012.
- Stephen, Tom L., Kyle K. Payne, Ricardo A. Chaurio, Michael J. Allegranza, Hengrui Zhu, Jairo Perez-Sanz, Alfredo Perales-Puchalt, Jenny M. Nguyen, Ana E. Vara-Ailor, Evgeniy B. Eruslanov, Mark E. Borowsky, Rugang Zhang, Terri M. Laufer, and Jose R. Conejo-Garcia (2017). “SATB1 Expression Governs Epigenetic Repression of PD-1 in Tumor-Reactive T Cells”. In: *Immunity* 46.1, pp. 51–64. ISSN: 10974180. DOI: 10.1016/j.immuni.2016.12.015.
- Stinchcombe, Jane C. and Gillian M. Griffiths (2007). “Secretory mechanisms in cell-mediated cytotoxicity”. In: *Annual Review of Cell and Developmental Biology* 23, pp. 495–517. ISSN: 10810706. DOI: 10.1146/annurev.cellbio.23.090506.123521.
- Stoeckius, Marlon, Christoph Hafemeister, William Stephenson, Brian Houck-Loomis, Pratip K. Chattopadhyay, Harold Swerdlow, Rahul Satija, and Peter Smibert (2017). “Simultaneous epitope and transcriptome measurement in single cells”. In: *Nature Methods* 14.9, pp. 865–868. ISSN: 15487105. DOI: 10.1038/nmeth.4380.
- Subramanian, Vijay G., Ken R. Duffy, Marian L. Turner, and Philip D. Hodgkin (2008). “Determining the expected variability of immune responses using the cyton model”. In: *Journal of Mathematical Biology* 56.6, pp. 861–892. ISSN: 03036812. DOI: 10.1007/s00285-007-0142-2.
- Sullivan, Brian M., Sébastien F. Emonet, Megan J. Welch, Andrew M. Lee, Kevin P. Campbell, Juan C. De La Torre, and Michael B. Oldstone (2011). “Point mutation in the glycoprotein of lymphocytic choriomeningitis virus is necessary for receptor binding, dendritic cell infection, and long-term persistence”. In: *Proceedings of the National Academy of Sciences of the United States of America* 108.7, pp. 2969–2974. ISSN: 00278424. DOI: 10.1073/pnas.1019304108.
- Surh, Charles D. and Jonathan Sprent (2008). “Homeostasis of Naive and Memory T Cells”. In: *Immunity* 29.6, pp. 848–862. ISSN: 10747613. DOI: 10.1016/j.immuni.2008.11.002.
- Tirosh, Itay, Benjamin Izar, Sanjay M. Prakadan, Marc H. Wadsworth, Daniel Treacy, John J. Trombetta, Asaf Rotem, Christopher Rodman, Christine Lian, George Murphy, Mohammad Fallahi-Sichani, Ken Dutton-Regester, Jia Ren Lin, Ofir Cohen, Parin Shah, Diana Lu, Alex S. Genshaft, Travis K. Hughes, Carly G.K. Ziegler, Samuel W. Kazer, Aleth Gaillard, Kellie E. Kolb, Alexandra Chloé Villani, Cory M. Johannessen, Aleksandr Y. Andreev, Eliezer M. Van Allen, Monica Bertagnolli, Peter K. Sorger, Ryan J. Sullivan, Keith T. Flaherty, Dennie T. Frederick, Judit Jané-Valbuena, Charles H. Yoon, Orit Rozenblatt-Rosen, Alex K. Shalek, Aviv Regev, and Levi A. Garraway (2016). “Dissecting the multicellular ecosystem of metastatic melanoma by single-cell RNA-seq”. In: *Science* 352.6282, pp. 189–196. ISSN: 10959203. DOI: 10.1126/science.aad0501.
- Traag, V. A., L. Waltman, and N. J. van Eck (2019). “From Louvain to Leiden: guaranteeing well-connected communities”. In: *Scientific Reports* 9.1, pp. 1–12. ISSN: 20452322. DOI: 10.1038/s41598-019-41695-z. arXiv: 1810.08473.
- Traub, B Y Erich (1936). “The epidemiology of lymphocytic choriomeningitis in white mice”. In: *Journal of Experimental Medicine* 63, pp. 533–546.
- Utzschneider, Daniel T., Mélanie Charmoy, Vijaykumar Chennupati, Laurène Pousse, Daniela Pais Ferreira, Sandra Calderon-Copete, Maxime Danilo, Francesca Alfei, Maike Hofmann, Dominik Wieland, Sylvain Pradervand, Robert Thimme, Dietmar Zehn, and Werner Held (2016a). “T Cell Factor 1-Expressing Memory-like CD8+ T Cells Sustain the Immune Response to Chronic Viral Infections”. In: *Immunity* 45.2, pp. 415–427. ISSN: 10974180. DOI: 10.1016/j.immuni.2016.07.021.

- (2016b). “T Cell Factor 1-Expressing Memory-like CD8+ T Cells Sustain the Immune Response to Chronic Viral Infections”. In: *Immunity* 45.2, pp. 415–427. ISSN: 10974180. DOI: 10.1016/j.immuni.2016.07.021.
- Utzschneider, Daniel T., Sarah S. Gabriel, David Chisanga, Renee Gloury, Patrick M. Gubser, Ajithkumar Vasanthakumar, Wei Shi, and Axel Kallies (2020). “Early precursor T cells establish and propagate T cell exhaustion in chronic infection”. In: *Nature Immunology* 21.10, pp. 1256–1266. ISSN: 15292916. DOI: 10.1038/s41590-020-0760-z.
- Utzschneider, Daniel T., Amandine Legat, Silvia a Fuertes Marraco, Lucie Carrié, Immanuel Luescher, Daniel E. Speiser, and Dietmar Zehn (2013). “T cells maintain an exhausted phenotype after antigen withdrawal and population reexpansion.” In: *Nature Immunology* 14.6, pp. 603–610. ISSN: 1529-2916. DOI: 10.1038/ni.2606.
- Venzon, Author D J and S H Moolgavkar (1988). “A Method for Computing Profile-Likelihood-”. In: *Journal of the Royal Statistical Society: Series C (Applied Statistics)* 37.1, pp. 87–94.
- Verdon, Daniel J., Matthias Mulazzani, and Misty R. Jenkins (2020). “Cellular and molecular mechanisms of CD8+ T cell differentiation, dysfunction and exhaustion”. In: *International Journal of Molecular Sciences* 21.19, pp. 1–28. ISSN: 14220067. DOI: 10.3390/ijms21197357.
- Virgin, Herbert W., E. John Wherry, and Rafi Ahmed (2009). “Redefining Chronic Viral Infection”. In: *Cell* 138.1, pp. 30–50. ISSN: 00928674. DOI: 10.1016/j.cell.2009.06.036.
- Wang, Xiaochen, Qifeng He, Haiyuan Shen, Anliang Xia, Wenfang Tian, Weiwei Yu, and Beicheng Sun (2019). “TOX promotes the exhaustion of antitumor CD8+ T cells by preventing PD1 degradation in hepatocellular carcinoma”. In: *Journal of Hepatology* 71.4, pp. 731–741. ISSN: 16000641. DOI: 10.1016/j.jhep.2019.05.015.
- Waterhouse, Paul, Josef M. Penninger, Emma Timms, Andrew Wakeham, Arda Shahinian, Kelvin P. Lee, Craig B. Thompson, Henrik Griesser, and Tak W. Mak (1995). “Lymphoproliferative disorders with early lethality in mice deficient in Ctlα-4”. In: *Science* 270.5238, pp. 985–988. ISSN: 00368075. DOI: 10.1126/science.270.5238.985.
- Wherry, E. John and Rafi Ahmed (2004). “MINIREVIEW Memory CD8 T-Cell Differentiation during Viral Infection”. In: *Society* 78.11, pp. 5535–5545. ISSN: 0022-538X. DOI: 10.1128/JVI.78.11.5535.
- Wherry, E. John, Joseph N. Blattman, Kaja Murali-Krishna, Robbert van der Most, and Rafi Ahmed (2003a). “Viral Persistence Alters CD8 T-Cell Immunodominance and Tissue Distribution and Results in Distinct Stages of Functional Impairment”. In: *Journal of Virology* 77.8, pp. 4911–4927. ISSN: 0022-538X. DOI: 10.1128/jvi.77.8.4911-4927.2003.
- Wherry, E. John, Sang Jun Ha, Susan M. Kaech, W. Nicholas Haining, Surojit Sarkar, Vandana Kalia, Shruti Subramaniam, Joseph N. Blattman, Daniel L. Barber, and Rafi Ahmed (2007). “Molecular Signature of CD8+ T Cell Exhaustion during Chronic Viral Infection”. In: *Immunity* 27.4, pp. 670–684. ISSN: 10747613. DOI: 10.1016/j.immuni.2007.09.006. arXiv: NIHMS150003.
- Wherry, E. John and Makoto Kurachi (2015). “Molecular and cellular insights into T cell exhaustion”. In: *Nature Reviews Immunology* 15.8, pp. 486–499. ISSN: 1474-1733. DOI: 10.1038/nri3862.
- Wherry, E. John, Volker Teichgräber, Todd C. Becker, David Masopust, Susan M. Kaech, Rustom Antia, Ulrich H. von Andrian, and Rafi Ahmed (2003b). “Lineage relationship and protective immunity of memory CD8T cell subsets”. In: *Nature Immunology* 4.3, pp. 225–234. ISSN: 15292908. DOI: 10.1038/ni889.

- Windt, Gerritje J.W. van der and Erika L. Pearce (2012). “Metabolic switching and fuel choice during T-cell differentiation and memory development”. In: *Immunological Reviews* 249.1, pp. 27–42. ISSN: 01052896. DOI: 10.1111/j.1600-065X.2012.01150.x.
- Wolf, F. Alexander, Fiona K. Hamey, Mireya Plass, Jordi Solana, Joakim S. Dahlin, Berthold Göttgens, Nikolaus Rajewsky, Lukas Simon, and Fabian J. Theis (2019). “PAGA: graph abstraction reconciles clustering with trajectory inference through a topology preserving map of single cells”. In: *Genome Biology* 20.1, pp. 1–9. ISSN: 1474760X. DOI: 10.1186/s13059-019-1663-x.
- Workman, Creg J. and Dario A. A. Vignali (2005). “Negative Regulation of T Cell Homeostasis by Lymphocyte Activation Gene-3 (CD223)”. In: *The Journal of Immunology* 174.2, pp. 688–695. ISSN: 0022-1767. DOI: 10.4049/jimmunol.174.2.688.
- Yang, Mengdi, Qianru Huang, Changcan Li, Zhiyuan Jiang, Jing Sun, Zhiyu Wang, Rui Liang, Dan Li, Bin Li, and Hui Zhao (2021). “TOX Acts as a Tumor Suppressor by Inhibiting mTOR Signaling in Colorectal Cancer”. In: *Frontiers in Immunology* 12.April. ISSN: 16643224. DOI: 10.3389/fimmu.2021.647540.
- Yao, Chen, Guohua Lou, Hong Wei Sun, Ziang Zhu, Yi Sun, Zeyu Chen, Daniel Chauss, E. Ashley Moseman, Jun Cheng, Marc A. D’Antonio, Wangke Shi, Junwei Shi, Kohei Kometani, Tomohiro Kurosaki, E. John Wherry, Behdad Afzali, Luca Gattinoni, Yuwen Zhu, Dorian B. McGavern, John J. O’Shea, Pamela L. Schwartzberg, and Tuoqi Wu (2021). “BACH2 enforces the transcriptional and epigenetic programs of stem-like CD8+ T cells”. In: *Nature Immunology* 22.3, pp. 370–380. ISSN: 15292916. DOI: 10.1038/s41590-021-00868-7.
- Yao, Chen, Hong Wei Sun, Neal E. Lacey, Yun Ji, E. Ashley Moseman, Han Yu Shih, Elisabeth F. Heuston, Martha Kirby, Stacie Anderson, Jun Cheng, Omar Khan, Robin Handon, Julie Reilley, Jessica Fioravanti, Jinhui Hu, Selamawit Gossa, E. John Wherry, Luca Gattinoni, Dorian B. McGavern, John J. O’Shea, Pamela L. Schwartzberg, and Tuoqi Wu (2019). “Single-cell RNA-seq reveals TOX as a key regulator of CD8+ T cell persistence in chronic infection”. In: *Nature Immunology* 20.7, pp. 890–901. ISSN: 15292916. DOI: 10.1038/s41590-019-0403-4.
- Yoon, Heesik, Taeg S. Kim, and Thomas J. Braciale (2010). “The cell cycle time of CD8+ T cells responding in Vivo is controlled by the type of antigenic stimulus”. In: *PLoS ONE* 5.11, pp. 1–12. ISSN: 19326203. DOI: 10.1371/journal.pone.0015423.
- Youngblood, Ben, J. Scott Hale, Haydn T. Kissick, Eunseon Ahn, Xiaojin Xu, Andreas Wieland, Koichi Araki, Erin E. West, Hazem E. Ghoneim, Yiping Fan, Pranay Dogra, Carl W. Davis, Bogumila T. Konieczny, Rustom Antia, Xiaodong Cheng, and Rafi Ahmed (2017). “Effector CD8 T cells dedifferentiate into long-lived memory cells”. In: *Nature* 552.7685, pp. 404–409. ISSN: 14764687. DOI: 10.1038/nature25144.
- Zajac, Allan J., Joseph N. Blattman, Kaja Murali-Krishna, David J.D. Sourdive, M. Suresh, John D. Altman, and Rafi Ahmed (1998). “Viral immune evasion due to persistence of activated T cells without effector function”. In: *Journal of Experimental Medicine* 188.12, pp. 2205–2213. ISSN: 00221007. DOI: 10.1084/jem.188.12.2205.
- Zander, Ryan, David Schauder, Gang Xin, Christine Nguyen, Xiaopeng Wu, Allan Zajac, and Weiguo Cui (2019). “CD4+ T Cell Help Is Required for the Formation of a Cytolytic CD8+ T Cell Subset that Protects against Chronic Infection and Cancer”. In: *Immunity* 51.6, pp. 1028–1042. ISSN: 10974180. DOI: 10.1016/j.immuni.2019.10.009.
- Zhang, Nu and Michael J. Bevan (2011). “CD8+ T Cells: Foot Soldiers of the Immune System”. In: *Immunity* 35.2, pp. 161–168. ISSN: 10747613. DOI: 10.1016/j.immuni.2011.07.010.

- Zhang, Xiaohong, Siquan Sun, Inkyu Hwang, David F. Tough, and Jonathan Sprent (1998). “Potent and selective stimulation of memory-phenotype CD8+ T cells in vivo by IL-15”. In: *Immunity* 8.5, pp. 591–599. ISSN: 10747613. DOI: 10.1016/S1074-7613(00)80564-6.
- Zhao, Dong-Mei, Shuyang Yu, Xinyuan Zhou, Jodie S. Haring, Werner Held, Vladimir P. Badovinac, John T. Harty, and Hai-Hui Xue (2010). “Constitutive Activation of Wnt Signaling Favors Generation of Memory CD8 T Cells”. In: *The Journal of Immunology* 184.3, pp. 1191–1199. ISSN: 0022-1767. DOI: 10.4049/jimmunol.0901199.
- Zhou, Xin, Srividya Ramachandran, Margaret Mann, and Daniel L. Popkin (2012). “Role of lymphocytic choriomeningitis virus (LCMV) in understanding viral immunology: Past, present and future”. In: *Viruses* 4.11, pp. 2650–2669. ISSN: 19994915. DOI: 10.3390/v4112650.
- Ziegler, Steven F., Fred Ramsdell, and Mark R. Alderson (1994). “The activation antigen CD69”. In: *Stem Cells* 12.5, pp. 456–465. ISSN: 15494918. DOI: 10.1002/stem.5530120502.
- Zinkernagel, Rolf M. and Peter C. Doherty (1973). “Cytotoxic thymus-derived lymphocytes in cerebrospinal fluid mice with lymphocytic choriomeningitis virus”. In: *Thymus* 156.August, pp. 628–633. ISSN: 0022-1007.

List of Figures

3.1. Subset-defining proliferation speed predicted by progressive model of differentiation.	31
3.2. Memory precursor (MP) cells incorporate less BrdU compared to non-memory precursor (non-MP) cells at day 4.5 p.i.	32
3.3. MP and non-MP T cells display differential cell cycle phase distribution after labelling with short BrdU pulses.	33
3.4. Quantification of the cell cycle speed <i>in vivo</i> reveals that memory precursor cells divide slower compared to non-memory precursors.	35
3.5. P14 T cells follow diverse fates after LCMV Armstrong infection.	37
3.6. The progeny sizes at day 8 p.i. with LCMV Armstrong range from many small clones to a few dominating giants.	38
3.7. Time-resolved transcriptional analysis of P14 T cells during LCMV Armstrong infection.	41
3.8. P14 T cells after LCMV Armstrong infection, exhibiting memory signature genes occupy distinct regions in the UMAP compared to P14 T cells expressing effector signature genes.	42
3.9. Identification of T cell subsets based on unsupervised clustering.	43
3.10. Subset-specific cell cycle drop out with the MP compartment arresting from cell cycle earlier compared to the EMP and EFF subsets.	46
3.11. Identification of subsets in the P14 T cell responses after LCMV Armstrong infection based on the expression of marker genes and cell cycle stage.	48
3.12. Inference of a descriptive mathematical model for CD8 ⁺ T cell responses after LCMV Armstrong infection using scRNA-seq trajectory analysis.	51
3.13. Single-cell transcriptomics analysis of OTI T cells after the infection with <i>L.m.-OVA</i>	53
3.14. Gene expression in scRNA-seq data coincides with protein expression.	54
3.15. Inference of a mathematical model topology to describe the OTI T cell response after <i>L.m.-OVA</i> infection using RNA velocities and PAGA connectivity graphs.	55
3.16. A by cell cycle drop-out extended progressive model supports the fate decision of P14 T cells during LCMV Armstrong infection.	57
3.17. Verification of cell cycle arrest progressive model using the Markov stochastic simulation.	58
4.1. Transcriptomic comparison of the P14 response during the acute phase of LCMV Armstrong and LCMV clone 13 infection.	61

4.2. Distinct T cell exhaustion signatures detectable early during LCMV clone 13 infection.	63
4.3. Subset identification based on the clustering by the Leiden algorithm identifies a LCMV Armstrong unique EFF cluster.	64
4.4. Changes in the proliferation activity among the most distinctive drivers between LCMV Armstrong and clone 13 at day 6 p.i.	67
4.5. A greater extent of cell cycle arrest is observed in clone 13-derived P14 T cells.	71
4.6. Mathematical models tested by forward selection to explain the fate-decision of P14 T cells during LCMV Armstrong and clone 13 infection.	74
4.7. Results after simultaneous fitting to the P14 T cell responses after the infection with LCMV Armstrong and clone 13.	75
4.8. A uniform model correctly depicts the population dynamics for the P14 T cell subsets and their proliferation and cell cycle exit kinetics.	76
4.9. Verification of the mathematical model by simulating the single CD8 ⁺ T cell responses after LCMV Armstrong and clone 13 infection.	77
4.10. Differential gene expression analysis suggests that the fate of P14 T cells during clone 13 LCMV infection is decided as early as day 4.5.	80
4.11. P14 T cells from day 4.5 LCMV clone 13 p.i. retain the potential to become functional effector cells.	82
4.12. According to RNA velocity analysis EFF subset cells are not formed during the infection with LCMV clone 13.	84
4.13. <i>Tox</i> ^{-/-} P14 T cells during LCMV clone 13 infection develop into terminal effector subsets.	87
4.14. Deflection in the progressive direction of differentiation during a clone 13 infection prevents the formation of effector cells.	88
4.15. Exhaustion driven only by the MP and non-MP subset explains the single cell transfer responses to LCMV clone 13.	89
4.16. EFF T cells do not exhaust upon re-transfer into chronic LCMV infection.	92
A.1. The progressive model of T cell differentiation describes the first and second order moments of the P14 T cell response after LCMV Armstrong infection.	169
A.2. Sorting strategy for the re-isolation of CD8 ⁺ T cells after infection with LCMV Armstrong or <i>L.m.-OVA</i>	170
A.3. Inference of cell cycle arrest from scRNA-seq data and RNA velocities.	171
A.4. Grouping Leiden clusters to define T cell subsets following an LCMV Armstrong infection.	172
A.5. Diffusion pseudo-time predicts similar differentiation trajectory as the RNA velocity and the CytoTRACE analysis.	172

A.6. During infection with <i>L.m.</i> -OVA cells from the MP subset cycle slower compared to the non-MP subset.	173
B.1. Analysis of the P14 T cells transcriptomes during the expansion phase of the T cell differentiation.	175
B.2. Disparate single-cell fates after the infection with LCMV Armstrong or clone 13.	176
B.3. TOX is expressed to low levels after acute infection with LCMV Armstrong. . .	177
B.4. Mathematical modelling of P14 T cell responses allowing exhaustion only of the MP subset.	178

List of Tables

3.1. Best fit parameters to the by cell cycle drop out extended progressive model of differentiation.	59
4.1. Best fit parameters to the by cell cycle drop out extended progressive model of differentiation where the model was fitted to the data for LCMV Armstrong and clone 13 simultaneously.	78
6.1. List of experimental equipment used in this study.	107
6.2. List of chemical compounds and reagents used in this study.	108
6.3. List of buffers and media used in this study.	109
6.4. List of antibodies used for analyses by flow cytometry.	110
6.5. List of oligonucleotide-conjugated antibodies used for protein expression analyses in combination with scRNA-seq.	111
6.6. List of primers used in this study.	112
6.7. Thermocycle protocol for hashtags	118
6.8. Thermocycle protocol for antibody-derived tags	118
A.1. Summary statistics and bootstrapped errors of the 40 single-cell derived P14 T cell responses at day 8 following the infection with LCMV Armstrong.	168
B.1. Summary statistics of the 29 single-cell derived P14 T cell responses at day 8 p.i. LCMV clone 13 with bootstrapped errors.	175
C.1. Summary of experimental data used for mathematical modelling in this study.	181

A. Appendix I

Table A.1.: Summary statistics and bootstrapped errors of the 40 single-cell derived P14 T cell responses at day 8 following the infection with LCMV Armstrong.

statistical quantity	subset	data
mean	total cell number	$(1577 \pm 846.)$
	absolute number of MP	(19.4 ± 11.3)
	absolute number of EMP	(907 ± 599)
	absolute number of EFF	$(636. \pm 357)$
CV	total cell number	(3.5 ± 1.1)
	absolute number of MP	(3.7 ± 0.8)
	absolute number of EMP	(3.6 ± 0.9)
	absolute number of EFF	(3.6 ± 1.1)
correlation coefficient	absolute number of MP vs. EMP	(0.79 ± 0.36)
	absolute number of MP vsb EFF	(0.48 ± 0.81)
	absolute number of EMP vs. EFF	(0.88 ± 0.16)
Gini coefficient	total cell number	(0.91)

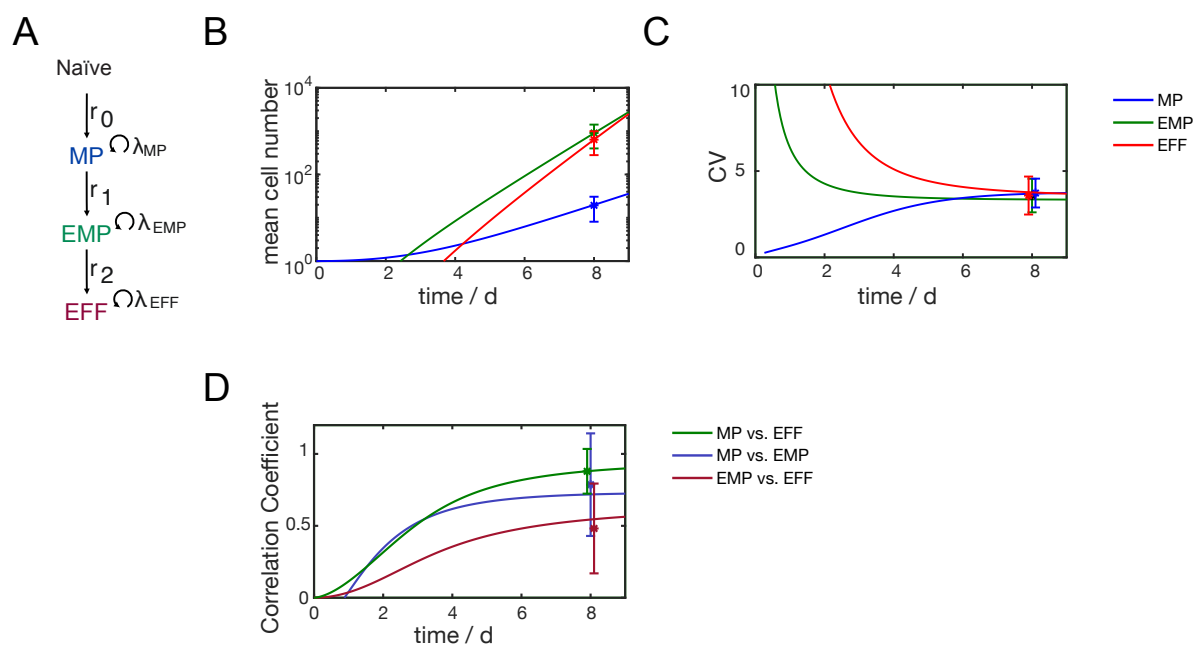


Figure A.1.: The progressive model of T cell differentiation describes the first and second order moments of the P14 T cell response after LCMV Armstrong infection. **A** Topology of the progressive model. The differentiation rates are described by r_{0-1} and the subset-specific proliferation rates are represented as λ_{MP} , λ_{EMP} and λ_{EFF} . The best fit of the progressive model to **B** the means, **C** the coefficients of variation and **D** the three pair-wise correlation coefficients. Data as in Figure 3.5 and 3.6

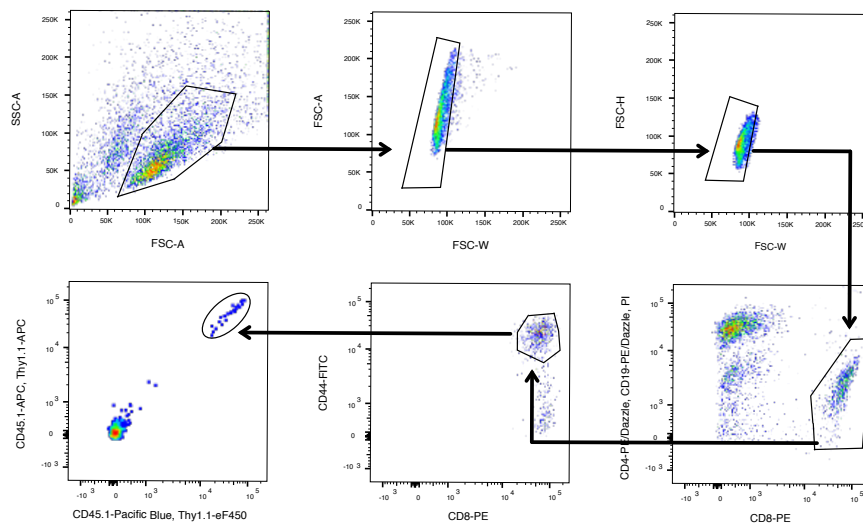


Figure A.2.: Sorting strategy for the re-isolation of CD8⁺ T cells after infection with LCMV Armstrong or *L.m.-OVA*. Pseudo-colour FACS plots are showing the gating strategy for the scRNA-seq experiments. The re-isolation of the P14 T cells from the spleens at day 6 p.i. with LCMV Armstrong is shown as representative. The same gating strategy was applied for the re-isolation of the P14 or OTI T cells after LCMV clone 13 or *L.m.-OVA* infection, respectively.

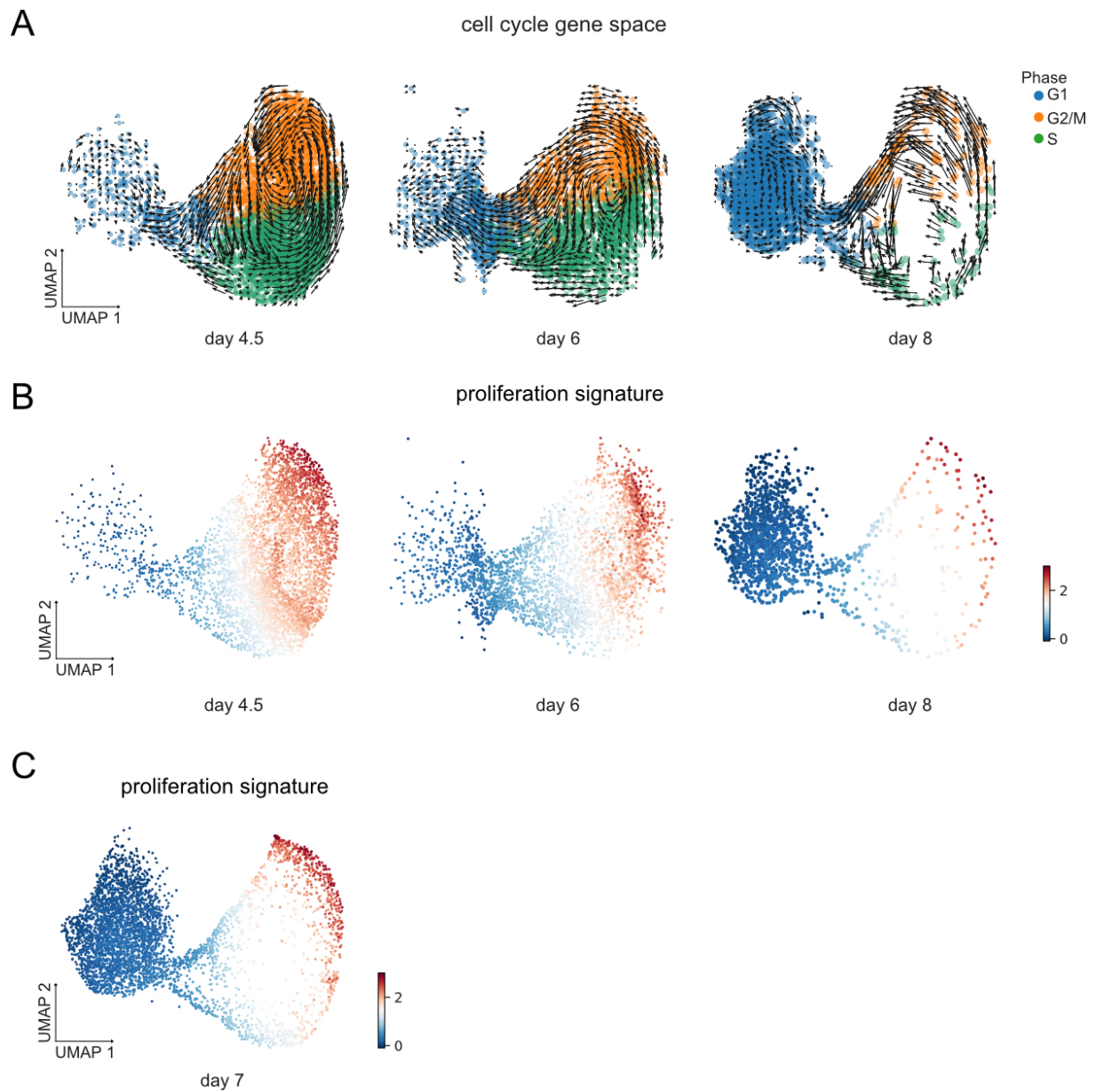


Figure A.3.: Inference of cell cycle arrest from scRNA-seq data and RNA velocities. **A- B** UMAP representation computed on cell cycle genes from Tirosh et al. 2016 at the days 4.5, 6 and 8 **A** with RNA velocities as in Figure 3.10 **C** and **A** displaying the proliferation signature score. **C** As in **B**, but at day 7 p.i.

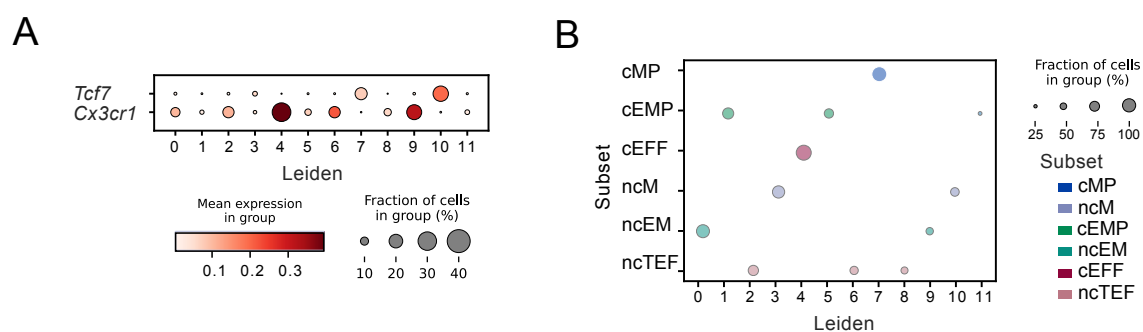


Figure A.4.: Grouping Leiden clusters to define T cell subsets following an LCMV Armstrong infection. **A** Dot plot depicting the expression of *Tcf7* and *Cx3cr1* genes in each Leiden cluster. Colour represents the mean expression and dot size, the fraction of cells in each group. **B** Composition of subsets based on the Leiden clusters. Dot size represents the fraction of cells from the contributing Leiden cluster.

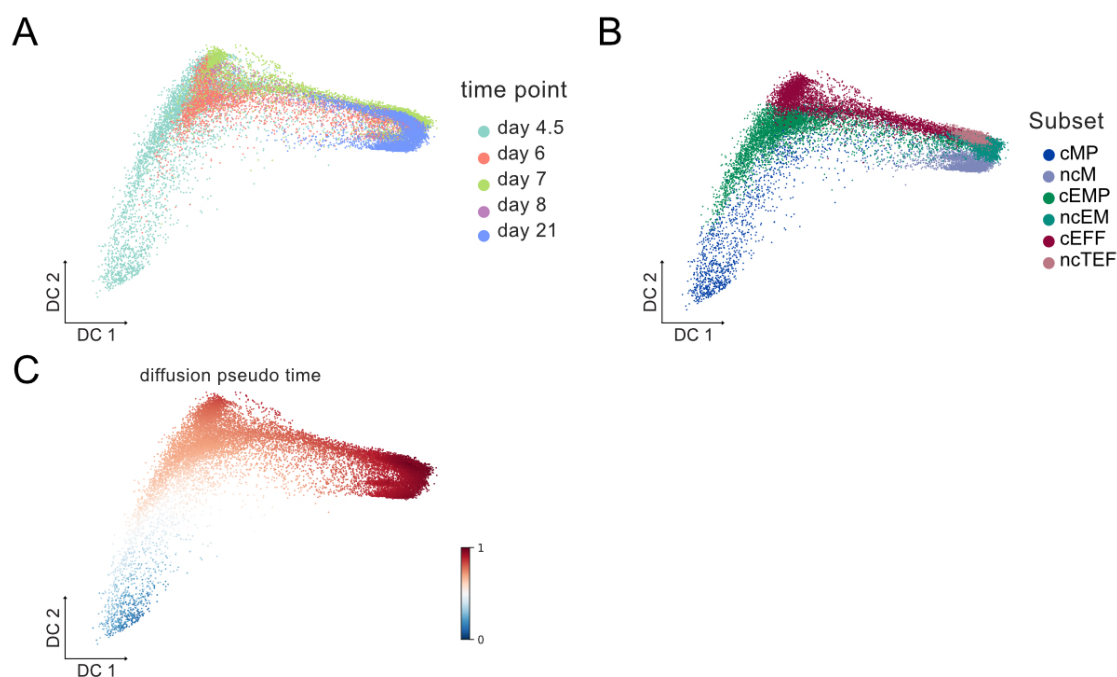


Figure A.5.: Diffusion pseudo-time predicts similar differentiation trajectory as the RNA velocity and the CytoTRACE analysis. **A-D** P14 T cells after the LCMV Armstrong infection in the diffusion map embedding. Diffusion map of the LCMV Armstrong data sets at the day 4.5, 6, 7, 8 and 21 p.i. as in the Figures 3.7, 3.10 and 3.11 coloured by **A** time point p.i. and by **B** subset grouping. **C-D** Diffusion pseudo-time analysis projected in **C** diffusion embedding.

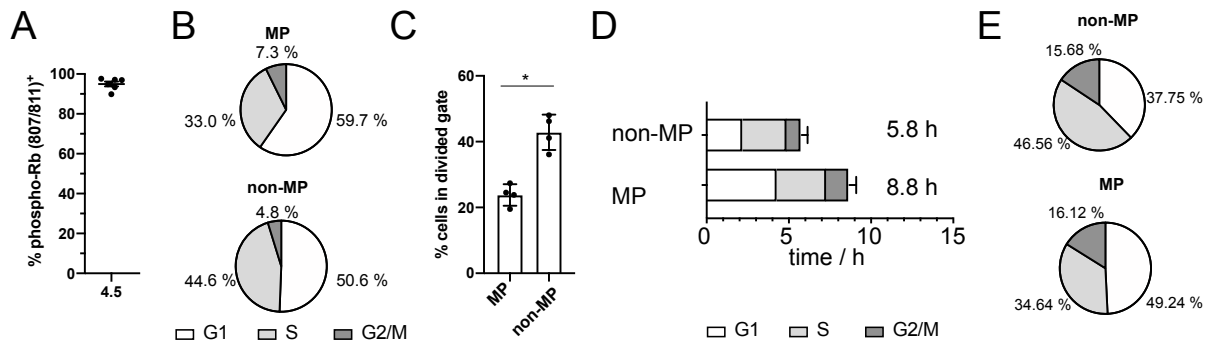


Figure A.6.: During infection with *L.m.-OVA* cells from the MP subset cycle slower compared to the non-MP subset. C57BL/6 mice received $1 \times 10^2 - 5 \times 10^4$ naïve OTI T cells and were subsequently infected with 5×10^3 CFU *L.m.-OVA*. On day 4.5, 8 and 12 p.i. phosphorylation of the Rb protein on the Y807/811 residues was assessed by flow cytometry. **A** Fraction of phospho-Rb⁺ OTI T cells over time. Mean and s.e.m. $n = 6 - 7$ per time point, data from one out of two similar experiments. **B** and **C** as in A, but 3 h (**B**) or 0.5 h (**C**) before analysis of the splenocytes at day 4.5, the mice received 1 mg/mL BrdU i.p. **B** Pie chart with the cell cycle phase distribution for the MP (CD62L⁺) and non-MP (CD62L⁻) after 0.5 h of BrdU labelling ($n = 1$). **C** Bar graphs depict the percentage of cycling cells gated as in Figure 3.2. Mean and std. * $P < 0.05$, Man-Whitney U rank test. **D** Quantified cell cycle speed for MP and non-MP cells and their corresponding cell cycle stage duration based on the mathematical quantification of the data shown in B and C. **E** Contribution of each cell cycle phase to the overall cell cycle length. Data as in D.

Data stems from own experiments, the cell cycle quantification in D was performed by my colleague Jonas Mir.

B. Appendix II

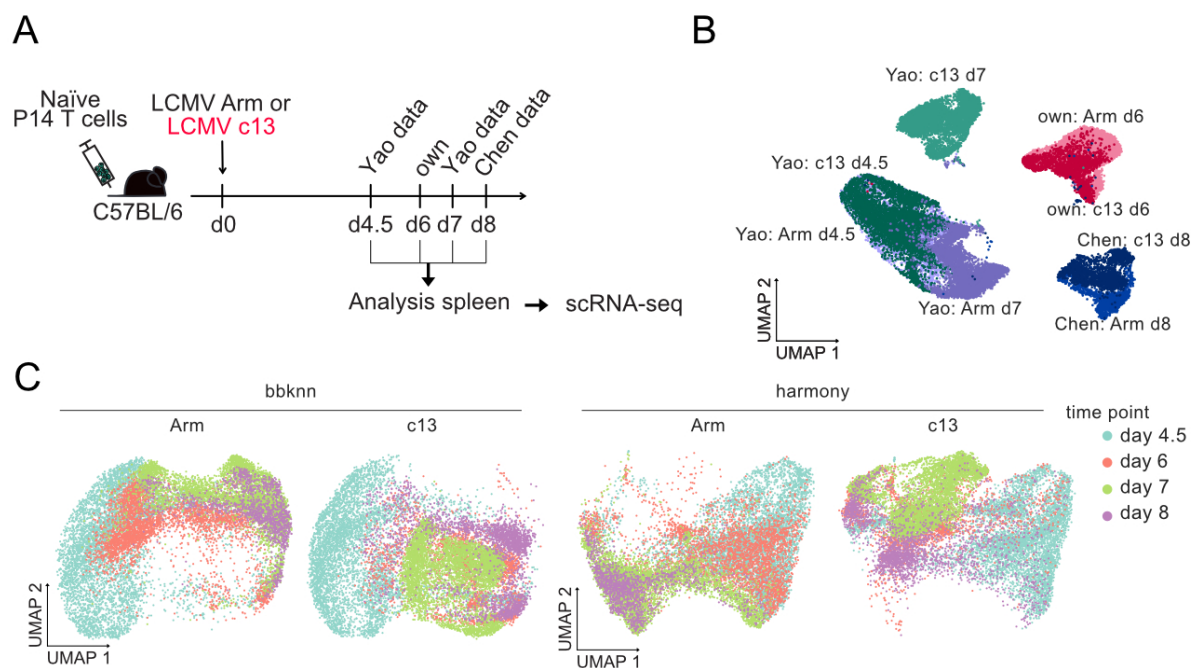


Figure B.1.: Analysis of the P14 T cells transcriptomes during the expansion phase of the T cell differentiation. **A** Scheme of experimental scRNA-seq set-up. C57BL/6 mice received naïve P14 T cells one day before infection with either 2×10^5 pfu LCMV Armstrong or 2×10^6 LCMV clone 13. On day 4.5, 6, 7 and 8 p.i. P14 T cells were collected from the spleen and enriched by flow cytometry before performing scRNA-seq ($10 \times$ Genomics). The data sets from day 4.5 and 7 stem from Yao et al. 2019, day 8 from Chen et al. 2019 and the data from day 6 p.i. was generated in-house. **B** UMAP of combined analysis of the eight data sets from both infections. Colour indicates the infection and the publication from which the data originates. **C** UMAP plot from the combined computed embedding after batch correction with bbknn (left) or Harmony (right) shown for LCMV Armstrong and clone 13, coloured by time-point p.i.

Table B.1.: Summary statistics of the 29 single-cell derived P14 T cell responses at day 8 p.i. LCMV clone 13 with bootstrapped errors.

statistical quantity	subset	data
mean	total cell number	(497 ± 90)
	absolute number of MP	(39 ± 13)
	absolute number of EMP	(250 ± 82)
	absolute number of EFF	(2.3 ± 0.8)
CV	total cell number	(1.7 ± 0.3)
	absolute number of MP	(1.9 ± 0.4)
	absolute number of EMP	(1.8 ± 0.3)
correlation coefficient	absolute number of MP vs. EMP	(0.47 ± 0.15)

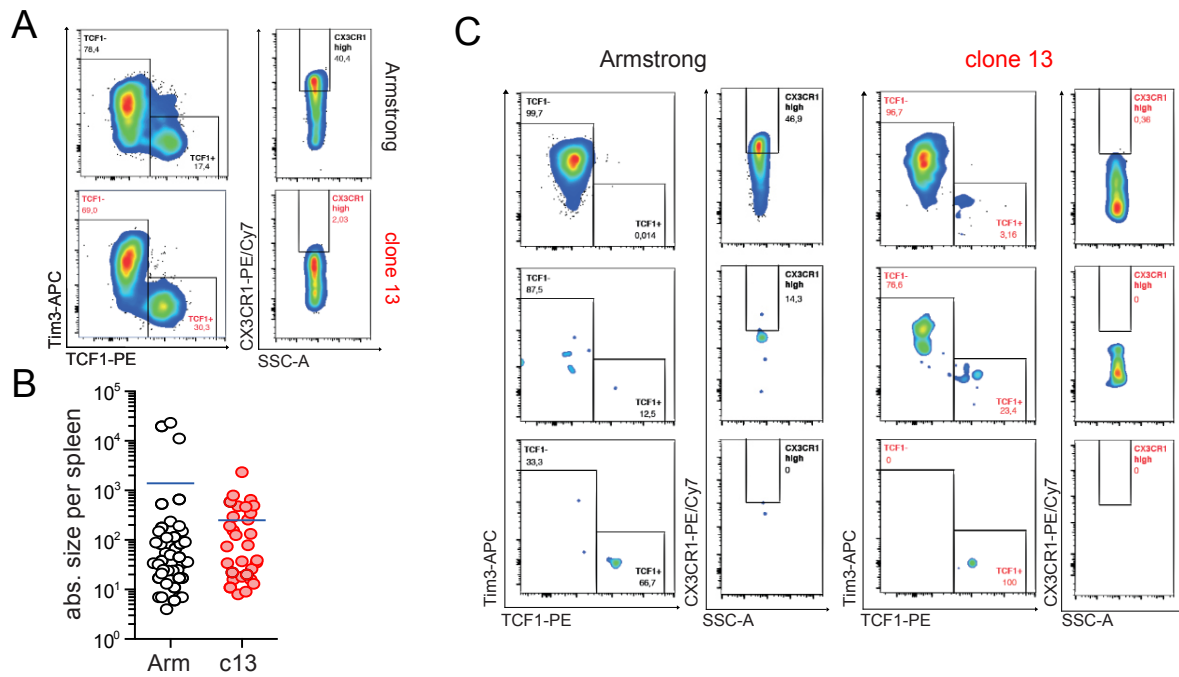


Figure B.2.: Disparate single-cell fates after the infection with LCMV Armstrong or clone 13. **A** Representative pseudo-color plot of the 5×10^2 -cell derived response on their expression of TCF1, Tim3 and CX3CR1 at day 8 p.i. with LCMV Armstrong (top row) or clone 13 (bottom row). **B** Total size of the single-cell derived progenies at day 8 p.i. with LCMV Armstrong or clone 13. **C** Representative pseudo-color plots of single-cell progenies ordered from large (top) to small (bottom) showing the expression of TCF1, Tim3 and CX3CR1 at day 8 p.i. for LCMV Armstrong (left) or clone 13 (right). Experiments were performed by Lorenz Kretschmer and Dr. med. Veit Buchholz. $n = 6 - 26$, data are pooled from two to four independent experiments.

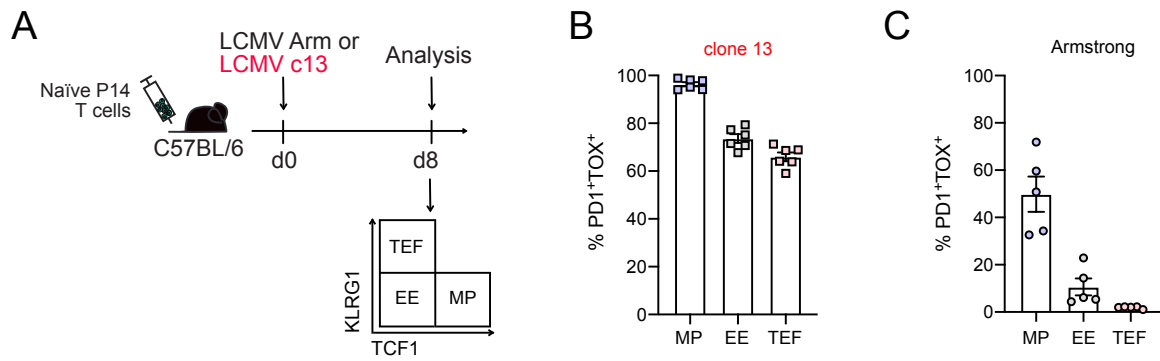


Figure B.3.: TOX is expressed to low levels after acute infection with LCMV Armstrong. **A** Experimental set-up. 5×10^2 naïve P14 T cells were adoptively transferred into C57BL/6 recipients that were infected with either LCMV Armstrong or LCMV clone 13 the next day. On day 8 p.i. the splenic P14 T cells were isolated and analysed by flow cytometry. Based on the expression for TCF1 and KLRG1, the cells were grouped into MP, EE and EFF subsets. Then, the fraction of PD1⁺TOX⁺ cells in the MP, EE and EFF subsets were analysed. **B** Bar graph depicts the percentage PD1⁺TOX⁺ P14 T cells following infection with LCMV clone 13. $n = 6$, Data from two independent experiments. Mean and s.e.m. **C** Bar graph is showing the fraction of PD1⁺TOX⁺ P14 T cells on day 8 after infection with LCMV Armstrong. $n = 5$, Data from two independent experiments. Mean and s.e.m. Data stems from Dr. med. Veit Buchholz and Lorenz Kretschmer.

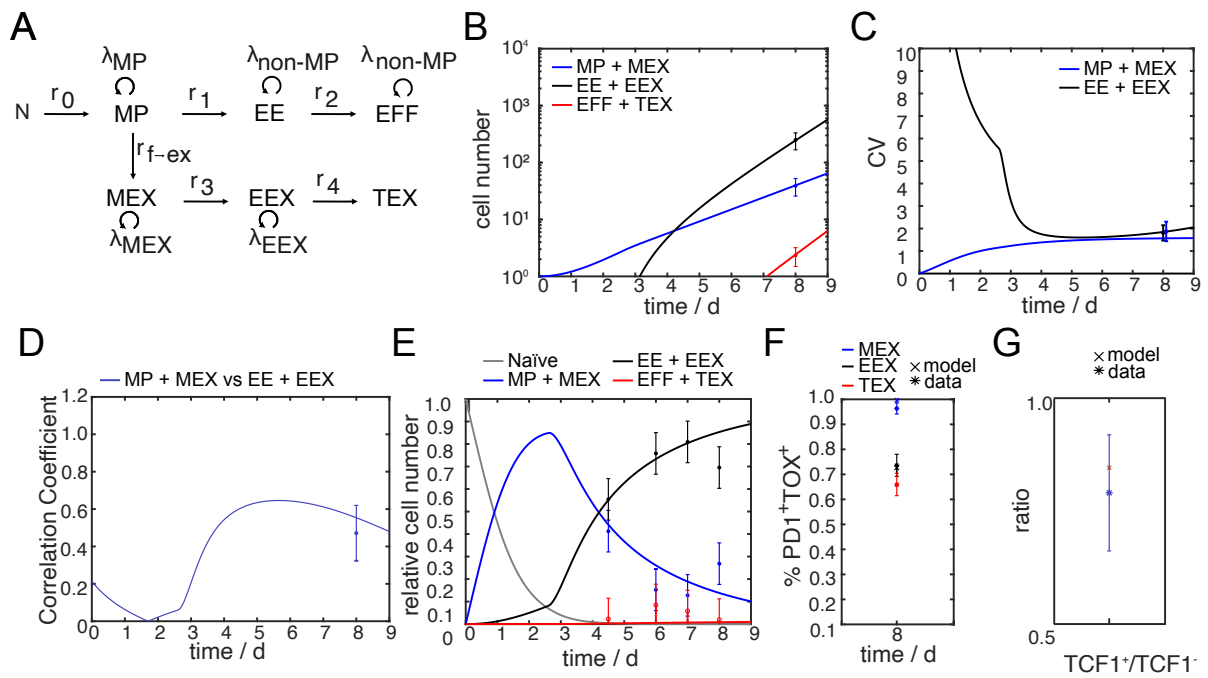


Figure B.4.: Mathematical modelling of P14 T cell responses allowing exhaustion only of the MP subset. **A** Scheme of the mathematical model. **B** Best fit to the mean, **C** the CV and **D** the correlation coefficient of the P14 T cells from day 8 after LCMV clone 13 infection. **E** Using the model in A, the best fit to the relative cell number in each subset, **F** the fraction of PD1⁺TOX⁺ MEX, EEX or TEX subset and **G** to the relative proliferation rate is shown. Experimental data shown in B-D and F stem from Dr. med. Veit Buchholz and Lorenz Kretschmer. Data shown in E and G stem from experiments performed by myself. I performed the mathematical modelling.

C. Appendix III

C.1. Summary of experimental data

The experimental data used to mathematically model CD8⁺ T cells responses directed against LCMV Armstrong, LCMV clone 13 or *L.m.*-OVA infection were obtained from different sources. Table C.1 provides an overview of the data type, its origin and names the person who performed the experiment and/or analysed the data, grouped by infection system.

Table C.1.: Summary of experimental data used for mathematical modelling in this study.

infection model	data type	data origin and analysis
LCMV Armstrong	single cell fate mapping	unpublished data, Buchholz lab
	rel. subset sizes	own data and analysis
	<i>in vivo</i> proliferation	own data and analysis
	cell cycle length quantification	own data, analysis by Jonas Mir
	cell cycle drop out	own data and analyses
	scRNA-seq day 6	own data and analysis
	scRNA-seq day 4.5 and 7	Yao et al. 2019, own analysis
	scRNA-seq day 8	Chen et al. 2019, own analysis
LCMV clone 13	single cell fate mapping	unpublished data, Buchholz lab
	rel. subset sizes	own data and analysis
	exhausted subsets day 8	unpublished data, Buchholz lab
	<i>in vivo</i> proliferation	own data and analysis
	cell cycle length quantification	own data, analysis by Jonas Mir
	cell cycle drop out	own data and analyses
	scRNA-seq day 6	own data and analysis
	scRNA-seq day 4.5 and 7	Yao et al. 2019, own analysis
scRNA-seq day 8	Chen et al. 2019, own analysis	
<i>L.m.</i> -OVA	single cell fate mapping	Buchholz et al. 2013a
	rel. subset sizes	Buchholz et al. 2013a
	<i>in vivo</i> proliferation	own data and analysis
	cell cycle length quantification	own data, analysis by Jonas Mir
	cell cycle drop out	own data and analyses
	scRNA-seq day 4.5, 8 and 12	own data, analysis by Jonas Mir

C.2. ODE system for first and second order moments for the cell cycle dropout extended progressive model

The ODEs, which describe the development of the mean values over time in the cell cycle dropout extended progressive model, were derived using the moments equations as described under section 6.4.3 and are listed here:

$$\begin{aligned}
\frac{d\langle N1(t) \rangle}{dt} &= -r_{N1N2}\langle N1(t) \rangle \\
\frac{d\langle N2(t) \rangle}{dt} &= r_{N1N2}\langle N1(t) \rangle - r_{N2N3}\langle N2(t) \rangle \\
\frac{d\langle N3(t) \rangle}{dt} &= r_{N2N3}\langle N2(t) \rangle - r_{N3N4}\langle N3(t) \rangle \\
\frac{d\langle N4(t) \rangle}{dt} &= r_{N3N4}\langle N3(t) \rangle - r_{N4N5}\langle N4(t) \rangle \\
\frac{d\langle N5(t) \rangle}{dt} &= r_{N4N5}\langle N4(t) \rangle - r_{N5C_A}\langle N5(t) \rangle \\
\frac{d\langle C_A(t) \rangle}{dt} &= 2r_{N5C_A}\langle N5(t) \rangle - (r_{C_AC_B} - \lambda_A + r_{C_ANC_A})\langle C_A(t) \rangle \\
\frac{d\langle C_B(t) \rangle}{dt} &= r_{C_AC_B}\langle C_A(t) \rangle - (r_{C_BC_C} - \lambda_B + r_{C_BNC_B})\langle C_B(t) \rangle \\
\frac{d\langle C_C(t) \rangle}{dt} &= r_{C_BC_C}\langle C_B(t) \rangle + (\lambda_C - r_{C_CNC_C(t)})\langle C_C(t) \rangle \\
\frac{d\langle NC_A(t) \rangle}{dt} &= r_{C_ANC_A}\langle C_A(t) \rangle - r_{C_ANC_A}\langle NC_A(t) \rangle \\
\frac{d\langle NC_B(t) \rangle}{dt} &= r_{C_BNC_B}\langle C_B(t) \rangle + r_{NC_ANC_B}\langle NC_A(t) \rangle - r_{NC_BNC_B}\langle NC_B(t) \rangle \\
\frac{d\langle NC_C(t) \rangle}{dt} &= r_{C_CNC_C}\langle C_C(t) \rangle + r_{NC_BNC_C}\langle NC_B(t) \rangle.
\end{aligned} \tag{C.1}$$

The ODEs describing the time evolution of the variances and co-variances for the cell cycle arrest extended progressive model were derived according to the second moments and the equations for the variances are summarised here:

$$\begin{aligned}
\frac{d\Sigma_{N1}(t)}{dt} &= -2r_{N1N2}\Sigma_{N1}(t) + r_{N1N2}\langle N1(t) \rangle \\
\frac{d\Sigma_{N2}(t)}{dt} &= 2r_{N1N2}\Sigma_{N1N2}(t) - 2r_{N2N3}\Sigma_{N2}(t) + r_{N1N2}\langle N1(t) \rangle + r_{N2N3}\langle N2(t) \rangle \\
\frac{d\Sigma_{N3}(t)}{dt} &= 2r_{N2N3}\Sigma_{N2N3}(t) - 2r_{N3N4}\Sigma_{N3}(t) + r_{N2N3}\langle N2(t) \rangle + r_{N3N4}\langle N3(t) \rangle \\
\frac{d\Sigma_{N4}(t)}{dt} &= 2r_{N3N4}\Sigma_{N3N4}(t) - 2r_{N4N5}\Sigma_{N4}(t) + r_{N3N4}\langle N3(t) \rangle + r_{N4N5}\langle N4(t) \rangle \\
\frac{d\Sigma_{N5}(t)}{dt} &= 2r_{N4N5}\Sigma_{N4N5}(t) - 2r_{N5C_A}\Sigma_{N5}(t) + r_{N4N5}\langle N4(t) \rangle + r_{N5C_A}\langle N5(t) \rangle \\
\frac{d\Sigma_{C_A}(t)}{dt} &= 4r_{N5C_A}\Sigma_{N5C_A}(t) + 4r_{N5C_A}\langle N5(t) \rangle - 2(r_{C_AC_A} - \lambda_A + r_{C_ANC_A})\Sigma_{C_A}(t) \\
&\quad + (\lambda_A + r_{C_AC_A} + r_{C_ANC_A})\langle C_A(t) \rangle
\end{aligned}$$

$$\begin{aligned}
\frac{d\Sigma_{C_B}(t)}{dt} &= 2r_{C_A C_B} \Sigma_{C_A C_B}(t) + r_{C_A C_B} \langle C_A(t) \rangle - 2(r_{C_B C_C} - \lambda_B + r_{C_B N C_B}) \Sigma_{C_A C_B}(t) \\
&\quad + (r_{C_B C_C} + \lambda_B + r_{C_B N C_B}) \langle C_B(t) \rangle \\
\frac{d\Sigma_{C_C}(t)}{dt} &= 2r_{C_B C_C} \Sigma_{C_B C_C}(t) + r_{C_B C_C} \langle C_B(t) \rangle + 2(\lambda_A - r_{C_C N C_C}) \Sigma_{C_C}(t) \\
&\quad + (\lambda_A + r_{C_C N C_C}) \langle C_C(t) \rangle \\
\frac{d\Sigma_{N C_A}(t)}{dt} &= 2r_{C_A N C_A} \Sigma_{C_A N C_A}(t) + r_{C_A N C_A} \langle C_A(t) \rangle - 2r_{C_A N C_A} \Sigma_{N C_A N C_A}(t) \\
&\quad + r_{C_A N C_A} \langle N C_A(t) \rangle \\
\frac{d\Sigma_{N C_B}(t)}{dt} &= 2r_{C_B N C_B} \Sigma_{C_B N C_B} + r_{C_B N C_B} \langle C_B(t) \rangle + 2r_{N C_A N C_B} \Sigma_{N C_B N C_C}(t) \\
&\quad + r_{N C_A N C_B} \langle N C_A(t) \rangle - 2r_{N C_B N C_C} \Sigma_{N C_B}(t) + r_{N C_B N C_C} \langle N C_B(t) \rangle \\
\frac{d\Sigma_{N C_C}(t)}{dt} &= 2r_{C_C N C_C} \Sigma_{C_C N C_C}(t) + r_{C_C N C_C} \langle C_C(t) \rangle + 2r_{N C_B N C_C} \Sigma_{N C_B N C_C}(t) \\
&\quad + r_{N C_B N C_C} \langle N C_B(t) \rangle,
\end{aligned} \tag{C.2}$$

and the equations for the co-variances here:

$$\begin{aligned}
\frac{d\Sigma_{N_1 N_2}(t)}{dt} &= r_{N_1 N_2} \Sigma_{N_1}(t) - (r_{N_1 N_2} + r_{N_2 N_3}) \Sigma_{N_1 N_2}(t) - r_{N_1 N_2} \langle N_1(t) \rangle \\
\frac{d\Sigma_{N_1 N_3}(t)}{dt} &= r_{N_2 N_3} \Sigma_{N_1 N_2}(t) - (r_{N_1 N_2} + r_{N_3 N_4}) \Sigma_{N_1 N_3}(t) \\
\frac{d\Sigma_{N_1 N_3}(t)}{dt} &= r_{N_2 N_3} \Sigma_{N_1 N_2}(t) - (r_{N_1 N_2} + r_{N_3 N_4}) \Sigma_{N_1 N_3}(t) \\
\frac{d\Sigma_{N_1 N_4}(t)}{dt} &= r_{N_3 N_4} \Sigma_{N_1 N_3}(t) - (r_{N_1 N_2} + r_{N_4 N_5}) \Sigma_{N_1 N_4}(t) \\
\frac{d\Sigma_{N_1 N_5}(t)}{dt} &= r_{N_4 N_5} \Sigma_{N_1 N_4}(t) - (r_{N_1 N_2} + r_{N_5 C_A}) \Sigma_{N_1 N_5}(t) \\
\frac{d\Sigma_{N_1 C_A}(t)}{dt} &= 2r_{N_5 C_A} \Sigma_{N_1 N_5}(t) - (r_{N_1 N_2} + r_{C_A C_B} - \lambda_A + r_{C_A N C_A}) \Sigma_{N_1 C_A}(t) \\
\frac{d\Sigma_{N_1 C_B}(t)}{dt} &= r_{C_A C_B} \Sigma_{N_1 C_A}(t) - (r_{N_1 N_2} + r_{C_B C_C} - \lambda_B + r_{C_B N C_B}) \Sigma_{N_1 C_B}(t) \\
\frac{d\Sigma_{N_1 C_C}(t)}{dt} &= r_{C_B C_C} \Sigma_{N_1 C_B}(t) - (r_{N_1 N_2} - \lambda_B + r_{C_C N C_C}) \Sigma_{N_1 C_C}(t) \\
\frac{d\Sigma_{N_1 N C_A}(t)}{dt} &= r_{C_A N C_A} \Sigma_{N_1 C_A}(t) - r_{N_1 N_2} \Sigma_{N_1 N C_A}(t) \\
\frac{d\Sigma_{N_1 N C_B}(t)}{dt} &= r_{C_B N C_B} \Sigma_{N_1 C_B}(t) - r_{N_1 N_2} \Sigma_{N_1 N C_B}(t) \\
\frac{d\Sigma_{N_1 N C_C}(t)}{dt} &= r_{C_C N C_C} \Sigma_{N_1 C_C}(t) - r_{N_1 N_2} \Sigma_{N_1 N C_C}(t) \\
\frac{d\Sigma_{N_2 N_3}(t)}{dt} &= r_{N_1 N_2} \Sigma_{N_1 N_3}(t) + r_{N_2 N_3} \Sigma_{N_2}(t) - (r_{N_2 N_3} + r_{N_3 N_4}) \Sigma_{N_2 N_3}(t) - r_{N_2 N_3} \langle N_2(t) \rangle \\
\frac{d\Sigma_{N_2 N_4}(t)}{dt} &= r_{N_1 N_2} \Sigma_{N_1 N_4}(t) + r_{N_3 N_4} \Sigma_{N_2 N_3}(t) - (r_{N_2 N_3} + r_{N_4 N_5}) \Sigma_{N_2 N_4}(t) \\
\frac{d\Sigma_{N_2 N_5}(t)}{dt} &= r_{N_1 N_2} \Sigma_{N_1 N_5}(t) + r_{N_4 N_5} \Sigma_{N_2 N_4}(t) - (r_{N_2 N_3} + r_{N_5 C_A}) \Sigma_{N_2 N_5}(t)
\end{aligned}$$

$$\begin{aligned}
\frac{d\Sigma_{N2C_A}(t)}{dt} &= r_{N1N2}\Sigma_{N1C_A}(t) + 2r_{N5C_A}\Sigma_{N2N5}(t) - (r_{N2N3} + r_{C_A C_B} - \lambda_A + r_{C_A N C_A})\Sigma_{N2C_A}(t) \\
\frac{d\Sigma_{N2C_B}(t)}{dt} &= r_{N1N2}\Sigma_{N1C_B}(t) + r_{C_A C_B}\Sigma_{N2C_A}(t) - (r_{N2N3} - r_{C_B C_C} + \lambda_B - r_{C_B N C_B})\Sigma_{N2C_B}(t) \\
\frac{d\Sigma_{N2C_C}(t)}{dt} &= r_{N1N2}\Sigma_{N1C_C}(t) + r_{C_C C_C}\Sigma_{N2C_B}(t) - (r_{N2N3} - \lambda_B + r_{C_C N C_C})\Sigma_{N2C_C}(t) \\
\frac{d\Sigma_{N2NC_A}(t)}{dt} &= r_{N1N2}\Sigma_{N1NC_A}(t) + r_{C_A N C_A}\Sigma_{N1C_A} - r_{N2N3}\Sigma_{N2NC_A}(t) \\
\frac{d\Sigma_{N2NC_B}(t)}{dt} &= r_{N1N2}\Sigma_{N1NC_B}(t) + r_{C_B N C_B}\Sigma_{N1C_B} - r_{N2N3}\Sigma_{N2NC_B}(t) \\
\frac{d\Sigma_{N2NC_C}(t)}{dt} &= r_{N1N2}\Sigma_{N1NC_C}(t) + r_{C_C N C_C}\Sigma_{N1C_C} - r_{N2N3}\Sigma_{N2NC_C}(t) \\
\frac{d\Sigma_{N3N4}(t)}{dt} &= r_{N2N3}\Sigma_{N2N4}(t) + r_{N3N4}\Sigma_{N3}(t) - (r_{N3N4} + r_{N4N5})\Sigma_{N3N4}(t) - r_{N3N4}\langle N3(t) \rangle \\
\frac{d\Sigma_{N3N5}(t)}{dt} &= r_{N2N3}\Sigma_{N2N5}(t) - r_{N4N5}\Sigma_{N3N4}(t) - (r_{N3N4} + r_{N5C_A})\Sigma_{N3N5}(t) \\
\frac{d\Sigma_{N3C_A}(t)}{dt} &= r_{N2N3}\Sigma_{N2C_A}(t) + 2r_{N4C_A}\Sigma_{N3N5}(t) - (r_{N3N4} + r_{C_A C_B} - \lambda_A + r_{C_A N C_A})\Sigma_{N3C_A}(t) \\
\frac{d\Sigma_{N3C_B}(t)}{dt} &= r_{N2N3}\Sigma_{N2C_B}(t) + r_{C_A C_B}\Sigma_{N3C_A}(t) - (r_{N3N4} + r_{C_B C_C} - \lambda_B + r_{C_B N C_B})\Sigma_{N3C_B}(t) \\
\frac{d\Sigma_{N3C_C}(t)}{dt} &= r_{N2N3}\Sigma_{N2C_C}(t) + r_{C_B C_C}\Sigma_{N3C_B}(t) + (\lambda_C - r_{C_C N C_C})\Sigma_{N3C_C}(t) \\
\frac{d\Sigma_{N3NC_A}(t)}{dt} &= r_{N2N3}\Sigma_{N2NC_A}(t) + r_{C_A N C_A}\Sigma_{N3C_A}(t) + r_{N3N4}\Sigma_{N3NC_A}(t) \\
\frac{d\Sigma_{N3NC_B}(t)}{dt} &= r_{N2N3}\Sigma_{N2NC_B}(t) + r_{C_B N C_B}\Sigma_{N3C_B}(t) + r_{N3N4}\Sigma_{N3NC_B}(t) \\
\frac{d\Sigma_{N3NC_C}(t)}{dt} &= r_{N2N3}\Sigma_{N2NC_C}(t) + r_{C_C N C_C}\Sigma_{N3C_C}(t) + r_{N3N4}\Sigma_{N4N5}(t) \\
\frac{d\Sigma_{N4N5}(t)}{dt} &= r_{N3N4}\Sigma_{N3N5}(t) + r_{N4N5}\Sigma_{N4}(t) - (r_{N4N5} + r_{N5C_A})\Sigma_{N4N5}(t) - r_{N4N5}\langle N4(t) \rangle \\
\frac{d\Sigma_{N4C_A}(t)}{dt} &= r_{N3N4}\Sigma_{N3C_A}(t) + 2r_{N5C_A}\Sigma_{N4N5}(t) - (r_{N3N4} + r_{C_A C_B} - \lambda_A + r_{C_A N C_A})\Sigma_{N4C_A}(t) \\
\frac{d\Sigma_{N4C_B}(t)}{dt} &= r_{N3N4}\Sigma_{N3C_B}(t) - r_{C_A C_B}\Sigma_{N4C_A}(t) - (r_{N4N5} + r_{C_B C_C} - \lambda_B + r_{C_B N C_B})\Sigma_{N4C_B}(t) \\
\frac{d\Sigma_{N4C_C}(t)}{dt} &= r_{N3N4}\Sigma_{N3C_C}(t) + r_{C_B C_C}\Sigma_{N4C_B}(t) - (r_{N4N5} - \lambda_B + r_{C_B N C_B})\Sigma_{N4C_C}(t) \\
\frac{d\Sigma_{N4NC_A}(t)}{dt} &= r_{N3N4}\Sigma_{N3NC_A}(t) - r_{N3N4}\Sigma_{N4NC_A}(t) + r_{C_A N C_A}\Sigma_{N4NC_A}(t) \\
\frac{d\Sigma_{N4NC_B}(t)}{dt} &= r_{N3N4}\Sigma_{N3NC_B}(t) - r_{N3N4}\Sigma_{N4NC_B}(t) + r_{C_B N C_B}\Sigma_{N4NC_B}(t) \\
\frac{d\Sigma_{N4NC_C}(t)}{dt} &= r_{N3N4}\Sigma_{N3NC_C}(t) - r_{N3N4}\Sigma_{N4NC_C}(t) + r_{C_C N C_C}\Sigma_{N4NC_C}(t) \\
\frac{d\Sigma_{N5C_A}(t)}{dt} &= r_{N4N5}\Sigma_{N4C_A}(t) + 2r_{N5C_A}\Sigma_{N5}(t) - (r_{N5C_A} + r_{C_A C_B} - \lambda_A + r_{C_A N C_A})\Sigma_{N5NC_A}(t) \\
&\quad - 2r_{N5C_A}\langle N5(t) \rangle \\
\frac{d\Sigma_{N5C_B}(t)}{dt} &= r_{N4N5}\Sigma_{N4C_B}(t) + r_{C_A C_B}\Sigma_{N5C_A}(t) - (r_{N5C_A} + r_{C_B C_C} - \lambda_B + r_{C_B N C_B})\Sigma_{N5C_B}(t)
\end{aligned}$$

$$\begin{aligned}
\frac{d\Sigma_{N_5C_C}(t)}{dt} &= r_{N_4N_5}\Sigma_{N_4C_C}(t) + r_{C_B C_C}\Sigma_{N_5C_B}(t) - (r_{N_5C_A} - \lambda_C + r_{C_C N_C})\Sigma_{N_5C_C}(t) \\
\frac{d\Sigma_{N_5NC_A}(t)}{dt} &= r_{N_4N_5}\Sigma_{N_4NC_A}(t) + r_{C_A NC_A}\Sigma_{N_5NC_A}(t) - r_{N_5C_A}\Sigma_{N_5NC_A}(t) \\
\frac{d\Sigma_{N_5NC_B}(t)}{dt} &= r_{N_4N_5}\Sigma_{N_4NC_B}(t) + r_{C_B NC_B}\Sigma_{N_5NC_B}(t) - r_{N_5C_A}\Sigma_{N_5NC_B}(t) \\
\frac{d\Sigma_{N_5NC_C}(t)}{dt} &= r_{N_4N_5}\Sigma_{N_4NC_C}(t) + r_{C_C NC_C}\Sigma_{N_5NC_C}(t) - r_{N_5C_A}\Sigma_{N_5NC_C}(t) \\
\frac{d\Sigma_{C_A C_B}(t)}{dt} &= 2r_{N_5C_A}\Sigma_{N_5C_B}(t) + r_{C_A C_B}\Sigma_{C_A}(t) \\
&\quad - (r_{C_A C_B} - \lambda_A + r_{C_A NC_A} + r_{C_B C_C} - \lambda_B + r_{C_B NC_B})\Sigma_{C_A C_B}(t) - r_{C_A C_B}\langle C_A(t) \rangle \\
\frac{d\Sigma_{C_A C_C}(t)}{dt} &= 2r_{N_5C_A}\Sigma_{N_5C_C}(t) + r_{C_A C_B}\Sigma_{C_A C_B}(t) \\
&\quad - (r_{C_A C_B} - \lambda_A + r_{C_A NC_A} - \lambda_C + r_{C_C NC_C})\Sigma_{C_A C_C}(t) \\
\frac{d\Sigma_{C_A NC_A}(t)}{dt} &= 2r_{N_5C_A}\Sigma_{N_5NC_A}(t) + r_{C_A NC_A}\Sigma_{C_A}(t) - (r_{C_A C_B} - \lambda_A + r_{C_A NC_A}) - r_{C_A NC_A}\langle C_A(t) \rangle \\
\frac{d\Sigma_{C_A NC_B}(t)}{dt} &= 2r_{N_5C_A}\Sigma_{N_5NC_B}(t) + r_{C_B NC_B}\Sigma_{C_A C_B}(t) - (r_{C_A C_B} - \lambda_A + r_{C_A NC_A})\Sigma_{C_A NC_B}(t) \\
\frac{d\Sigma_{C_A NC_C}(t)}{dt} &= 2r_{N_5C_A}\Sigma_{N_5NC_C}(t) + r_{C_C NC_C}\Sigma_{C_A C_C}(t) - (r_{C_A C_B} - \lambda_A + r_{C_A NC_A})\Sigma_{C_A NC_C}(t) \\
\frac{d\Sigma_{C_B C_C}(t)}{dt} &= r_{C_A C_B}\Sigma_{C_A C_C}(t) + r_{C_B C_C}\Sigma_{C_B}(t) \\
&\quad - (r_{C_B C_C} - \lambda_B + r_{C_B NC_B} - \lambda_C + r_{C_C NC_C})\Sigma_{C_B C_C}(t) - r_{C_B C_C}\langle C_B(t) \rangle \\
\frac{d\Sigma_{C_B NC_A}(t)}{dt} &= r_{C_A NC_A}\Sigma_{C_A C_B}(t) + r_{C_A C_B}\Sigma_{C_A NC_A}(t) - (r_{C_B C_C} - \lambda_B + r_{C_B NC_B})\Sigma_{C_B NC_A}(t) \\
\frac{d\Sigma_{C_B NC_B}(t)}{dt} &= r_{C_A C_B}\Sigma_{C_A NC_B}(t) + r_{C_B NC_B}\Sigma_{C_B}(t) \\
&\quad - (r_{C_B C_C} - \lambda_B + r_{C_B NC_B})\Sigma_{C_B NC_B}(t) - r_{C_B NC_B}\langle C_B(t) \rangle \\
\frac{d\Sigma_{C_B NC_C}(t)}{dt} &= r_{C_A C_B}\Sigma_{C_A NC_C}(t) + r_{C_C NC_C}\Sigma_{C_B C_C}(t) - (r_{C_B C_C} - \lambda_B + r_{C_B NC_B})\Sigma_{C_B NC_C}(t) \\
\frac{d\Sigma_{C_C NC_A}(t)}{dt} &= r_{C_A NC_A}\Sigma_{C_A C_C}(t) + r_{C_B C_C}\Sigma_{C_B NC_A}(t) + (\lambda_C - r_{C_C NC_C})\Sigma_{C_C NC_A}(t) \\
\frac{d\Sigma_{C_C NC_B}(t)}{dt} &= r_{C_B NC_B}\Sigma_{C_B C_C}(t) + r_{C_B C_C}\Sigma_{C_B NC_B}(t) + (\lambda_C - r_{C_C NC_C})\Sigma_{C_C NC_B}(t) \\
\frac{d\Sigma_{C_C NC_C}(t)}{dt} &= r_{C_B C_C}\Sigma_{C_B NC_C}(t) + r_{C_C NC_C}\Sigma_{C_C}(t) + (\lambda_C - r_{C_C NC_C})\Sigma_{C_C NC_C}(t) - r_{C_C NC_C}\langle C_C(t) \rangle \\
\frac{d\Sigma_{NC_A NC_B}(t)}{dt} &= r_{C_A NC_A}\Sigma_{C_A NC_B}(t) + r_{C_B NC_B}\Sigma_{C_B NC_A}(t) \\
\frac{d\Sigma_{NC_A NC_C}(t)}{dt} &= r_{C_A NC_C}\Sigma_{C_A NC_B}(t) + r_{C_C NC_C}\Sigma_{C_C NC_A}(t) \\
\frac{d\Sigma_{NC_B NC_C}(t)}{dt} &= r_{C_B NC_B}\Sigma_{C_B NC_C}(t) + r_{C_C NC_C}\Sigma_{C_C NC_B}(t)
\end{aligned} \tag{C.3}$$

C.3. ODE system for first and second order moments for the arrested model of T cell exhaustion

The ODEs describing the mean values over time for the early bifurcation model, that was introduced during chapter 4, were derived according to the master equation for the moments as described under section 6.4.3 and are listed here:

$$\begin{aligned}
\frac{d\langle N(t) \rangle}{dt} &= -r_{NA_f} \langle N(t) \rangle \\
\frac{d\langle A_f(t) \rangle}{dt} &= r_{NA_f} \langle N(t) \rangle - (r_{A_f B_f} - \lambda_{A_f} + r_{A_f A_{ex}}) \\
\frac{d\langle B_f(t) \rangle}{dt} &= r_{A_f B_f} \langle A_f(t) \rangle - (r_{B_f C_f} - \lambda_{B_f} + r_{B_f B_{ex}}) \\
\frac{d\langle C_f(t) \rangle}{dt} &= r_{B_f C_f} \langle B_f(t) \rangle + (\lambda_{C_f} + r_{C_f C_{ex}}) \\
\frac{d\langle A_{ex}(t) \rangle}{dt} &= r_{A_f A_{ex}} \langle A_f(t) \rangle + (\lambda_{A_{ex}} + r_{A_{ex} B_{ex}}) \\
\frac{d\langle B_{ex}(t) \rangle}{dt} &= r_{B_f B_{ex}} \langle B_f(t) \rangle + r_{A_{ex} B_{ex}} \langle A_{ex}(t) \rangle - (r_{B_{ex} C_{ex}} - \lambda_{B_{ex}}) \\
\frac{d\langle C_{ex}(t) \rangle}{dt} &= r_{C_f C_{ex}} \langle C_f(t) \rangle + r_{B_{ex} C_{ex}} \langle B_{ex}(t) \rangle
\end{aligned} \tag{C.4}$$

The equation to quantify the time development for the variances and co-variances were deduced from equation (??). The ODEs for the variances are listed below:

$$\begin{aligned}
\frac{d\Sigma_N(t)}{dt} &= -2r_{NA_f} \Sigma_N(t) + r_{NA_f} \langle N(t) \rangle \\
\frac{d\Sigma_{A_f(t)}}{dt} &= r_{NA_f} \langle N(t) \rangle + (\lambda_{A_f} + r_{A_f B_f} + r_{A_f A_{ex}}) \langle A_f(t) \rangle + 2r_{NA_f} \Sigma_{NA_f}(t) \\
&\quad - 2(r_{A_f B_f} - \lambda_{A_f} + r_{A_f A_{ex}}) \Sigma_{A_f}(t) \\
\frac{d\Sigma_{B_f(t)}}{dt} &= r_{A_f B_f} \langle A_f(t) \rangle + (\lambda_{B_f} + r_{B_f C_f} + r_{B_f B_{ex}}) \langle B_f(t) \rangle + 2r_{A_f B_f} \Sigma_{A_f B_f}(t) \\
&\quad - 2(r_{B_f C_f} - \lambda_{B_f} + r_{B_f B_{ex}}) \Sigma_{B_f}(t) \\
\frac{d\Sigma_{C_f(t)}}{dt} &= r_{B_f C_f} \langle B_f(t) \rangle + (\lambda_{C_f} + r_{C_f C_{ex}}) \langle C_f(t) \rangle + 2r_{B_f C_f} \Sigma_{B_f C_f}(t) + 2(\lambda_{C_f} - r_{C_f C_{ex}}) \Sigma_{C_f}(t) \\
\frac{d\Sigma_{A_{ex}(t)}}{dt} &= r_{A_f A_{ex}} \langle A_f(t) \rangle + (\lambda_{A_{ex}} + r_{A_f A_{ex}}) \langle A_{ex}(t) \rangle + 2r_{A_f A_{ex}} \Sigma_{A_f A_{ex}}(t) + 2(\lambda_{A_{ex}} - r_{A_f A_{ex}}) \Sigma_{A_{ex}}(t) \\
\frac{d\Sigma_{B_{ex}(t)}}{dt} &= r_{B_f B_{ex}} \langle B_f(t) \rangle + r_{A_{ex} B_{ex}} \langle A_{ex}(t) \rangle + (\lambda_{B_{ex}} + r_{B_f B_{ex}}) \langle B_{ex}(t) \rangle + 2(r_{B_f B_{ex}} - \lambda_{B_{ex}}) \Sigma_{B_{ex}}(t) \\
&\quad + 2r_{B_f B_{ex}} \Sigma_{B_f B_{ex}}(t) + 2r_{A_{ex} B_{ex}} \Sigma_{A_{ex} B_{ex}}(t) \\
\frac{d\Sigma_{C_{ex}(t)}}{dt} &= r_{C_f C_{ex}} \langle C_f(t) \rangle + c \langle B_{ex}(t) \rangle + 2r_{C_f C_{ex}} \Sigma_{C_f C_{ex}}(t) + 2r_{B_{ex} C_{ex}} \Sigma_{B_{ex} C_{ex}}(t).
\end{aligned} \tag{C.5}$$

The ODE equations for the co-variances are listed here:

$$\begin{aligned}
\frac{d\Sigma_{NA_f}(t)}{dt} &= -r_{NA_f}\langle N(t) \rangle + r_{NA_f}\Sigma_N(t) - (r_{NA_f} + r_{A_fB_f} - \lambda_{A_f} + r_{A_fA_{ex}})\Sigma_{NA_f}(t) \\
\frac{d\Sigma_{NB_f}(t)}{dt} &= r_{A_fB_f}\Sigma_{NA_f}(t) - (r_{NA_f} + r_{B_fC_f} - \lambda_{B_f} + r_{B_fB_{ex}})\Sigma_{NB_f}(t) \\
\frac{d\Sigma_{NC_f}(t)}{dt} &= r_{B_fC_f}\Sigma_{NB_f}(t) - (r_{NA_f} - \lambda_{C_f} + r_{C_fC_{ex}})\Sigma_{NC_f}(t) \\
\frac{d\Sigma_{NA_{ex}}(t)}{dt} &= r_{A_fA_{ex}}\Sigma_{NA_f}(t) - (r_{NA_f} - \lambda_{A_{ex}} + r_{A_{ex}B_{ex}})\Sigma_{NA_{ex}}(t) \\
\frac{d\Sigma_{NB_{ex}}(t)}{dt} &= r_{B_fB_{ex}}\Sigma_{NB_f}(t) + r_{A_{ex}B_{ex}}\Sigma_{NA_{ex}}(t) - (r_{NA_f} - \lambda_{B_{ex}} + r_{B_{ex}C_{ex}})\Sigma_{NB_{ex}}(t) \\
\frac{d\Sigma_{NC_{ex}}(t)}{dt} &= r_{C_fC_{ex}}\Sigma_{NC_f}(t) + r_{B_{ex}C_{ex}}\Sigma_{NB_f}(t) - r_{NA_f}\Sigma_{NC_{ex}}(t) \\
\frac{d\Sigma_{A_fB_f}(t)}{dt} &= -r_{A_fB_f}\langle A_f(t) \rangle + r_{A_fB_f}\Sigma_{A_f}(t) + r_{NA_f}\Sigma_{NB_f}(t) \\
&\quad - (r_{A_fB_f} - \lambda_{A_f} + r_{A_fA_{ex}} - \lambda_{B_f} + r_{B_fB_{ex}})\Sigma_{A_fB_f}(t) \\
\frac{d\Sigma_{A_fC_f}(t)}{dt} &= r_{NA_f}\Sigma_{NC_f}(t) + r_{B_fC_f}\Sigma_{A_f}(t) \\
&\quad + (\lambda_{C_f} - r_{C_fC_{ex}} - r_{A_fB_f} - \lambda_{A_f} + r_{A_fA_{ex}})\Sigma_{A_fC_f}(t) \\
\frac{d\Sigma_{A_fA_{ex}}(t)}{dt} &= -r_{A_fA_{ex}}\langle A_f(t) \rangle + r_{A_fA_{ex}}\Sigma_{A_f}(t) + r_{NA_f}\Sigma_{NB_f}(t) \\
&\quad + (\lambda_{A_{ex}} - r_{A_{ex}B_{ex}} - r_{A_fB_f} - \lambda_{A_f} + r_{A_fA_{ex}})\Sigma_{A_fA_{ex}}(t) \\
\frac{d\Sigma_{A_fB_{ex}}(t)}{dt} &= r_{NA_f}\Sigma_{NB_{ex}}(t) + r_{B_fB_{ex}}\Sigma_{A_fB_f}(t)r_{A_{ex}B_{ex}}\Sigma_{A_fA_{ex}}(t) \\
&\quad - (r_{B_{ex}C_{ex}} - \lambda_{B_{ex}} - r_{A_fB_f} - \lambda_{A_f} + r_{A_fA_{ex}})\Sigma_{A_fB_{ex}}(t) \\
\frac{d\Sigma_{A_fC_{ex}}(t)}{dt} &= r_{NA_f}\Sigma_{NC_{ex}}(t) + r_{C_fC_{ex}}\Sigma_{A_fA_{ex}}(t) + r_{B_{ex}C_{ex}}\Sigma_{A_fB_{ex}}(t) \\
&\quad + (r_{A_fB_f} - \lambda_{A_f} + r_{A_fA_{ex}})\Sigma_{A_fC_{ex}}(t) \\
\frac{d\Sigma_{B_fC_f}(t)}{dt} &= -r_{B_fC_f}\langle B_f(t) \rangle + r_{B_fC_f}\Sigma_{B_f} + r_{A_fB_f} + \Sigma_{A_fC_f}(t) \\
&\quad - (r_{B_fC_f} - \lambda_{B_f} + r_{B_fB_{ex}} - \lambda_{C_f} + r_{C_fC_{ex}})\Sigma_{B_fC_f}(t) \\
\frac{d\Sigma_{B_fA_{ex}}(t)}{dt} &= r_{A_fA_{ex}}\Sigma_{A_fB_f} + r_{A_fB_f}\Sigma_{A_fA_{ex}} \\
&\quad - (r_{B_fC_f} - \lambda_{B_f} + r_{B_fB_{ex}} - \lambda_{A_{ex}} + r_{A_{ex}B_{ex}})\Sigma_{B_fA_{ex}}(t) \\
\frac{d\Sigma_{B_fB_{ex}}(t)}{dt} &= -r_{B_fB_{ex}}\langle B_f(t) \rangle + r_{B_fB_{ex}}\Sigma_{B_f} + r_{A_fB_f} + \Sigma_{A_fB_{ex}}(t) + r_{A_{ex}B_{ex}} + \Sigma_{B_fA_{ex}}(t) \\
&\quad - (r_{B_fC_f} - \lambda_{B_f} + r_{B_fB_{ex}} - \lambda_{B_{ex}} + r_{B_{ex}C_{ex}})\Sigma_{B_fB_{ex}}(t) \\
\frac{d\Sigma_{B_fC_{ex}}(t)}{dt} &= r_{A_fB_f} + \Sigma_{A_fC_{ex}}(t) + r_{C_fC_{ex}} + \Sigma_{B_fC_f}(t) + r_{B_{ex}C_{ex}} + \Sigma_{B_fB_{ex}}(t) \\
&\quad - ((r_{B_fC_f} - \lambda_{B_f} + r_{B_fB_{ex}})\Sigma_{B_fC_{ex}}(t) \\
\frac{d\Sigma_{C_fA_{ex}}(t)}{dt} &= r_{A_fA_{ex}} + \Sigma_{A_fA_{ex}}(t) + r_{B_fC_f} + \Sigma_{B_fA_{ex}}(t) + (\lambda_{C_f} - r_{C_fC_{ex}} + \lambda_{A_{ex}} - r_{A_{ex}B_{ex}})\Sigma_{C_fA_{ex}}(t)
\end{aligned}$$

$$\begin{aligned}
\frac{d\Sigma_{C_f B_{\text{ex}}}(t)}{dt} &= r_{B_f B_{\text{ex}}} + \Sigma_{B_f C_f}(t) + r_{B_f C_f} + \Sigma_{B_f B_{\text{ex}}}(t) + r_{A_{\text{ex}} B_{\text{ex}}} + \Sigma_{C_f B_{\text{ex}}}(t) \\
&\quad - (r_{C_f C_{\text{ex}}} - \lambda_{C_f} + r_{B_{\text{ex}} C_{\text{ex}}} - \lambda_{B_{\text{ex}}}) \Sigma_{C_f B_{\text{ex}}}(t) \\
\frac{d\Sigma_{C_f C_{\text{ex}}}(t)}{dt} &= -r_{C_f C_{\text{ex}}} \langle C_f(t) \rangle + r_{C_f C_{\text{ex}}} \Sigma_{C_f}(t) + r_{B_f C_f} + \Sigma_{B_f C_{\text{ex}}}(t) + r_{B_{\text{ex}} C_{\text{ex}}} + \Sigma_{C_f B_{\text{ex}}}(t) \\
&\quad + (\lambda_{C_f} + r_{C_f C_{\text{ex}}}) \Sigma_{C_f C_{\text{ex}}}(t) \\
\frac{d\Sigma_{A_{\text{ex}} B_{\text{ex}}}(t)}{dt} &= -r_{A_{\text{ex}} B_{\text{ex}}} \langle A_{\text{ex}}(t) \rangle + r_{A_{\text{ex}} B_{\text{ex}}} \Sigma_{A_{\text{ex}}}(t) + r_{A_f A_{\text{ex}}} \Sigma_{A_f B_{\text{ex}}}(t) + r_{B_f B_{\text{ex}}} \Sigma_{B_f A_{\text{ex}}}(t) \\
&\quad - (r_{A_{\text{ex}} B_{\text{ex}}} - \lambda_{A_{\text{ex}}} - \lambda_{B_{\text{ex}}} + r_{B_{\text{ex}} C_{\text{ex}}}) \Sigma_{A_{\text{ex}} B_{\text{ex}}}(t) \\
\frac{d\Sigma_{A_{\text{ex}} C_{\text{ex}}}(t)}{dt} &= r_{A_f A_{\text{ex}}} \Sigma_{A_f C_{\text{ex}}}(t) + r_{C_f C_{\text{ex}}} \Sigma_{C_f A_{\text{ex}}}(t) + r_{B_{\text{ex}} C_{\text{ex}}} \Sigma_{A_{\text{ex}} B_{\text{ex}}}(t) \\
&\quad + (\lambda_{A_{\text{ex}}} + r_{A_{\text{ex}} B_{\text{ex}}}) \Sigma_{A_{\text{ex}} C_{\text{ex}}}(t) \\
\frac{d\Sigma_{B_{\text{ex}} C_{\text{ex}}}(t)}{dt} &= -r_{B_{\text{ex}} C_{\text{ex}}} \langle B_{\text{ex}}(t) \rangle + r_{B_{\text{ex}} C_{\text{ex}}} \Sigma_{B_{\text{ex}}}(t) + r_{B_f B_{\text{ex}}} \Sigma_{B_f C_{\text{ex}}}(t) + r_{C_f C_{\text{ex}}} \Sigma_{C_f B_{\text{ex}}}(t) \\
&\quad + r_{A_{\text{ex}} B_{\text{ex}}} \Sigma_{A_{\text{ex}} B_{\text{ex}}}(t) - (r_{B_{\text{ex}} C_{\text{ex}}} - \lambda_{B_{\text{ex}}}) \Sigma_{B_{\text{ex}} C_{\text{ex}}}(t)
\end{aligned} \tag{C.6}$$